Modelling Mesopause OH* Emissions using a

Global Circulation Model

A thesis submitted to

Maynooth University

for the degree of

Doctor of Philosophy

September 2015

Presented By

Dean J. McCarthy, B.Sc.

Department of Experimental Physics

Faculty of Science and Engineering

Head of Department: Prof. J. Anthony Murphy

Research Supervisor: Dr. Frank J. Mulligan

Table of Contents

Figure Contents

Acronyms

Acronym	Name	Notes
AURA	-	NASA satellite.
Caltech 1-D	California Institute of Technology 1-D Model	1-D Photochemical Model.
CCM	Coupled Community Model	Predecessor of WACCM.
CCM2	Coupled Community Model 2	Predecessor of WACCM.
CIRA	Cospar International Reference Atmosphere	Used by M1-D model for initial O^3 profiles.
CMAT	Coupled Middle Atmosphere and Thermosphere	Predecessor of CMAT2.
CMAT2	Coupled Middle Atmosphere and Thermosphere 2	GCM employed in this thesis.
CME	Coronal Mass Ejection	
CTIM	Coupled Thermosphere and Ionosphere Model	Predecessor of CMAT2.
CTIP	Coupled Thermosphere Ionosphere Plasmasphere	Predecessor of CMAT2.
EDMF	Electronic Dipole Moment Function	Used to calculate Einstein A coefficients.
EM	Electro-Magnetic	
ENIAC	Electronic Numerical Integrator And Calculator	First computer used for weather predictions.
ENVISAT	Environment Satellite	ESA satellite.
ESA	European Space Agency	
EUV	extreme ultra violet	
FUV	far ultra violet	
GCM	Global Climate Model General Circulation Model	A type of 3-D model.
GOMOS	Global Ozone Monitoring by Occultation of Stars	Provides global observations of ozone. Instrument on board

		ENVISAT satellite.
GSWM	Global Scale Wave Model	Model used to simulate tides.
HALOE	HALogen Occultation Experiment	Provides initial conditions for CMAT2.
HAMMONIA	Hamburg Model of the Neutral and Ionised Atmosphere	A GCM developed at MPI in Hamburg.
IMF	Interplanetary Magnetic Field	
IR	infra-red	
JHU/APL 2-D	John Hopkins University/Applied Physics Laboratory 2-D Model	
JPL	Jet Propulsion Laboratory	
LTE	Local Thermodynamic Equilibrium	
M1-D	Maynooth 1-D Model	1-D Model developed for this thesis.
MLS	Microwave Limb Sounder	Instrument on AURA satellite.
MLT	Middle Lower Thermosphere	
MPI	Max Planck Institute	
MSISE-90	Mass Spectrometer and ground based Incoherent Scatter Extended	Used by CMAT2 for initial concentrations of major species.
NASA	National Aeronautics and Space Administration	
NCAR	National Centre for Atmospheric Research	
NLC	Noctilucent Clouds	
NRL-CHEM1-D	Naval Research Laboratory, 1-D Chemical Model	A 1-D Photochemical Model.
ROSE	-	A chemical transport model. Considered a GCM.
SABER	Sounding of the Atmosphere using Broadband Emission Radiometry	Instrument used to look at OH^* emissions onboard

		TIMED satellite.
SCIAMACHY	SCanning Imaging Absorption spectroMeter for Atmospheric CHartographY	Instrument used to look at OH^* emissions onboard ENVISAT satellite.
SHIMMER	Spatial Heterodyne Imager for Mesospheric Radicals	Used to look at OH in middle atmosphere.
SME	Solar Mesosphere Explorer	First satellite to look at OH^* emissions. Operational from 1981-1989.
STPSat1	Space Test Programme Satellite 1	NASA satellite.
TIME	Thermosphere Ionosphere Mesosphere Energetics	A GCM.
TIMED	Thermosphere-Ionosphere-Mesosphere Energetics and Dynamics	NASA satellite.
UARS	Upper Atmosphere Research Satellite	NASA satellite.
UCL	University College London	Development place of CMAT2.
UGAMP	Universities Global Atmospheric Modelling Programme	Used by CMAT2 for O_3 climatologies.
UV	ultra violet	
ver	volume emission rate	
vmr	volume mixing ratio	
WACCM	Whole Atmosphere Community Climate Model	A GCM.
WINDII	Wind Imaging Interferometer	Interferometer onboard the UARS satellite.

Abstract

Nightglow within the mesopause region of the atmosphere is dominated by the infrared emissions from vibrationally excited hydroxyl (OH^*) radicals at ~ 87 km altitude. These emissions provide a signal from which the behaviour of the middle atmosphere can be studied and in recent years a wealth of observational data on the global distribution of OH^* has been collected by instruments such as SABER on board NASA's TIMED satellite and SCIAMACHY on board the ESA's ENVISAT.

General Circulation Models (GCM's) represent the best tools available to test our understanding of the physical, chemical and radiative processes of the middle atmosphere. In this thesis, a one-dimensional (1-D) model of the first nine vibrational states of OH^* is developed and incorporated into the University College London CMAT2 GCM. Unlike in other GCMs these vibrational levels are treated as distinct chemical species from OH in the ground state as suggested in Pickett *et al.* (2006). The results are compared to both satellite observations and predictions from other models.

It is found that the 1-D model successfully predicts many of the observed features including the magnitude of OH^* concentrations and a vibrational level dependence on the emission peak altitudes which is consistent with previously published results. The influence of atomic oxygen on the peak altitude of individual emission layers is found to be a more complex function than suggested in previous studies. Increased atomic oxygen increases the rate of OH^* production but this is modulated by increased quenching rates particularly at the upper edge of the layers.

On incorporation of the 1-D model into CMAT2, it is found that the model can generally make accurate predictions of both the temporal and spatial variability in the emissions, although the magnitude of the emissions are typically a factor of two or more higher than expected. This is attributed to increased O concentrations predicted by the model. Diurnal and seasonal variability is well represented, as are changes with respect to altitude and latitude. At equinox, a single peak in the emission is observed over the equator while during solstice, additional peaks occur in the mid- to high-latitude regions resulting from transport of oxygen by the mean circulation. Longitudinal variations are not well represented and suggest an underestimation of the effects of non-migrating tides. Migrating tides are shown to modulate the emission, in particular at the low

latitudes although reduced effects are also observed in the mid- to high-latitude regions. Migrating tides have proven difficult in previous modelling studies prompting investigators to double tidal amplitudes in an effort to obtain better agreement with observations (Marsh *et al.*, 2006). Similar tuning of the model's dynamical routines may be required in the case of CMAT2.

.

Acknowledgements

I wish to thank all of the staff members of the Department of Experimental Physics at Maynooth University, most notably Dr. Frank Mulligan who has been my supervisor throughout my doctoral work. I could not have asked for a better mentor. I'm sure at times, given the numerous other jobs I undertook, he sometimes doubted I would ever finish this thesis and indeed without his constant and unwavering support I doubt I would have finished it either. He has inspired me throughout, to constantly strive for perfection in all things and instilled in me the vital importance of even the most minor details.

I would like to thank Dr. Priscilla Mooney for her invaluable help especially at the early stages of this thesis and her encouragement throughout. Without her assistance I doubt I would ever have succeeded in getting this project up and running. To Prof. Alan Aylward who allowed me on numerous occasions to visit the UCL Atmospheric Physics Laboratories, who made me feel at home in London, and who worked tirelessly with me on these occasions, I offer my sincere thanks.

A huge thank you must also go the Ms. Grainne Roche for her assistance with just about everything and anything in the Department of Physics and to Mr. John Kelly who sorted out my many technical issues, as well as performing emergency surgery on my laptop on more than a few occasions when I felt all was lost.

I would like to formally acknowledge and thank the Irish Research Council (formerly the Irish Research Council for Science, Engineering and Technology) for funding much of my PhD through the Embark Initiative.

There have been a number of times during this PhD when I believed that the task was insurmountable. During these times I could always rely on the support of my family who not only endured my frustration but consistently encouraged me to continue my work, sometimes just one month at a time. In particular I would like to thank my mother for sitting down beside me during the final stages of the write up, often well past midnight, in order to pull the individual components of this thesis together.

To all my friends, I am a lucky person to have such wonderful people in my life. Each of you has helped me in some way or another over the past number of years through

encouragement, slagging or just being available when I needed something else to do during an evening. I would like to especially thank Aoife, Ben, Richie, Max, and James for their proof reading of this thesis even though it was the last thing they wanted to do.

Chapter 1

General Introduction, Literature Review and Background Theory

1.1   Introduction

The goal of this thesis is to develop a computational model which can simulate the night-time infrared emissions from the vibrationally excited hydroxyl radical (OH^*). This is accomplished by modifying an existing atmospheric general circulation model (GCM), known as the Coupled Middle Atmosphere and Thermosphere (CMAT2) model, to include new physical, energetic and chemical routines relevant to OH^* photochemistry.

One of the most prominent features of the night sky is the infrared (IR) emissions from the OH^* within the Earth's mesopause. The terrestrial night-time airglow (nightglow) within the atmosphere is dominated by these infrared emissions which can reach a total emission strength of about 1 mega Rayleigh (Turnbull and Lowe, 1983). (1 Rayleigh is defined as a column emission rate of 1×10^{10} photons per square meter per column per second (Baker and Romick, 1976)).

Since their discovery in the upper atmosphere by Meinel (1950) numerous studies have been carried out in order to identify (Bates and Nicolet, 1950; Herzberg, 1951; Krassovsky and Lukashenia, 1951; Krassovsky *et al.,* 1961; Nicolet, 1970; Breig, 1970) and explain (Battaner and Lopez-Moreno, 1979; LeTexier *et al.,* 1987; Sivjee and Hamwey, 1987; McDade *et al.,* 1987a; Johnston and Broadfoot, 1993) the mechanisms and processes that account for the behaviour of this particular chemical species.

Today, these studies remain an important topic in aeronomy and the recent detection of OH^* emissions on Mars (Clancy *et al.,* 2013) and Venus (Piccione *et al.,* 2008) have

prompted renewed interest in this field. The energy released via the chemical reaction of atomic hydrogen and ozone, the primary source of OH^* within the region,
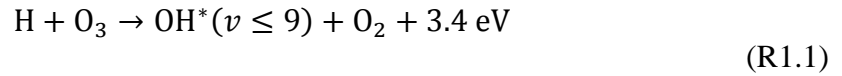
$$H + O_3 \rightarrow OH^*(v \leq 9) + O_2 + 3.4 \text{ eV}$$

(R1.1)

provides the single largest chemical source of heat within the mesopause (Mlynczak and Solomon, 1993; Kaufmann *et al.,* 2007) and contributes significantly to the local energy budget.

The OH^* emissions significantly reduce the energy available for heat within the middle atmosphere and provide a signal from which the chemical energy deposition rate within the mesopause can be derived (Mlynczak *et al.,* 1998). These emissions further provide a useful remote sensing tool in the study of the photochemical and dynamical processes that play a role in the upper atmosphere (Xu *et al.,* 2012), and allow for derivations of the atomic hydrogen concentrations (Mlynczak *et al.,* 1998), and atomic oxygen concentrations (Russell and Lowe, 2003; Smith *et al.,* 2010), within the region, provided that the concentration of ozone is well known and assumed to be in photochemical equilibrium.

In this chapter, an introduction to the atmosphere and the basic physical principles that govern it will be discussed. An overview of the atmospheric structure will be presented with a more detailed look at the middle atmosphere, the mesosphere. The more complex photochemistry and energetics associated with the OH radical itself will not be discussed until **Chapter 3**.

A basic history of atmospheric modelling will also be provided before an introduction to GCMs is presented. It is through the use of these GCMs that the fundamental atmospheric equations are solved in order to investigate the characteristics of the principal dynamical and energetic features within the atmosphere. Therefore, within the final sections of this chapter a description of the laws of physics employed by these atmospheric models will also be provided.

1.2 The Atmosphere

The vertical structure of Earth's atmosphere is divided into a number of layers based on the temperature gradient pertaining in a given layer. There are a total of five main

layers or *spheres* under this classification namely the troposphere, stratosphere, mesosphere, thermosphere and exosphere. The boundary between each layer is referred to as a *pause*. An idealised vertical profile of the atmosphere showing the different temperature structure and mean molecular mass of the atmosphere is shown in **Figure 1.1**.
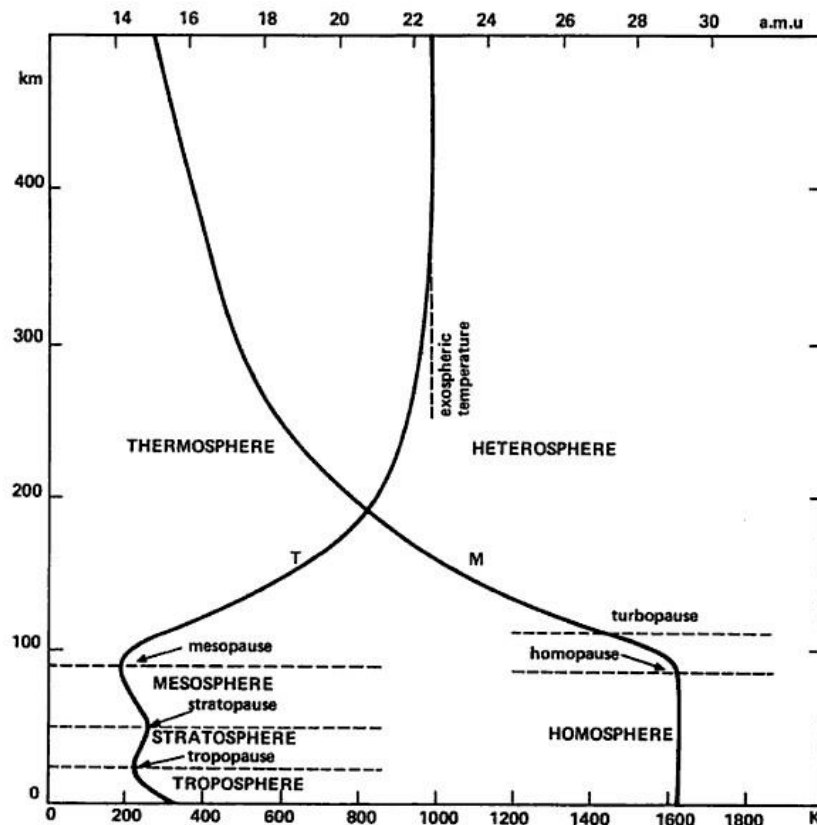
Figure 1.1: The temperature (T) and mean molecular mass (M) profiles of the Earth's atmosphere (Giraud and Petit, 1978).

1.2.1 The Troposphere

The troposphere is the lowest region of the atmosphere and is characterized by its positive lapse rate in temperature i.e. the temperature decreases with increasing altitude. The name originates from the Greek word *tropos* for 'turning' which is caused by unstable conditions (Seinfeld and Pandis, 2006). This is reflected in the troposphere in which warm air, which is lighter, sits below the colder, heavier, air above and represents a very unstable state. It is the region of the atmosphere in which all weather events occur and contains approximately 90% of the overall atmospheric mass (Iribane and Cho, 1980). Within this region, heat is generated primarily from shortwave radiation emitted by the Sun which has been absorbed by the Earth's surface and is re-emitted as

infrared radiation. As the air above ground level heats up it starts to rise until it reaches an altitude at which it is at the same temperature as the surrounding air. The cooling of the air as it rises is attributed to adiabatic expansion resulting from decreasing atmospheric pressure with altitude and leads to a reduction in temperature.

The depth of the troposphere varies depending on latitude and time of year. At the equator the troposphere typically extends to an altitude of 18 km with a temperature of approximately 190 K. Over the poles it typically extends to only 8 km and temperatures of approximately 220 K at this much lower altitude. At times, during the winter months, there exists no troposphere in the polar regions as no sunlight reaches the ground. This results in the total absence of the convective processes that provide the driving force behind the troposphere within these regions.

The tropopause is the dividing region between the troposphere and stratosphere and is marked by the temperature minimum between the two regions. Typically the tropopause is located approximately 15 km above sea level. The main feature of the tropopause is its ability to act as a barrier layer. Convection is rarely strong enough to transport air through this barrier and there does not appear to be any method of transport that allows for the fast movement of particles through this region (Seinfeld and Pandis, 2006).

1.2.2   The Stratosphere

The stratosphere is the next layer of the atmosphere and is characterized by its negative lapse rate i.e. temperature increases with increasing altitude. It extends from approximately 15 km to 50 km and was discovered by Leon Philippe Teisserene de Bort at the turn of the twentieth century. The name originates from the Latin word, *stratum,* meaning layer. The increase in atmospheric temperatures within this layer is the result of the absorption of solar radiation by ozone in the 240 – 295 nm range (Seinfeld and Pandis, 2006; Andrews, 2000). This absorption protects organisms in the lower regions which would otherwise be exposed to harmful amounts of ultra-violet (UV) radiation.

Typically ozone within this region is created in the tropical regions surrounding the equator as a result of the higher levels of incident UV radiation at these latitudes. The

ozone then diffuses towards the poles. Since ozone is also destroyed by UV radiation the concentration of this atmospheric constituent exhibits both daily and seasonal fluctuations tending to reach a maximum in late winter and early spring (Boeker and van Grondelle, 1995).

A north-south temperature gradient also exists within this region as a result of seasonal differences in hemispheric heating. When combined with forces generated by the Coriolis effect, this results in the production of strong zonal jets that are eastward in the winter and westward in the summer hemispheres.

The stratopause is marked by a temperature maximum between the stratosphere and mesosphere. It is located approximately 50 km above the Earth's surface and reaches temperatures of up to 270 K.

1.2.3   The Mesosphere

The mesosphere, after the Greek word *mesos* for middle, is the next highest region of the Earth's atmosphere and exhibits a positive lapse rate in temperature. This is due to lower concentrations of ozone within the region as well as atmospheric cooling processes associated with the vibrational relaxation of carbon dioxide. The properties of the mesopause are greatly influenced by atmospheric processes that take place in the lower layers of the atmosphere, in particular the stratosphere, where the absorption of UV radiation by ozone provides a significant amount of the energy input and is the driving force behind the circulation of the region (Wayne, 1985).

Noctilucent clouds (NLC) are a unique feature of the mesosphere and were first observed in the late 19th century after the eruption of Tambora on Krakatoa where large amounts of dust and aerosol were injected into the stratosphere. These clouds are formed of sub-micron ice crystals which grow larger when the mesosphere reaches its coldest temperatures during the summer months. It is only during this time that NLCs become visible.

The upper boundary of this region, the mesopause, occurs at an altitude of approximately 85 km. A more detailed description of the mesopause will be presented in **Section 1.3**.

1.2.4   The Thermosphere

The thermosphere, after the Greek word *thermos* for heat, is the next layer of the atmosphere and is marked by large increases in temperature that result from the absorption of solar UV and extreme ultra-violet (EUV) radiation. Depending on the time of day, latitude and level of solar activity the temperature can vary from 400 – 2000 K. It is characterised by low molecular densities, low pressures and large molecular mean free paths. Cooling within this region occurs through the downward conduction of heat into the mesopause and represents another source of energy input into the mesosphere. Above altitudes of 150 – 200 km molecular heat conduction dominates and the temperature becomes relatively stable at altitudes between 400 – 600 km.

1.2.5   The Exosphere

Above altitudes of 600 km the atmosphere has become so rarefied that particles are unaffected by collisions and are able to move about with large velocities. In some instances particles can build up enough kinetic energy to escape the Earth's gravitational pull. This region is known as the exosphere and marks the transition from the terrestrial atmosphere to the interplanetary gas.

1.2.6   The Homosphere and Heterosphere

An alternative method of classifying the atmosphere is to divide it into regions based on changes in atmospheric composition and mixing. In the lower region (the homosphere) the major constituents of the atmosphere are uniformly mixed by turbulence and the molecular mean weight of air ($\sim$29 amu) varies little with altitude, as shown in **Figure 1.1**. The two exceptions to this are O_3 and H_2O which are relatively minor constituents but play a very important role in the overall atmospheric structure. Turbulence and eddy diffusion dominate transport of particles in this region. In the upper region (the heterosphere) the proportion of atomic oxygen in the atmosphere increases and the molecular mean weight of air decreases with increasing altitude. Turbulent mixing and eddy diffusion of particles becomes less important and bulk motion of the atmosphere is no longer possible. At this point, molecular diffusion starts to separate the different constituents according to their respective masses. This can be seen in **Figure 1.2** which

graphs the molecular and eddy diffusion coefficients with respect to altitude as well as the mean free path of the overall atmosphere. At altitudes above approximately 100 km the molecular diffusion coefficient can be seen to take precedence over the eddy diffusion coefficient.
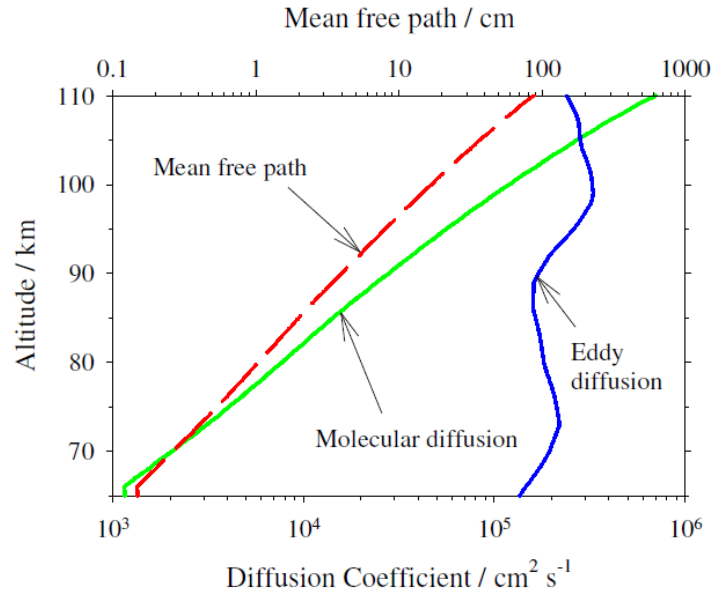
Figure 1.2: Molecular and eddy diffusion profiles in the atmosphere (Plane, 2009).

The region dividing the homosphere and heterosphere within the atmosphere is referred to as the turbopause and is located, near the top of the mesopause, at altitudes of approximately 100 km as illustrated in **Figure 1.1**.

It has been argued that the turbopause represents the "edge of space". Justification for this claim lies in the fact that it marks the end of the fully mixed atmosphere. Below this region certain transport effects can often be ignored by atmospheric models. Above this region molecular diffusion dominates and additional transport effects must be included if an accurate model of atmospheric behaviour is to be developed.

1.2.7   The Ionosphere

The ionosphere is an electrically conducting atmospheric layer, the existence of which was first proposed in the 19th century to explain the observed diurnal variations within the terrestrial magnetic field. In 1901 Marconi transmitted the first radio signals from Europe to North America. Later Kennelly and Heaviside proposed that this was possible due to reflection of the radio waves off a conducting layer at an altitude of

approximately 80 km. This layer was subsequently named the ionosphere and since that time numerous studies have shown that it plays an important role in atmospheric dynamics, energetics and composition.

The upper and lower boundaries of the ionosphere are not well defined with the lower boundary occurring between $50 - 60$ km. The upper boundary of the layer exists at approximately 1000 km where it merges with the magnetosphere, an area surrounding the Earth in which ion motion is controlled entirely by the Earth's magnetic field. Different layers within the ionosphere are defined by electron density profiles. This is illustrated in **Figure 1.3**.
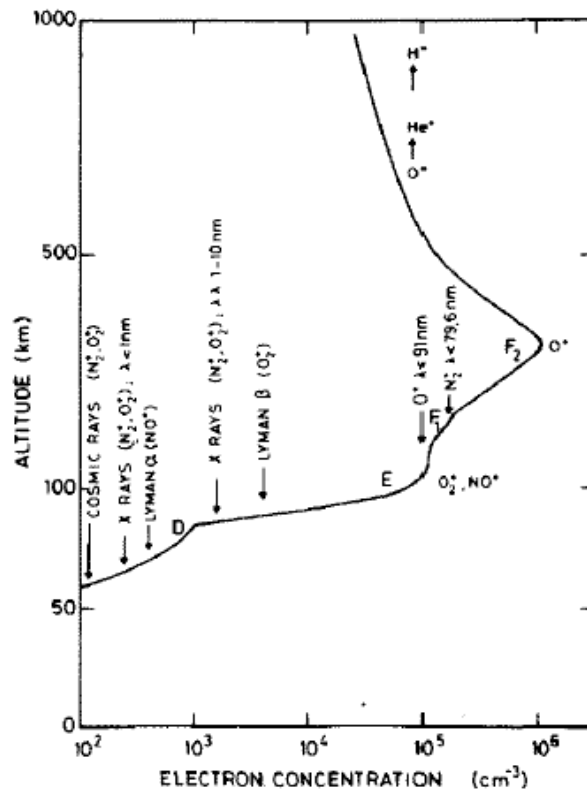
Figure 1.3: Definition of the ionospheric layers based on electron density distribution (Brasseur and Solomon, 1986).

The D-region of the ionosphere extends from the lower boundary up to altitudes of approximately 85 km. Ionisation within this layer is dominated by the photoionisation of nitric oxide (NO) from solar radiation at the Lyman α line at 121.6 nm. Radiation of this wavelength penetrates deep into the atmosphere. High-energy cosmic rays are also capable of penetrating deep into the atmosphere and contribute to the creation of ions within the D-region. The rate of ionisation resulting from cosmic rays is highly

dependent on the amount of solar activity, with increased activity resulting in less ionisation. This is due to the fact that increased solar activity leads to increases in the solar wind which can in turn deflect cosmic rays away from the solar system.

The E-region of the ionosphere starts at approximately 85 km and extends upwards to altitudes of approximately 130 km. This region is the result of photoionisation of both molecular nitrogen and molecular oxygen by solar UV radiation. Photoionisation of atomic oxygen by solar radiation in the X-ray region and at the Lyman α line at 102.6 nm also contributes. N_2^+ is typically only short lived and undergoes rapid charge exchange reactions with O. O_2^+ is rather long lived and is present in large quantities within the region along with NO^+ which is created through reactions of N_2^+ with O. NO^+ and O_2^+ are therefore the dominant ions within the E-region.

Above the E-region the F-region begins and is divided into two layers namely, the F_1, and the F_2 regions. Within the F-region O^+ is the dominant ion present and is created through the photoionisation of O by solar EUV radiation with wavelengths between $10 - 100$ nm. N_2^+ is also created within this region from EUV radiation. However, as the amount of EUV radiation reaching the Earth is highly variable, and dependent on solar activity, the location and size of the electron density peak, which falls within the F-region, is also highly variable. This is shown in **Figure 1.4** which displays the diurnal variation in the ionospheric layers during solar maximum and solar minimum.
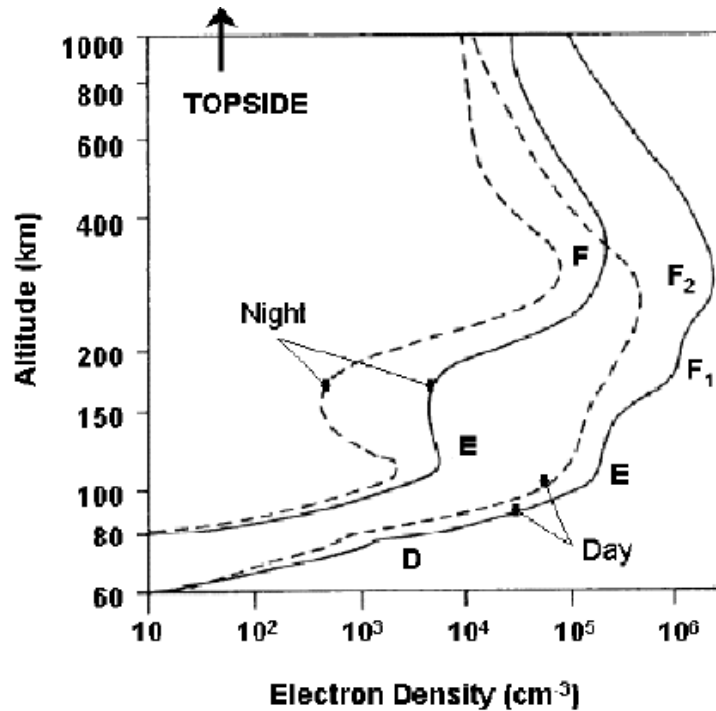
Figure 1.4: The diurnal variation of the ionospheric layers during solar maximum (solid line) and solar minimum (dashed line) (Hargreaves, 1979).

A typical peak in the electron density maximum for midday conditions is approximately 10^6 /cm^3 at altitudes between 250 km and 300 km.

Within the bottom three, D-, E- and F_1- regions of the ionosphere, the lifetime of ions created is typically quite short when compared to transport timescales. As such the concentration of charged particles can be assumed to be controlled by photochemical equilibrium between the production and loss mechanisms. Given that the amount of ion production is directly related to the amount of incoming ionising solar radiation, a clear difference exists between the day and night-time ionospheres.

Within the D-region, the photoelectrons created during the day all but disappear during the night as they recombine with other charged constituents. The electron densities within the E and F_1 regions are also significantly reduced during the night.

However, above the F_1 region the rate of recombination decreases and dynamical processes such as molecular diffusion begin to play a major role. Thus the F_2 region exists within the ionosphere during both the day and night. Above a further electron density peak within the F_2 region the concentration of electrons within the ionosphere starts to decrease rapidly. At altitudes above 600 km electrons are no longer prominent

and ions of helium and hydrogen dominate. At these altitudes the ions no longer form horizontal layers above the planet but are instead aligned with the Earth's magnetic field.

An important feature of ionisation by high energy photons is that once a neutral particle has absorbed the photon, the photoelectrons which are produced typically have enough energy to ionise other particles. It is therefore important to distinguish between primary and secondary photoelectrons. The number of secondary ions produced as a result of the initial photon energy is capable of being large enough to significantly alter ionospheric structure.

1.2.8 Geomagnetic Activity and Particle Precipitation

The interplanetary magnetic field (IMF) is an extension of the Sun's magnetic field which is said to be 'frozen in' to the solar wind. The concentration and energy spectrum of particles entering the Earth's atmosphere is highly affected by the orientation of the IMF relative to the Earth's magnetic field. The Earth's magnetic field is shown diagrammatically in **Figure 1.5**.
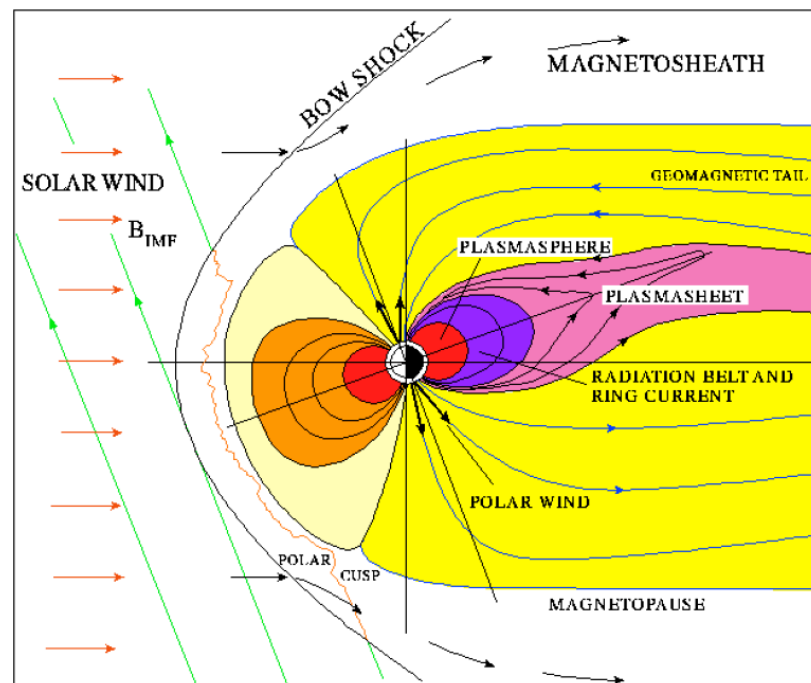
Figure 1.5: Schematic representation of the structure of the magnetosphere (Dobbin, 2005).

If the IMF has a strong southward component, magnetic reconnection can occur which leads to a coupling of the magnetic fields in the magnetosphere and the solar wind. Plasma from the solar wind can therefore enter the Earth's atmosphere through the magnetosphere and along the Earth's magnetic field lines.
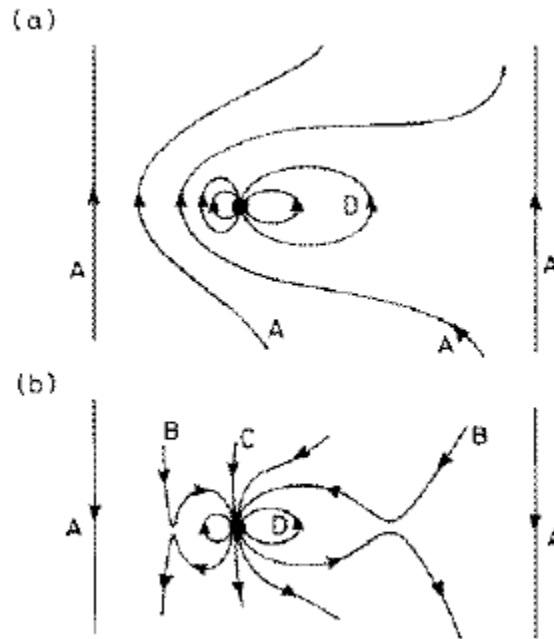
Figure 1.6: Illustration of both closed and open magnetic field lines under conditions of northwards IMF (a) and southwards IMF (b) (Hargreaves, 1979).

Figure 1.6 illustrates the behaviour of the Earth's magnetic field under northward (a) and southward (b) IMF conditions. When the IMF points northward the magnetic field lines around the Earth are closed. When pointing southward the magnetic field lines are open allowing for coupling of the magnetosphere with the solar wind. As the magnetic reconnection process is highly complex, only a brief outline of the process will be given here.

Energetically charged particles which enter the atmosphere, through the high-latitudes, provide an important energy input into the middle and upper atmosphere by heating and ionising neutral particles.

Within the polar regions, where the Earth's magnetic field lines are open, particles generally enter the atmosphere with lower energy than those within the auroral zones and have typical energies between $1 - 10$ keV. These particles precipitate into the Earth's atmosphere from the magnetospheric plasmasheet creating the aurora. Particles

with energies of a few MeV are observed in the equatorward cusp of the auroral oval and are capable of penetrating deep into the atmosphere.

These high energy particles can produce substantial amounts of secondary electrons through ionisation, with energies ranging from $10 - 100 \, \text{eV}$ which are responsible for a significant fraction of the energy transfer from the primary particle to the atmosphere.

During stellar events, such as solar flares and coronal mass ejections (CMEs), large amounts of high speed plasma are injected into the solar wind containing protons with energies ranging from $10 - 300 \, \text{MeV}$. On arrival at the magnetopause, shown in **Figure 1.5**, if the solar wind has a southward magnetic field, the energy and particles within the solar wind will effectively be coupled into the Earth's atmosphere and a geomagnetic storm will ensue. When a geomagnetic storm occurs particle precipitation increases and the auroral oval expands to lower than normal latitudes. Such events can result in increased ionisation within the D region of the ionosphere particularly at high-latitudes and change the composition of the neutral atmosphere.

The standard measure of geomagnetic activity is the planetary 3-hour K_p index (Bartels, 1932). This is obtained from the mean value of the disturbance levels in the north-south geomagnetic field as observed at 13 stations. The levels at each station are determined by measuring the range of the disturbance relative to an assumed quiet day curve during three hour time intervals. This range is then converted into a local K index which takes values from $0 - 9$ according to a quasi-logaritmic scale. The three hourly a_p index is a linear scale directly related to the K_p index while A_p is a daily index obtained from the average of the a_p indices for that day.

1.3 The Mesopause

Now that the main atmospheric layers have been discussed it is necessary to look at the mesopause layer, the primary focus of this thesis, in more detail. Many of the details that follow are found in Smith (2004).

The mesopause represents the coldest layer of the Earth's atmosphere reaching temperatures as low as $120 \, \text{K}$ in the summer polar region. The fact that this region is colder during the summer rather than the winter makes it unique in the atmosphere.

This property is referred to as 'the mesopause anomaly' and will be discussed in **Section 1.3.5**.

The mesopause is located at altitudes of approximately $85 - 95\,\text{km}$, although the altitude can vary by up to $15\,\text{km}$. Typically, the mesopause rises during the summer months and descends during the winter.

It is the least well understood area of the atmosphere primarily due to the inherent complexity of the region and because of its location. It is too high for balloon measurements, too low for *in-situ* satellite observations, and is therefore reliant on remote-sensing techniques. Only in the last number of years have satellites begun to probe the region adequately and large amounts of data have been collected by satellites such as NASA's TIMED and ESA's ENVISAT missions using both nadir and limb scanning techniques.

The complexity of the mesopause stems from the interplay of chemistry, radiation and dynamics within the region which is currently not very well understood. This is illustrated in **Figure 1.7**. **Figure 1.7** will be explained in detail in the following sections of this chapter and will be referred to at various stages.
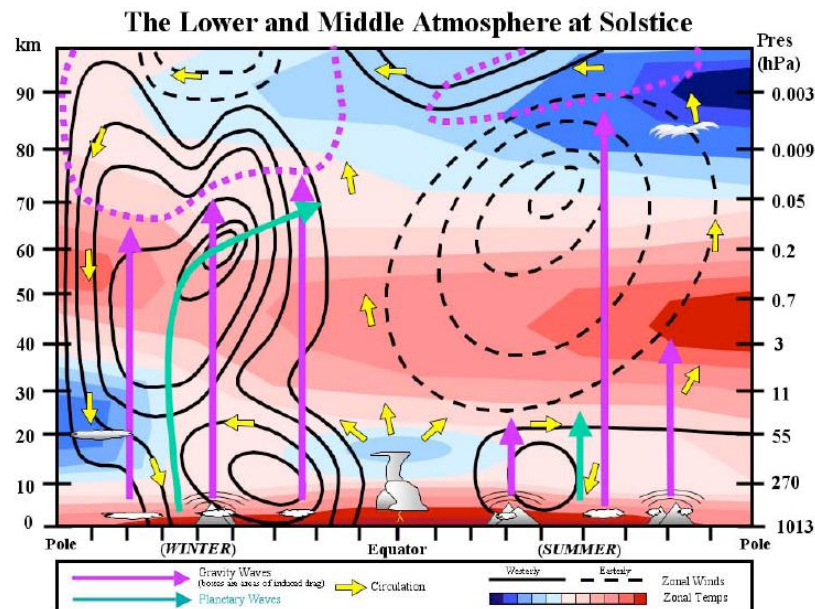
Figure 1.7: The lower and middle atmosphere (Meriwether and Gerrard, 2004). Purple arrows represent gravity waves, blue arrows represent planetary waves. Atmospheric circulation is represented by yellow arrows. Solid lines represent westerly wind flow and dashed lines represent easterly wind flow.

1.3.1   Chemistry of the Mesopause

The primary source of energy production within the mesopause is through exothermic chemical reactions involving the odd oxygen and odd hydrogen families. This differs from the surrounding atmospheric regions where absorption of UV and EUV rays represent the primary source of energy. This can be seen in the thermal structure of the region presented in **Figure 1.8**, which shows the annual mean temperature of the upper mesosphere, mesopause and lower thermosphere.
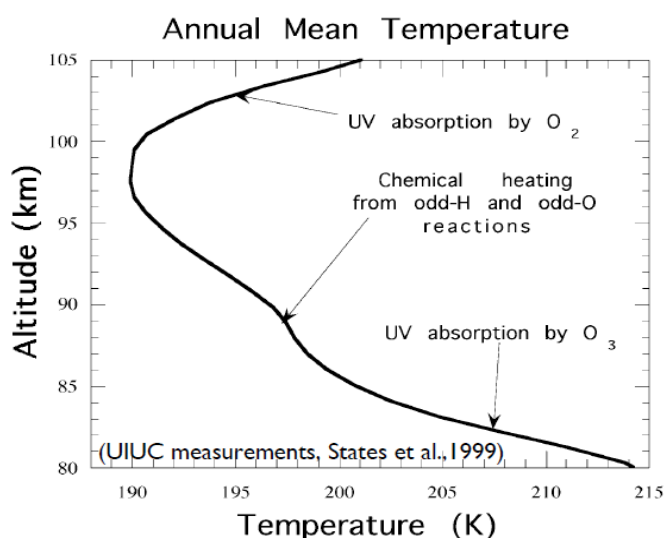
Figure 1.8: Illinois lidar observations of chemical heating (States and Gardner, 1999).

At altitudes above 80 km the absorption of UV radiation by O_3 decreases rapidly due to its diminished concentration and results in a drop in temperature. At altitudes above 100 km absorption of UV radiation by O_2 increases resulting in increasing temperatures. However, at mesopause altitudes, absorption of UV radiation is at a minimum and exothermic chemical reactions provide the dominant source of heat. This temperature minimum at mesopause altitudes is visible in **Figure 1.7** at altitudes of approximately 90 km in summer.

Chemistry in the mesopause region is dominated by the increasing concentration of atomic oxygen within the region. O is produced by the photodissociation of molecular oxygen during the day and is one of the key components in the atmosphere at mesospheric and lower thermospheric altitudes. A typical O-concentration profile is shown in **Figure 1.9**.
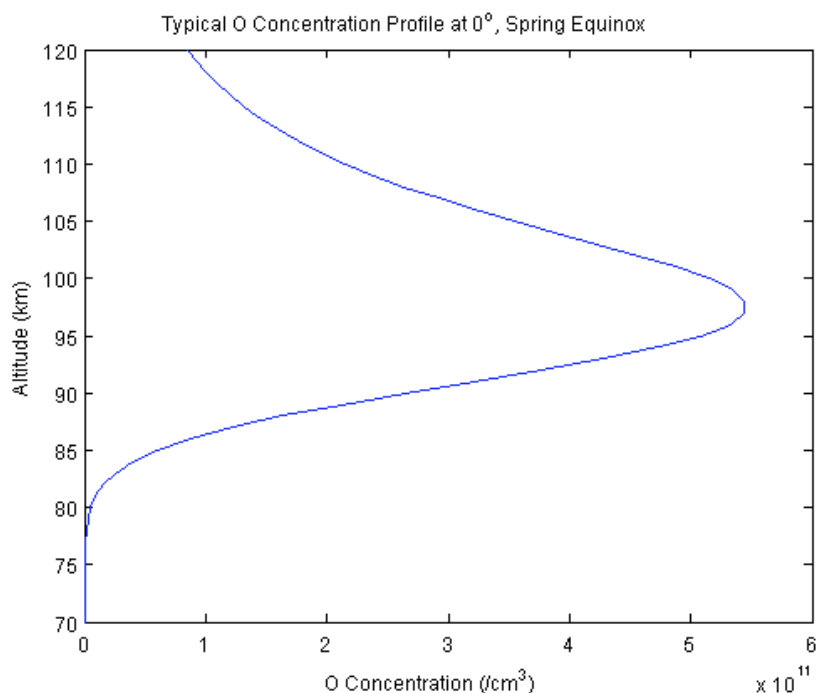
Figure 1.9: Typical atomic oxygen concentration profile over the equator for March equinox conditions.

Atomic oxygen is the most abundant minor species within the mesopause and is highly chemically active with a mixing ratio that reaches 10^{-2} at an altitude of 90 km (Russell and Lowe, 2003). Within this region of the atmosphere it is typically produced during the day by the photolysis of O_2 in the Schumann-Runge continuum ($130 - 175$ nm) and the Schumann-Runge bands ($175 - 195$ nm) via the following two mechanisms.

$$O_2 + h\upsilon \rightarrow O + O \qquad\qquad (175 - 230 \text{ nm}) \qquad\qquad\qquad (R1.2)$$

$$O_2 + h\upsilon \rightarrow O + O(^1D) \qquad\qquad (<175 \text{ nm}) \qquad\qquad\qquad (R1.3)$$
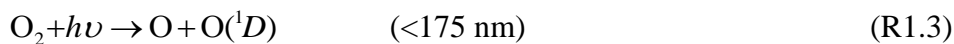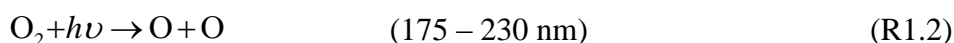
This atomic oxygen is then removed from the atmosphere by the two separate reaction sequences presented below (Winick *et al.*, 1983).

Reaction Sequence 1   Reaction Sequence 2

$O + O_2 + M \rightarrow O_3 + M$ (R1.4) $H + O_2 + M \rightarrow HO_2 + M$ (R1.6)

$H + O_3 \rightarrow OH^*(v = 6 - 9) + O_2$ (R1.1) $HO_2 + O \rightarrow OH^*(v \leq 6) + O_2$ (R1.7)

$O + OH \rightarrow H + O_2$ (R1.5) $O + OH \rightarrow H + O_2$ (R1.8)
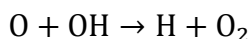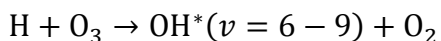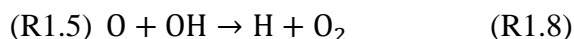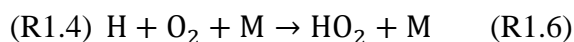
It can be seen that the relative abundance of OH^* in the mesosphere is heavily dependant on the amount of atomic oxygen in the surrounding atmosphere. This will be discussed in more detail in **Chapter 3**. However, the net result of both of these reaction sequences is the same, i.e., two atomic oxygen atoms recombine to form O_2 (Winick *et al.*, 1983).

As the atmospheric pressure at mesopause altitudes is low, the rates at which these reactions occur are slower than might be expected in the lower atmosphere as the chemical lifetimes of the reactants increase. This is illustrated in **Figure 1.10** in which the chemical lifetime of the HO_x family (OH, HO_2 and H) is shown to increase considerably above approximately $82\ km$. Chemical families will the discussed in **Chapter 2**.
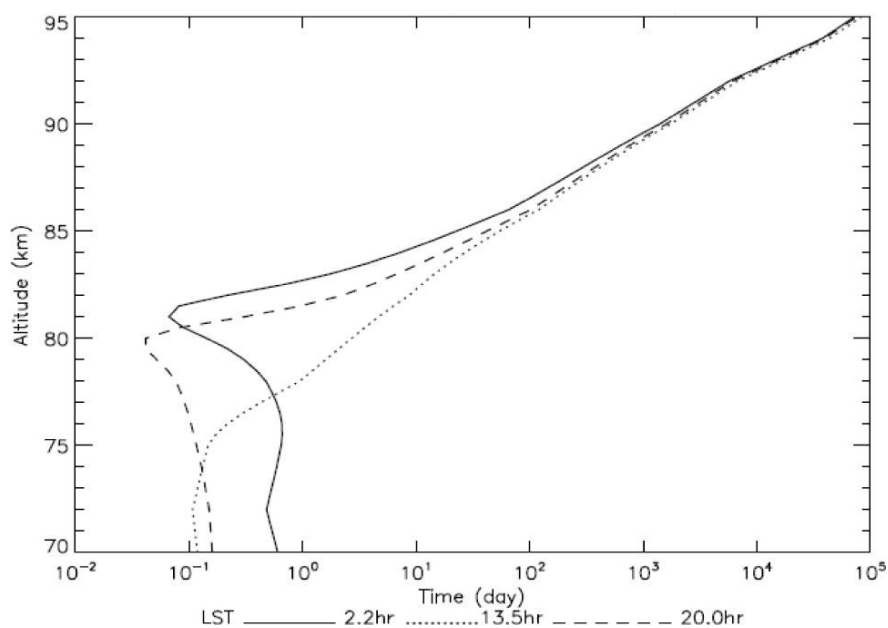
Figure 1.10: Calculated chemical lifetimes of HOx for Sept. 23, 2004 at latitude 34N at three different local solar times: 2.2 hr, 13.5 hr and 20 hr (Pickett *et al.,* 2006).

These slower reaction rates in the middle and upper atmosphere lead to relatively large concentrations of these minor constituents within the region. **Figure 1.11** shows the mixing ratios of these minor constituents during both the day and the night. It can be seen that the mixing ratios increase by many orders of magnitude with altitude before subsequently declining.
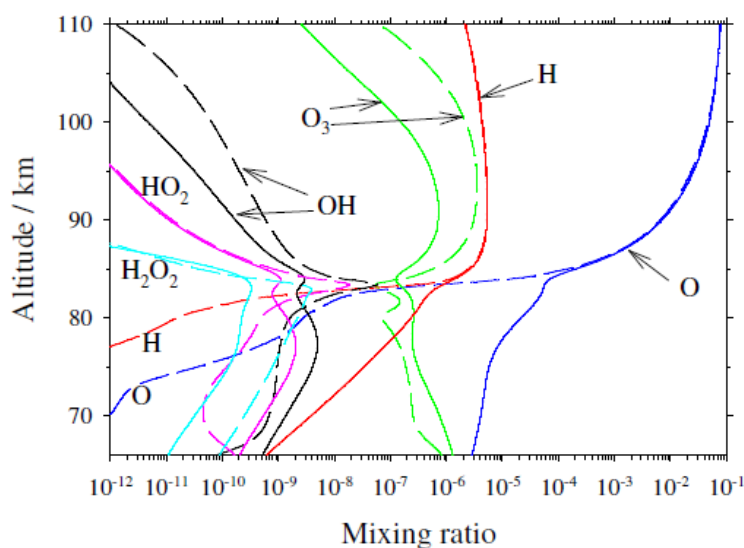
Figure 1.11: Minor constituent mixing ratios in the middle atmosphere at day (solid lines) and night (dashed lines) (Plane, 2009).

Of particular relevance to this thesis is the behaviour of the OH radical and the reactions involved in its production and loss. These are discussed in detail in **Chapter 3**.

1.3.2 Gravity waves

Gravity waves represent another significant source of the energy input into the mesopause and originate in the troposphere (Andrews 1991). This is shown by the purple arrows in **Figure 1.7**. They are small scale perturbations in wind, temperature, and density within the atmosphere which oscillate in the transverse plane to the direction of propagation. These waves are generated in the troposphere when air has been displaced in the vertical direction and the atmosphere subsequently attempts to return to its equilibrium position. They are caused by a number of different mechanisms which include winds over surface topography, such as in the presence of mountainous regions, and meteorological features, like thunderstorm updrafts and wind shears.

If air is forced to rise in a stable region of the atmosphere, its natural tendency will be to return to its original position. However, due to conservation of momentum, the parcel of air will overshoot its original position numerous times before settling in its equilibrium position. This results in the production of a gravity wave which will propagate vertically upwards through the atmosphere. As the atmospheric pressure drops with increasing altitude, the amplitude of the gravity wave will increase until it

reaches the mesopause. Within the mesopause it will break (as explained following **Equation 1.3** below) and deposit its momentum and energy as illustrated in **Figure 1.7**. Atmospheric models which fail to take into account the effects of gravity waves typically underestimate the temperature variations in the mesosphere and mesopause regions.

As these waves travel upwards and into the middle atmosphere their amplitudes increase exponentially as a result of decreasing density. This can be shown easily by considering the conservation of kinetic energy density given by $\frac{1}{2}\rho|V|^2$ where ρ is the density of the atmosphere at a height z and $|V|$ is the amplitude of the vertical velocity component. If c is defined as a constant then

$$|V(z)| = \frac{c}{\sqrt{\rho}}.$$

(1.1)

However, since density varies as

$$\rho_0 \exp\left(\frac{-z}{H}\right)$$

(1.2)

where ρ_0 is the density at a height $z = 0$ km and H is the scale height it follows that

$$|V(z)| = \frac{c}{\sqrt{\rho_0}} \exp\left(\frac{-z}{2H}\right)$$

(1.3)

and it can be seen that the wave amplitude increases exponentially with height.

Buoyancy forces act to restore the resulting oscillation until an altitude is reached where the local temperature perturbation induced by the wave produces a superadiabatic lapse rate. At such a point the atmosphere is unstable and the wave begins to break or dissipate. A cascade of turbulence is triggered within the region of breaking and the energy and momentum of the wave are deposited into the region.

Lindzen (1981) and Weinstock (1982) proposed the idea that above the breaking level, turbulent diffusion resulting from wave breaking prevents the wave amplitudes from growing any larger. Using this idea it is possible to determine expressions for turbulent

diffusion and momentum deposition which are both functions of $\bar{u} - c$, being the difference between the zonally averaged wind $\bar{u}$ and the horizontal phase speed of the wave c. At an altitude where the horizontal phase speed is equal to the background wind speed such that $\bar{u} - c = 0$, it is no longer possible for the wave to propagate and it is completely absorbed. Momentum deposition occurs between the breaking level and this upper limit.

It is the zonal mean forces arising from the gravity wave breaking which cause the reversal of the mid-latitude zonal mean jets. Gravity waves in the mesosphere drive the meridional circulation which causes the observed latitudinal temperature gradient to be the reverse of that expected in the absence of wave driving (i.e. the summer mesopause is colder than the winter).

Hickey and Walterscheid (1994) proposed that the time averaged effect of gravity waves on the chemical exothermic heating could lead to heating rates that are greater than those suggested by Mlynczak and Solomon (1991a, 1991b, 1993). Several studies suggest that gravity waves can lead to changes in the thermal structure of the middle atmosphere through the dissipation of waves as well as wave-wave interactions (Liu and Hagan, 1998; Liu *et al.,* 2000; Medvedev and Klassen, 2003).

Gravity wave representation within numerical models will be discussed further in **Chapter 2**. However, it is worth noting here that the scale of GCM coordinate grids are typically too large to explicitly solve these small-scale oscillations and that applying grids with better resolution results in prohibitive computing overheads. As a result, a number of gravity wave parameterizations have been developed which require the specification of a gravity wave source spectrum in the lower atmosphere as input. A full review of gravity wave dynamics and their effects in the middle atmosphere is provided by Fritts and Alexander (2003).

1.3.3   Planetary Waves

The thermal structure of the stratosphere is strongly modulated by dynamical features, as is the mesosphere. (Andrews, 2000)   During solstice conditions the summer hemisphere is not far removed from thermodynamic equilibrium. However, the winter hemisphere is found to be warmer than it should be if it were controlled by radiative

processes alone. The extra heating of the winter hemisphere is a result of the *Brewer-Dobson* circulation and is illustrated in **Figure 1.12**.
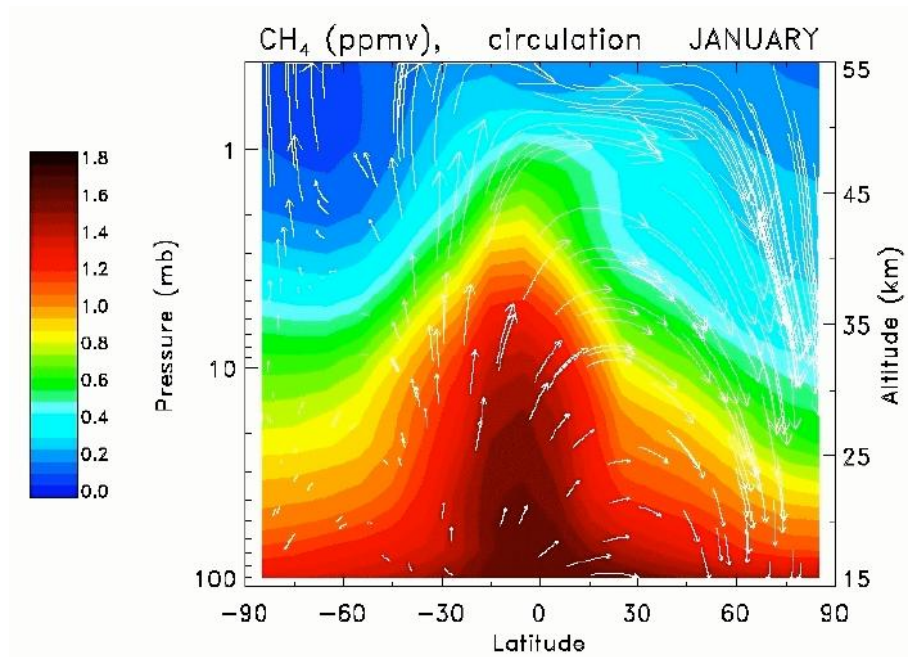
Figure 1.12: Zonally averaged methane volume mixing ratio in ppmv for January. The Brewer-Dobson circulation pattern is superimposed using white arrows (Ojeda, 2006).

Air rises within the tropics before moving poleward and subsequently descending again into the troposphere in the mid- to high-latitudes. This circulation is represented above by the white arrows overlapping the concentrations of methane within the atmosphere. It is caused by the dissipation of planetary waves in the extra tropical winter stratosphere.

Planetary waves are stationary, or slowly moving westward propagating oscillations, that are generated in the troposphere and propagate up into the middle atmosphere. They arise from background wind interactions with topographic and thermal features in the troposphere such as land masses and land-ocean heating contrasts. These waves are unable to propagate under conditions of westward flow as they cannot move through regions where the background wind is equal to the planetary wave horizontal phase speed (Charney and Drazin, 1961). This is illustrated by the summer hemispheric blue arrow in **Figure 1.7**. For this reason significant planetary wave activity is limited to regions in the stratosphere, and lower mesosphere, where the zonal flow is eastward, such as in the case of the winter hemisphere. This is illustrated by the winter hemispheric blue arrow shown in **Figure 1.7**. Planetary waves therefore propagate

upwards in the winter hemisphere before dissipating in the middle and upper stratosphere as also shown in **Figure 1.7** and with more detail in **Figure 1.13**.
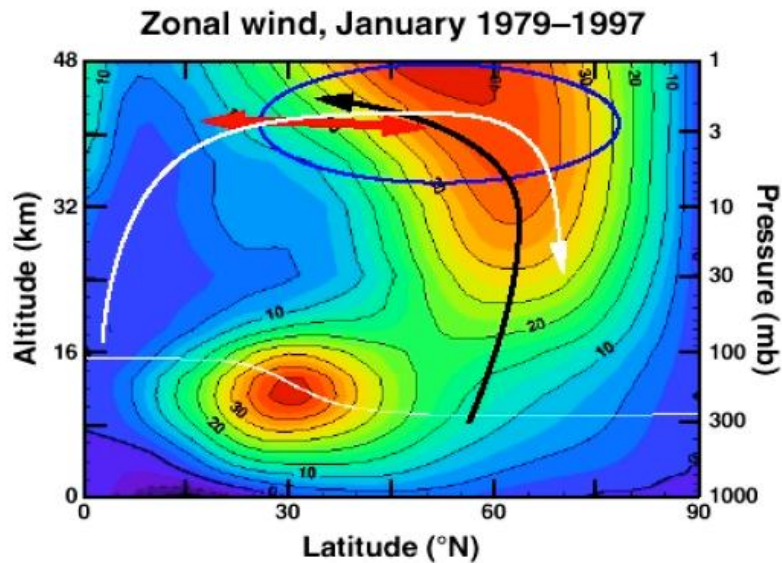
Figure 1.13: Zonal mean wind for January 1979 – 1997, (NASA, 2000).

The dissipation of planetary waves can occur as a result of two processes, namely radiative damping and wave breaking. Radiative dampening relates to the thermal dissipation of the wave in which radiative processes decrease the temperature gradient associated with the wave. The timescale for these processes is sufficiently long that it is unlikely to play a major role in controlling the amplitude of the planetary waves.

Wave breaking occurs in regions where the velocity of the planetary wave is the same as the velocity of the mean flow. This is believed to be the dominant process by which planetary waves dissipate within the stratosphere (Shepherd, 2000). Wave breaking of stationary planetary waves occurs in the subtropics of the winter hemisphere where the zonal wind speed is zero.

When planetary waves break within the vicinity of the winter time stratospheric polar night jet stream they deposit their westward momentum into the region. This results in a deceleration and displacement of the jet stream. This displacement allows mid- to low-latitude air to enter into the polar regions resulting in sudden stratospheric warmings. Radiative cooling within the polar winter region must then occur if thermodynamic equilibrium is to be restored. This cooled air subsequently sinks and is replaced by warm air from lower altitudes in the mid- to low-latitudes which rises to replace it. In this fashion the equator to pole Brewer-Dobson circulation is set up

allowing for the transport of momentum, energy and atmospheric constituents from low to high-latitudes. Without this circulation the winter stratospheric pole would be significantly cooler than is actually measured.

It is found that the Northern hemisphere winter experiences a greater deposition of momentum by planetary waves relative to the southern hemispheric winter. As a result of this the Brewer-Dobson circulation within the Northern hemisphere is stronger than in the southern which in turn leads to stronger downwelling over the north pole and thus warmer temperatures over the north pole than over the south. This asymmetry in planetary wave activity results from the fact that planetary waves are primarily forced by topography and land-sea contrasts which are much stronger in the Northern hemisphere than in the southern. The northern winter hemisphere therefore experiences greater planetary wave forcing than the southern winter hemisphere.

1.3.4 Tides

All planetary atmospheres experience gravitational tides as a result of their motion around their local star. Gravitational tides will also be induced by any orbiting satellites or moons the most common of which is the tide in the Earth's oceans, due primarily to the gravitational attraction of the Moon. Tides can also be thermal in nature and driven by solar heating of the atmosphere. These tides, also referred to as migrating tides, follow the apparent motion of the Sun moving westward throughout the day. In the Earth's atmosphere thermal tides are the more dominant of the two types although non migrating tides still play an important role.

Atmospheric tides are present throughout the different layers of the atmosphere from the troposphere to the thermosphere. They can be described as planetary scale oscillations that have periods which are sub-multiples of the 24 hour day. Diurnal tides refer to tides with a period of 24 hours, while semidiurnal and terdiurnal tides have periods of 12 and 8 hours respectively. These tides can exhibit a profound effect on the background atmosphere and play an important role in the chemistry, radiation and dynamics of the atmosphere particularly in the mesosphere lower thermosphere (MLT) region.

Absorption of solar infrared (IR) radiation by water in the troposphere, UV radiation by ozone in the stratosphere, and EUV radiation of molecular oxygen and nitrogen in the

thermosphere are the major drivers of the Earth's thermal tides. The tides generated in the lower atmospheric levels, such as the troposphere and stratosphere have components which can propagate upwards into the thermosphere (Chapman and Lindzen, 1970). These tides dominate those generated locally.

Ground level measurements of atmospheric pressure show that the semidiurnal tide is more dominant than the diurnal tide (Bartels, 1932). In 1860 Lord Kelvin put forward the theory that this was due to atmospheric resonance at the semidiurnal frequency. This theory would go on to be the dominant theory for the next seventy years until it was disproved by Taylor (1936). Taylor showed that the atmosphere had a very weak response to the semidiurnal resonant frequencies. Further work by Pekeris (1937) on the temperature distribution of the atmosphere appeared to lend support to the theory when his predictions of the atmospheric temperature distribution conformed with the observational data collected by Martyn and Pulley (1936). It wasn't until after World War II when rocket measurements of the atmospheric temperature profile were recorded and the resulting profiles were found to differ from that of Martyn and Pulley, that Jacchia and Kopal (1951) concluded that the resonance theory was insufficient to account for the increase in the amplitude of the semidiurnal tide with height.

Lindzen (1967) carried out a theoretical investigation of the diurnal tide and was able to explain the observed features. Using the tidal equations of Laplace, Lindzen showed that polewards of ±30° latitude the diurnal tide was incapable of propagating vertically while the semidiurnal tides were. This is due to the fact that, treating the diurnal tide as a gravity wave and considering the Coriolis parameter $f = 2\Omega\sin\emptyset$ (where Ω is the Earth's rotational velocity and $\emptyset$ is latitude), the diurnal tide cannot propagate vertically if the frequency is less than $2\Omega sin\emptyset$. Since at these locations 24 hours is longer than the local pendulum day, the diurnal tide can no longer propagate. Furthermore, equatorwards of ±30° latitude only 20% of the diurnal forcing goes into propagating modes. The result is that the diurnal tide is shown to be much weaker than the semidiurnal.

In addition, diurnal components of the tides have smaller vertical wavelengths when compared to the semidiurnal tides resulting from their long period and narrower latitudinal range. They are therefore more susceptible to destructive interference and damping (Hines, 1960; Chapman and Lindzen, 1970).

Numerous other theoretical investigations of the atmospheric response to global tides using the Laplace equations have been conducted (Chapman and Lindzen, 1970; Holton, 1975; and Volland, 1988).

Assuming the atmosphere is in geostropic balance, detailed in **Section 1.8.6**, leads to more simplified forms of the equations of energy and momentum to which oscillations can be applied. These are known as the *Laplace Tidal Equation* and the *Vertical Structure Equation* which describe the latitudinal structure of tidal amplitudes and vertical structure of tides in the atmosphere respectively. The theory predicts that any global tidal perturbation can be resolved into eigenfunctions, referred to as *Hough modes* which are written in the form (*s,n*) and are characterised by longitudinal wavenumber, *s*, and a latitudinal wavenumber, *n*. Diurnal tides have a zonal wavenumber 1 and are described by the set of (*1,n*) Hough modes. The semidiurnal tides are described by the set of (*2,n*) Hough modes and so on. Positive values of *n* are used to describe vertically propagating modes while negative values are used to describe modes where the forcing is physically trapped and therefore do not propagate vertically through the atmosphere. Even values of *n* are then used to describe modes which are symmetric around the geographical equator while odd values describe modes that are asymmetric.

Tides can have a profound influence on the chemistry, composition and dynamics of the atmosphere and will be looked at in detail in this thesis. Changes in temperature and local density as a result of tides can have a significant effect on composition and the atmospheric physical structure through modulation of temperature dependant reaction rates in the chemistry. Variations in the dynamics of the atmosphere and in the winds can further alter transport of the atmospheric constituents. Furthermore, interactions with other atmospheric oscillations, such as gravity and planetary waves, can enhance the influence tides have on the background atmosphere (Dobbin, 2005).

1.3.5 The Mesopause Anomaly

If the atmosphere is assumed to be in radiative equilibrium it would be expected that the atmospheric temperature would be closely related to the distribution of solar heating in the atmosphere. The temperature of the mesopause would reach a maximum over the summer pole at solstice where the sun shines for 24 hours a day. A temperature

minimum would be expected at the winter pole where radiative heating would be considerably diminished during the polar night.

In reality this is not the case. The temperature maximum of the mesopause is located over the winter pole while the temperature minimum is located over the summer pole. These extremely low temperatures in the mesopause during the summer months are believed to cause the appearance of noctilucent, or polar mesospheric, clouds in the middle atmosphere as stated in **Section 1.2.3**.

An explanation for this anomaly was first proposed by Murgatroyd and Singleton (1961) who suggested the idea of an inter-hemispheric circulation. As air rises in the summer hemisphere it is cooled adiabatically. In the winter hemisphere downwelling air is heated adiabatically as it descends. This sets up a summer to winter meridional circulation in the mesopause region which accounts for the observed mesopause temperatures. This is illustrated in **Figure 1.14**.
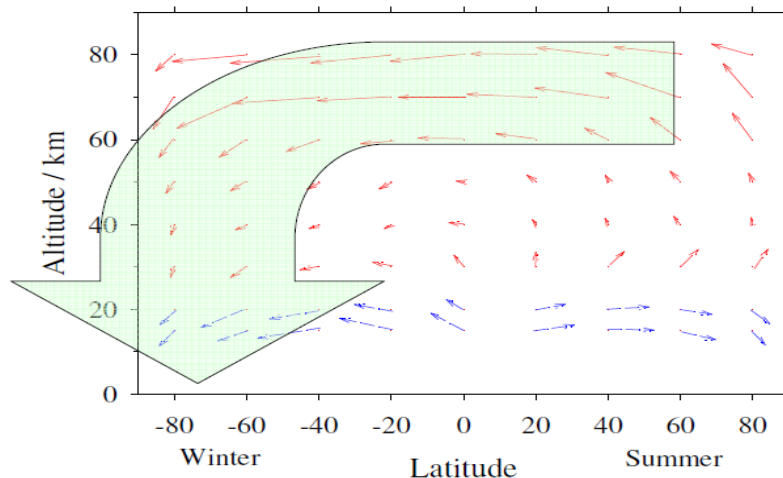
Figure 1.14: Meridional circulation of atmosphere into the winter hemisphere (Plane, 2009). Arrows represent the path of warm (red) and cold (blue) air respectively.

In order for this to occur, a westward drag in the mesospheric winter hemisphere and an eastward drag in the mesospheric summer hemisphere must exist to balance the Coriolis force associated with the meridional circulation. Houghton (1978) proposed that gravity waves may be able to provide the required drag. Later Lindzen (1981) showed that if vertically propagating waves were selectively absorbed as they travelled from the troposphere to the mesosphere more westward waves should be present in the winter mesosphere and more eastward waves present in the summer mesosphere. Currently it

is believed that breaking of these gravity waves in the mesopause is enough to drive the observed meridional circulation.

1.4   Atmospheric Heating

In order to accurately predict the energy balance within the middle and upper atmosphere a number of key physical and chemical processes must be considered. Factors including the absorption of solar radiation by the atmosphere, the storage and release of chemical energy, the transport of energy, the dissipation of wave disturbances, auroral and airglow heating and cooling by radiative emissions all contribute to the total energy budget of the atmosphere.

Typically high energy, short wavelength ($< 100 \, \text{nm}$), radiation is absorbed in the thermosphere at altitudes above approximately $100 \, \text{km}$. Longer wavelength radiation in the visible and infrared is capable of reaching the planetary surface. **Figure 1.15** from Brasseur and Solomon (1986) shows the depth of penetration of high energy radiation as a function of wavelength within the atmosphere up to wavelengths of $300 \, \text{nm}$. The principal absorber species over this wavelength range are also shown.
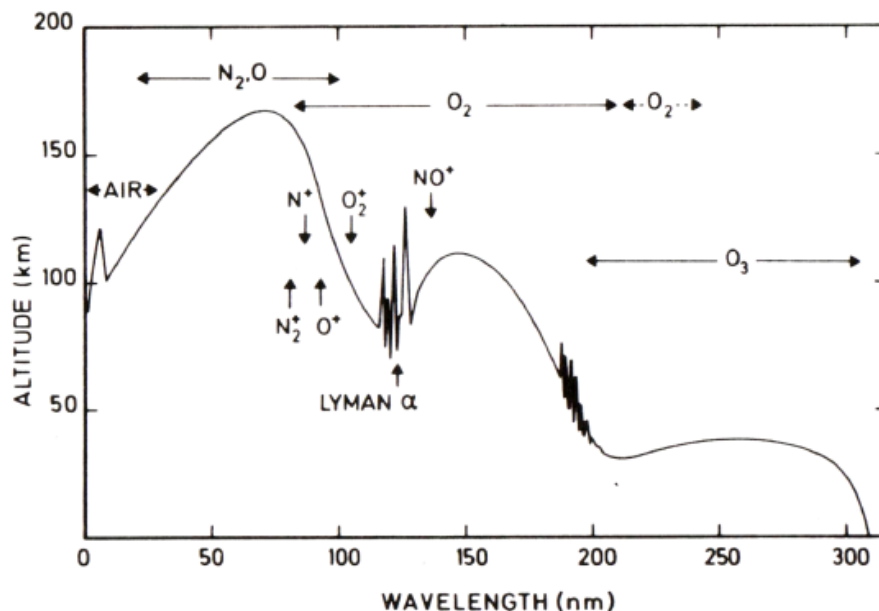
Figure 1.15: Depth of penetration of solar radiation as a function of wavelength. Altitudes correspond to an attenuation of $1/e$. Principal absorbing species and ionisation limits are indicated (Brasseur and Solomon, 1986).

It can be seen that at wavelengths less than 100 nm radiation is highly attenuated within the thermosphere. Radiation with a wavelength above 100 nm is typically absorbed by two atmospheric species, O_2 and O_3, within the middle atmosphere.

Taking each atmospheric layer in turn, the primary source of heat within the stratosphere is the absorption of solar UV radiation by O_3 within the Hartley $(203 - 305 \, \text{nm})$ bands, shown in **Figure 1.15**, and the Huggins $(305 - 397 \, \text{nm})$ bands. This can result in a heating rate that reaches approximately 12 Kelvin per day near the stratospause depending on the amount of ozone present.

Within the mesosphere O_2, O_3 and CO_2 are the principal absorber species absorbing radiation at wavelengths ranging from the Lyman α line (121.5 nm), in the UV, to the mid infrared at $(4.3 \, \mu\text{m})$. As the concentration of ozone decreases with altitude within the mesosphere, so too does the amount of absorption of radiation within the Hartley and Huggins bands. As a result, the heating of the atmosphere associated with these bands also decreases contributing to the temperature gradient within the mesosphere. Typically most of the energy input into the mesosphere, as a result of the absorption of radiation by O_2 and O_3, does not result in heating of the atmosphere. It is instead redistributed as chemical potential energy or internal energy of electronically and vibrationally excited species which are produced as a result of photolysis reactions. This internal energy can either by quenched through collisions with other atmospheric constituents resulting in heating of the mesosphere or it may be radiated away in the form of airglow thereby significantly reducing the energy available for heat. The heating rate of the mesosphere therefore strongly depends on where and how this chemical and internal energy are deposited.

One example of this feature is the transport of absorbed solar energy resulting from the dissociation and eventual recombination of O_2. Atomic oxygen resulting from the dissociation of O_2 typically retains much of the energy absorbed in the photodissociation reaction as chemical energy. At altitudes above 75 km atomic oxygen has a lifetime of approximately one day and can therefore be transported significant distances from the site of the original photodissociation reaction. When recombination occurs the stored chemical energy is subsequently released as thermal energy.

Within altitudes of 70 km to 95 km heating of the atmosphere as a result of exothermic chemical reactions between neutral constituents is a significant source of heat. It can, in fact, exceed heating resulting from the absorption of radiation. In the mesosphere a local temperature maximum arises from the recombination of O and O_2 forming O_3 as well as from quenching of $O(^1D)$ which is created during the photodissociation of ozone. Reactions with odd hydrogen species further augment this exothermic heating of the mesosphere, in particular the reaction of atomic hydrogen and ozone, which will be discussed in greater detail in **Chapter 3**.

Above 80 km the majority of incoming radiation at wavelengths below 200 nm is absorbed due to the large absorption cross sections of the atmospheric constituents. Absorption of radiation by O_2 within the Schumann-Runge bands $(175 - 200 \, \text{nm})$ results in direct heating of the atmosphere within the lower thermosphere. This heating subsequently increases with altitude as O_2 starts to absorb radiation within the Schumann-Runge continuum $(130 - 175 \, \text{nm})$. At altitudes of approximately 150 km this can result in a heating rate of $30 - 40$ Kelvin per day.

At altitudes above 150 km, heating of the atmosphere results from the absorption of EUV radiation with wavelengths between 10 and 100 nm. Heating rates resulting from absorption of this radiation are strongly dependent on the solar cycle and produce maximum heating rates that vary from $500 - 2000$ K per day depending on whether the solar cycle is at a minimum or maximum. This can lead to significant changes in temperature within the thermosphere over the course of a solar cycle.

Furthermore, within the thermosphere, the primary atmospheric constituents undergo photodissociation. If the incoming radiation is energetic enough, these photodissociation reactions can also result in the production of photoelectrons. When ejected these photoelectrons carry away a proportion of the energy released during the dissociation reaction as kinetic energy, while the remaining energy is stored as chemical energy within the ion product.

Collisions between these photoelectrons and other atmospheric constituents can result in heating of the atmosphere as the kinetic energy of the electrons is transformed into heat energy during the collision. In some cases, if the photoelectrons have sufficient energy, these collisions may result in further ionization reactions, or electronic or vibrational

excitation of the atmospheric constituents with which they collide. These excited constituents can subsequently be quenched through collisions producing heat, or radiate the energy in the form of airglow emissions.

The chemical energy of the ion produced during the dissociation reaction can either be regained during recombination with an electron, or can be transferred to other ions through charge transfer reactions.

Exothermic reactions within the thermosphere can also play a role in the distribution of energy. Atomic oxygen, produced as a result of chemical reactions after photodissociation, can play a significant role in transporting energy. These O atoms travel downwards into the lower altitudes where three body recombination of O_2 can occur through the reaction

$$O + O + M \rightarrow O_2 + M.$$

(R1.9)

In this way thermal energy released in the thermosphere is transported away from the site of the original dissociation reaction and into the middle atmosphere.

Another form of heating within the thermosphere results from the solar wind. At high-latitudes the solar wind is capable of depositing large amounts of heat into the atmosphere through Joule heating and particle precipitation. Joule heating is the result of collisions between neutral particles within the atmosphere and energetic ions that have been accelerated to higher velocities by the high-latitude electric field. Heating as a result of particle precipitation results from the collision of neutral particles and energetic ions that have been accelerated along the Earth's magnetic field lines and into the polar region. The depth of penetration of these electrons is highly dependent on the strength of the magnetic field and perturbations within the field can result in large variations in the amount of incoming electrons and in the subsequent thermospheric heating.

Dynamical processes can also play a role in the deposition and redistribution of energy within the atmosphere. For example, the dissipation of gravity waves within the mesosphere has been shown by Liu *et al.* (2000) to produce chemical heating rates of up to 10 K per day. Subsequently Medvedev and Klassen (2003) described the thermal

effects of gravity waves on the mean flow, concluding that the effect of saturating gravity waves was to produce both differential heating and cooling within the atmosphere. Unlike heating and cooling resulting from chemical and radiative processes, dynamical processes are often very difficult to measure. It is often the case that modelling studies are used to infer the effects of dynamical processes using accurate knowledge of the chemical and radiative sources and sinks of energy.

A summary table of the primary sources of heating within the atmosphere resulting from incoming solar radiation is presented in **Table 1.1** below adapted from Beig *et al.* (2003) and Dobbin (2005).

Feature	Wavelength Range	Principal Atmospheric Absorber	Location
Middle infrared bands	$2.0, 2.7, 4.3\ \mu$m	CO_2	Mesosphere
Atmospheric band	762 nm	CO_2	Mesosphere
Chappuis Band	$397 - 850$ nm	O_3	Troposphere
Huggins Band	$305 - 397$ nm	O_3	Troposphere and stratosphere
Hartley Band	$203 - 305$ nm	O_3	Stratosphere and troposphere
Herzberg Continuum	$200 - 240$ nm	O_2 and O_3	Mesosphere
Schumann-Runge Bands	$175 - 200$ nm	O_2	Lower and middle thermosphere
Schumann-Runge Continuum	$130 - 175$ nm	O_2	Middle thermosphere
Lyman α	121.5 nm	O_2 NO‡	Mesosphere Lower thermosphere
FUV	$100 - 200$ nm	O, O_2, N_2 O_2^+, N_2^+	Middle and upper thermosphere
EUV	$10 - 100$ nm	O, O_2, N_2 O_2^+, N_2^+	Middle and upper thermosphere

Table 1.1: Primary absorbers of solar radiation from the stratosphere to the thermosphere with associated wavelength ranges (Beig *et al.,* 2003; Dobbin, 2005).

1.5   Atmospheric Cooling

The thermal structure of the stratosphere and mesosphere layers of the atmosphere arises from a state of equilibrium between absorption of UV radiation and emissions in the IR. Cooling within these layers is dominated by radiative emissions and in particular through emissions from CO_2 at $15\,\mu$m. Other radiative emitters within the lower mesosphere include O_3 at $9.6\,\mu$m and H_2O at $80\,\mu$m and in the upper mesosphere the OH^* Meinel Bands which span the IR spectrum. There is also a minor contribution to cooling resulting from downward turbulent heat conduction.

Below 70 km a state of local thermodynamic equilibrium is typically assumed to exist as collisions between atmospheric constituents are quite frequent. At higher altitudes this assumption no longer holds. The increasingly rarefied nature of the atmosphere with altitude and factors such as radiative absorption between energy levels and energy transitions due to collisions with other atmospheric constituents need to be considered. For example, the deactivation of vibrationally excited CO_2 through collisions with atomic oxygen results in a CO_2 cooling maximum at the mesopause. This is a complex process and the calculation of cooling rates within the mesosphere is not a trivial task.

Above altitudes of approximately 140 km, the concentration of CO_2 drops significantly and downward molecular heat conduction becomes the dominant source of cooling. Between altitudes of $120 - 200$ km the radiative emissions of NO at $5.3\,\mu$m contribute significantly to the total cooling rate. In the upper thermosphere emissions resulting from the fine structure of O at $63\,\mu$m are the dominant source of radiative cooling although it plays only a minor role in the overall thermal balance.

The atmospheric heating and cooling mechanism described in **Sections 1.4** and **1.5** are summarised in **Figures 1.16** and **1.17** which show the global heating and cooling rates within the middle and upper atmosphere as calculated by the NCAR globally averaged mesosphere thermosphere model under solar minimum conditions expressed in units of K/day.
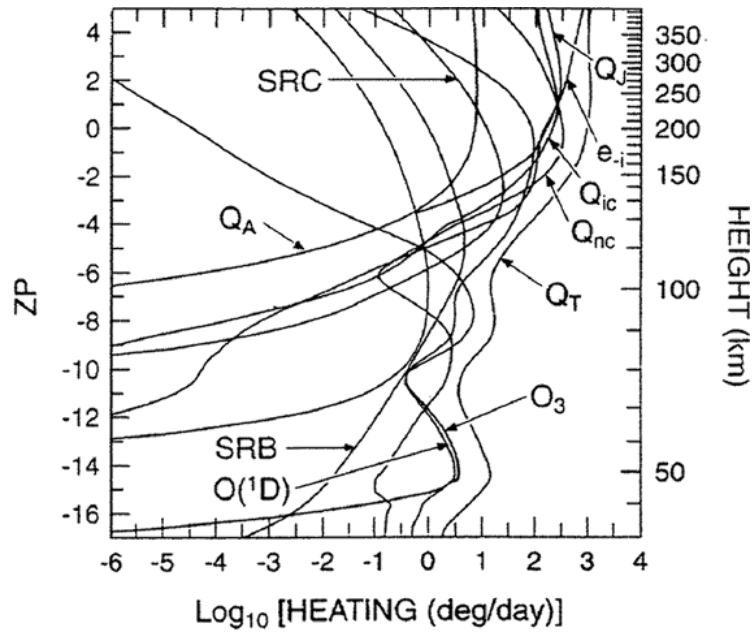
Figure 1.16: Global heating rates calculated by the NCAR globally averaged mesosphere thermosphere model for solar minimum (Roble, 1995). Units are $\log_{10}(K/day)$, where QT is the total heating rate, Qic is heating due to ion-neutral exothermic chemical reactions, Q_{nc} is heating due to neutral-neutral exothermic chemical reactions, Q_J is Joule heating, Q_A is heating due to particle precipitation, e_{-i} is heating due to collisions between thermal electrons, ions and neutrals, $O(^1D)$ is heating due to quenching of $O(^1D)$, SRB and SRC are heating due to absorption by O_2 in the Schumann-Runge continuum and bands, O_3 is heating due to absorption by O_3 in the Hartley, Huggins and Chappuis bands.
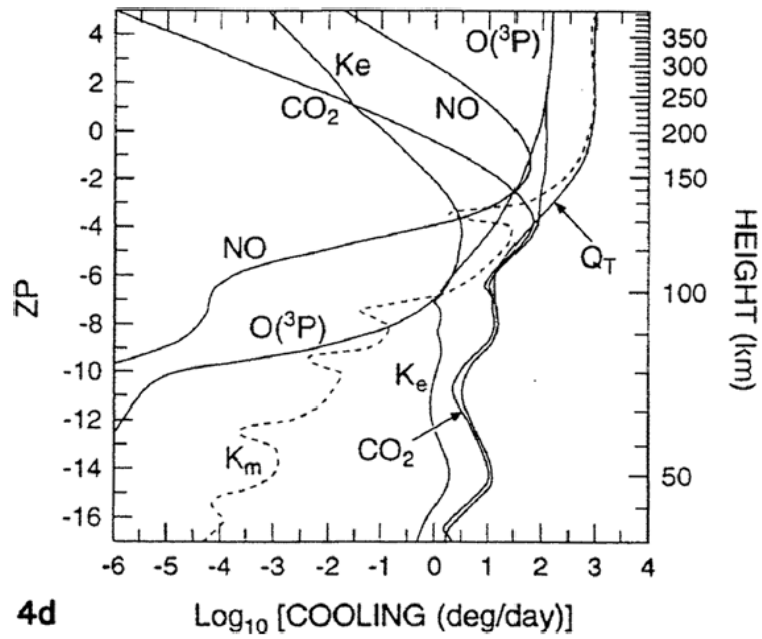
Figure 1.17: Global mean cooling rates calculated by the NCAR globally averaged mesosphere thermosphere model for solar minimum (Roble, 1995). Units are $\log_{10}(\text{K}/\text{day})$ where QT is the total neutral gas cooling rate, KM is the cooling rate due to downward molecular thermal conduction, K_T is the cooling rate due to eddy thermal conduction, NO is radiative cooling due to the $5.3\,\mu$m emission from nitric oxide, CO_2 is radiative cooling due to the $15\,\mu$m band emission from carbon dioxide, $O(^3P)$ is radiative cooling from the $63\,\mu$m fine structure emission of atomic oxygen, O_3 is radiative cooling due to the $9.6\,\mu$m emission from ozone.

1.6   Atmospheric Modelling

The history of atmospheric modelling begins with weather forecasting. For thousands of years human societies have attempted to predict weather events so that farmers could produce crops, sailors could survive at sea and settlers could avoid potential weather related disaster areas. Even some 2000 years ago the Roman poet Virgil forecast that "Rain and wind increase after a thunderclap" (Jacobson, 2005).

Not until the 1870's did weather forecasting, based on observation and experience, become a recognised profession and even during this period, despite the ever increasing amount of data available to forecasters, many viewed the profession as more of an art form than a science and much of these data were ignored. It wasn't until 1903 that Vilhelm Bjerknes of Norway promoted the idea that weather forecasting should be based on the laws of physics. V. Bjerknes (1904) suggested that the evolution of the atmosphere could be described in terms of seven primary variables, namely pressure, temperature, air density, air water content, and the three components of wind velocity.

Bjerknes further realised that many of these variables could be determined using the laws of physics already discovered, including the continuity equation of air, the ideal gas law, the hydrostatic equation, the first law of thermodynamics and Newton's second law of motion although he doubted that they could be solved analytically.

In 1918 Lewis Fry Richardson first proposed a practical means of finding solutions for the above variables using numerical integration methods. Richardson (1922) showed how this might be accomplished although the forecast used to test the method was ultimately unsuccessful. For the next twenty years much of Richardson's work was therefore ignored until John von Neumann proposed that the primary task of ENIAC, (Electronic Numerical Integrator and Calculator), the world's first electronic digital computer, should be weather forecasting.

Subsequently, under the directorship of Jule Charney, ENIAC produced the first one-day numerical weather forecast in 1950 for a 1 dimensional (1-D) barotropic atmosphere, i.e. a homogeneous atmosphere of uniform density and in which there is no vertical motion. The results of the project are discussed in Charney, Fjörtoft and von Neumann (1950). In the following years baroclinic models, in which vertical motion is allowed, were quickly developed. Over the past 60 years, as a direct result of vast

improvements in computational capabilities, numerous primitive equation models, which solve the basic equations of motion, continuity and energy within the atmosphere, and which require colossal numbers of calculations, have been developed.

Today the age old concerns of farmers and sailors are still as pertinent as ever. The added concerns of society such as global warming, increased CO_2 emissions in industry worldwide, aerosol emissions, and overall general pollution has necessitated numerous branches of these atmospheric models. These models are used to test our understanding of the physical, chemical and radiative processes that govern our atmosphere, to assess the validity of our scientific theories and to make predictions about the long, and short, term behaviour of our atmosphere. In the following section, one type of atmospheric model known as a General Circulation Model (GCM) will be introduced.

1.7 General Circulation Models (GCMs)

The very first atmospheric GCM's focused primarily on the troposphere level of the atmosphere. It was believed that, as a result of their rarefied nature, the upper atmospheric layers could not have a significant influence over the lower atmospheric layers. Therefore, the upper layers could not have an influence over the terrestrial climate. GCM's are for the most part split into two distinct groups. The first group focuses on the lower atmospheric layers, such as the U.K. Meteorological Office Unified Model and the U.S. National Centre for Atmospheric Research (NCAR) Coupled Community Model (CCM2). Both models are actively involved in weather prediction and climate research. The second group focuses on the upper atmospheric layers such as the National Centre for Atmospheric Research (NCAR) Thermosphere-Ionosphere-Mesosphere-Energetics (TIME) GCM, the Max Planck Institute (MPI) Hamburg Model of the Neutral and Ionised Atmosphere (HAMMONIA) GCM and the University College London (UCL) Coupled Middle Atmosphere and Thermosphere (CMAT2) GCM employed in this thesis. Chemical and transport models such as the NCAR ROSE Model also exist and are sometimes classified as GCM's.

In more recent years the importance of "Whole Atmosphere Models" has become apparent and new models such as the Whole Atmosphere Community Climate Model (WACCM) are under constant development (Garcia *et al.,* 2007). Currently this model extends from the surface of the planet up to altitudes of approximately 140 km, into the

lower thermosphere. To date, there is no GCM that fully extends from ground level to the upper thermosphere. It is expected that with further development of the model code WACCM will be the first GCM to extend from the surface to altitudes of approximately 500 km. The UK Met Office is also in the process of coupling their unified model to CMAT2 representing another attempt at a whole atmosphere model aimed at producing better space weather predictions although significant amounts of work remain to be completed.

CMAT2 is an extension of the very first global 3-dimensional (3-D), time dependent GCMs developed by Fuller-Rowell and Rees (1980) and Dickinson *et al.* (1981), which self consistently solved the fully coupled non-linear time-dependant equations of energy and momentum within the upper atmosphere (Dobbin, 2005). Since their inception in 1980 these models have undergone numerous developments incorporating self-consistent calculations of atmospheric composition and ionospheric parameters (Fuller-Rowell*,* 1984; Roble and Ridley, 1994; Fuller-Rowell *et al.,* 1996; Millward *et al.,* 1996; Dobbin, 2005) dynamical processes such as tidal forcing (Müller-Wodarg, 1997), gravity wave parameterisations (Meyer, 1999a; Meyer, 1999b; Yiğit *et al.,* 2008) as well as undergoing a number of overhauls in order to increase model efficiency (Harris, 2001; Harris *et al*, 2002). The latest versions of these codes are regularly used in studies of the middle and upper atmosphere and continue to evolve. More details of the CMAT2 model will be presented in **Chapter 2**.

For this thesis the CMAT2 model was chosen for incorporation of OH^* chemistry above the more well established models of WACCM and HAMMONIA. The primary reason for this choice was the CMAT2 model adaptability. Since CMAT2 can be described as an 'up and coming model' there is greater scope for model alterations than with either WACCM or HAMMONIA. Much of the code is not locked in, as with WACCM, and therefore major changes to atmospheric routines can be implemented and their effects on atmospheric features examined. Atmospheric features such as tides and gravity waves can also be easily turned on or off between individual model runs.

The WACCM model was considered unsuitable for this thesis primarily because it outputs model data at 24 hour model day intervals. This effectively eliminates the models capability to look at longitudinal variations which are independent of local time. This is shown in Kowalewski *et al.* (2014). CMAT2 outputs model results at hourly

intervals making it much more suitable for such studies. The WACCM model's vertical resolution is also substantially less than that of the CMAT2 model at mesospheric altitudes making studies of the altitudinal distribution difficult to accomplish.

The HAMMONIA model was discounted for its high horizontal resolution. With a spectral model grid with triangular truncation (T31) the model has a horizontal resolution of 3.75° which would significantly increase the processing power required and time necessary to complete model runs. The horizontal resolution at mesospheric altitudes is also less than that of CMAT2 at approximately 3 km and depends on temperature. Since the inclusion of OH^* chemistry is expected to require high computational resources it makes sense to choose a model with lower resolution in one axis which offsets this requirement. The longitudinal resolution of the CMAT2 model, set at 18°, meets this requirement.

Finally, in the literature to date, the author is unaware of any 3-D models which have incorporated OH^* chemistry apart from the ROSE chemical model. The model resolutions of ROSE and CMAT2 are also the most similar and both models maintain the same lower boundary of 15 km making the results from these models more suitable for comparison. In the following section the basic equations solved for by GCM's will be presented.

Table 1.2 below provides some summary details of the GCMs discussed in this thesis.

Model	Name	Description	Details
CMAT2	Coupled Middle Atmosphere and Thermosphere	Harris (2000) Dobbin (2005)	GCM adopted for this thesis. Adaptable. Low longitudinal resolution.
WACCM	Whole Atmosphere Community Climate Model	Garcia *et al.* (2007)	Code locked in, low vertical resolution and data output at 24 hr intervals.
HAMMONIA	Hamburg Model of the Neutral and Ionised Atmosphere	Schmidt *et al.* (2006)	Triangular truncation grid. High horizontal resolution. Too high for inclusion of OH^*.

ROSE	National Centre for Atmospheric Research (NCAR) Model	Marsh *et al.* (2006)	Most similar to CMAT2 model. Same lower boundary. Officially classed as Chemical and Transport model.

Table 1.2: Summary of GCMs discussed in this thesis including official names, papers with model descriptions and relevant details.

1.8 Basic Physical Principles

As mentioned in **Section 1.6** it was pointed out by Bjerknes (1904) that the evolution of the atmosphere could be described in terms of the seven variables pressure, temperature, air density, air water content, and the three components of wind velocity. These variables can be solved for using the continuity equation of air, the ideal gas law (or equation of state), the hydrostatic equation, the first law of thermodynamics and Newton's second law of motion. It is therefore necessary to discuss each of these laws and principles, as well as some related features.

However firstly, it is worth noting that a quick consideration of these laws will reveal that they can be reduced even further into problems related to the basic physical principles of:

a) conservation of momentum
b) conservation of mass
c) conservation of energy.

Since Newton's second law essentially embodies the principle of conservation of momentum, this will allow for the determination of wind velocities. The continuity equation embodies the principle of conservation of mass, accounting for both air density and water content. The first law of thermodynamics is a statement of the principle of conservation of energy allowing for determinations of heat and temperature. Finally, the ideal gas law, in conjunction with these principles, allows for the relation of quantities such as pressure, temperature and density.

1.8.1   The Hydrostatic Equation

Due to the fact that the atmosphere surrounding the Earth is subject to the planet's gravitational field the density of the atmosphere will fall off exponentially with altitude. The atmosphere can therefore be thought of as a very thin "gaseous envelope" surrounding the planet. Since the atmosphere is very thin the scope of vertical motion is typically quite small, especially when compared to horizontal motions. As such the assumption of hydrostatic equilibrium within the atmosphere, under which gravitational forces on any parcel of air are balanced by buoyancy forces, is often a very good starting point when constructing atmospheric models.   This can be expressed mathematically as

$$\frac{dp}{dz} = -g\rho$$

(1.4)

where ρ is the density of the atmosphere and p is the pressure at an altitude z above the surface of the planet. g represents acceleration due to gravity and is typically held as a constant as it falls only slightly over the total depth of the atmosphere.

1.8.2   Geopotential

A useful quantity that emerges from the hydrostatic equation is geopotential, Φ, which is defined as the work that must be done in order to raise an air parcel of unit mass through an altitude z within the Earth's gravitational field.

If z is the height of a surface of constant pressure p on which two neighbouring points A and B have the same y coordinate (y is an axis on the plane of constant pressure) then

$$\frac{\partial p}{\partial x}\Delta x + \frac{\partial p}{\partial z}\Delta z = \Delta p = 0.$$

(1.5)

Using the hydrostatic equation, (**Equation 1.4**), this can be rearranged to show that

$$g\frac{\partial z}{\partial x} = \frac{1}{\rho}\frac{\partial p}{\partial x}$$

(1.6)

and similarly for $\frac{\partial z}{\partial y}$ such that

$$g\rho\nabla_p z = \nabla_z p$$

<div align="right">(1.7)</div>

where $\nabla_z p$ is the gradient of z in the surface of constant pressure. **Equation 1.7** relates the gradient of pressure in a horizontal surface to the gradient of height in a surface of constant pressure (Houghton, 2002).

However, since g varies with both altitude and latitude it is useful to define geopotential as

$$\Phi = \int_0^z g\,dz$$

<div align="right">(1.8)</div>

or

$$d\Phi = g\,dz.$$

<div align="right">(1.9)</div>

Geopotential is typically expressed in terms of *geopotential height* given by Φ/g_0 where g_0 is the standard value of g. It will be shown in **Section 1.8.6** that geopotential simplifies the equations of motion by eliminating density from the equations.

1.8.3   The Equation of State

The equation of state for a perfect gas with a molecular weight m_r and at a temperature T can be expressed as

$$\rho = \frac{m_r p}{RT}$$

<div align="right">(1.10)</div>

where R is the gas constant per mole. Substituting this equation into **Equation 1.4** it can be shown that

$$\frac{dp}{p} = -\frac{dz}{H}$$

<div align="right">(1.11)</div>

where $H = \frac{RT}{m_r g}$ and is known as the *scale height*. H represents the increase in altitude for which the pressure falls off by a factor of e (~ 2.72).

The value of H differs for the different atmosphere constituents due to their different molecular weights. However, within the atmosphere turbulent mixing below the turbopause allows for the calculation of a 'whole atmosphere' scale height of approximately $8\ \text{km}$ up to altitudes of almost $100\ \text{km}$. Above the turbopause (~ 100 km) the pressure of each atmospheric constituent will subsequently fall off at its own particular scale height.

On integration of **Equation 1.11** an expression for the pressure of the atmosphere at an altitude z can be found and is given by

$$p = p_0 \exp\left\{-\int_0^z \frac{dz}{H}\right\}$$

(1.12)

where p_0 is the pressure of the atmosphere at the planet's surface.

It is therefore possible, under the assumption of hydrostatic equilibrium, to investigate variations in the first variable proposed by Bjerknes (1904), pressure.

1.8.4   The First Law of Thermodynamics

The first law of thermodynamics describes the principle of conservation of energy within the atmosphere and can be expressed as

$$\Delta U = Q - W$$

(1.13)

where ΔU is the change in the internal energy of a system, Q is the heat absorbed by a system and W is the work done by the system.

Consideration of this law on an atmosphere in hydrostatic equilibrium leads to the calculation of an important quantity within the atmosphere known as the *adiabatic lapse rate for dry air*, Γ_d. Γ_d describes the temperature gradient of a dry atmosphere with altitude. This quantity can be used to investigate temperature gradients within the atmosphere as well as identify both stable and unstable conditions within the

atmosphere depending on whether the temperature gradient dT/dz is less than, or greater than, Γ_{d}. As such this accounts for the second atmospheric variable proposed by Bjerknes, temperature.

1.8.5 The Adiabatic Lapse Rate

Considering an atmosphere in hydrostatic equilibrium, the vertical motion of a parcel of air at a pressure p, temperature T, with a specific volume V, and of unit mass can be described by the first law of thermodynamics expressed as

$$\frac{dq}{dt} = c_v \frac{dT}{dt} + p \frac{dV}{dt}$$

(1.14)

where c_v is the specific heat capacity at constant volume. If no heat enters, or leaves, the parcel $\frac{dq}{dt} = 0$ and the motion of the parcel is said to be *adiabatic*.

Under such conditions, if the temperature of the parcel increases, and it subsequently ascends, the pressure on the parcel will decrease and the volume of the parcel will increase. However, expansion of the parcel requires that work is done and as such the temperature of the parcel will drop leading to a decrease in pressure and density. The parcel can then descend leading to an increase in pressure and a subsequent increase in temperature. This cycle can then continue.

Differentiation of the equation of state, **Equation 1.10**, gives

$$pdV + Vdp = \frac{R}{m_r} dT$$

(1.15)

leading to

$$pdV + Vdp = \left(c_p - c_v\right)dT$$

(1.16)

since for a perfect gas $c_p - c_v = R/m_r$ where c_p is the specific heat capacity at constant pressure. Substituting for pdV from **Equation 1.16** into **Equation 1.14** it can be seen that

$$c_p dT - V dp = dq = 0$$

(1.17)

and on substitution of dp from **Equation 1.4** into **Equation 1.17** it can be determined that

$$\frac{dT}{dz} = -\frac{g}{c_p} = -\Gamma_d$$

(1.18)

which when calculated, Γ_d is found to be approximately 10 K/km.

The actual lapse rate of the atmosphere is not entirely adiabatic as factors such as incoming solar radiation will result in cases where $dq/dt \neq 0$. Therefore, if the lapse rate of the atmosphere is calculated to be less than Γ_d and a parcel of air is displaced upwards in altitude from a point A to a point B, the parcel will be colder than the surrounding atmosphere on arrival at point B and will sink demonstrating a stable condition.

If the lapse rate of the atmosphere is greater than the adiabatic lapse rate the parcel of air will have a higher temperature than the surrounding atmosphere on arrival at point B and will therefore continue to rise, demonstrating an unstable condition within the atmosphere.

Under such conditions where the lapse rate of the atmosphere is perfectly adiabatic, and if the background atmosphere is considered to be at rest, the parcel of air will oscillate vertically at what is known as the Brunt-Väisälä frequency.

1.8.6   The Equations of Motion

When applying the laws of motion to a fluid such as the atmosphere, it is important to remember that the fluid will in general move with respect to a chosen rotating frame of reference. It is therefore at times necessary to relate the total derivative with respect to time of a quantity, which follows the fluid, to a partial, or local, derivative of the quantity appropriate to a fixed point within the frame of reference.

When applied to a fluid with a density given by ρ and where there exists a pressure gradient given by $\nabla \rho$, ignoring any frictional terms, Newton's Second Law can be written as

$$\frac{d\mathbf{V}}{dt} = -\frac{1}{\rho}\nabla p + f\mathbf{V} \times \mathbf{k}$$

<div align="right">(1.19)</div>

where $\mathbf{V}$ is the velocity of an element within the fluid, and $\mathbf{k}$ is a unit vector along the axis of rotation of the coordinate system. f is known as the Coriolis factor and is given by $f = 2\Omega \sin\phi$ where Ω is the angular velocity of the rotating frame, usually the Earth's rate of angular rotation, and ϕ is the angle of latitude.

The first term on the right hand side of **Equation 1.19** accounts for velocities stemming from pressure gradient forces generated as a result of heating by incoming solar radiation. The second term accounts for velocities resulting from the Coriolis force.

When these two forces balance, such that $\frac{d\mathbf{V}}{dt} = 0$, the resulting motion of a parcel is referred to as geostropic motion and the geostropic velocity, $\mathbf{V_g}$, can be calculated from

$$f\mathbf{V_g} \times \mathbf{k} = \frac{1}{\rho}\nabla p.$$

<div align="right">(1.20)</div>

$\mathbf{V_g}$ is typically used as an approximation of wind velocities, parallel to isobars, (lines of constant pressure), around points of high and low pressure within the atmosphere at altitudes above $1\,\text{km}$ where frictional terms are low. $\mathbf{V_g}$ is also used as an approximation for the velocities of the mesospheric jets which result from the global pressure gradient associated with the latitudinal variation in solar heating. Geostrophic balance within the mesosphere forces these jets to flow westward in the summer hemisphere and eastward in the winter hemisphere. However, above altitudes of approximately $100\,\text{km}$ geostropic approximations no longer hold as frictional terms resulting from factors such as ion drag increase significantly.

Typically **Equation 1.20** is written in terms of geopotential such that

$$\mathbf{V_g} = \frac{1}{f}\mathbf{k} \times \nabla_p \Phi$$

(1.21)

so that density disappears from the equation and **Equation 1.21** can be applied to any level of the atmosphere without change.

Using the above laws and principles it is possible to calculate the three components of wind velocity within the atmosphere accounting for the third, fourth and fifth variables within the atmosphere as proposed by Bjerknes (1904).

1.8.7   The Continuity Equation

The continuity equation describes the conservation of mass within an atmosphere. Consider a three dimensional box with sides Δx, Δy and Δz in which air with a density ρ travels at velocities u, v, and w along the Cartesian axes. The mass entering the box per unit time at x through the face $\Delta y \Delta z$ can be calculated as $\rho(x)u(x)\Delta y\Delta z$ while the mass leaving the box at $x + \Delta x$ is $\rho(x + \Delta x)u(x + \Delta x)\Delta y\Delta z$.
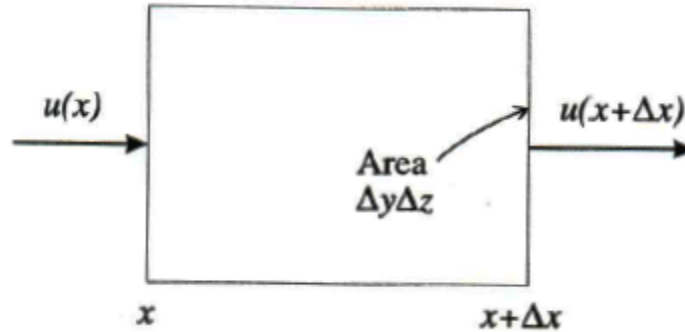
Figure 1.18: Diagrammatic representation of a box with sides Δx, Δy and Δz in which air with a density ρ travels through (Andrews, 2000).

Subtracting these values it can be shown that

$$[\rho(x)u(x) - \rho(x + \Delta x)u(x + \Delta x)]\Delta y\Delta z \approx -\frac{\partial(\rho u)}{\partial x}\Delta x \cdot \Delta y\Delta z.$$

(1.22)

Adding all three components together, where v is the component of velocity in the $y-$direction and w, the component of velocity in the $z-$direction, it is then found that

46

$$\frac{\partial(\rho u)}{\partial x} + \frac{\partial(\rho v)}{\partial y} + \frac{\partial(\rho w)}{\partial z} = -\frac{\partial(\rho)}{\partial t}$$

(1.23)

or

$$\nabla \cdot \rho \mathbf{V} = -\frac{\partial(\rho)}{\partial t}$$

(1.24)

where **V** is the wind velocity. **Equation 1.24** is the continuity equation and allows for investigations of the local rate of change of density within the atmosphere, the sixth variable proposed by Bjerknes.

The final variable proposed by Bjerknes, conservation of water mass, can now also be solved as this is effectively a single constituent component of the continuity equation.

1.9   Chapter 1 Summary

In this chapter the hydroxyl radical and the important role it plays in the chemical and radiative features of the middle atmosphere have been briefly introduced. The goal of this thesis, to develop a computational model which can simulate the night-time infrared emissions from vibrationally excited hydroxyl, has also been set.

The basic structure and general theory of the atmosphere have been discussed with a more detailed focus on the middle atmosphere and the features that govern the chemistry, radiation and dynamics of the region.

A brief description on the history of atmospheric modelling was presented and one particular type and atmospheric model, the GCM, was introduced. Three GCM's were considered for this thesis namely WACCM, HAMMONIA and CMAT2 and the reasons behind the choice of CMAT2 were explained. Within GCM's the fundamental atmospheric equations are solved in order to investigate characteristics within our atmosphere. The chapter concludes with an introduction to these equations and related topics.

Chapter 2

The Coupled Middle Atmosphere and Thermosphere Model (CMAT2)

2.1 Introduction

In **Chapter 1** the background theory of the atmosphere was presented. A brief introduction to the different types of atmospheric models utilised by scientists today, and the fundamental equations which they attempt to solve, was also given.

Within this chapter, one particular GCM, the Coupled Middle Atmosphere and Thermosphere (CMAT2) model will be discussed. This discussion will include a brief history of the CMAT2 model and its development over the past number of years before a detailed description of the model itself is presented. Within this description:

1) the basic assumptions of the model will be discussed,
2) the fundamental equations (described previously in **Chapter 1**) will be presented and modified to appear in their appropriate forms,
3) details of the model grid will be described,
4) the numerical methods used to solve these equations will be presented,
5) the boundary and initial conditions will be discussed.

This will be followed by an exhaustive, but necessary, description of the model parameters, as well as the chemical, energetic and dynamical routines. A quick review of these topics will be presented in the summary before a discussion of the OH radical itself is presented in **Chapter 3**.

2.2   CMAT2 Model History and Development

The University College London (UCL) thermospheric model, first developed by Fuller-Rowell and Rees (1980) was one of the first 3-D time dependant general circulation models (GCMs). The model code was written using the FORTRAN computer language and was designed to determine neutral winds and temperatures at altitudes above 80 km within the thermosphere. Since its inception numerous updates have been made to the original code advancing this model's capabilities significantly.

The first update to the model was incorporated by Fuller-Rowell and Rees (1983) allowing for the calculation of atmospheric densities assuming only two major constituent species N_2 and O_2. This was subsequently increased to the three major atmospheric species N_2, O_2, and O in Fuller-Rowell (1984). Later, this model was coupled with the high-latitude self consistent ionospheric model of Quegan *et al.* (1982) as detailed in Fuller-Rowell and Evans (1987). This update led to the model being named the Coupled Thermosphere and Ionosphere Model (CTIM).

Lower boundary tidal forcing was first incorporated into CTIM by Parish (1989); however, self consistent tidal forcing was not achieved until Müller-Wodarg (1997). Incorporation of the mid- and low-latitude ionospheric and plasmaspheric model of Millward *et al.* (1996) resulted in the model being renamed the Coupled Thermosphere Ionosphere Plasmasphere (CTIP) model.

A major overhaul of the CTIM and CTIP model codes was completed by Harris (2001) resulting in the development of the first Coupled Middle Atmosphere and Thermosphere (CMAT) model. CMAT was developed primarily using a version of the CTIM code in which the ionospheric model of Quegan *et al*. (1982) and tidal forcing of Müller-Wodarg (1997) had already been incorporated. Within CMAT, however, numerous alterations were made to the compositional, dynamical and energetic routines of CTIM in order to incorporate the mesosphere. The vertical resolution was also increased while the lower boundary of the model was extended downwards from 80 km to 30 km.

A significant advance in the nitric oxide (NO) chemistry within the model was incorporated by Dobbin (2005) while Yiğit (2009) introduced updated gravity wave

routines allowing for investigations of the effects of gravity wave dissipation in the upper atmosphere. Streamlining of the existing CMAT model code as well as the incorporation of these newest features resulted in the CMAT2 updated model which is utilised within this project. Depending on the complexity of the input parameters, such as the gravity wave scheme employed, or whether minor chemistry within the model is activated or not, a standard 1 week model run time can take between 4-8 hours.

2.3 CMAT2 Model Assumptions

In order to solve the equations necessary to describe the different features within the atmosphere, such as compositional changes, energetics and dynamics, CMAT2 is forced to make a number of assumptions. These assumptions are:

a) The atmosphere is in a state of local thermodynamic equilibrium. Given that over the height range of the model, collisional excitation and de-excitation of atmospheric constituents typically dominates over radiative transitions this is acceptable.

b) The atmosphere is in a state of hydrostatic equilibrium i.e. the force of gravity at any point within the model grid is exactly balanced by the vertical pressure gradient at that point.

c) The atmosphere is assumed to be an ideal gas and acceleration due to gravity is assumed to be constant.

Hydrostatic equilibrium and the ideal gas law have already been discussed in **Sections 1.8.1** and **1.8.3** and further details are provided in **Sections 2.7.1** and **2.7.4**. Therefore only Local Thermodynamic Equilibrium remains to be discussed in this section.

2.3.1 Local Thermodynamic Equilibrium

Within the lower atmosphere it is often useful to assume a state of local thermodynamic equilibrium (LTE). For a gas at an equilibrium temperature T, statistical mechanics shows that the number of molecules n_1 and n_2, with energy states E_1 and E_2, and with degeneracies g_1 and g_2, will satisfy a Boltzmann distribution.

If the interaction between radiation and matter within the gas is sufficiently weak this Boltzmann distribution of particles and energy states will be maintained through

collisions between the gas particles, provided that the pressure within the gas is sufficiently high. This occurs when the mean time between collisions of the gas molecules is shorter than the radiative lifetime of the excited states. Excitation and de-excitation of the gas molecules therefore occurs through collisions with other molecules rather than through radiative absorption or emission.

On the whole, the atmosphere does not have a uniform temperature and therefore is not strictly in thermodynamic equilibrium. However, at sufficiently high pressures, collisions between atmospheric constituents are rapid enough that within portions of the atmosphere at the same local temperature, LTE can be assumed.

If the net energy gain, or loss, through radiative processes or if the rates of radiative absorption or emission are comparable to the rates of excitation and de-excitation through collisions then the assumption no longer holds and the atmosphere is said to be in a state of non-local thermodynamic equilibrium (non-LTE).

2.4 The Fundamental Equations

As previously described in **Chapter 1**, the fundamental equations the CMAT2 model is required to solve are based on three fundamental principles of physics, namely:

a) conservation of mass,
b) conservation of momentum (given by Newton's 2nd law)
c) conservation of energy (given by the first law of thermodynamics).

In the following sections the equations used to solve these problems are presented in their general form and the contributing atmospheric components are identified and explained.

2.4.1 The Continuity Equation (Conservation of Mass)

The equation of continuity is given by

$$\nabla \cdot \rho \mathbf{V} = -\frac{\partial(\rho)}{\partial t}$$

(2.1)

as previously discussed in **Section 1.8.7**.

2.4.2 The Momentum Equation

When Newton's 2nd Law is applied to a neutral atmosphere the equation for conservation of momentum takes the following form

$$\frac{d\bar{V}_3}{dt} = -2\bar{\Omega} \times \bar{V}_3 + \bar{g} - \frac{1}{\rho}\bar{\nabla}_3 P + \frac{1}{\rho}\bar{\nabla}_3(\mu\bar{\nabla}_3)\bar{V}_3 - v_{ni}(\bar{V}_3 - \bar{U}_{i3})$$

(2.2)

where $\bar{\Omega}$ is the Earth's angular rotation vector, $\bar{V}_3$ is the 3 dimensional neutral wind velocity vector, $\bar{g}$ is acceleration due to gravity, the mass density is denoted by ρ, pressure is P, μ is the summed total of the molecular and turbulent coefficients of viscosity, v_{ni} is the neutral-ion collision frequency and $\bar{U}_{i3}$ is the 3 dimensional ion velocity vector (Rishbeth and Garriott, 1969).

The above terms represent the factors contributing to the conservation of momentum and are, from left to right, the Coriolis term, gravitational acceleration, the pressure gradient term, horizontal and vertical viscosity, and ion drag. Details of each of these components are presented in **Sections 2.4.2.1** to **2.4.2.5.**

Equation 2.2 is clearly representative of 3 dimensional factors. However, since the vertical components of acceleration are much smaller than the horizontal components, the vertical components can be ignored allowing $\bar{V}_3$, $\bar{U}_{i3}$ and $\bar{\nabla}_3$ to be replaced by 2 dimensional horizontal counterparts $\bar{V}$, $\bar{U}$ and $\bar{\nabla}$. The momentum equation used within the model is therefore assumed to be quasi-horizontal consistent with the assumption of quasi-hydrostatic equilibrium.

It should be noted that the left hand side of **Equation 2.2** is presented as a Lagrangian derivative and must be converted from Lagrangian to Eulerian coordinates. This can be accomplished by applying the transformation detailed in **Section 2.5.**

2.4.2.1 The Coriolis Term

A Coriolis force exists wherever an object is in motion with respect to a rotating reference frame. This force acts perpendicularly to the direction in which the object is in motion and the rotational axis of the reference frame. While this force does no work, it does act to change the direction of motion of a moving object. Any object moving

within the Northern hemisphere of the planet will be pushed in a clockwise direction while in the Southern hemisphere it will be pushed in an anticlockwise direction. This force is described by the first term on the right hand side of the momentum equation.
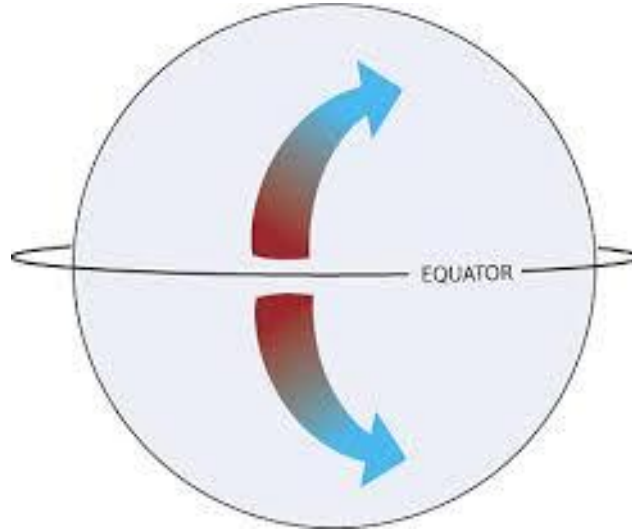
Figure 2.1: Diagrammatic representation of the Coriolis effect on a parcel of air travelling from the equator (NOAA, 2008).

The horizontal component of the Coriolis force, associated with a horizontal velocity $\bar{V}$, can be calculated from $f\bar{V} \times \hat{k}$ where $f = 2\Omega_T \sin \phi$, $\hat{k}$ is the unit vector along the Earth's rotational axis, and ϕ is the latitude. Ω_T is the total angular rotation rate and is the sum of two components, the first of which is due to the angular rotational rate of the Earth. The second component contributing to the Earth's total angular momentum results from the atmosphere being constrained to move on a spherical surface. For an eastward wind with a velocity V_y at a latitude ϕ the total angular rotation rate is

$$2\Omega + \frac{V_y}{R\cos \phi}$$

(2.3)

where R is the radius of the Earth (Dobbin, 2005).

2.4.2.2   Acceleration Due to Gravity

The second term of the momentum equation refers to the force of gravity exerted by the Earth on a parcel of air. Due to the fact that the atmosphere is a very thin layer of gas in which the variation in g is small this term is taken to be a constant by the model. A

value of 9.5 m/s^2 is adopted which corresponds to the value of g at an altitude of approximately 130 km.

2.4.2.3   The Pressure Gradient Term

Pressure gradients exist throughout the atmosphere and can be the result of a number of different processes such as heating by solar radiation. Neutral winds in the atmosphere are a direct result of pressure gradients. Wherever a pressure gradient exists, a force will act on the local atmosphere causing it to move down the pressure gradient. This is captured in the third term of the momentum equation.

2.4.2.4   The Viscosity Term

Viscosity refers to the atmosphere's internal resistance to flow and its attempts to reduce existing velocity gradients in the wind field. It is represented by the fourth term in the momentum equation. The vertical component of this term is the dominant of the two as the vertical wind shears in the atmosphere tend to be much more powerful than the horizontal (Fuller-Rowell, 1981). Similar to turbulent and molecular diffusion in the atmosphere, turbulent viscosity is dominant over molecular viscosity below the turbopause while molecular viscosity is dominant above.

2.4.2.5   The Ion Drag Term

The final term on the right hand side of the momentum equation represents the momentum generated through interactions between the neutral atmosphere and the ionosphere. Collisions between ions and the neutral atmospheric constituents can have either an enhancing or dampening effect on the momentum due to the different processes governing the behaviour of both ions and neutral particles in the upper atmosphere.

At high-latitudes the ion drift velocity is greater than the neutral wind velocity as the electric field drives ions to high velocities (Rishbeth, 1972). Where this is the case the ions will have an enhancing effect on the neutral wind velocity and as such the ion drag term becomes a source of momentum within the atmosphere. At lower latitudes where ions are not driven to high velocities, the ion drag term becomes a momentum sink acting to reduce the velocity of the neutral winds through collisions.

The single species momentum equation for charged particles is given by Rishbeth (1972) as

$$\frac{d\bar{U}_{i3}}{dt} = \bar{g} + \bar{\nabla} \cdot \frac{P_i + P_e}{Nm_i} + \frac{e}{m_i}(\bar{E} + \bar{U}_{i3} \times \bar{B}) - v_{in}(\bar{U}_{i3} - \bar{V}_3)$$

(2.4)

where $\bar{U}_{i3}$ and $\bar{V}_3$ are the ion and neutral constituent velocities. P_i and P_e are the ion and electron partial pressures, N is the ion number density (assumed to be equal to the electron number density), e is the charge on an electron, m_i is the mass of the ion, $\bar{E}$ is the electric field vector, $\bar{B}$ is the magnetic field vector and v_{in} is the ion-neutral collision frequency. Note that in this equation the Coriolis term given in the original momentum equation as $(-2\Omega \times \bar{U}_{i3})$ is neglected. This is due to the fact that v_{in} is large and therefore the Coriolis term becomes negligible.

Assuming steady state conditions the horizontal components of the above equation for ions and electrons can be written as

$$eN_i(\bar{E} + \bar{U}_i \times \bar{B}) - \rho_i v_{in}(\bar{U}_i - \bar{V}) = 0$$

(2.5)

$$-eN_e(\bar{E} + \bar{U}_e \times \bar{B}) - \rho_e v_{en}(\bar{U}_e - \bar{V}) = 0$$

(2.6)

where ρ_i and ρ_e are the ion and electron mass densities, v_{en} is the electron-neutral collision frequency and $\bar{U}_e$ is the electron velocity.

Assuming the total number of electrons is equal to the total number of ions i.e. ($eN_i = eNe$ and adding these two equations together

$$eN_i(\bar{U}_i \times \bar{B}) - eN_e(\bar{U}_e \times \bar{B}) - \rho_i v_{in}(\bar{U}_i - \bar{V}) - \rho_e v_{en}(\bar{U}_e - \bar{V}) = 0.$$

(2.7)

Using the substitution $\bar{J} = eN_i\bar{U}_i - eN_e\bar{U}_e$ for the current density

$$J \times B - \rho_i v_{in}(\bar{U}_i - \bar{V}) - \rho_e v_{en}(\bar{U}_e - \bar{V}) = 0.$$

(2.8)

Rearranging

$$v_{in}(\bar{U}_i - \bar{V}) = \frac{1}{\rho_i}(\bar{J} \times \bar{B}) - \frac{\rho_e}{\rho_i}v_{en}(\bar{U}_e - \bar{V}).$$

(2.9)

Taking Newton's Third Law, which states that

$$\rho_i v_{in} = \rho_n v_{ni}$$

(2.10)

it can be shown that

$$-v_{ni}(\bar{V} - \bar{U}_i) = \frac{1}{\rho_n}(\bar{J} \times \bar{B}) - \frac{\rho_e}{\rho_n}v_{en}(\bar{U}_e - \bar{V}).$$

(2.11)

Considering that $\rho_e \ll \rho_n$ the final term on the right hand side of this equation can be ignored thus removing the ion drag terms dependence on the ion velocity. The expression

$$-v_{ni}(\bar{V} - \bar{U}_i) = \frac{1}{\rho_n}(\bar{J} \times \bar{B})$$

(2.12)

can therefore be used to calculate the ion drag.

The current density $\bar{J}$ in the above equation is calculated using Ohm's Law

$$\bar{J} = \sigma \cdot (\bar{E} + \bar{V} \times \bar{B})$$

(2.13)

where σ is the conductivity tensor, $\bar{E}$ is a convection field applied externally or an internal polarisation electric field and $\bar{V} \times \bar{B}$ is the dynamo electric field. The values for $\bar{E}$ and $\bar{B}$ are known quantities and are specified in the climatological datasets contained within the model. The only unknown value in this equation is the value of the conductivity tensor σ which is a function of the magnetic dip angle, I, and the parallel-, σ_0, Pedersen-, σ_1, and Hall-, σ_2, conductivities.

Pedersen conductivity refers to the component that is in the same direction as the applied electric field. Hall conductivity on the other hand refers to the component

perpendicular to the applied electric field. Both the Pedersen and Hall conductivity components are also perpendicular to the magnetic field. The conductivity component lying along the magnetic field as a result of a parallel electric field is then called the parallel, or longitudinal, component of conductivity. Each component has its peak in a separate region of the atmosphere. The Hall component has the lowest peak at approximately 100 km. Pedersen conductivity peaks at a higher altitude of approximately 130 km in the E-region of the atmosphere. Above 400 km the parallel component of conductivity is dominant.

Using the discussion of Rishbeth and Garriott (1969) this 3x3 conductivity tensor is simplified into a 2x2 tensor through the assumption of layer conductivity. Thus if a layer is limited in vertical extent then any vertical currents which are produced by the dynamo will lead to a build up of charge at the layer boundary. These charges then modify the $\bar{V} \times \bar{B}$ field until the resultant flow is horizontal.

Considering only horizontal layer conductivity

$$\sigma_1 = \begin{pmatrix} \sigma_{xx} & \sigma_{xy} \\ \sigma_{yx} & \sigma_{yy} \end{pmatrix}$$

(2.14)

where

$$\sigma_{xx} = \frac{\sigma_0 \sigma_1}{\sigma_1 \cos^2 I + \sigma_0 \sin^2 I} \approx \frac{\sigma_1}{\sin^2 I}$$

(2.15)

$$\sigma_{xy} = -\sigma_{yx} = \frac{\sigma_0 \sigma_2 \sin I}{\sigma_1 \cos^2 I + \sigma_0 \sin^2 I} \approx \frac{\sigma_2}{\sin^2 I}$$

(2.16)

$$\sigma_{yy} = \frac{\sigma_0 \sigma_1 \sin^2 I + (\sigma_1^2 + \sigma_2^2) \cos^2 I}{\sigma_1 \cos^2 I + \sigma_0 \sin^2 I} \approx \sigma_1$$

(2.17)

The values for the Pedersen and Hall conductivities are calculated in the model using the expressions of Rishbeth and Garriott (1969)

$$\sigma_1 = \frac{N_i e r}{B(1 + r^2)}$$

(2.18)

$$\sigma_2 = r\sigma_1$$

(2.19)

where the ratio of collision to gyro frequencies is denoted by r and determined from $r = m_i v_{in}/(eB)$. N_i is again the electron and ion densities which are assumed to be equal, e is the charge on an electron and m_i is the mean ion mass. v_{in} is the ion-neutral collision parameter of Schunk and Walker (1973) for molecular ions O_2^+ and NO^+ and of Salah (1993) for O^+.

$$v_{in-molecular} = 4.34 \times 10^{-6}[N_2] + 4.28 \times 10^{-16}[O_2] + 2.44 \times 10^{-6}[O]$$

(2.20)

$$v_{in-O^+} = 6.82 \times 10^{-16}[N_2] + 6.66 \times 10^{+16}[O_2] + 3.42$$
$$\times 10^{-17}[O]\sqrt{T}(1.08 - 0.139\log_{10} T + 4.51 \times 10^{-3}(\log_{10} T)^2).$$

(2.21)

The values for the electric field, $\bar{E}$, and the magnetic field, $\bar{B}$, are specified in empirical datasets within the climatological section of the model and are based on the statisitical model of Foster *et al.* (1986) and the International Geomagnetic Magnetic Field described in Langel (1992) respectively. More details of these models are presented in **Sections 2.11.3** and **2.11.4**.

2.4.3 The Energy Equation

The first law of thermodynamics is analogous to the principle of conservation of energy and states that the energy change of a system is equal to the sum total of all energy exchange processes acting across its boundaries. Looking at the atmosphere as a compressible fluid this process can be described by $(\Delta U = Q - W)$ **Equation 1.13** in **Chapter 1**. This equation calculates the rate at which the specific internal energy density of the fluid changes over time. When calculating the temperature distribution in the atmosphere an expression is needed that includes all possible sources and sinks of energy. Transport in both the horizontal and vertical directions must be considered as well as any energy transformations to and from the internal, potential and kinetic

components. In order to calculate this, an expression for the conservation of total energy density per unit mass is required.

By taking the momentum equation (**Equation 2.2**) and multiplying it by $\bar{V}$ an expression for the kinetic energy per unit mass can be obtained as

$$\bar{V}\frac{d\bar{V}}{dt} = \frac{1}{2}\frac{d\bar{V}^2}{dt}.$$

(2.22)

The total rate of change of energy within the fluid can be obtained by summing the internal, kinetic and potential energies. The expression for the geopotential component is given by $(d\Phi = gdz)$ **Equation 1.9** in **Chapter 1**. More details in relation to the energy equation will be presented in **Section 2.7.7** after it has been transformed into spherical co-ordinates.

2.5 The Lagrangian Derivative

The horizontal coordinates used by the CMAT2 model are fixed above the surface of the Earth. These coordinates can be viewed as fixed points in the atmosphere through which the numerous atmospheric constituents flow. This coordinate system is in Eulerian space.

Looking back at **Equation 2.2** (the momentum equation), the term on the left hand side is the Lagrangian, or inertial derivative. This relates to the rate of change in the velocity of an atmospheric parcel moving with the atmosphere and along a particular path or trajectory. In order to be applied within the model this equation must be converted from its Lagrangian to its Eulerian form. The following transformation can be applied in order to accomplish this for any variable *A*.

$$\frac{dA}{dt} = \frac{\partial A}{\partial t} + (\bar{V}_3 \cdot \bar{\nabla}_3)A$$

(2.23)

where $\bar{V}_3$ is the 3-D velocity vector and $\bar{\nabla}_3$ is the 3-D del operator. The left hand term of this transformation relates to the rate of change of the variable *A* at a given point which is moving with the atmosphere. The first term on the right hand side of the transformation is the Eulerian derivative and represents the rate of change of the

variable A at a fixed point in space which is momentarily occupied by a parcel in the atmosphere. The second term on the right hand side of the transformation is the non linear advective term where $\bar{V}_3$ is the 3 dimensional neutral wind velocity vector and $\bar{\nabla}_3$ is the three dimensional del operator. In this context, advection refers to the carrying of properties within the parcel through the atmosphere. This term accounts for the fact that the fixed point within the atmosphere is occupied by successive parts of the parcel, taking its motion through the atmosphere into consideration.

2.6　　　The Co-ordinate System

The equations presented thus far have been in Cartesian co-ordinates where the x-axis is positive in a northwards direction, the y-axis points in an easterly direction and the z-axis points vertically upwards from the lower boundary. However, the CMAT2 model uses a spherical co-ordinate system where the vertical co-ordinate z has been transformed into a pressure co-ordinate P. This simplifies the mathematics involved in calculating the fundamental equations assuming that the atmosphere is in hydrostatic equilibrium and that acceleration due to gravity remains constant, independent of position or altitude. The fundamental equations are also transformed from Lagrangian to Eulerian coordinates as described in **Section 2.5** where necessary.

The transformation between z and P co-ordinate systems in the x direction for any scaler S presented below is adopted from Dobbin (2005) and Harris (2001) and states

$$\left(\frac{\partial S}{\partial x}\right)_P = \left(\frac{\partial S}{\partial x}\right)_z + \left(\frac{\partial z}{\partial x}\right)_P \left(\frac{\partial S}{\partial z}\right).$$

(2.24)

From **Equation 1.9** for geopotential it can be seen that

$$\left(\frac{\partial z}{\partial x}\right)_P = \frac{1}{g}\left(\frac{\partial \Phi}{\partial x}\right)_P.$$

(2.25)

Substituting **Equation 2.25** and the hydrostatic equilibrium equation ($dP/dz = -\rho g$) into the above transformation (**Equation 2.24**)

$$\left(\frac{\partial S}{\partial x}\right)_z = \left(\frac{\partial S}{\partial x}\right)_P + \rho \left(\frac{\partial \Phi}{\partial x}\right)_P \left(\frac{\partial S}{\partial P}\right).$$

(2.26)

Note that $\left(\frac{\partial S}{\partial x}\right)_z$ and $\left(\frac{\partial S}{\partial x}\right)_P$ have switched sides and as such the – from the hydrostatic equation disappears. Applying the same procedure in the y and t directions

$$\left(\frac{\partial S}{\partial y}\right)_z = \left(\frac{\partial S}{\partial y}\right)_P + \rho \left(\frac{\partial \Phi}{\partial y}\right)_P \left(\frac{\partial S}{\partial P}\right)$$

(2.27)

$$\left(\frac{\partial S}{\partial t}\right)_z = \left(\frac{\partial S}{\partial t}\right)_P + \rho \left(\frac{\partial \Phi}{\partial t}\right)_P \left(\frac{\partial S}{\partial P}\right).$$

(2.28)

The transformation is also applied to the horizontal del operator in the z co-ordinate system such that

$$\overline{\nabla}_z S = \overline{\nabla}_P S + \rho \overline{\nabla}_P \Phi \left(\frac{\partial S}{\partial P}\right)$$

(2.29)

where $\overline{\nabla}_P$ is the horizontal del operator in the P co-ordinate system.

For any two dimensional vector $\bar{A}_2$

$$\overline{\nabla}_z \bar{A}_2 = \overline{\nabla}_P \bar{A}_2 + \rho \overline{\nabla}_P \Phi \left(\frac{\partial \bar{A}_2}{\partial P}\right).$$

(2.30)

In the vertical direction, using the hydrostatic equilibrium equation,

$$\frac{\partial S}{\partial z} = \frac{\partial S}{\partial P}\frac{\partial P}{\partial z} = -g\rho \frac{\partial S}{\partial P}$$

(2.31)

and in the horizontal direction

$$\frac{\partial \bar{A}_2}{\partial z} = \frac{\partial \bar{A}_2}{\partial P}\frac{\partial P}{\partial z} = -g\rho \frac{\partial \bar{A}_2}{\partial P}.$$

(2.32)

61

2.7   Transformed Equations

In **Section 2.4** details of how CMAT2 solves the basic physical principles of conservation of mass, momentum and energy were described. However, the equations involved were expressed in terms of Cartesian coordinates while, as detailed in **Section 2.6,** CMAT2 uses a spherical coordinate system.

The following section presents the seven fundamental equations, described in **Chapter 1,** expressed in their final forms after transformations from Lagrangian to Eulerian, and Cartesian to spherical coordinates have been applied. The full derivations of these equations will not be presented but are provided by Fuller-Rowell and Rees (1980) and Fuller-Rowell (1981).

2.7.1   The Hydrostatic Equation

Substituting Φ for S in **Equation 2.32** the vertical transform becomes

$$\frac{\partial \Phi}{\partial P} = -\frac{1}{\rho}$$

(2.33)

and the hydrostatic equation is now described using the alternative pressure co-ordinates.

2.7.2   The Pressure Gradient

The horizontal pressure gradient, $\overline{\nabla}_z \overline{P}$, can also be expressed in pressure co-ordinates using the same transformation. Taking into consideration that $\overline{\nabla}_P \overline{P} = 0$ it can be shown that

$$\overline{\nabla}_z \overline{P} = \rho \overline{\nabla}_P \Phi$$

(2.34)

2.7.3   Vertical Velocity

Using the P coordinate system the vertical velocity is defined as

$$w = \frac{dP}{dt}$$

$$(2.35)$$

while the horizontal velocity is expressed in the same way as in the original z co-ordinate system. Here w is the vertical velocity relative to the isobaric surface and is positive in the downwards direction. Positive values of w therefore represent falling parcels of air while negative values of w represent rising motion relative to a surface of constant pressure.

The vertical velocity in the z co-ordinate system, V_z, can be determined by applying the Eulerian expression of the total derivative $\frac{d}{dt}$ to the expression for geopotential in the P co-ordinate system.

The Eulerian expansion

$$\frac{d}{dt} = \left(\frac{\partial}{\partial t}\right) + \bar{V}_2 \bar{\nabla}_P + w \frac{\partial}{\partial P}$$

$$(2.36)$$

when applied to the geopotential gives

$$\frac{d\Phi}{dt} = \left(\frac{\partial \Phi}{\partial t}\right) + \bar{V}_2 \bar{\nabla}_P \Phi + w \frac{\partial \Phi}{\partial P}.$$

$$(2.37)$$

Using the geopotential **Equation 1.9** and the hydrostatic equilibrium **Equation 2.33**, **Equation 2.37** can be rewritten as

$$\frac{d\Phi}{dt} = g\frac{dz}{dt} = \left(\frac{\partial \Phi}{\partial t}\right)_P + \bar{V}_2 \bar{\nabla}_P \Phi - \frac{w}{\rho}$$

$$(2.38)$$

and therefore V_z, given by $V_z = dz/dt$, is given by

$$V_z = \frac{dz}{dt} = \frac{1}{g}\left(\frac{\partial \Phi}{\partial t}\right)_P + \frac{1}{g}\bar{V}_2 \bar{\nabla}_P \Phi - \frac{w}{g\rho}.$$

$$(2.39)$$

The above equation forms an expression for the vertical velocity in the z co-ordinate system and can be separated into two different components. The first component

63

consists of the sum of the first two terms on the right hand side of the equation and gives the barometric vertical velocity, i.e., the vertical motion of an isobaric surface due to expansion and contraction in the z coordinate system. The final term on the right hand side of the equation is called the divergence vertical velocity and is the component of the vertical velocity attributable to convergences and divergences in horizontal velocity relative to an isobaric layer.

2.7.4 The Perfect Gas Law

$$P = \frac{\rho R T}{M} = \rho g H$$

(2.40)

where R is the gas constant.

2.7.5 The Continuity Equation

$$\frac{\partial w}{\partial P} + \nabla_P \bar{V} = 0.$$

(2.41)

2.7.6 The Momentum Equation

Using the pressure coordinate system described earlier the equation of momentum can be rewritten as

$$\frac{\partial \bar{V}_2}{\partial t} = -\bar{V}_2 \bar{\nabla}_p \bar{V}_2 - w \left(\frac{\partial \bar{V}_2}{\partial P} \right) - \bar{\nabla}_P \Phi - \left(2\Omega + \frac{V_y}{R \sin \theta} \right) \cos \theta \, \underline{k} \times \bar{V}_2$$

$$+ g \frac{\partial}{\partial P} \left((\mu_m + \mu_t) \frac{P}{H} \frac{\partial \bar{V}_2}{\partial P} \right) + \frac{\mu_m}{\rho} \bar{\nabla}_P^2 \bar{V}_2 + \frac{1}{\rho} (\bar{J} \times \bar{B})$$

(2.42)

where w is the vertical velocity, P is the pressure, Ω is the rotation rate of the Earth, the radius of the Earth is R, μ_m and μ_t are the molecular and turbulent viscosity coefficients, H is the scale height, $\bar{J}$ is the current density and $\bar{B}$ is the magnetic field.

The first two terms on the right hand side represent horizontal and vertical advection, geopotential is accounted for by the third term, the fourth represents the Coriolis

contribution, the fifth and sixth terms represent vertical and horizontal viscous drag and the last term in the equation is the ion drag term.

When converted into spherical coordinates and divided into its meridional and zonal components this equation becomes

$$
\frac{\partial V_\theta}{\partial t} = -\frac{V_\theta}{R}\frac{\partial V_\theta}{\partial \theta} - \frac{V_\phi}{R\sin\theta}\frac{\partial V_\theta}{\partial \phi} - w\frac{\partial V_\theta}{\partial P} - \frac{g}{R}\frac{\partial h}{\partial \theta} + \left(2\Omega + \frac{V_\phi}{R\sin\theta}\right)V_\phi\cos\theta
$$

$$
+ g\frac{\partial}{\partial P}\left[(\mu_m + \mu_t)\frac{P}{H}\frac{\partial V_\theta}{\partial P}\right]
$$

$$
+ \frac{1}{\rho}\left(\overline{\nabla}_P^2 V_\theta + \frac{1}{R^2}\frac{\partial \mu}{\partial \theta}\frac{\partial V_\theta}{\partial \theta} + \frac{1}{R^2\sin^2\theta}\frac{\partial \mu}{\partial \phi}\frac{\partial V_\theta}{\partial \phi} + \frac{1}{\rho}(\bar{J}\times\bar{B})\right)
$$

(2.43)

where V_θ and V_ϕ are the velocity components in the southward and eastward directions. θ is the co-latitude, ϕ is the longitude, and other symbols retain their previous meanings. The derivation of these equations can be found in Fuller-Rowell and Rees (1980); Fuller-Rowell (1981); and Müller-Wodarg *et al*. (2001).

2.7.7   The Energy Equation

In CMAT2 the energy equation appears as

$$
\frac{\partial \in}{\partial t} + \bar{V}_2 \cdot \overline{\nabla}_P(\in +\Phi) + w\frac{\partial(\in +\Phi)}{\partial P}
$$

$$
= Q_{EUV} + Q_{IR} + g\frac{\partial}{\partial P}\frac{(K_M + K_T)}{H}P\frac{\partial T}{\partial P} + \frac{1}{\rho}(K_M + K_T)\overline{\nabla}_P^2 T - g\frac{\partial}{\partial P}\frac{K_T g}{C_P}
$$

$$
+ \frac{\bar{J}\cdot\bar{E}}{\rho} + \bar{V}_2 \cdot g\frac{\partial}{\partial P}\frac{\mu}{H}P\frac{\partial}{\partial P}\bar{V}_2.
$$

(2.44)

On the left hand side of this equation the rate of change of internal energy within a gas, the kinetic energy density and the potential energy per unit mass have been combined and converted into the pressure coordinate system. The first term on the left hand side of the equation invokes the specific enthalpy plus the kinetic energy per unit mass given

by $\in= {}^1\!/_2\, \bar{V}_2^2 + C_P T.$ The second and third terms account for horizontal and vertical advection.

The right hand side of the **Equation 2.44** lists the individual components contributing to the total energy namely solar heating, infrared cooling, vertical molecular and turbulent conduction, horizontal molecular and turbulent conduction, vertical turbulent heat conduction as a result of the adiabatic lapse rate, ion drag, Joule heating and vertical viscous drag. The values for the coefficients of molecular and turbulent conductivity are K_M and K_T respectively.

2.8 The CMAT2 Model Grid

The CMAT2 model uses a grid system divided into points which are separated by 18° longitude, 2° latitude and has a total of 63 pressure levels on the vertical axis covering a height range from 15 km to between 250 and 600 km depending on the level of solar activity. The vertical resolution of the model is 1/3 scale height. However, just below the upper boundary, at the last three grid points between levels 61 and 63, the model grid changes to a vertical resolution of one scale height. The simple explanation for this change in vertical resolution is to maintain numerical stability within the model. Greater detail will be provided in **Section 2.10**.

Figure 2.2: Diagrammatic representation of a 2-D model grid.

Each point on the model grid is fixed relative to the surface of the Earth. The pressure at each level point can be obtained from

$$P = P_0 e^{-Z/H} = P_0 e^{\Delta_n(1-n)}$$

(2.45)

where H is the scale height, the height over which the pressure, given by P, decreases by a factor of e. The value of Δ_n is 1/3 for pressure levels 1 to 61 and 1 for levels 61 to 63. n is the pressure level coordinate and takes a value between 1 and 63 inclusive.

2.9   Numerical Integration Method

In order to generate numerical solutions to the non linear terms of the continuity, energy and momentum equations described in **Chapter 1**, a finite difference integration scheme is used at each grid point.

For any function given by

$$F_j = F(x_j)$$

(2.46)

where x_j represents a grid point such that

$$x_j = x_1 + \sum_{n=1}^{j-1} \Delta x_n$$

(2.47)

the two point centre differenced approximation of the first order horizontal and first order vertical spatial derivatives are required. This is given by

$$\frac{dF_j}{dx} = \frac{F_{j+1} - F_{j-1}}{2\Delta_j}$$

(2.48)

where Δ_j is the grid's step length.

The second derivative is then expressed as

$$\frac{d^2 F_j}{dx^2} = \frac{F_{j+1} + F_{j-1} - 2F_j}{\Delta_j^2}$$

$$(2.49)$$

where the subscripts $j+1$, $j-1$, and j are all points on the model grid and are equidistant, Δ_j.

The value of each model parameter is determined using its previous value at the time $t-1$ and then integrating the above differential expressions over the length of the time step in an iterative process which is repeated at all model grid points. In this way the value of the parameter can be calculated for any time t as long as an initial value, t_0, is known.

The energy and momentum equations which are expressed in the form

$$\frac{\partial F(t)}{\partial t} = LF(t)$$

$$(2.50)$$

can be integrated by applying a finite approximation with respect to time where L is the spatial differential operator and contains the first and second order derivatives. The higher order derivatives are ignored. Integrating over a time Δt then gives a solution

$$F_{n+1} = F_n + LF_n \Delta t.$$

$$(2.51)$$

This approximation is stable for differential equations that contain 2nd order spatial derivatives and is known as the Euler method. It is not stable, however, for expressions of the form

$$\frac{\partial F}{\partial t} + \frac{\partial F}{\partial x} = 0$$

$$(2.52)$$

containing only 1st order spatial derivatives. Since certain terms, such as advective terms, within the model contain first order derivatives a numerical diffusion term is added to the Euler method in order to increase the method's stability. This modified version of the Euler method is then stable for equations with both first and second order spatial derivatives and is expressed as

$$F_{n+1} = F_n + LF_n - \frac{1}{2}\Delta t(\bar{V} \cdot \bar{\nabla})(\bar{\nabla} \cdot \bar{V})F_n.$$

(2.53)

This is the numerical scheme used by the model and is referred to as an explicit Forward Time Centred Space (FTCS) scheme more details of which can be found in Harris (2001) and Harris *et al.* (2002).

2.10 Numerical Instabilities

As discussed in **Section 2.9**, the modified Euler method used by the model results in stable solutions to differential equations containing second order spatial derivatives as well as equations with components containing first order spatial derivatives. An example would be a diffusion type equation of the form

$$\frac{\partial F}{\partial t} + K\frac{\partial^2 F}{\partial x^2} = 0$$

(2.54)

with an integration time step $\Delta t < \frac{\Delta^2}{2K}$, where K is a diffusion coefficient and Δ is the grid step length in the x direction.

In the upper regions of the atmosphere, namely the upper thermosphere, vertical transport is dominated by molecular diffusion. In order to maintain numerical stability within the model, a time step of less than 10 s would typically be required. This however, would be computationally very expensive if applied to the entire vertical range and would drastically increase the model run time and processing requirements to the point of making the model impractical. An alternative solution to this problem is to reduce the vertical resolution of the model within this region. As a result, the integration time step of 60 s used by the model can be safely maintained while model run times are unaffected. It is for this reason that the vertical resolution of the model is reduced to one scale height at the topmost two pressure levels approaching the upper boundary.

2.11   Model Parameters

2.11.1   Coefficients of Thermal Conductivity

The coefficient of thermal conductivity, denoted by K_m, is obtained from the empirical expression of Rees (1989) given as

$$K_m = K_0 T^s \ [\text{Wkg}^{-1}\text{K}^{-1}\text{m}^{-1}]$$

$$(2.55)$$

where the K_0 and s parameters are known quantities for each of the major constituents. To find an overall value of K_m a number density weighted mean due to O, O_2, and N_2 is calculated.

In order to obtain the coefficient of turbulent conductivity, denoted by K_t, the relationship

$$K_t = c_P \rho D$$

$$(2.56)$$

is used where c_P is the specific heat capacity at constant pressure, ρ is the mass density, and D is the turbulent diffusion coefficient.

2.11.2   Coefficients of Viscosity

The expression of Dalgarno and Smith (1962) is used to determine the value of the coefficient of molecular viscosity. This expression is given as

$$\mu_m = 4.5 \times 10^{-5} \left(\frac{T}{1000}\right)^{0.71} [\text{kgm}^{-1}\text{s}^{-1}].$$

$$(2.57)$$

Using the coefficient of turbulent conductivity the coefficient of turbulent viscosity can be determined such that

$$\mu_t = \frac{2K_t}{c_P} \ [\text{kgm}^{-1}\text{s}^{-1}]$$

$$(2.58)$$

where c_P is the specific heat capacity at constant pressure. The factor of 2 given in the expression is the ratio of kinematic viscosity to thermal diffusivity within the model and is referred to as the Prandtl number.

2.11.3 Magnetic Field

The Earth's magnetic field is determined using the International Geomagnetic Magnetic Field (IGMF) of Langel (1992) which is an empirical representation of the magnetic field based on worldwide magnetometer readings. This representation of the field also includes the offset dipole nature of the geomagnetic field.

2.11.4 Electric Field and Particle Precipitation Models

A number of important high energy inputs exist within the thermospheric region of the atmosphere. A horizontal convective field, for example, is generated as a result of solar wind plasma blowing across the Earth's magnetic field lines. This field maps itself onto the magnetic field lines of the planet and down into the high-latitude ionosphere resulting in currents that generate Joule heating. Particles with high energy precipitating into the auroral zones deliver additional energy to the thermosphere while also influencing its composition.

The statistical model of Foster *et al.* (1986), which uses measurements of plasma motion in the F region of the atmosphere recorded by the Millstone Hill incoherent scatter radar, forms the basis for the high-latitude electric field model used within CMAT2. Codrescu *et al.* (2000) showed that Joule heating within the thermosphere is generated as a result of both the mean electric field and the observed small scale variability in the electric field with each factor contributing equally to overall heat generated. This is accounted for in the model by taking a random value from a Gaussian distribution with a standard deviation of 0.01 Vm^{-1} and adding it to the existing mean field x and y components if they exceed 0.001 Vm^{-1}.

This model is used in conjunction with a precipitation model based on TIROS/NOAA satellite auroral particle measurements (Fuller-Rowell and Evans, 1987). Statistical maps of the energy influx are generated by integrating the total energy flux carried towards the atmosphere by electrons and positive ions over an energy range of 300 eV

to 1000 eV. A specific auroral activity level (the TIROS level), which is related to the geomagnetic activity index, shown in **Table 2.1** below, is provided to CMAT2. The electric field patterns, as well as the auroral energy input to the model and the ion production rates for the major species due to particle precipitation are determined from the level of activity specified.

Average K_p	1^-	1^0	1^+	2^-	2^+	3^-	3^+	4^0	5^-	6^-
Tiros Level	1	2	3	4	5	6	7	8	9	10

Table 2.1: Tiros Prediction / K_p index relationship (Dobbin, 2005).

Medium energy particles within the range of 30 keV to 2.5 MeV have also been shown to have a significant effect on the electron density and atmospheric composition in the polar mesosphere (Codrescu *et al.,* 1997) and this energy range is accounted for in CMAT2 using the precipitation patterns developed by Codrescu *et al.* (1997).

2.11.5 High-latitude Ionospheric Model

Electron densities, electron and ion temperatures, field aligned velocities and the distribution of ion species under the assumption of photochemical equilibrium are calculated by the high-latitude ionosphere model in CMAT2 and is described in detail by Quegan *et al.* (1982) and Fuller-Rowell and Evans (1987).

2.12 Chemistry and Composition

Within CMAT2 a full thermospheric and mesospheric chemical scheme is adopted which is based on the mesospheric oxygen and hydrogen scheme of Allen *et al.* (1984), the CO and CO_2 chemistry described in Solomon *et al.* (1985), and the mesospheric odd nitrogen reaction of Garcia and Solomon (1983) which is outlined in Fuller-Rowell (1993). JPL-97 reaction rate coefficients of DeMore *et al.* (1997) are applied to the reactions. Within the D-region of the ionosphere atmospheric species are calculated by assuming photochemical equilibrium and using the incorporated Sheffield University Coupled High-latitude Ionosphere Model described in Quegan *et al.* (1982) and Fuller-Rowell *et al.* (1996).

The chemical species for which CMAT2 solves are presented in **Table 2.2** while **Table 2.3** presents the chemical families. Chemical families will be discussed in further detail in **Section 2.12.1**.

Major Constituents	Minor Constituents
N_2	$N(^2D)$
O_2	$N(^4S)$
O	CO_2
Minor Constituents	CO
O_3	He
H	CH_4
OH	$O(^1D)$
HO_2	H_2O_2
NO	NO^+
NO_2	N_2^+
H_2O	O_2^+
H_2	O^+

Table 2.2: Chemical constituents solved for by CMAT2.

Chemical Families
$O_x = O + O_3$
$NO_x = NO + NO_2$
$HO_x = H + OH + HO_2$

Table 2.3: Chemical families within CMAT2.

Within the atmosphere the concentration of the majority of these atmospheric species can be determined by balancing the photochemical production and loss terms and the rate of atmospheric transport. Determining the relative importance of the chemical and dynamical processes can be achieved by evaluating time constants that are associated with each of these processes.

The chemical reaction rate is a quantity that describes the rate at which an atmospheric constituent is either produced or consumed via a chemical reaction. Consider the reaction

$$A \rightarrow C + D \ (k_n)$$

$$(2.59)$$

where $[A], [C]$ and $[D]$ are atmospheric constituents and k_n is the reaction rate at which $[A]$ is consumed and $[C]$ and $[D]$ are produced.

The reaction rate is given by

$$\frac{d[A]}{dt} = -\frac{d[C]}{dt} = -\frac{d[D]}{dt} = -k_n[A]$$

$$(2.60)$$

and can be expressed in units of s^{-1} for a one body reaction.

Rearranging this equation, however, yields

$$\frac{d[A]}{[A]} = -k_n dt$$

$$(2.61)$$

which upon integration gives

$$[A] = [A]_0 e^{-k_n t}$$

$$(2.62)$$

where $[A]_0$ is the concentration of A at time $t = 0$.

$1/k_n$ is then the chemical lifetime of the species and is defined as the time required for the concentration of A to decrease to $1/e$ of its initial value.

In order to determine the lifetime and the rate of change of a species in the atmosphere all possible production and loss mechanisms must be considered. Consider the following list of reactions

$$A + B \rightarrow Products \ (k_1)$$

$$(2.63)$$

$$A + C + M \rightarrow Products \ (k_2)$$

$$(2.64)$$

$$D + E \rightarrow A + Products \ (k_4).$$

$$(2.65)$$
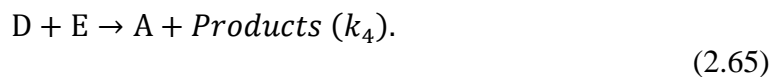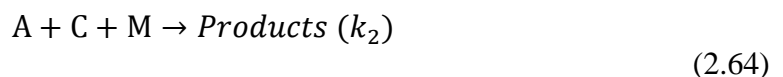
Firstly it should be noted that the reaction rate constants k_1 and k_2 are in units of m^3/s^1 for two body reactions while for a three body reaction the units are m^6/s^1.

The rate of change of A can be expressed as

$$\frac{d[A]}{dt} = -k_1[A][B] - k_2[A][C][M] + k_4[D][E]$$

(2.66)

$$= -L[A] + P$$

(2.67)

where L represents the sum of the loss processes and P represents the sum of the production processes. For a one body reaction this can be integrated from a time $t = 0$ to t and an expression for $[A]$ at time t is

$$[A] = \frac{P - (-[A]_0 L + P)e^{-Lt}}{L}.$$

(2.68)

The chemical lifetime can be found by substituting $A = A_0/e$ into the above equation such that

$$\tau = \frac{1}{L}.$$

(2.69)

If the densities of species B, C, D and E are not changing over the time scale considered and the lifetime is short compared to transport timescales then A is said to be in photochemical equilibrium. In such a situation

$$\frac{d[A]}{dt} = 0$$

(2.70)

and the production is equal to the loss. The concentration of A is then

$$[A] = \frac{P}{L}.$$

(2.71)

The time constants for dynamical effects on atmospheric constituents can be determined assuming that the number density n, of a constituent i, decreases by a factor of e over its scale height H_i (assuming that H_i is not variable with height). Thus

$$n_i = n_{i0} \exp\left(\frac{-z}{H_i}\right)$$

$$(2.72)$$

where z is the altitude and n_{i0} is the initial density of i at a reference altitude.

The vertical gradient of the species can be expressed as

$$\frac{dn_i}{dz} = -\frac{1}{H_i} n_{i0} \exp\left(\frac{-z}{H_i}\right) = -\frac{1}{H_i} n_i.$$

$$(2.73)$$

In a case where changes in the density of a species are due only to vertical winds w (where the positive wind direction points downwards) then

$$\frac{dn_i}{dt} = -\frac{d(n_i w)}{dz} = -\frac{w}{H_i} n_i.$$

$$(2.74)$$

Integrating from a time $t = 0$ to t gives an expression for the density of a species i at time t written as

$$n_{i,t} = n_{i,0} \exp\left(-\frac{w}{H_i} t\right)$$

$$(2.75)$$

where $n_{i,0}$ is the density of i at time $t = 0$.

Thus the density of a species will be $1/e$ of its original value in time H_i/w which defines the time constant for transport by vertical winds.

In a similar fashion, time constants for transport by meridional and zonal winds can be derived by replacing the scale height, H_i, with the scale length. Gradients of chemical species are less known in the horizontal directions making the assessment of the horizontal time constants more difficult to determine. Any incorrect assumptions about

the gradient of a species can lead to errors in the calculation of the dynamical time constants and thus the implied importance of dynamical processes.

For chemically active species the vertical time constant is of the order of days in the upper mesosphere and months in the stratosphere. Similar timescales are estimated for transport by meridional winds. The time constant for transport by zonal winds is of the order of days throughout the middle atmosphere (Brasseur and Solomon, 1986).

A final source of vertical transport to be considered is referred to as eddy or turbulent diffusion and describes the transport of mass by small scale eddies. Eddies are defined as fluctuations about the zonal mean. The time constant for transport by vertical eddy diffusion is given by H^2/K_z where K_z is the vertical eddy diffusion coefficient (Brasseur and Solomon, 1986).

Comparison of the chemical and transport timescales can help determine which processes determine the constituent concentration at a particular point in the atmosphere. Considering a case where the transport timescale of a species is much larger than the chemical timescale then the concentration of the species will be determined by chemistry and transport may be neglected to a first order approximation. Alternatively if the transport timescale of the species is much smaller than the chemical timescale the constituents will be well mixed. If the two timescales are comparable then the distribution of the species will be dependent on both dynamics and chemistry.

It should be noted that when a species is in photochemical equilibrium the concentration of that species may be affected through temperature changes associated with dynamical effects or through the transport of longer lived constituents that contribute to its chemistry. Thus transport processes can indirectly affect the species concentration and cannot be neglected.

2.12.1 Chemical Families

In the previous section chemical lifetimes were discussed and it is therefore now appropriate to discuss the concept of chemical families. When utilising a time dependent numerical model to calculate the variation in time of a species that has a very short chemical lifetime it is important to use a time step that is shorter than that lifetime.

This can be very computationally expensive and thus chemical families are introduced which have lifetimes much longer than those of their constituent members.

Taking the odd oxygen family, O_x, which is made up of $O(^3P)$, $O(^1D)$ and O_3, as an example, the production and loss equations yield chemical lifetimes of 0.4 s, 1 s, and 2000 s respectively at 30 km (Brasseur and Solomon, 1986). The short lifetimes are the result of fast reactions between the members of this family. However, if the entire family is treated as one chemical species then reactions between the individual members can be treated as an exchange, or partitioning, of the family members and not as production and loss terms. This leads to a substantial increase in the lifetime of the family from the order of seconds to the order of weeks as only reactions that cause a net production or loss of O_x need to be considered in the O_x continuity equation.

In total three chemical families are incorporated into CMAT2. The first is the O_x family described above. The second is the NO_x family made up of NO and NO_2. The third family is the HO_x family comprised of H, OH and HO_2.

In order to calculate the relative concentrations of each component within a particular family, partitioning of the species is carried out. This is accomplished by integrating the linearised production and loss differential equations of each family member. The partitioning ratios are determined from the integrated concentrations as shown in the following sections.

2.12.1.1 Odd Oxygen - $O_x = O_3 \; and \; O$

The odd oxygen family within the CMAT2 model consists of both atomic oxygen and ozone. The production and loss of these constituents is shown below and is adapted from Dobbin (2005)

$$\frac{d[O_3]}{dt} = \{[O]^2[O_2]k_{1a} + [O][O_2]^2k_{1b} + [O][O_2][N_2]k_{1c} + [O][O_2][M]k_2\}$$
$$- O_3\{(J_{O_{3a}} + J_{O_{3b}}) + [H]a_2 + [OH]a_6 + [HO_2]a_{6b} + [O_3][NO]b_4$$
$$+ [NO_2]b_9 + [O]k_3\}.$$

(2.76)

$$\frac{d[O]}{dt} = \big\{[OH]^2 a_{16} + [H][HO_2]a_{23c} + [N^4S][O_2]b_7 + [N^2D][O_2]b_{7b} + [N^2D][NO]b_{6a}$$

$$+ [N^4S][NO]b_6 + J_{NO_2}[NO_2] + J_{NO_3 a}[NO_3] + \big(J_{O_3 a} + J_{O_3 b}\big)[O_3]$$

$$+ 2\big(J_{SRB,HZ} + J_{SRC}\big)[O_2] + \text{ion}_{\text{prod}_O} - [O^1D][H_2]a_{3b} - [O^1D][H_2O]a_{1b}$$

$$- [O^1D][CH_4]c_{1a}\big\}$$

$$- [O]\big\{[H_2]a_3 + [OH]a_5 + [HO_2]a_7 + [H_2O_2]a_{31} + [CO][M]a_{37}$$

$$+ [NO_2]b_3 + [O][CH_4]c_3 + [ClO]d_3 + [O_2^2]k_{1b} + [N_2][O_2]k_{1c}$$

$$+ [O_2][M]k_2 + [O_3]k_3 + \text{ion}_{\text{loss}_O}\big\} - [O]^2\big\{[O_2]k_{1a}\big\}$$

$$(2.77)$$

where

$$\text{ion}_{\text{prod}_O} = [N^+][O_2]R_4 + [O_2^+][N^4S]R_8 + [O^+][O_2]R_{10} + 2[O_2^+][e^-]R_7$$

$$+ [NO^+][e^-]R_2 + 0.33(aurqo2)$$

$$(2.78)$$

$$\text{ion}_{\text{loss}_O} = [N^+]R_6 + [N_2^+]R_1 + Ji_O(1 + pe\_O(z)) + aurqo$$

$$(2.79)$$

where $aurqo$ and $aurqo2$ are the ionisation rates as a result of auroral sources.

$pe\_O(z)$ is the ratio of the photoelectron ionisation to the initial solar photon ionisation at altitude z and is described in more detail in **Section 2.13.2.**

These equations are simplified so that

$$\frac{d[O_3]}{dt} = A - B[O_3]$$

$$(2.80)$$

$$\frac{d[O]}{dt} = -X[O]^2 - Y[O] + Z$$

$$(2.81)$$

where A and B represent the production and loss of ozone while Z represents the production of O and X and Y represent the loss of O. These equations can be linearised such that the values of A and B are kept constant. The equation can then be integrated over a time step h from t to $t + h$ giving

$$\int_{O_3(t)}^{O_3(t+h)} \frac{d[O_3]}{(A - B[O_3])} = \int_{t}^{t+h} dt$$

(2.82)

$$\left[\frac{1}{-B} \ln (A - B[O_3])\right]_{t}^{t+h} = h$$

(2.83)

$$\ln \left[\frac{A - B[O_3]_{(t+h)}}{A - B[O_3]_{(t)}}\right] = -Bh$$

(2.84)

$$[O_3]_{(t+h)} = \frac{-(A - B[O_3]_{(t)})e^{-Bh} + A}{B}$$

(2.85)

$$[O_3]_{(t+h)} = \frac{A}{B}(1 - e^{-Bh}) + [O_3]_{(t)}e^{-Bh}.$$

(2.86)

In a similar fashion

$$\int_{O_{(t)}}^{O_{(t+h)}} \frac{d[O]}{-X[O]^2 - Y[O] + Z} = \int_{t}^{t+h} dt$$

(2.87)

$$\frac{1}{\sqrt{Y^2 + 4XZ}} \left[\ln \left(\frac{-2X[O] - Y - \sqrt{Y^2 + 4XZ}}{-2X[O] - Y + \sqrt{Y^2 + 4XZ}}\right)\right]_{t}^{t+h} = h.$$

(2.88)

If

$$\beta = \left(\frac{-2X[O]_t - Y - \sqrt{Y^2 + 4XZ}}{-2X[O]_t - Y + \sqrt{Y^2 + 4XZ}}\right)e^{h\sqrt{Y^2 + 4XZ}}$$

(2.89)

it is possible to say that

$$[O]_{(t+h)} = \frac{\beta\left(Y - \sqrt{Y^2 + 4XZ}\right) - \left(Y + \sqrt{Y^2 + 4XZ}\right)}{2X - \beta 2X}.$$

(2.90)

Equations 2.89 and **2.90** can therefore be used to determine the ratio of O to O_3 and therefore their relative concentrations within the odd oxygen family.

The minor species $O(^1D)$ is assumed to be in photochemical equilibrium by the model such that

$$\frac{d[O(^1D)]}{dt} = 0 = J_{O_{3_a}}[O_3] + J_{SRC}[O_2] + J_{H_2O_b}[H_2O]$$
$$- [O(^1D)]\{[H_2O]a_{1b} + [H_2]a_{3b} + [CH_4]c_{1a} + [O_2]k_{4b} + [N_2]k_{4c}\}$$

(2.91)

giving

$$[O^1(D)] = \frac{J_{O_{3_a}}[O_3] + J_{SRC}[O_2] + J_{H_2O_b}[H_2O]}{\{[H_2O]a_{1b} + [H_2]a_{3b} + [CH_4]c_{1a} + [O_2]k_{4b} + [N_2]k_{4c}\}}.$$

(2.92)

2.12.1.2 Odd Hydrogen - $HO_x = H \; and \; OH \; and \; HO_2$

The chemical production and loss equations for the odd hydrogen family members from Harris (2001) are

$$\frac{d[HO_x]}{dt} = 2\Big\{J_{H_2O_a}[H_2O] + J_{H_2O_2}[H_2O_2] + [O(^1D)][H_2]a_{3b} + [O(^1D)][H_2O]a_{1b}$$
$$+ [O(^1D)][CH_4]c_{1a} + [O][H_2]a_3\Big\}$$
$$- 2\{[HO_2][H](a_{23b} + a_{23b}) + [OH][HO_2]a_{17} + [HO_2]^2a_{27} + [OH]^2a_{16}$$
$$+ [OH][CH_4]c_2\}.$$

(2.93)

Simplifying the above, as before, yields

$$\frac{d[OH]}{dt} = -X_{OH}[OH]^2 - Y_{OH}[OH] + Z_{OH}$$

(2.94)

81

where

$$X_{OH} = 2a_{16}$$

(2.95)

$$Y_{OH} = [O]a_5 + [O_3]a_6 + [HO_2]a_{17} + [H_2]a_{19} + [H_2O_2]a_{30} + [CO]a_{36} + [N^4S]b_{10}$$

(2.96)

$$Z_{OH} = J_{H_2O_a}[H_2O] + [O(^1D)][H_2]a_{1b} + [O_3][H]a_2 + [O_3][HO_2]a_{6b} + [HO_2][O]a_7$$
$$+ 2[H][HO_2]a_{23a} + [NO][HO_2]a_{26} + 2J_{H_2O_2}[H_2O_2] + [O(^1D)][H_2]a_{3b}$$
$$+ [O(^1D)][CH_4]c_{1a} + [O][H_2]a_3 + [H_2O_2][O]a_{31}.$$

(2.97)

$$\frac{d[HO_2]}{dt} = -X_{HO_2}[HO_2]^2 - Y_{HO_2}[OH] + Z_{HO_2}$$

(2.98)

where

$$X_{HO_2} = 2a_{27}$$

(2.99)

$$Y_{HO_2} = [O_3]a_{6b} + [O]a_7 + [H](a_{23a} + a_{23b} + a_{23c}) + [NO]a_{26} + [OH]a_{17}$$

(2.100)

$$Z_{HO_2} = [H][O_2][M]a_1 + [OH][H_2O_2]a_{30} + [O][H_2O_2]a_{31} + [OH][O_3]a_6.$$

(2.101)

$$\frac{d[H]}{dt} = -X_H[H]^2 - Y_H[H] + Z_H$$

(2.102)

where

$$X_H = 2a_{24}[M]$$

(2.103)

$$Y_H = [O_2][M]a_1 + [O_3]a_2 + [HO_2](a_{23a} + a_{23b} + a_{23c})$$

(2.104)

$$Z_H = [O][OH]a_5 + J_{H_2O_a}[H_2O]a_{1b} + [O(^1D)][H]a_{3b} + [O][H_2]a_3 + [OH][H_2]a_{19}$$
$$+ [CO][OH]a_{36} + [N^4S][OH]b_{10}.$$

(2.105)

The production and loss equations for the HO_x family are partitioned such that

$$\frac{[OH]}{[HO_x]} = \frac{1}{1 + \dfrac{[H]}{[OH]} + \dfrac{[HO_2]}{[OH]}}.$$

(2.106)

The hydrogen peroxide minor species is assumed to be in photochemical equilibrium and therefore

$$\frac{d[H_2O_2]}{dt} = 0 = a_{27}[HO_2]^2 - [H_2O_2]\left\{J_{H_2O_2} + [OH]a_{30} + [O]a_{31}\right\}$$

(2.107)

giving

$$[H_2O_2] = \frac{a_{27}[HO_2]^2}{\left\{J_{H_2O_2} + [OH]a_{30} + [O]a_{31}\right\}}.$$

(2.108)

2.12.1.3 Odd Nitrogen - $NO_x = NO$ *and* NO_2

Using the same techniques described in the previous sections

$$\frac{d[NO_x]}{dt} = \left\{[O_2][N^2D]b_{7b} + [O_2][N^4S]b_7 + [NO_3]\left(J_{NO_{3a}} + J_{NO_{3b}}\right) + [N^4S][OH]b_{10}\right.$$
$$+ 2[N_2O][O(^1D)]b_{13} + [N^+][O]R_{4a}\Big\}$$
$$- \{[NO]J_{NO} + [NO][N^4S]b_{6b} + [NO][N^2D]b_{6a} + [NO]Ji_{NO}$$
$$+ [NO_2][O_3]b_9\}.$$

(2.109)

Simplifying as before this leads to

$$\frac{d[NO]}{dt} = A_{NO} - B_{NO}[NO]$$

(2.110)

83

where

$$A_{\text{NO}} = [\text{NO}_2][\text{O}]b_3 + [\text{N}^4\text{S}][\text{O}_2]b_7 + [\text{N}^2\text{D}][\text{O}_2]b_{7b} + [\text{N}^4\text{S}][\text{OH}]b_{10} + [\text{NO}_2]J_{\text{NO}_2}$$
$$+ 2[\text{N}_2\text{O}][\text{O}(^1\text{D})]b_{13} + [\text{NO}_3]J_{\text{NO}3b} + [\text{N}^+][\text{O}]R_{4a}$$

(2.111)

$$B_{\text{NO}} = [\text{HO}_2]a_{26} + [\text{O}_3]b_4 + [\text{N}^4\text{S}]b_6 + [\text{N}^2\text{D}]b_{6a} + [\text{O}_2^+]R_9 + J_{\text{NO}} + Ji_{\text{NO}} + [\text{ClO}]d_4.$$

(2.112)

$$\frac{d[\text{NO}_2]}{dt} = A_{\text{NO}_2} - B_{\text{NO}_2}[\text{NO}_2]$$

(2.113)

where

$$A_{\text{NO}_2} = [\text{HO}_2][\text{NO}]a_{26} + [\text{NO}][\text{O}_3]b_4 + [\text{NO}_3]J_{\text{NO}3_a} + [\text{NO}][\text{ClO}]d_4$$

(2.114)

$$B_{\text{NO}_2} = [\text{O}]b_3 + [\text{O}_3]b_9 + J_{\text{NO}_2} + [\text{NO}_3]b_{12}.$$

(2.156)

Partitioning of the different constituent species yields

$$\frac{[\text{NO}_2]}{[\text{NO}_x]} = \frac{1}{1 + \dfrac{[\text{NO}]}{[\text{NO}_2]}}$$

(2.116)

and

$$\frac{[\text{NO}]}{[\text{NO}_x]} = \frac{1}{1 + \dfrac{[\text{NO}_2]}{[\text{NO}]}}.$$

(2.117)

Photochemical equilibrium is assumed for the NO_3 constituent. In the upper stratosphere this leads to

$$\frac{d[\text{NO}_3]}{dt} = 0 = [\text{O}_3][\text{NO}_2]b_9 - [\text{NO}_3]\{b_{12}[\text{M}][\text{NO}_2] + J_{\text{NO}3}\}$$

(2.118)

giving

$$[NO_3] = \frac{[O_3][NO_2]b_9}{\{b_{12}[M][NO_2] + J_{NO_3}\}}.$$

(2.119)

Having described the O_x, HO_x, and NO_x chemical familes above, the following sections present the continuity equations for the remaining atmospheric species considered by the CMAT2 model.

2.12.2   Atomic Nitrogen N(^{4}S)

Atomic nitrogen N^4S is calculated from

$$\frac{d[N^4S]}{dt} = ion_{prod_{N^4S}} + [NO]J_{NO} + [O][N^2D]b_8 + [N^2D]b_{xx1} + [N^2D][e^-]R_{13}$$
$$- [N^4S]\{[O_2]b_7 + [NO]b_6 + [OH]b_{10} + [O_2^+]R_8 + J_{N4S}\}$$

(2.120)

where $ion_{prod_{N^4S}}$ is the ionospheric production of N^4S and is given by

$$ion_{prod_{N^4S}} = 0.25(Ji_{PN_2}) + 0.15[NO^+][e^-]R_2 + 0.90(0.44[N_2^+][e^-]R_3)$$
$$+ [O^+][N_2]R_{11} + [N^+][O_2]R_5 + [N^+][O]R_6$$
$$+ 0.40\left((1.34)Pe\_N_2(z)Ji_{N_2}\right) + Ji_{N_2}\left(N\_N_p(z)\right) + 0.24Pe_{N_2(z)}$$
$$+ 0.5(aurqn2 * 0.24) + 0.25(aurqn2 * 1.24).$$

(2.121)

$Pe\_N_2(z)$ is the ratio of photoelectron ionisation to the initial solar ionisation at an altitude z while $N\_N_p(z)$ is the ratio of N^+ production to primary photon ionisation of $N_2(Ji_{N_2})$ at an altitude z. The ionisation rate of N_2 as a result of auroral sources is given by $aurqn2$. Ji_{PN_2} is the predissociation rate of N_2 referring to the process in which N_2 molecules are excited by incident photons to *predissociation states* decaying by dissociation of the N_2 molecule rather than by radiation. The resulting atomic nitrogen is then partitioned between the ground state N^4S and excited state N^2D using the partitioning factors of Fuller-Rowell (1993).

2.12.3 Atomic Nitrogen $N(^2D)$

Atomic nitrogen N^2D is calculated from

$$\frac{d[N^2D]}{dt} = ion_{prod_{N^2D}} - [N^2D]\{[O_2]b_{7b} + [NO]b_{6a} + [O]b_8 + b_{xx1} + [e^-]R_{13}\}$$

(2.122)

where, as before, $ion_{prod_{N^2D}}$ is the ionospheric production of N^2D and is given by

$$ion_{prod_{N^2D}} = [N_2^+][O]R_1 + 0.75(Ji_{PN_2}) + 0.85[NO^+][e^-]R_2 + 0.1(2[N_2^+][e^-]R_3)$$
$$+ 0.90\left((0.56)Pe\_N_2(z)Ji_{N_2}\right) + 10Ji_{N_2}\left(N_{N_p(z)} + 0.24Pe\_N_2(z)\right)$$
$$+ 0.5(aurqn2 * 0.24) + 0.75(aurqn2 * 1.24).$$

(2.123)

2.12.4 Water Vapour H_2O

Water vapour within the atmosphere is calculated from

$$\frac{d[H_2O]}{dt} = [OH][OH]a_{16} + [OH][HO_2]a_{17} + [OH][H_2O_2]a_{30} + [OH][H_2]a_{19}$$
$$+ [H][HO_2]a_{23c} + [CH_4][OH]c_2 + [H_2O]\left(J_{H2O_a} + J_{H2O_b}\right).$$

(2.124)

2.12.5 Molecular Hydrogen H_2

Molecular hydrogen is calculated from

$$\frac{d[H_2]}{dt} = [HO_2][H]a_{23b} + [H_2O]J_{H_2O_b} + [H]^2[M]a_{24}$$
$$- [H_2]\{[OH]a_{19} + [O^1D]a_{3b} + [O]a_3\}.$$

(2.125)

2.12.6   Methane CH_4

Methane is calculated using

$$\frac{dCH_4}{dt} = -[CH_4]\{[OH]c_2 + [O]c_3 + [O^1D]c_{1a}\}.$$

(2.126)

2.12.7   Carbon Dioxide CO_2

Carbon dioxide is calculated from

$$\frac{d[CO_2]}{dt} = [CO][OH]a_{36} + [CO][O][M]a_{37}.$$

(2.127)

2.12.8   Carbon Monoxide CO

Carbon monoxide is calculated using

$$\frac{d[CO]}{dt} = [CH_4][O^1D]c_{1a} + [CH_4][O]c_3 + [CH_4][OH]c_2 - [CO]\{[OH]a_{36} + [O][M]a_{37}\}.$$

(2.128)

2.12.9   Helium He

Helium is considered to be in photochemical equilibrium such that

$$\frac{d[He]}{dt} = 0.$$

(2.129)

2.12.10   Ion Chemistry

CMAT2 uses the ion chemistry code derived from the original CTIM model routines developed by Fuller-Rowell (1996). Within these routines the distribution of O^+ is determined first and is followed by calculations of the distributions of N^+, O_2^+, N_2^+, and NO^+ assuming photochemical equilibrium. The concentrations of N^2D and N^4S are calculated self-consistently within the code. Within the tropical regions, at latitudes between $\pm 25°$, the density of O^+ as well as the electron and ion temperatures are calculated from a linear interpolation of their values at the boundary of the high-latitude

code. By using the interpolated values, the electron and ion densities can be calculated. Photoionisation and dissociation rates will be discussed in more detail in **Section 2.13.2.**

2.12.11 Start Up Constituent Climatologies/Initial Conditions

CMAT2 uses start up climatologies for a number of different constituents. These data come from a number of different sources. The concentrations of constituents O, O_2, and H are determined from the MSISE-90 reference model (Hedin, 1991) while the concentration of N_2 is determined as the remainder of the whole atmosphere minus the other major constituents. The Upper Atmosphere Research Satelite (UARS) reference atmosphere as described in Remedios *et al.* (1998) is used as the source for startup climatological data on O_3, H_2O, N_2O and CH_4 where the data is available. The global means of O_3, H_2O, and CH_4 as calculated by the John Hopkins University Applied Physics Laboratory two-dimensional model (JHU/APL 2-D), from Zhu *et al.* (1999), are used to determine the concentrations of these species above the altitude range covered by the UARS satellite. The concentration of N_2O is linearly interpolated from its value at the upper boundary of the UARS detection range. NO and NO_2 values are taken from data collected by the UARS HALogen Occultation Experiment (HALOE). These data have been collected from monthly zonal mean dawn observations. Above 56 km where data from HALOE is unavailable, the concentrations of NO, N^4S, and N^2D are taken as global means from the NCAR TIME-GCM as described in Roble *et al.* (1987). Up to the turbopause, CO_2 is assumed to have a constant mixing ratio of 360 ppm above which the concentration falls off with its scale height. For the remainder of the constituents, the global mean profiles of Roble (1995) are used.

At the uppermost two pressure levels the concentration of atomic hydrogen is taken from MSISE-90. With regards to all other constituents, diffusive equilibrium is assumed at the upper boundary. A more detailed description of the start-up climatologies and the boundary mixing ratios is presented in Harris (2001).

2.13   Energetics

Up to this point the effects of incoming solar radiation have been largely ignored. However, the atmosphere is not transparent to incoming radiation and as such absorption of solar radiation by the atmosphere requires consideration.

The Lambert-Beer law states that at any point within the atmosphere the intensity of solar radiation can be calculated from

$$I(\lambda) = I_\infty(\lambda) \exp(-\tau(\lambda))$$

(2.130)

where $I(\lambda)$ is the intensity of radiation at a wavelength λ, $I_\infty(\lambda)$ is the irradiance of the radiation at 1 AU (1 astronomical unit = 1.496×10^{11} m) and $\tau(\lambda)$ is the optical depth of the radiation and measures the attenuation of the radiation by the atmosphere. The wavelength dependent optical depth is given by

$$\tau_{z0}(\lambda) = \sum_j \sigma_j(\lambda) \int_{z_0}^{\infty} n_j(z) \sec \chi \, dz$$

(2.131)

where $\sigma_j(\lambda)$ is the wavelength dependant absorption cross section of an atmospheric constituent j and $n_j(z)$ is the height profile of the constituents concentration. $\sec \chi \, dz$ represents the volume of atmosphere through which the radiation transverses at an angle of χ to the vertical as shown in **Figure 2.3** below.
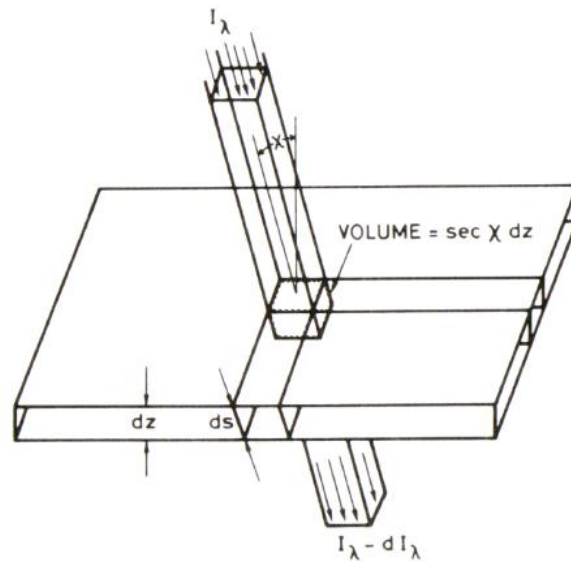
Figure 2.3: Absorption of solar radiation in an atmospheric layer of unit area (Brasseur and Solomon, 1986).

The angle at which solar radiation enters the atmosphere is dependent on a number of factors including latitude, local time, and day of year such that the cosine of the solar zenith angle is

$$\cos \chi = \cos \phi \cos \delta \cos H + \sin \phi \sin \delta$$

(2.132)

where ϕ is the angle of latitude, δ is a seasonally dependent solar declination angle, and H is the hour angle which is 0° for local noon.

At sunrise and sunset, when the solar zenith angle is greater than 75° however, the curvature of the Earth makes the atmospheric column content a much more complicated function of solar zenith angle. As a result, the Chapman grazing incidence function, $Ch(\chi)$, (discussed in greater detail in **Section 2.13.4**) which describes the ratio of the total amount of absorbent along a path to the amount of absorbent in the vertical, replaces the solar zenith angle (Swider and Gardner, 1969).

2.13.1   Solar Irradiance

The Lambert-Beer exponential absorption law, described in the previous section, is used by CMAT2 to calculate the level of absorption of solar radiation and thus the rate at which radiation heats up the atmosphere. Due to the fact that the CMAT2 model has an

upper boundary, the contribution to the integral within this equation resulting from the atmosphere above this boundary must also be accounted for. This is accomplished using the expression of Rishbeth and Garriott (1969) which shows that for a species with a local number density n_0, where the local scale height is given by H_0, the total number density per unit area, referred to as the column density, can be determined from $n_0 H_0$.

2.13.2 Photoionisation and Dissociation

Photoionisation occurs within the atmosphere when radiation of a suitable wavelength excites electrons within atmospheric constituents to the point that they are capable of ejecting themselves entirely from the constituent. The result is a layer of the atmosphere known as the ionosphere. The photoionisation rate J^i of an atmospheric species j at an altitude z can be calculated from

$$J_z^i(j, l) = n_z(j) \int_{\lambda_{th}}^{0} I_z(\lambda) b_j^i(\lambda, l) \sigma_j^i(\lambda) d\lambda$$

(2.133)

adapted from Brasseur and Solomon (1986) where $n_z(j)$ is the concentration of a constituent j at altitude z, λ_{th} represents the ionisation threshold wavelength, $I_z(\lambda)$ is the intensity of radiation at a wavelength λ at altitude z, and $\sigma_j^i(\lambda)$ is the ionisation cross section. $b_j^i(\lambda, l)$ represents the branching ratios which specify the production of ions within both the ground state and electronically excited states l. For each constituent

$$\sum_l b_j^i(\lambda, l) = 1.$$

(2.134)

Equation 2.134 needs to be integrated from the ionisation threshold wavelength, for the production of ions in the ground state, to the minimum wavelength for which the photon flux contributes to the production of ions. In atmospheric modelling it is common practice to specify the total photionisation cross sections and branching rations for specific wavelength intervals.

Photodissociation of O_2 explains why O is the major atmospheric species within the thermosphere above altitudes of approximately 200 km. The photodissociation rate of an atmospheric constituent j at an altitude z is

$$J_z^d = n_z(j) \int_{\lambda_d}^{\lambda_i} I_z(\lambda)\sigma_j^4(\lambda)d\lambda$$

$$(2.135)$$

where $\sigma_j^4(\lambda)$ is the photodissociation cross section. The integration is carried out from the wavelength below which photons play a part in the process, λ_d, to the ionisation limit, λ_i where photon absorption leads almost entirely to ionisation.

2.13.3   Solar Heating

The atmospheric heating as a result of the absorption of solar radiation with a wavelength λ can be calculated using

$$Q(\lambda) = n\frac{hc}{\lambda}\varepsilon(\lambda)\sigma_a(\lambda)I_\infty(\lambda)\exp\big(-\tau(\lambda)\big)$$

$$(2.136)$$

(Dobbin, 2005), adapted from Andrews (2000) and Houghton (1986), where n is the concentration of the constituent, the photon energy is given by hc/λ, h is Planck's constant and c is the speed of light in a vacuum. The heating efficiency is represented by $\varepsilon(\lambda)$ and is the fraction of the incoming energy that is converted into heat. $\sigma_a(\lambda)$ is the absorption cross section of the particular constituent and $I_\infty(\lambda)$ is the intensity of the radiation at wavelength λ at a distance of 1 AU. $\tau(\lambda)$ is the optical depth and is a measure of the quantity of radiation removed through scattering or absorption as it travels along its path. The total heat generated over a particular range of wavelengths can also be obtained by integrating the above equation over the full range of wavelengths.

2.13.4   The Thermospheric Heating Routine

The current thermospheric heating routine in CMAT2 calculates the thermospheric UV and EUV heating and ionisation at 5 nm spectral intervals while also accounting for the

effects of line emission. This routine was developed by Fuller-Rowell (1981) and has since undergone numerous updates. In one update by Fuller-Rowell (1993) the routine was amended to calculate the Chapman grazing incidence functions for each of the absorbing species. The ionisation spectral range was also extended to include soft and hard x-rays. The equations used within the routine, from Swider and Gardner (1969), are

$$Ch\left(x, \chi \leq \frac{\pi}{2}\right) = \left(\frac{\pi x}{2}\right)^{\frac{1}{2}}\left(1 - erf\left(x^{\frac{1}{2}}\cos\frac{\chi}{2}\right)\right)\exp\left(x\cos^2\frac{\chi}{2}\right)$$

(2.137)

$$Ch\left(x, \chi \geq \frac{\pi}{2}\right) = \left(\frac{\pi x}{2}\sin\chi\right)^{\frac{1}{2}}\left(1 + erf\left(-\cot\chi\left(\frac{x\sin\chi}{2}\right)^{\frac{1}{2}}\right)\right)\left(1 + \frac{3}{8x\sin\chi}\right)$$

(2.138)

where $x = \dfrac{(a + z)}{H}$, a is the radius of the Earth, z is the altitude and H is the scale height of the absorber species under consideration. The purpose of these equations is to account for the curvature of the Earth at large solar zenith angles and were not included in the original thermospheric code.

The UV fluxes from the Schumann-Runge continuum between 105 and 180 nm are from Torr *et al.* (1980a). The modified Hinteregger (1970) fluxes due to Torr *et al.* (1979) measured by the AE satellite are used within the EUV spectral range between 1.8 and 105 nm. Corresponding O, O_2, and N_2 ionisation and absorption cross sections are from Torr *et al.* (1979) although below 40 nm the values for O have been modified in accordance with Samson and Pareek (1985). For wavelengths below 5 nm the cross sections are from Oshio *et al.* (1966) and Banks and Kockarts (1973). The cross sections for the O_2 Schumann Runge continuum are from Torr *et al.* (1980b).

Processes such as airglow emissions, secondary electron events and electron collisions also act as sinks of energy within the thermosphere. At the time of writing none of these processes are accounted for by the model. However, the photon energy channelled into these events must still be accounted for and as such the EUV heating

efficiencies of Roble *et al.* (1987) are applied. These heating efficiencies also account for ion-neutral exothermic reaction contributions.

Dissociative heating of O_2 between 130 and 240 nm, requiring 5.08 eV, and occurring at altitudes between 100-130 km is the main source of solar heating within the UV spectral range. Since the lifetime of atomic oxygen within the lower thermosphere is large, with a value larger than a day, recombination does not occur locally and due to transport effects the chemical energy absorbed during the photolysis of O_2 is transported downwards before being released. Once below 100 km the energy stored is released through recombination reactions. Since this is the dominant source of solar heating within the UV range it is therefore not necessary to apply UV heating efficiencies within the model. Instead the $(O - O)$ bond energy is simply subtracted and the recombination exothermic heating is calculated self consistently after transport.

Within the range of the Schumann Runge bands (between 175 and 200 nm) the absorption of radiation by O_2 and subsequent dissociative heating in the lower thermosphere is calculated using the parameterisation of Strobel (1978) given as

$$\frac{Q_{SRB}}{[O_2]} = \frac{1}{0.67[C_{O_2}] + 3.44 \times 10^9 [C_{O_2}]^{\frac{1}{2}}}$$

(2.139)

where $[O_2]$ is the molecular oxygen number density in cm^{-3}. $[C_{O_2}]$ is the total slant column density of O_2 in cm^{-2} and Q_{SRB} is the heating rate in 0.1 Wm^{-3}.

If $[C_{O_2}] < 10^{18}$ cm^{-2}

$$\frac{Q_{SRB}}{[O_2]} = 2.43 \times 10^{-19}.$$

(2.140)

2.13.5 The Mesospheric Heating Routine

Heating within the mesosphere is primarily due to the dissociation of O_3 in the Hartley (242-310 nm), Huggins (310-400 nm) and Chappuis (400-850 nm) bands. Absorption of radiation by O_2 within the Herzberg continuum (200-242 nm) is also a contributing factor. Within the model the contributions of the parameters listed above are calculated

using the heating algorithms of Strobel (1978). The dissociation rate coefficient of the Hartley continuum is also calculated using the absorption cross sections and fluxes provided by Strobel (1978). The heating algorithms are:

$$\frac{Q_{HART}}{[C_{O_3}]} = 4.8 \times 10^{-14} \exp\left(-8.8 \times 10^{-18}[C_{O_3}]\right)$$

(2.141)

$$\frac{Q_{HU}}{O_3} = \frac{1}{[C_{O_3}]}\left[4.66 \times 10^3 - 7.8 \times 10^2 \exp\left(-1.77 \times 10^{-19}[C_{O_3}]\right) - 3.88 \right.$$
$$\left. \times 10^3 \exp\left(-4.22 \times 10^{-18}[C_{O_3}]\right)\right]$$

(2.142)

$$\frac{Q_c}{O_3} = 1.05 \times 10^{-15} \exp\left(-2.85 \times 10^{-21}[C_{O_3}]\right)$$

(2.143)

$$Q_{HERZ} = 1.5 \times 10^3 (6.6 \times 10^{-24}[O_2] + 4.9 \times 10^{-18}[O_3]) \exp\left(-6.6 \times 10^{-24}[C_{O_2}]\right.$$
$$\left. - 4.9 \times 10^{-18}[C_{O_3}]\right)$$

(2.144)

where Q_{HART}, Q_{HU}, and Q_C are the heating rates due to absorption in the Hartley, Huggins and Chappuis bands in 0.1 W/m^3. Q_{HERZ} is the Herzberg heating rate in W/m^3 and contains a contribution from O_2 absorption, $[O_3]$ is the ozone local number density in cm^{-3} and finally $[C_{O_3}]$ is the ozone slant column density.

Modulation of these bands as a result of variations in the solar cycle are 3% in the Hartley, Huggins and Chappuis bands and 4% in the Herzberg continuum (Brasseur, 1993).

It is important to note that CMAT2 does not account for scattering of incident photons. Within the stratosphere, where the atmosphere is sufficiently dense, incident photons can undergo a large degree of scattering. As a result of collisions particles can absorb energy from incoming photons and then reradiate the energy outwards in all directions. The optical depth of the stratosphere therefore decreases as the attenuation of radiation is now a result of two contributing factors; absorption and scattering. The effect of this is to increase the heating rates within the upper stratosphere by approximately 20% between 30 and 40 km taking a surface albedo of 0.3 (Brasseur and Solomon, 1986).

2.13.6   Mesospheric Heating Efficiencies

The heating efficiencies of Mlynczak and Solomon (1993) in their study of the energy paths after the dissociation of O_3 and O_2 are used within the model and account for a loss in the heating efficiency of between 5-20% primarily as a result of airglow within the region.

2.13.7   Atomic Oxygen Cooling

Atomic oxygen cooling within the atmosphere is a direct result of the fine structure 63 µm radiative emission from oxygen at altitudes typically above 110 km. It is accounted for in the model using the Bates (1951) parameterisation given as

$$Q_{IR(O)} = \frac{1.67 \times 10^{-25} \exp(-228/T_n)}{1 + 0.6 \exp(-288/T_n) + 0.2 \exp(-325/T_n)} \times [O]$$

$$(2.145)$$

where T_n is the neutral temperature and $[O]$ is the atomic oxygen number density in m^{-3}. However, considering uncertainties in the validity of this parameterisation, more details of which can be found in Harris (2001), a reduction factor of 0.5 is applied (Roble *et al.,* 1987). Due to an overestimation of the cooling within the lower regions of the thermosphere, attributed to the increasing opacity below 120 km, a dampening factor of

$$Q_{IR(O)-NEW} = Q_{IR(O)} \left(\exp\left(\frac{-[z - 80.0]}{6.4} \right) \right)$$

$$(2.146)$$

is applied where z is the altitude in km (Dobbin, 2005). For altitudes below 80 km the atomic oxygen cooling is set to zero.

2.13.8   NO Radiative Cooling

The 5.3 µm non-LTE band emission from NO between 150-200 km is calculated using

$$Q_{NO} = h\upsilon n\omega A_{10} \left(\frac{g_1}{g_0}\right) \exp\left(\frac{-h\upsilon}{kT}\right)$$

$$(2.147)$$

from Kockarts (1980). Q_{NO} is the cooling rate measured in ergs/s, and n is the concentration of NO molecules in the ground vibrational level $(v = 0)$. The energy of the photon emitted when vibrationally excited $NO_{v=1}$ undergoes the reaction

$$NO_{v=1} \rightarrow NO_{v=0} + h\upsilon$$

$$(2.148)$$

is given by $h\upsilon$. A_{10} is the Einstein A coefficient for the spontaneous emission of a photon from $NO_{v=1}$ and is taken to be 13.3 s^{-1} (King and Crawford, 1972). g_1 and g_0 are the statistical weights for vibrational levels $(v = 1)$ and $(v = 0)$ and are assumed to be equal. The Boltzmann constant is given by k and the kinetic temperature given by T. Finally, ω represents a dilution factor expressing the non-LTE departure from a Boltzmann distribution of energy levels and is expressed as

$$\omega = \frac{k_{10}n(M)}{k_{10}n(M) + A_{10}}$$

$$(2.149)$$

where k_{10} is the deactivation rate coefficient of NO by collisions with another constituent, denoted by (M) between vibrational levels $(v = 1)$ and $(v = 0)$. n is the number concentration of the constituent (M). Given that the deactivation of NO by N_2 and O_2 is much smaller than by O such that $k_{10}[N_2] < k_{10}[O_2] \ll k_{10}[O]$ only deactivation through collisions with O are considered. A value of $k_{10}[O] = 6.5 \times 10^{-11}$ cm^{-3}s^{-1} at 300 K is used (Fernando and Smith, 1979).

2.13.9 CO_2 Cooling

Cooling within the MLT region of the atmosphere is primarily due to the LTE and non-LTE 15 μm band emission of CO_2. This is calculated within CMAT2 using the parameterisation of Fomichev *et al.* (1998), more details of which can be found in Harris, (2001). The collisional deactivation rate constants of Shved *et al.* (1998) are used to calculate the deactivation of $CO_2 (01^10)$ by N_2, O_2 and O and are

$$k_{N_2} = 5.5 \times 10^{-17}\sqrt{T} + 6.7 \times 10^{-10}\exp\left(-83.8T^{\frac{1}{3}}\right)$$

$$(2.150)$$

$$k_{O_2} = 10^{-15}\exp\left(23.37 - 230.9T^{\frac{1}{3}} - 564T^{\frac{2}{3}}\right)$$

$$(2.151)$$

$$k_{O} = 3 \times 10^{-12}.$$

$$(2.152)$$

The values for k above are all measured in units of cm^3/s. Within the non-LTE region between $85 - 115$ km collisions with O are the dominant source of deactivation. However, there is a large degree of uncertainty regarding this particular rate constant and this has a significant impact on all calculations related to the energy budget of the region.

2.13.10 O_3 Cooling

Within an altitude range of 20-75 km there is a minor contribution to cooling resulting from the 9.6 μm band emission of ozone. The CMAT2 model accounts for this minor contributor using the parameterisation of Formichev and Schved (1985).

2.13.11   Exothermic Chemical Heating

At altitudes above 100 km molecular oxygen is dissociated by incoming ultraviolet radiation leading to the production of atomic oxygen. However, above altitudes of 80 km the lifetime of atomic oxygen exceeds 24 hours (Smith *et al.*, 2010). Therefore, chemical potential energy created by the photolysis of molecular oxygen can be transported away from the site of the photolysis reaction. This energy can subsequently be released via neutral-neutral reactions and is calculated for by CMAT2 after transport of the constituents has taken place.

Heating efficiencies are also applied to a number of chemical reactions in order to account for the loss of energy through radiative emissions. For example, in the case of the reaction between hydrogen and ozone

$$H + O_3 \rightarrow OH^*(v = 1 - 9) + O_2 + 3.4eV$$

$$(R2.1)$$
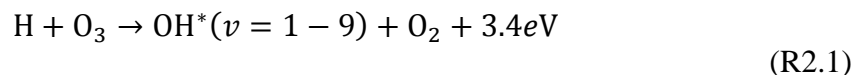
a heating efficiency of 0.6 is applied by CMAT2 following Mlynczak and Solomon (1993). This accounts for loss of energy through radiative emissions in the form of airglow. Vibrationally excited hydroxyl is a major contributor to the exothermic heating of the middle atmosphere and this radical will be discussed in greater detail in **Chapter 3**.

2.14 Dynamics

2.14.1 Lower Boundary Forcing

Data from the Mass Spectrometer and ground based Incoherent Scatter Extended MSISE-90 empirical model (Hedin, 1991) is used to determine the daily zonal means of geopotential height. These data are then applied to the lower boundary of the model. Data from MSISE-90 is both date and pressure dependent and allows for a realistic representation of seasonally varying wind structure in the lower atmosphere. The zonal mean temperature and wind fields at the lower boundary are calculated typically from a liner extrapolation of the two lowermost levels above the boundary. Details of other methods are provided in Harris (2001).

2.14.2 Tidal Forcing

Using classical tidal theory, described in Müller-Wodarg (1997), perturbations in the self consistent geopotential height can be derived and then used to apply tidal forcing at the CMAT2 lower boundary. This is a necessary step when modelling a more realistic middle atmospheric wind structure. Details of the implementation of this can be found in Harris (2001).

Hough modes are used to describe the horizontal structure in tidal oscillations and are implemented in the model. With each mode there is a phase shift that corresponds to the local time of the maximum and the tidal amplitude both of which need to be specified. Hough decompositions of the Global Scale Wave Model (GSWM) (M. Hagen *et al.,* 1999), are used to determine the phases and amplitudes of the tides at the CMAT2 lower boundary and are listed in a table provided in Harris (2001).

Within the model the (1,1), (2,2), (2,3), (2,4) and (2,5) Hough modes (described in **Section 1.3.4**) are all implemented. After summing the tidal geopotential height

perturbations to the MSISE-90 geopotential height field, perturbations in the lower boundary winds and temperatures, associated with tidal oscillations, can be calculated using the methods described in Harris (2001) but are typically calculated from the linear extrapolation of the two lowermost levels above the lower boundary.

2.14.3   Gravity Wave Parameterisations

Within the CMAT2 code there are a total of four separate gravity wave schemes of varying complexity. The basic scheme, referred to as the Rayleigh scheme, is typically used only during the spin-up phase of a model run before being replaced by one of the more detailed parameterisations. The Rayleigh scheme was designed to approximate the effects of planetary waves within the atmosphere after initial simulations of planetary wave forcing at the CMAT2 lower boundary were shown to be incapable of producing realistic results. The Rayleigh scheme approximates planetary wave effects through the implementation of zonal and meridional Rayleigh friction terms. These terms are tuned to be consistent with the planetary wave drag morphology profiles of Brasseur *et al.* (1990) and are described in Harris (2001).

After the initial spin-up phase of the model run, one of the alternative three gravity wave parameterisations is initiated. These are referred to as the Hybrid-Lindzen-Matsuno (HLM) scheme based on the work of Lindzen (1981) and Matsuno (1982), the Medvedev and Klassen (MK) scheme based on (Medvedev and Klassen, 1995; Medvedev *et al.,* 1997; Medvedev and Klassen, 2000) and the Alexander and Dunkerton scheme (AD) based on the work of Alexander and Dunkerton (1999). Details of each of these parameterisations can be found in the respective papers above and their implementation into the CMAT2 code is described in detail in Harris (2001), Dobbin (2005), and Yiğit *et al.* (2008).

A gravity wave parameterisation can be defined as "a numerical approximation of the dynamical effects of vertically propagating sub-grid scale atmospheric gravity waves in a GCM" (Yiğit *et al.*, 2008). Many of the initial studies into gravity waves were based on the gravity wave drag parameterisations of Lindzen (1981). Since then a number of more complicated gravity wave schemes have been developed. Despite these more complicated routines however, the implementation of gravity wave schemes into

GCM's is still not a trivial task (Fritts and Alexander, 2003) and in many cases can lead to high levels of instability within the model.

The purpose of these schemes is to reproduce the observed mesospheric zonal mean wind reversals observed during solstice as well as the associated meridional temperature reversal within the mesopause which results from the deposition of gravity wave momentum and energy as described in **Section 1.3.5**. In order to accomplish this the parameterisations must accurately determine the amount of energy and momentum to be injected into the atmosphere and subsequently deposit it at the correct altitude within the mesosphere. This is often accomplished through experimentation with various gravity wave settings such as wave amplitudes and fluxes in a process often referred to as 'tuning' (Yiğit *et al.*, 2008). All gravity wave schemes require a certain amount of tuning and the majority of schemes introduce an *intermittency factor* which is used to reduce the amount of gravity wave drag and thus scale down the amount of gravity wave momentum deposition.

Each of the gravity wave schemes mentioned in this section requires the specification of an initial gravity wave spectrum at some altitude in the lower atmosphere. Typically in GCM's the altitude chosen for the launch of gravity waves is the lower boundary. In CMAT2 this corresponds to an altitude of 15 km. The subsequent evolution of gravity waves as they propagate upwards is very much dependent on this launch level.

For the purpose of this thesis the Alexander and Dunkerton (AD) gravity wave scheme was used in model calculations. As gravity waves are not a primary focus of this thesis only a brief summary of the implementation of this scheme is discussed. A detailed discussion of the implementation can be found in Yiğit *et al.* (2008) and Yiğit *et al.* (2009). The initial spectrum is given by

$$\overline{u'w'}(c) = sgn(\hat{c}_0)\overline{u'w'}_{max} \times \exp\left[-\left(\frac{c-c_s}{c_w}\right)^2\right]$$

$$(2.153)$$

where $\overline{u'w'}(c)$ is the vertical flux of horizontal momentum, $\hat{c}_0 = c - \bar{u}_0$ is the intrinsic phase speed at the launch level, $sgn(c) = c - \bar{u}_0/|c - \bar{u}_0|$ is the relative direction of a particular harmonic with respect to the mean flow at the source level $\bar{u}_0$, c_w is the half-width of the Gaussian at half maximum and c_s is the momentum flux shift which is

eastward if $c_s > 0$ m/s and westward if $c_s < 0$ m/s (Yiğit *et al.*, 2008). The configuration of the spectrum is shown in **Figure 2.4** and extends from -60 to $+60$ m/s for a total of 121 harmonics.
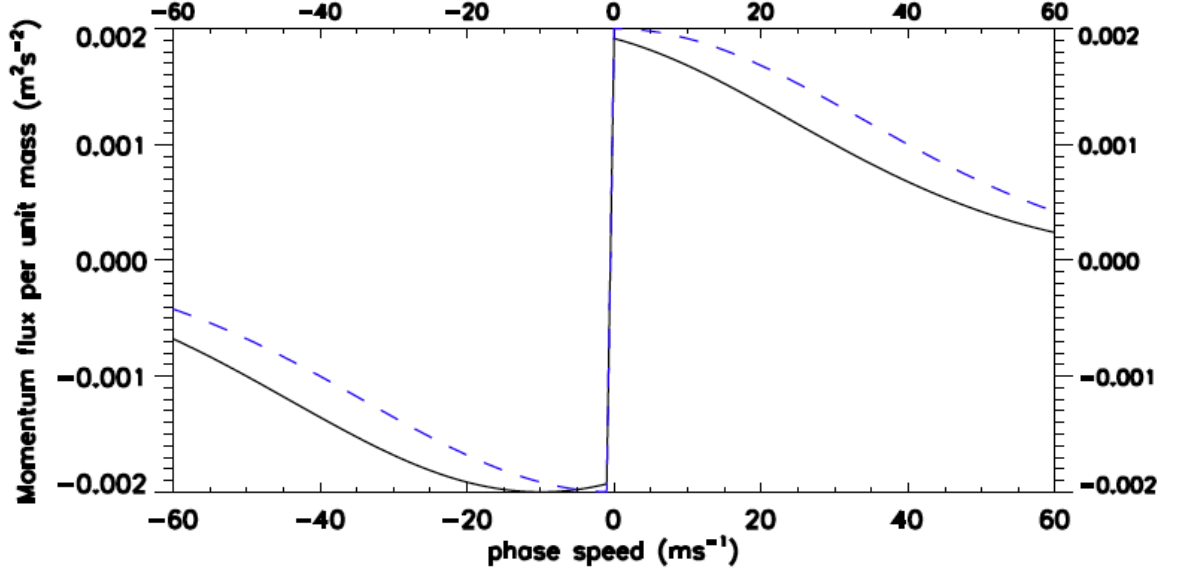
Figure 2.4: Initial gravity wave phase speed spectrum for the AD gravity wave scheme (Yiğit *et al.*, 2008).

The intermittency factor used by the AD scheme is given by

$$e = B_t / (\rho_0 \Sigma_i \overline{u'w'}_i)$$

(2.154)

where B_t is the time averaged momentum flux of the spectrum and specified at the beginning of the model run, ρ_0 is the background density at the source level and $\Sigma_i \overline{u'w'}_i$ is the sum of the momentum flux in the launch spectrum (Yiğit *et al.,* 2008).

Filtering of the individual harmonics within the spectrum occurs using *critical layer filtering*. At each vertical pressure level the sign of $\hat{c}$ is checked. If the sign of $\hat{c}$ changes between two pressure levels n and $n + 1$ then absorption of the associated harmonic has occurred between these two levels and the momentum and energy of the gravity wave are deposited into the region.

With an appropriate initial gravity wave spectrum, intermittency factor, and filtering process gravity wave drag for the dissipating harmonics can be calculated at each vertical model grid point. This is done by calculating the momentum deposited by each

individual wave which are then linearly superimposed to calculate the resultant drag. The total gravity wave drag at a given vertical level is calculated by the AD scheme as

$$a = \frac{\rho_0 e}{\rho dz} \sum_i F_i$$

(2.155)

where a is the total gravity wave drag at a given vertical level, e is the intermittency factor, dz is the distance between two consecutive pressure levels and $\sum_i F_i$ is the total wave flux and determines the direction of forcing.

2.15   Major Species Transport

Molecular nitrogen, molecular oxygen and atomic oxygen form the three major species in the model. The composition of each of the three main constituents is calculated using the continuity equation

$$\frac{\partial \chi_i}{\partial t} = \frac{1}{\rho} m_i S_i - V_2 \cdot \overline{\nabla}_P \chi_i - w \frac{\partial \chi_i}{\partial P} - \frac{1}{\rho} \overline{\nabla}_P \cdot (n_i m_i C_i) + \frac{1}{\rho} \overline{\nabla}_P (D_{EDDY} n \overline{\nabla}_P m \chi_i)$$

(2.167)

(Fuller Rowell, 1984) where the first term on the right hand side of the equation is the chemical production and loss of the constituent, the second and third term represent horizontal and then vertical advection and the fourth and fifth terms represent molecular and turbulent diffusion respectively. χ_i is the mass mixing ratio of the species i. The sources and sinks of the constituent are represented by S_i. m_i is the molecular mass of the constituent i, while m is the mean molecular mass. n_i is the number density, C_i is the molecular diffusion velocity and D_{EDDY} is the eddy diffusion coefficient.

For each of the main constituents the diffusion velocity C_i is found by simultaneously solving the generalised diffusion equation for a multiple species non-uniform gas given by Chapman and Cowling (1952) as

$$\frac{1}{n} \sum_{i \neq j} \left(\frac{\chi_j}{m_i D_{ij}} n_j m_j C_j - \frac{\chi_i}{m_j D_{ij}} n_i m_i C_i \right) = \overline{\nabla} \chi_i + \frac{\chi_i}{m} \overline{\nabla} m + \left(1 - \frac{m_i}{m} \right) \frac{\chi_i}{P} \overline{\nabla} P$$

(2.157)

where D_{ij} is the mutual molecular diffusion coefficient of a constituent i through the constituent j, m is the mean molecular mass determined from

$$m = \frac{n_1 m_1 + n_2 m_2 + n_3 m_3 + \cdots}{n}$$

(2.158)

and n is the total number density. The value taken is then the weighted mean of the velocity through each constituent.

2.15.1 Molecular Diffusion Coefficients

Molecular diffusion within the atmosphere is a direct result of atmospheric density gradients. Gas molecules diffuse along a path in the opposite direction to the density gradient. The flux of the molecules is directly proportional to the density gradient in the atmosphere and is calculated from $\Phi = -D\nabla n$. The molecular diffusion coefficient is given by the proportionality factor D.

The major constituent mutual molecular diffusion coefficients used by the model are assumed to be symmetric such that $D_{ij} = D_{ji}$ and are presented in the **Table 2.4** (Colgrove *et al.*, 1966).

$i - j$	D_{ij} $[\text{m}^2\text{s}^{-1}]$
$O - O_2$	$[T/273.0]^{1.75} \left[1.01325 \times 10^5 / P\right] 2.60 \times 10^{-5}$
$O - N_2$	$[T/273.0]^{1.75} \left[1.01325 \times 10^5 / P\right] 2.60 \times 10^{-5}$
$O_2 - N_2$	$[T/273.0]^{1.75} \left[1.01325 \times 10^5 / P\right] 1.81 \times 10^{-5}$

Table 2.4: CMAT2 model mutual molecular diffusion coefficients where P is pressure in pascals and T is temperature in Kelvin (Colgrove *et al.,* 1966).

2.15.2 Eddy Diffusion Coefficient

While attempts have been made to self consistently calculate the turbulent diffusion coefficient profile in the model within the gravity wave parameterisation scheme, the results of these attempts were found to be unpredictable and the model was shown to produce unrealistic wind profiles (Harris, 2001). The turbulent diffusion coefficient profile, D, therefore used in the model is from Roble (1995).

2.16 Minor Species Transport

Within the model the composition of the minor species is calculated in a similar way to that of the major species. However, when dealing with the minor species the transport effects that these constituents have on the major species are ignored. As such molecular diffusion is not mutual and is therefore analogous to turbulent diffusion. The diffusion equation therefore takes the form

$$\frac{\partial \chi_i}{\partial t} = \frac{1}{\rho} m_i S_i - V_2 \cdot \overline{\nabla}_P \chi_i - w \frac{\partial \chi_i}{\partial P} + \frac{1}{\rho} \overline{\nabla}_P \big((D_{EDDY} + D_{MOL}) n \overline{\nabla}_P m \chi_i \big).$$

(2.159)

2.16.1 Minor Diffusion Coefficients

The majority of minor species molecular diffusion coefficients used in the model are obtained from the empirical expressions of Banks and Kockarts (1973). These expressions are used to calculate the diffusion coefficients of most of the minor species through N_2 and O_2 while diffusion through O is calculated using the empirical expression of Fuller *et al.* (1966). For the diffusion of minor species $N(^4S)$, $N(^2D)$ and NO through N_2, O_2, and O the molecular diccusion coefficients of Levin *et al.* (1990) are used.

The overall diffusion coefficient of each minor constituent through the major species is determined using Wilke (1950) calculating the weighted means of the coefficients from

$$D_{1-mixture} = \frac{1}{\dfrac{v_2}{D_{1-2}} + \dfrac{v_3}{D_{1-3}} + \cdots}$$

(2.160)

where v_n is the volume mixing ratio of the major constituent and D_{1-n} is the molecular diffusion coefficient of the species through that major constituent. For chemical families the values of D_{1-n} are the weighted means of the diffusion coefficients of each family member through the major constituent in question.

2.17   Chapter 2 Summary

In this chapter the CMAT2 model has been described in extensive detail. This description has included a detailed account of the assumptions made by the model, the governing equations which are solved by the model, the numerical methods utilised in solving these equations, and a description of the model grid. A detailed account of the parameters defined within the model, including initial and boundary conditions and an extensive description of its chemical, energetic and dynamical routines are also presented.

While this chapter has no doubt tried the patience of the reader with what must have appeared a never-ending series of complex equations, it is hoped that the necessity for this level of detail, in particular in relation to the chemical routines, is clear. These routines will subsequently be modified in order to incorporate the chemistry of OH^*. In the following chapter the hydroxyl radical will be discussed and the features exhibited by this radical in the night-time airglow of the atmosphere will also be described.

Chapter 3

The Hydroxyl Radical (OH)

3.1 Introduction

In **Chapter 2**, the CMAT2 model was described in detail. This description included a detailed account of the fundamental equations solved, the model parameters and the chemical, dynamical and energetic routines. In this chapter the hydroxyl radical itself will be discussed. This will include a distinction between ground state (OH) and vibrationally excited hydroxyl (OH^*) which will be followed by a description of the OH^* photochemistry. The energetics and quantum mechanical selection rules of the radical will also be described and as well as the determination of its electric dipole moment function (EDMF) and the resultant inverse radiative lifetimes which govern the OH^* emissions. General features of the emissions, which this thesis attempts to simulate, will also be presented.

As discussed in **Chapter 1**, the terrestrial night-time airglow (nightglow) in the atmosphere is dominated by the infrared emissions of vibrationally excited hydroxyl radicals (OH^*) in the mesopause. This brightness of the emission can reach 1 mega Rayleigh (Turnbull and Lowe, 1983). Since their discovery in the upper atmosphere by Meinel (1950) numerous studies have been carried out in order to identify and explain the mechanisms and processes that account for the behaviour of this particular chemical species as outlined in **Section 1.1**.

Today these studies are still an important topic in aeronomy as the energy released via the reaction of atomic hydrogen and ozone, the primary source of OH^* within the region,
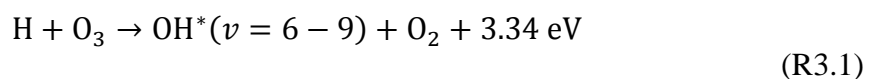
$$H + O_3 \rightarrow OH^*(v = 6 - 9) + O_2 + 3.34 \text{ eV}$$

<div align="right">(R3.1)</div>

provides the single largest chemical source of heat within the mesopause (Mlynczak and Solomon, 1993; Kaufmann *et al.,* 2007). This significantly contributes to the local energy budget of the mesopause. The subsequent OH^* emissions significantly reduce the energy available for heat and provide a signal from which the chemical energy deposition rate within the mesopause can be derived (Mlynczak *et al.,* 1998). These emissions further provide a useful remote sensing tool in the study of the photochemical and dynamical processes that play a role in the upper atmosphere (Xu *et al.,* 2012), and allow for derivations of the atomic hydrogen concentrations (Mlynczak *et al.,* 1998) and atomic oxygen concentrations (Russell and Lowe, 2003) within the region, provided that the concentration of ozone is well known.

3.2 The Hydroxyl Radical (OH)

The hydroxyl radical is composed of an oxygen atom combined, through a covalent bond, with a hydrogen atom. Given that it is one electron short of a closed shell configuration, and has one unpaired valence electron, this molecule is a very reactive species and is often referred to as a 'radical' or 'free radical'.

The structure of the radical, shown diagrammatically in **Figure 3.1**, leads to a significantly weighted electric charge distribution within the molecule. As a result a large dipole moment exists with a value of approximately 1.7 debye (Nelson *et al.,* 1990) compared to other typical diatomic molecules such as CO and NO which have dipole moments of 0.13 D and 0.16 D respectively (Mahan, 1966).
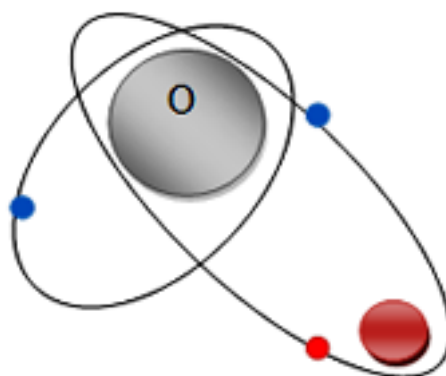
Figure 3.1: Conceptual diagram of the hydroxyl radical.

In its ground state, hydroxyl can be found in a number of atmospheric layers including the upper troposphere, stratosphere and mesosphere. Within the lower layers of the

atmosphere, up to altitudes of approximately 65 km, it is primarily produced during the day where the photolysis of ozone, given by

$$O_3 + h\nu \rightarrow O(\,^1D) + O_2$$

(R3.2)

resulting from incoming solar radiation in the Chappuis $(397 - 850\,\text{nm})$, Huggins $(305 - 397\,\text{nm})$, and Hartley $(203 - 305\,\text{nm})$, bands is followed by the chemical reaction

$$O(\,^1D) + H_2O \rightarrow 2OH.$$

(R3.3)

Above altitudes of 65 km photodissociation of H_2O, resulting from incoming solar radiation at the Lyman α emission line $(121.6\,\text{nm})$, is the dominant source of day-time hydroxyl (Summers *et al.,* 1997).

Hydroxyl produced via these reactions acts as a significant oxidising agent (Seinfeld and Pandis, 2006), if not "arguably the single most important natural oxidising agent in Earth's atmosphere". Furthermore, it accounts for significant amounts of ozone destruction within the atmosphere between altitudes of $15 - 90\,\text{km}$ (Summers *et al.,* 1997).

For these reasons numerous studies of ground state hydroxyl in the different atmospheric layers have been conducted and this radical has often been referred to as a "detergent" of the atmosphere. This is due to its ability to control the atmosphere's capacity to cleanse itself of various pollutants (Li *et al.,* 2008) via chemical reactions within a number of catalytic cycles involving nitrogen and chlorine species (Summers *et al.,* 1997).

Since the focus of this thesis is primarily on upper atmospheric, and vibrationally excited hydroxyl (OH^*), involved in establishment of the airglow layer previously mentioned, ground state hydroxyl within the lower layers of the atmosphere will not be discussed further. Studies of ground state hydroxyl produced at altitudes above approximately 60 km, within the mesosphere region, will be discussed briefly.

Pickett *et al.* (2006) used observational data obtained from the Microwave Limb Sounder (MLS) instrument onboard NASA's Aura satellite in conjunction with the Caltech 1-D photochemical model to investigate the characteristics of night-time upper mesospheric hydroxyl in the ground state. This study shows the existence of a night-time layer of OH at altitudes of approximately 82 km as illustrated in **Figure 3.2**.
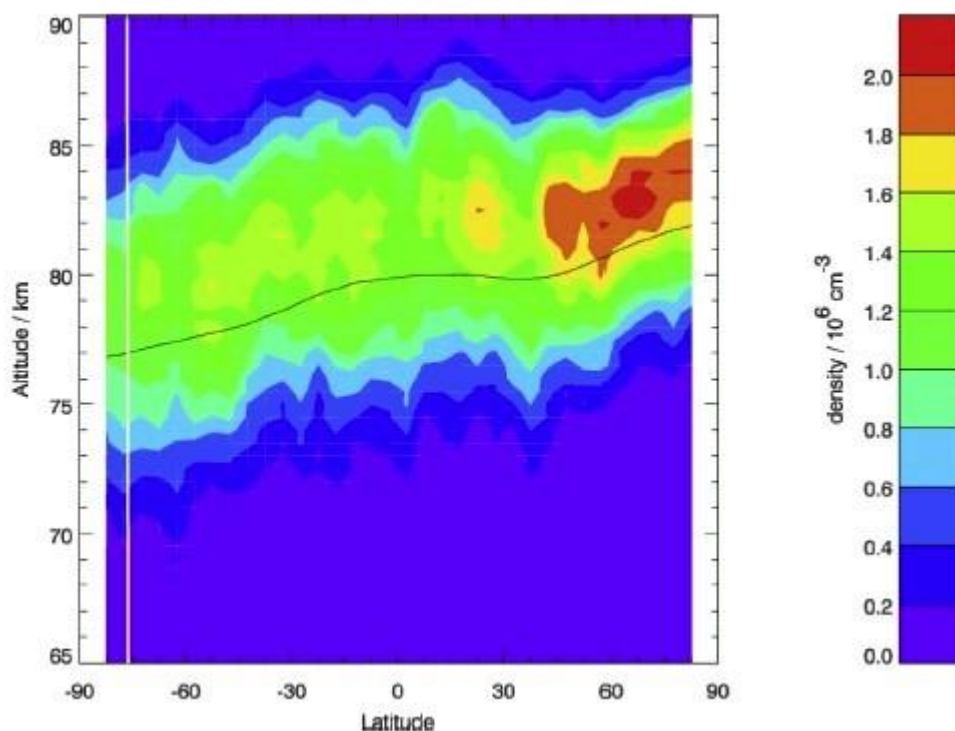
Figure 3.2: Zonal mean MLS observations of OH density with solar zenith angle of $> 100°$ on June 22, 2005. The black line is the height of the 1 Pa pressure level. The vertical white line is the latitude where the noon SZA is $100°$ (Picket *et al.,* 2006).

Figure 3.2 shows a typical night-time OH layer as recorded by MLS for June 22nd, 2005. The black line represents a line of constant pressure at $1\,Pa$ and is used by Pickett *et al.* (2006) to show that pressure is often a better coordinate than altitude in studies of OH. The particular date used, which corresponds to the June solstice, was chosen to emphasise the differences between the OH profiles within the northern and Southern hemispheres. The layer of OH that can be seen has concentrations typically between $1 - 2 \times 10^6$ per cm^3; however, the peak in concentrations can be seen to exist in the high-latitudes of the summer hemisphere. This is more evident in **Figure 3.3** which shows the global distribution of the OH layer, at this pressure line, for 2008. The peak in OH concentrations can be seen to follow the summer hemisphere.
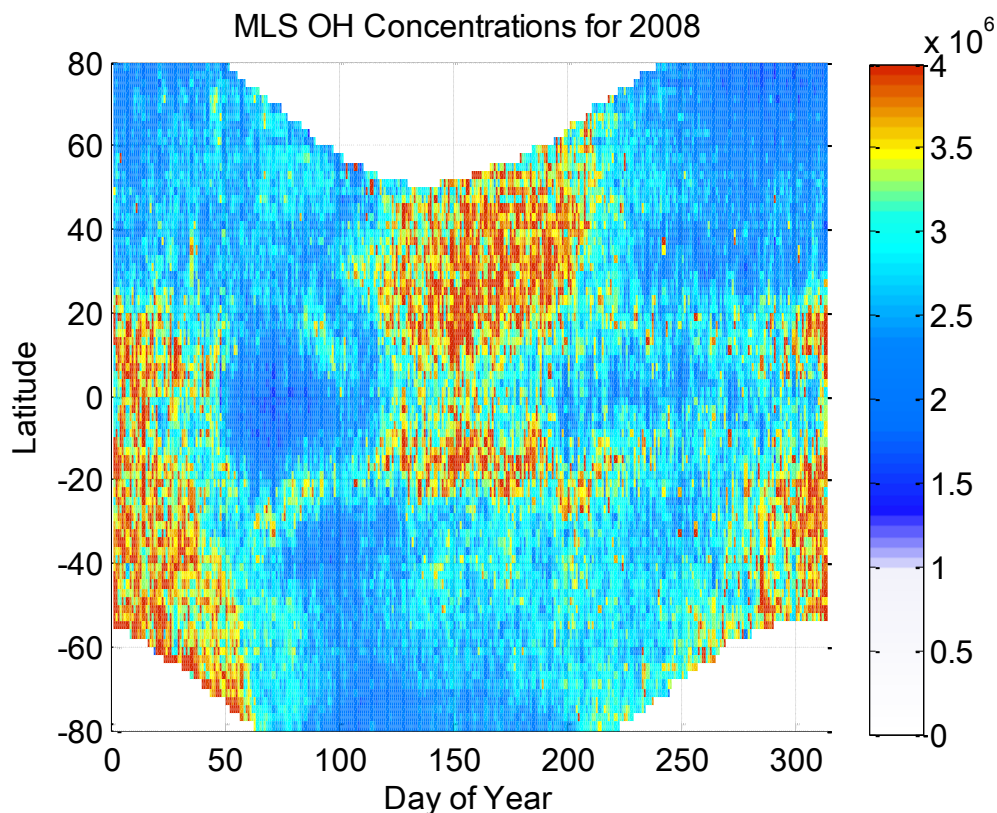
Figure 3.3: Concentration of ground state OH for the year 2008 as measured by the MLS instrument. Units per cm^3.

Using model predictions, Pickett *et al.* (2006) extended their study by calculating typical night-time concentrations of OH^* within the first nine vibrational levels for comparison with measurements of OH concentrations. **Figure 3.4** shows the calculated profiles of some of these vibrational levels as well as a measured profile of OH at 34°N on September 23rd, 2004 at $02\text{:}20$ hr local time.
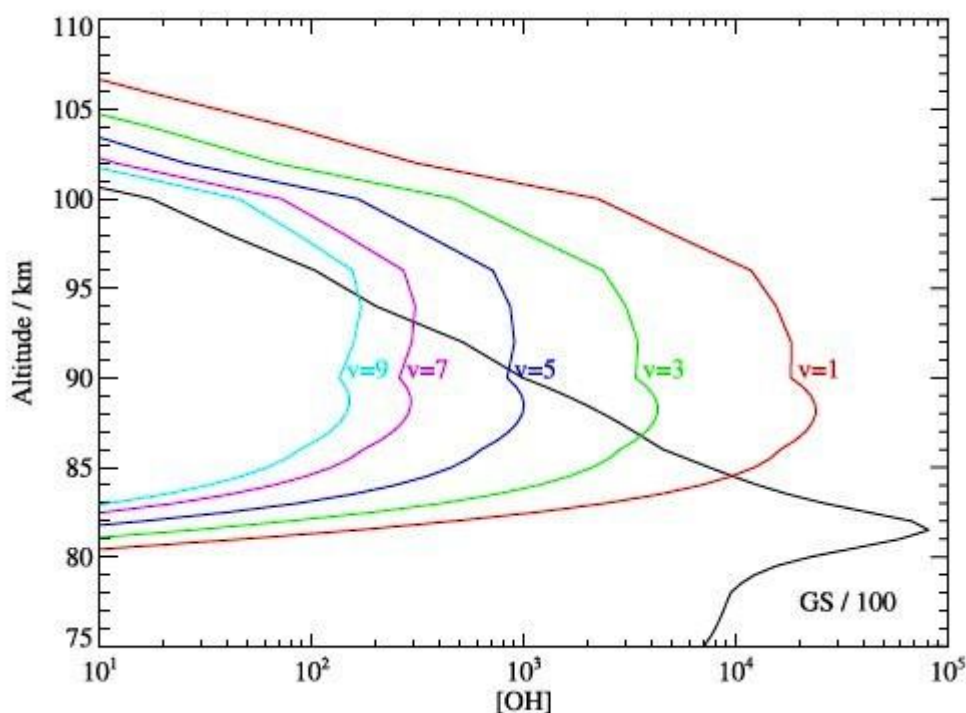
Figure 3.4: Calculated night profiles of vibrationally excited OH* densities for September 23rd, 2004 at latitude 34° N, at 02:20 hrs local solar time (Pickett *et al.,* 2006).

It can be seen that OH* represents approximately only 1% of the total OH up to altitudes of 84 km. At altitudes of 90 km it represents approximately 20% of the total OH. Pickett *et al.* (2006) attribute this to decreasing pressure at altitudes above 80 km. This slows the rate of HO$_2$ recombination and therefore increases the relative importance of the hydrogen and ozone reaction responsible for the creation of OH*.

Throughout their study, Pickett *et al.* (2006) emphasise the importance of treating OH and OH* as distinct chemical species due to the different chemical reactions involved in their respective production and loss. In this thesis, this approach is adopted and the first nine vibrational levels of OH* are considered as distinct chemical species. This will be seen and detailed further in **Chapter 4** and **Chapter 5**.

Englert *et al.* (2008) used MLS data, in conjunction with observations from SHIMMER (Spatial Heterodyne Imager for Mesospheric Radicals) onboard the STPSat-1, to investigate the diurnal variation of day-time upper mesospheric hydroxyl in the ground state. **Figure 3.5** shows a comparison of the day-time profiles of OH at approximately 55°N on July 16th, 2007 and at approximately 12:35 hrs local time as measured by

both SHIMMER and MLS as well as model predictions of the NRL-CHEM1D photochemical model.
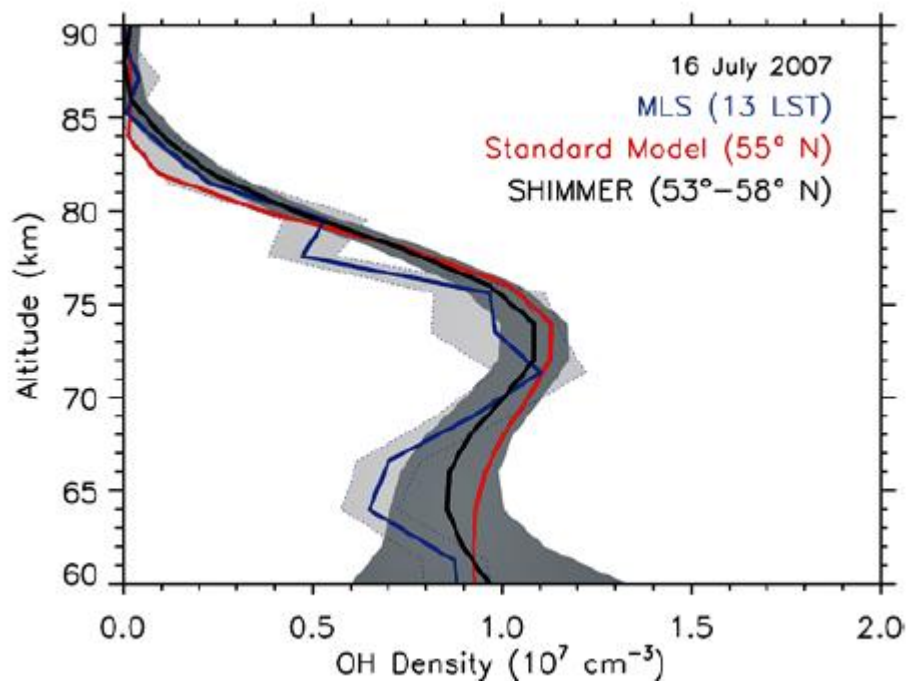
Figure 3.5: Comparison of OH vertical density profiles measured by SHIMMER (black) and MLS (blue) and calculated by the NRL-CHEM1D photochemical model (red) (Englert *et al.,* 2008).

Grey areas surrounding both the blue MLS line and black SHIMMER line represent their respective errors. All three profiles generated are in agreement with a clear peak in OH concentrations in the mesosphere at altitudes of approximately 72 km during the day. This peak in OH concentrations results from the photolysis of H_2O within the mesosphere while below this peak OH is primarily produced via reactions (R3.2) and (R3.3) described previously.

Englert *et al.* (2008) further investigated the diurnal variation in day-time OH using SHIMMER data. **Figure 3.6** shows the diurnal variation in day-time OH at 6 altitudes between 74 and 84 km. Data for these figures are gathered from SHIMMER measurements over a time period of approximately one month between June 27th and August 1st, 2007.
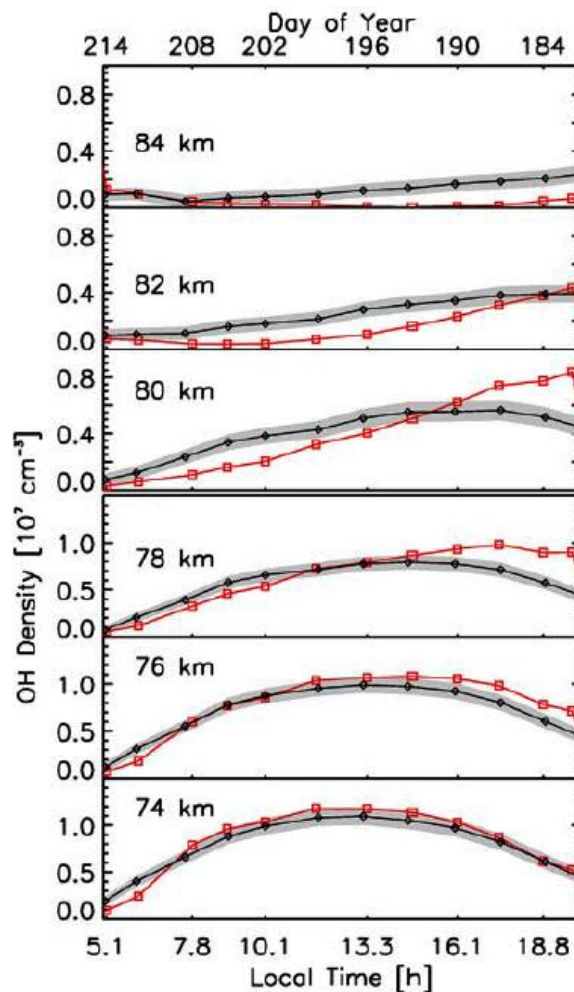
Figure 3.6: Diurnal behaviour of OH as measured by SHIMMER (black diamonds) compared with CHEM1D calculations (red squares). The error envelope of the SHIMMER measurements reflects an estimate of the combined systematic and statistical errors. SHIMMER local times vary from 20.6 hrs on day 178 to 5.1 hrs on day 214. The CHEM1D curves represent a composite of 12 separate calculations for the days indicated by the top axis (Englert *et al.,* 2008).

At altitudes of 74 km there is agreement between the model predictions and SHIMMER measurements. Slight differences between the measured and calculated profiles amplify with increasing altitude. Above 78 km there exist significant variations between the two profiles as the modelled OH reaches its peak much later in the day and the concentrations differ by a factor of two or more. Englert *et al.* (2008) attribute the differences in these profiles to reactions of the odd hydrogen species, namely H, OH, and HO_2, with ozone.

It should be noted that Englert *et al.* (2008) focus primarily on altitudes surrounding 74 km and do not discuss the higher altitudes in any great detail. At these higher altitudes, despite the differences in the SHIMMER and model predictions, both profiles show little diurnal variation and the concentrations of OH recorded by SHIMMER, with values between $1 - 2 \times 10^6 \text{ cm}^{-3}$, are still in agreement with observations from the MLS instrument. This agreement can be extended into the night-time concentrations of OH discussed previously. In their night-time profile for June 22$^{\text{nd}}$, 2005 Pickett *et al.* (2006) show concentrations within the same range of values, suggesting that at higher altitudes there may not exist a large diurnal variation in ground state OH concentrations. Pickett *et al.* (2006) also suggest this stating "the distribution of OH seems unaffected by the absence of sunlight".

With the nature and variations of ground state OH in the upper atmosphere now explained it remains to discuss the nature of vibrationally excited hydroxyl OH*.

3.3 The Vibrationally Excited Hydroxyl Radical (OH*)

Figure 3.7, from Roach and Gordon (1973), shows the emission intensities of the principal upper atmospheric emitters as a function of wavelength. The atomic oxygen red, green and blue lines contributing to the Aurora are easily identified as well as the yellow sodium D doublet which contributes to the nightglow. However, the OH* vibration-rotation bands, labelled OH(Δv) in the figure, can be seen to dominate the total night-time emission.
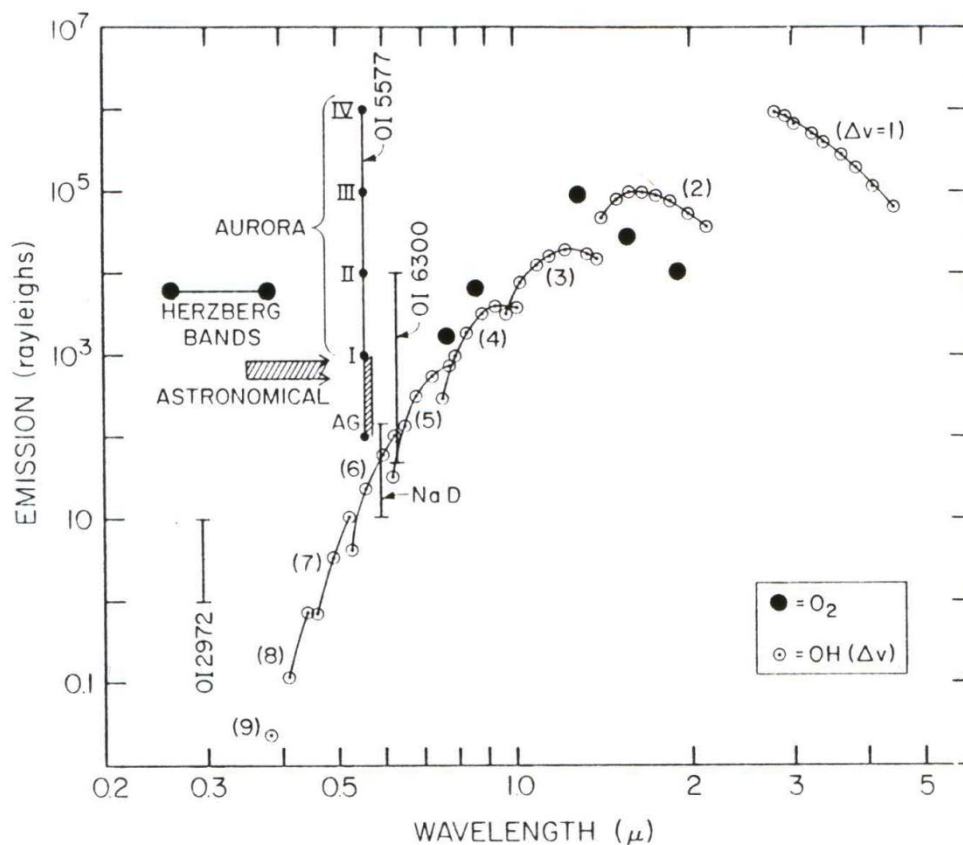
Figure 3.7: Emission intensity as a function of wavelength for the principal upper atmospheric emissions (Roach and Gordon 1973).

These emissions occur when OH^*, within a particular vibrational level, undergoes a radiative transition releasing a photon. There is only one possible ($\Delta v = 9$) radiative transition, denoted by $\odot$, which occurs when $OH^*(v = 9)$, the highest vibrational state allowed by reaction (R3.1), decays to OH in the ground state and releases a photon with a wavelength of approximately 370 nm corresponding to an energy of approximately 3.34 eV.

There are subsequently two possible ($\Delta v = 8$) radiative transitions, each denoted by $\odot$, which occur when $OH^*(v = 9)$ decays to $OH^*(v = 1)$ and when $OH^*(v = 8)$ decays to OH in the ground state. This pattern continues with three possible ($\Delta v = 7$) radiative transitions and so on.

The curved lines joining each vibrational transition (Δv), and forming the vibrational-rotation bands shown in **Figure 3.7**, are also important features of the emissions and can be seen to follow a Boltzmann distribution curve. This is most evident in the ($\Delta v = 2$) band where the peak in the distribution is visible. The shape of these curves results

116

from the fact that the population of the rotational states within each vibrational state follows a Boltzmann distribution and the subsequent vibration-rotation transitions from these states form the observed bands.

Figure 3.8 shows a night sky spectrum from Sheen and Byun (2004) with numerous features which fall into the visible range of the EM spectrum. Again, the oxygen and sodium lines can easily be identified as well as a number of additional sodium and mercury line emissions from street lamps. On the right of **Figure 3.8** is more qualitatively shown a number of vibration-rotation bands for a set of OH^* transitions spanning a wavelength range from $6000 - 9000\,\text{Å}$. The individual vibration-rotation transitions described above are evident within their respective bands.
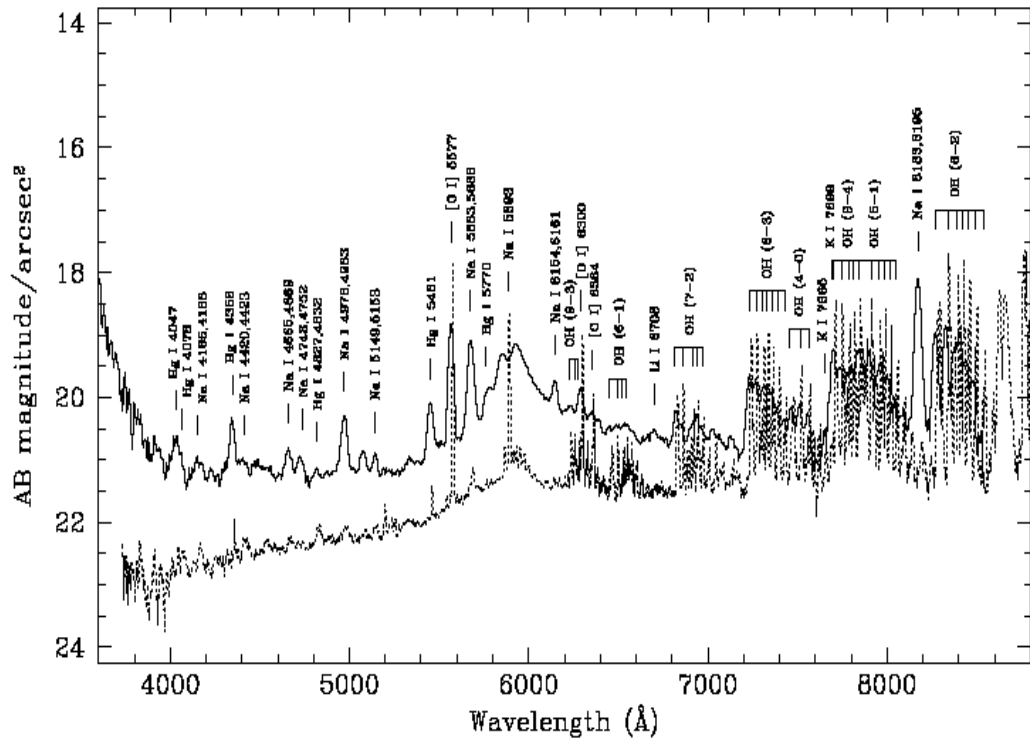
Figure 3.8: Emission intensity as a function of wavelength for the OH^* radical at Mount Bohyun (Sheen and Byun, 2004).

The selection rules governing these vibration-rotation transitions will be discussed in subsequent sections of this chapter. However, an overview of the typical features associated with OH^* will be presented first.

Figure 3.9, from Baker and Stair (1988) shows a number of profiles obtained from rocket measurements of the OH* volume emission rate (VER) between January and March of 1975 and July of 1977.
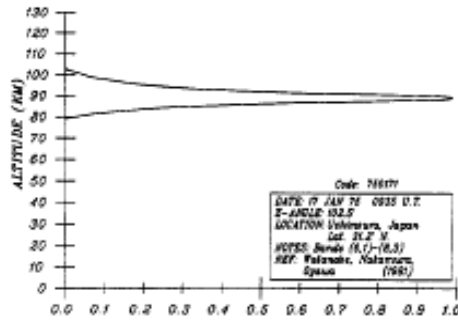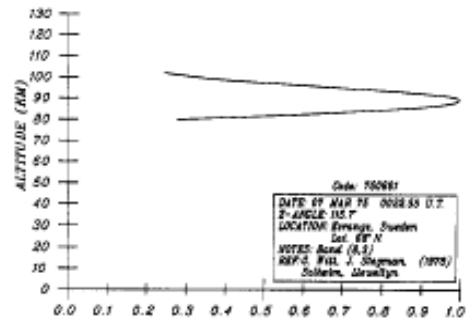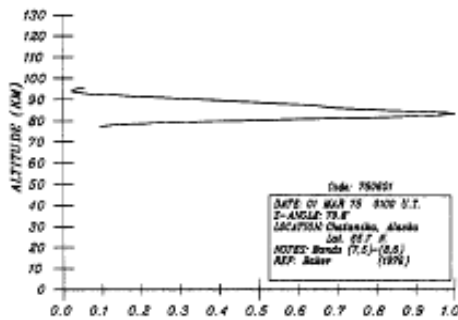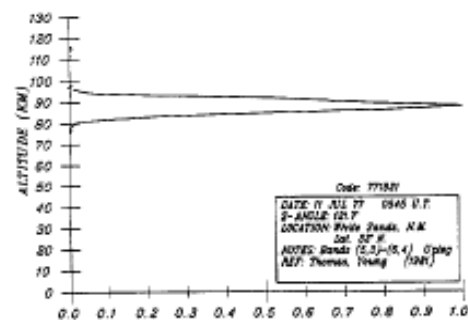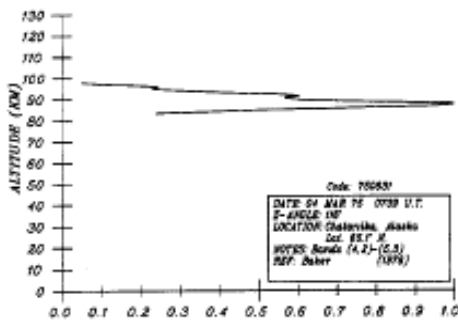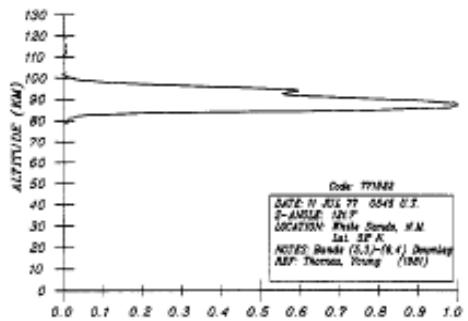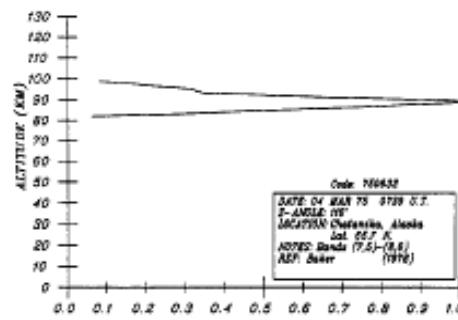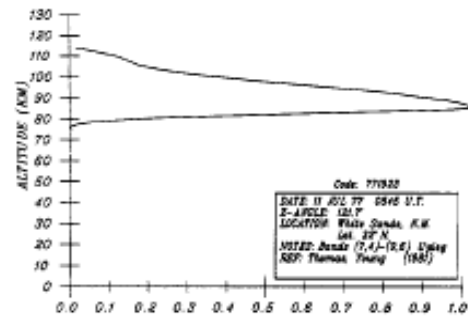
Figure 3.9: Multiple volume emission rate profiles recorded by rocket experiments (Baker and Stair, 1988).

These measurements are broadly representative of the altitudinal profiles of the OH^* bands which vary significantly with location, time of day, and time of year. Baker and Stair (1988) provides a detailed account of a number of these variations after examining over 50 altitudinal profiles obtained from 34 rocket experiments at various latitudes, local times, and times of year.

Figure 3.10 from Liu and Shepherd (2006) shows further examples of typical volume emission rate (VER) profiles for the $OH^*(8 - 3)$ band in the nightglow recorded by the Wind Imaging Interferometer (WINDII) instrument onboard NASA's Upper Atmospheric Research Satellite (UARS). These profiles were obtained at three different locations and local times on August 29th, 1992 and have been fitted with a Gaussian function so that the altitude of the emission peak can be determined.
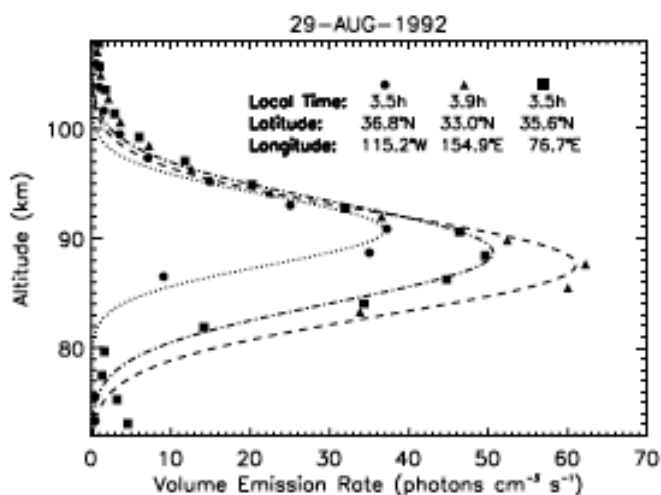
Figure 3.10: Examples of volume emission rate profiles of the OH^* nightglow emission as observed by WINDII. The curves are obtained from Gaussian fitting (Liu and Shepherd, 2006).

At all three locations there is a layer of OH^* which varies significantly with location and time. Using over 50,000 profiles obtained from the WINDII instrument, over the course of 6 years between 1991 and 1997, Liu and Shepherd (2006) determined an empirical formula to calculate the peak height of the emission layer from the integrated emission rate which varies with changes in the concentrations of atomic oxygen.

While these emission profiles only depict a small part of the overall emission spectra it can be seen clearly that an OH^* airglow layer exists at altitudes surrounding 87 km. This raises two fundamental questions:

1)   Why is there an OH^* layer at these particular altitudes?

2)   Why is OH^* such a dominant emitter in the night sky?

3.4   Production and Loss of OH^*

In this section the first of these questions will be answered. An account of the origins of this layer will be given and the reasons why this layer exists at this particular height will be presented. The second question will then be addressed at the end of the section.

OH^* photochemistry is governed primarily by atomic oxygen. The production of OH^* within the mesopause region of the atmosphere is controlled by the reaction

$$H + O_3 \rightarrow OH^*(v = 6 - 9) + O_2.$$

(R3.1) repeated here
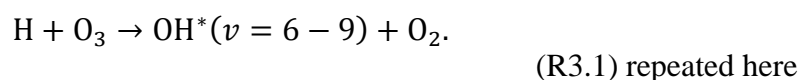
This reaction produces OH^* in multiple vibrational levels typically assumed to be between $v = 6 - 9$. The proportion of OH^* in each of these levels is governed by associated branching ratios and several sets of these branching ratios exist (Klenerman and Smith, 1987; Steinfeld, 1987; Ohoyama *et al.,* 1985). The values in each set differ although there is consensus that the majority of OH^* produced ($> 60\%$) will be in vibrational states $v = 9$ and $v = 8$.

Reaction R3.1 depends significantly on the amount of ozone available within the region of the atmosphere. Ozone is produced by the reaction

$$O + O_2 + M \rightarrow O_3 + M$$

(R3.4)

where M represents both N_2 and O_2 (Melo *et al.,* 2000).

The amount of OH^* within the mesopause is therefore proportional to $[O][O_2][M]$, or effectively $[O][M]^2$. Thus OH^* is linearly dependant on O and has a squared dependence on O_2 and N_2. **Figure 3.11** shows a typical night-time atomic oxygen profile as well as a typical atmospheric density profile which has been divided by 1000.
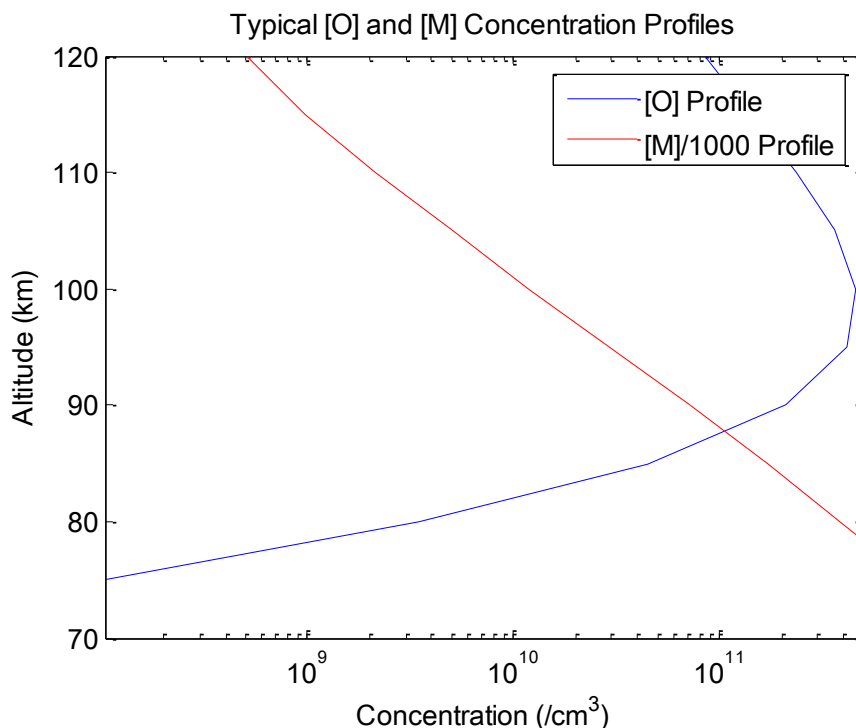
Figure 3.11: Concentrations of [O] and [M]/1000 showing altitudinal layer where OH* can optimally be produced.

It is evident from **Figure 3.11** that this linear O dependence and squared M dependence results in the creation of layer, centred at approximately $87\,\text{km}$, within which the production of OH* is maximized (Melo *et al.,* 2001). This layer forms at the lower boundary of the atomic oxygen layer in the atmosphere. Within the layer, OH* is highly sensitive to changes in O at its lower boundary since the concentration of O is the limiting factor for O$_3$ and hence OH* production. The upper boundary is more sensitive to changes in O$_2$ and N$_2$ concentrations which are decreasing exponentially with increasing altitude. This explains the altitudinal location of the OH* layer. Investigations of these sensitivities will be presented in **Chapter 4**.

Additional sources of OH* production have also been considered. Debate over the possible contribution of the perhydroxyl reaction

$$HO_2 + O \rightarrow OH^*(v \leq 6) + O_2$$

<div align="right">(R3.5)</div>
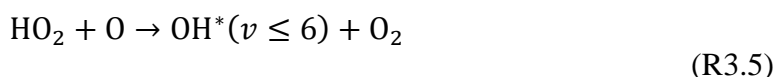
to concentrations of OH* in the lower vibrational levels and first proposed in Breig (1970) still exists, although its contribution is considered negligible by the majority of

the scientific community today. For this thesis, this reaction is considered to contribute to the concentration of ground state hydroxyl only.

The loss of OH^* is much more complicated as chemical, radiative, collisional and quenching loss terms need to be considered. The chemical loss of OH^* is governed principally by the reaction

$$OH^* + O \rightarrow H + O_2$$

<div align="right">(R3.6)</div>

for which the reaction rate is not well known. The model of Makhlouf *et al.* (1995) suggests a value of 25×10^{-11} cm^3/s while Smith *et al.* (2010) suggest a slower reaction rate of 5×10^{-11} cm^3/s. Furthermore, Spencer and Glass (1977) suggest that there is a vibrational level dependence on the reaction rate.

Collisional deactivation and quenching of OH^* occurs through reactions involving O_2 and N_2

$$OH^*(v) + O_2 \rightarrow OH^*(v') + O_2$$

<div align="right">(R3.7)</div>

$$OH^*(v) + N_2 \rightarrow OH^*(v-1) + N_2$$

<div align="right">(R3.8)</div>
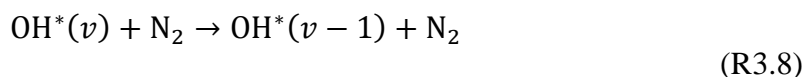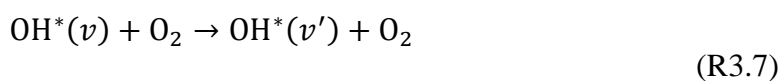
where v denotes an initial vibrational level and v' denotes a final vibrational level. The different notation within these two reactions stems from the fact that O_2 is much more efficient at collisional deactivation with OH^* than N_2. Collisional deactivation with O_2 can be either single or multi-quantum while deactivation through collisions with N_2 is considered to be single quantum only. The reaction rates of Alder-Golden (1997) are typically utilised for these reactions although adjusted rates are available in Xu *et al.* (2012).

Quenching also occurs via

$$OH^*(v) + O \rightarrow OH + O.$$

<div align="right">(R3.9)</div>

In this reaction even OH^* in the high vibrational levels is quenched immediately in the collision. It is therefore considered a pure quenching reaction rather than a stepwise collisional deactivation reaction.

The final contribution to OH^* loss is through the radiative emissions which make up the airglow features. These can be expressed as

$$OH^*(v) \rightarrow OH^*(v') + hv.$$

(R3.10)
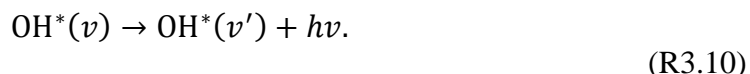
Emissions are typically multi-quantum for the high vibrational levels and single quantum at the low vibrational levels and are governed by the inverse radiative lifetimes or associated Einstein *A* coefficients. Large uncertainties also exist in these values as the values obtained are highly sensitive to electronic dipole moment function used in their calculations. Multiple sets of coefficients exist (Mies, 1974; Turnbull and Lowe, 1988; Nelson *et al.,* 1990) which vary substantially.

Figure 3.12 shows a basic diagrammatic representation of these production and loss mechanisms that has been modified from Baker *et al.* (2007). While simplistic this figure does give a good overall impression of the photochemistry involved.
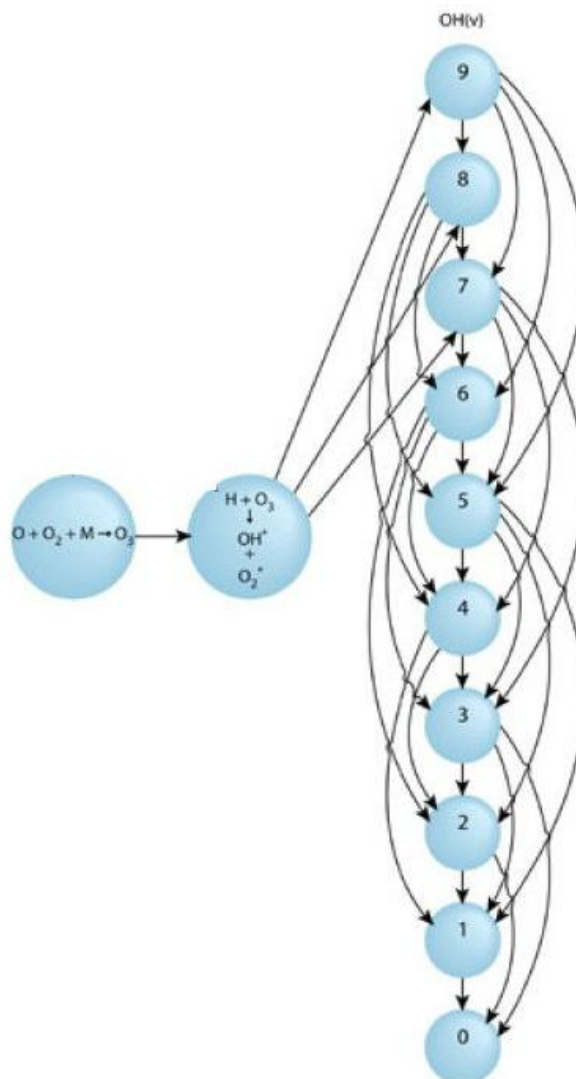
Figure 3.12: Diagrammatic representation of the OH^* production and cascading paths (Baker *et al.,* 2007).

In order to answer the second question posed above it is necessary to consider both the number density of the individual vibrational states of OH^* governed by the production and loss terms described in this section and the transition probabilities associated with each of these states. For a complete consideration, a more detailed account of the nature of the hydroxyl radical is required, starting with a discussion of the radical's energy levels.

3.5   OH Energy Levels

As mentioned previously, this thesis focuses primarily on vibrationally excited hydroxyl within the mesopause. The mesopause region of the atmosphere, and its characteristic

features, have been discussed in **Chapter 1**. It remains necessary to discuss, and distinguish, the different energy levels of the OH radical.

Given that the hydroxyl radical is a diatomic molecule, the total energy of the molecule can be described as a function of the potential and kinetic energies of both the electrons and the individual nuclei, ignoring both spin and any magnetic interactions (Herzberg, 1989). Therefore, while two individual and isolated atoms have three degrees of freedom, each specified by their motion along their three coordinate axes, a diatomic molecule has six degrees of freedom. Three of these degrees of freedom describe the motion of the centre of mass of the molecule along the three coordinate axes and hence describe the electronic energy states associated with the molecule.

3.5.1 Electronic Energy Levels

The electronic state of a diatomic molecule is typically described by the quantum number Λ, which defines the orbital angular momentum of the molecule along the internuclear axis. Λ is denoted by the Greek letters $\Sigma, \Pi, \Delta, ...$, in a similar manner to the $S, P, D, ...$ notation used in atomic physics when describing the orbital angular momentum (L) of an atom (Herzberg, 1989).

Unlike in atomic structure, where electrons are said to move in a spherically symmetric field around the nucleus, the electric field surrounding a diatomic molecule is only symmetric about the internuclear axis. As a result, only the component of orbital angular momentum projected along the internuclear axis, denoted by (M_L), will remain constant as L precesses about this axis, shown in **Figure 3.13** from Herzberg (1989).
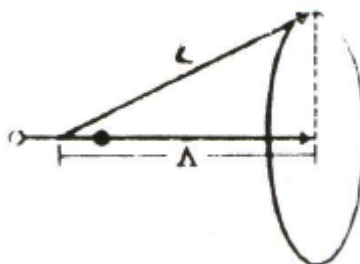
Figure 3.13: Precession of the orbital angular momentum L about the internuclear axis (Herzberg, 1989)

M_L, as in atomic physics, can take on any of the values $M_L = -L, ..., +L$. However, since it remains constant, unlike L, it therefore makes sense to describe the electronic state of diatomic molecules in terms of $|M_L|$ rather than L. $|M_L|$ is therefore given its own quantum number Λ and can take on the values of $\Lambda = |M_L| = 0,1,2, ..., L$. As previously stated Λ is then denoted by the Greek letters $\Sigma, \Pi, \Delta, ...$

Since the electronic states $\Pi, \Delta, ...$, corresponding to $\Lambda = |M_L| = 1,2, ..., L$, can take on the values $+\Lambda$ and $-\Lambda$, and since a change in sign of $|M_L|$ only denotes a reversal of the direction of motion of the electrons within the electric field, for which there is no change in energy, these states are referred to as doubly degenerate states as they are states of the same energy.

In order to fully describe the electronic state of a molecule it is important to also take account of the contribution to the angular momentum resulting from electron spin. In atomic structure this contribution is described in terms of the quantum number S which can be either an integer or half integer number depending on whether the total number of electrons within the atom is even or odd, given that electrons are fermion particles of spin $\frac{1}{2}$.

Within the Σ electronic states S remains unaffected by the electric field provided the molecule is not placed within an external magnetic field, or exhibits any rotary motion. For all other electronic states there will be a precession of S about the internuclear axis as a result of the internally generated magnetic field within the molecule. In a similar fashion to what has been described previously for the orbital angular momentum, S has a constant component projected along the internuclear axis given by the quantum number M_S. This component of the spin angular momentum is typically denoted by the quantum number Σ and should not be confused with the molecular electronic state Σ denoted by the same greek letter. The allowed values of Σ are $\Sigma = -S, ..., +S$.

The total angular momentum along the internuclear axis can be determined by summing the orbital and spin components resulting in the new quantum number Ω. Mathematically this can be expressed as

$$\Omega = |\Lambda + \Sigma|$$

(3.1)

126

where Ω denotes the total angular momentum along the internuclear axis.

All electronic states for which $\Lambda \neq 0$ split into $2S + 1$ states, each of which have different possible values of Ω and thereby result in molecular electronic states of somewhat different energies. The number given by $2S + 1$ is defined as the *multiplicity* of the electronic state.

To this point, only the components of the angular momentum projected along the internuclear axis of a diatomic molecule have been discussed. It remains to determine the total angular momentum of the molecule (J) which is given by the resultant of the three components of angular momentum i.e. orbital, spin and rotational. This rotational term, referred to as the nuclear rotational angular momentum, lies perpendicular to the internuclear axis and is denoted by the letter N and the total angular momentum is given by

$$J = \Omega + N.$$

(3.2)

Relating all of the above to the OH radical, which has spin $(S) = \frac{1}{2}$ as a result of its single unpaired electron, the lowest electronic state is given by $^2\Pi$ where 2 is the multiplicity of the state and given by $2S + 1$. The ground electronic state of OH is thereby a doublet state for which Σ can be either $\pm \frac{1}{2}$. Using this information the two ground states of OH can be identified through **Equation 3.1** as

$$\Omega = |\Lambda + \Sigma| = \left|1 + \frac{1}{2}\right| = {}^2\Pi_{\frac{3}{2}}$$

(3.3)

$$\Omega = |\Lambda + \Sigma| = \left|1 - \frac{1}{2}\right| = {}^2\Pi_{\frac{1}{2}}.$$

(3.4)

3.5.2 Vibrational Energy Levels

Referring back to the six degrees of freedom available to OH, the fourth describes any vibrational motion along the internuclear axis and hence the vibrational energy of the

molecule. The focus of this thesis is primarily on vibrational transitions within the ground electronic states.

Since the overall energy of the molecule is typically lower than the sum of the individual atomic energies this leads to an energetically stable system. A graph of the potential energy of a typical diatomic molecule in its ground electronic state is shown in **Figure 3.14** from Thorne (1988).
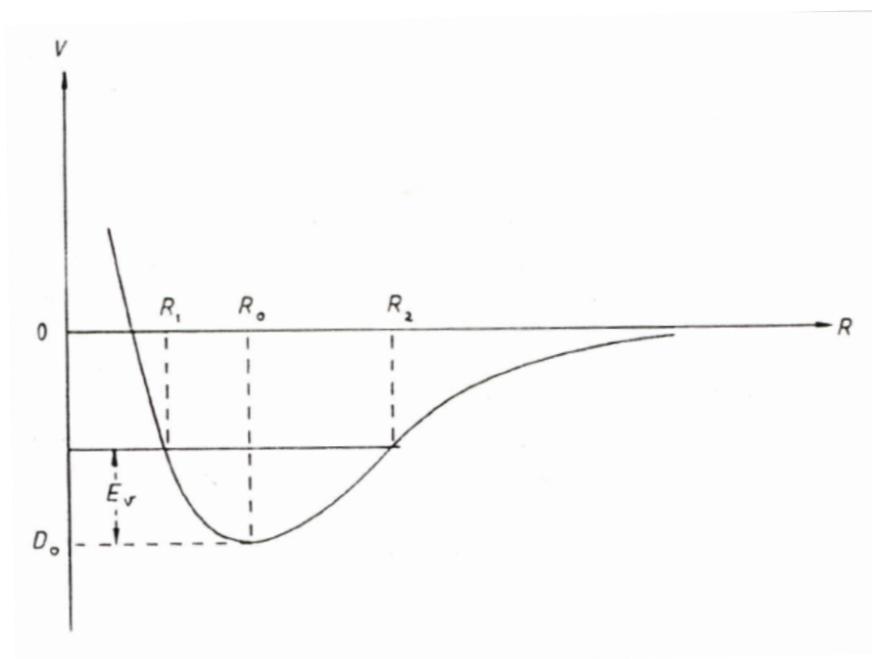
Figure 3.14: Vibrational energy of a diatomic molecule where R_1 and R_2 are the classical turning points for vibrational energy E_v (Thorne, 1988).

The internuclear distance, denoted by R_0, represents the nuclear separation of the lowest energy level and corresponds to the average internuclear separation, or in the case of OH, the average distance between the hydrogen and oxygen nuclei. According to Newtonian mechanics, should the internuclear distance differ from R_0, the molecule will be forced back to its equilibrium position (Brode, 1958). This forcing will cause the molecule to overshoot the equilibrium position from which point on it will oscillate about the position.

The Morse potential is an empirical expression that is used to approximate the potential energy function of a diatomic molecule. Given below as

$$V = D_e\left(1 - e^{-\beta x}\right)^2$$

(3.5)

where D_e is the depth of the potential well, x is the displacement of the nuclei from the equilibrium position and β is a constant, the Morse function approximates the potential energy function of a diatomic molecule. If the displacement is small then this potential can be expanded as

$$V = D_e\beta^2 x^2\left(1 - \frac{\beta x}{2} + \cdots\right)$$

(3.6)

which, at least to the first order, is the potential associated with a simple harmonic oscillator. Using this function as the potential in the Schrödinger equation yields only certain physical solutions with energies given by

$$E_v = h\nu_0\left(v + \frac{1}{2}\right)$$

(3.7)

where ν_0 is the classical frequency of the oscillator and v is the vibrational quantum number. Solving Schrödinger's equation for the full Morse potential, instead of just the first term in the expansion, leads to vibrational energy levels given by

$$E_v = h\nu_0\left(v + \frac{1}{2}\right) - x_e h\nu_0\left(v + \frac{1}{2}\right)$$

(3.8)

where x_e is a small, positive number referred to as the anharmonicity constant (Thorne, 1988). With the introduction of this term, the vibrational energy levels come closer together with increasing v as shown in **Figure 3.15** from Chang (1971).
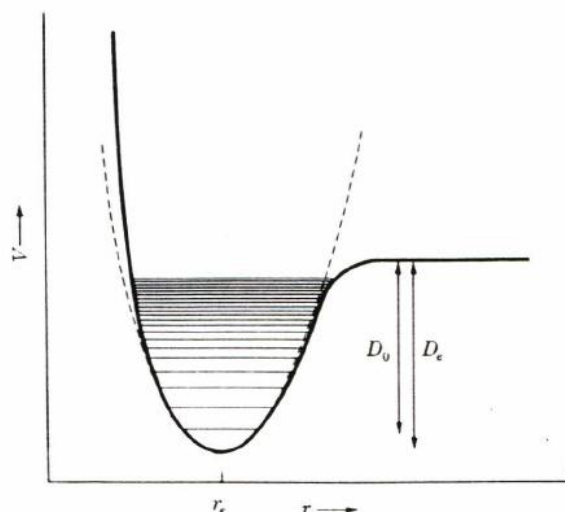
Figure 3.15: Potential energy curve for a diatomic molecule illustrating the decreasing distance between energy levels for increasing v (Chang, 1971). The dotted line represents the potential curve of a harmonic oscillator.

With the above information it is possible to calculate the energies of the lowest vibrational energy levels for OH^*. **Figure 3.16** from Krassovsky *et al.* (1962), shows the potential curve of hydroxyl in the ground electronic state in units of reciprocal centimetres. To the side are displayed the equivalent vibrational level energies in eV for the 9 lowest vibrational states of OH^*.
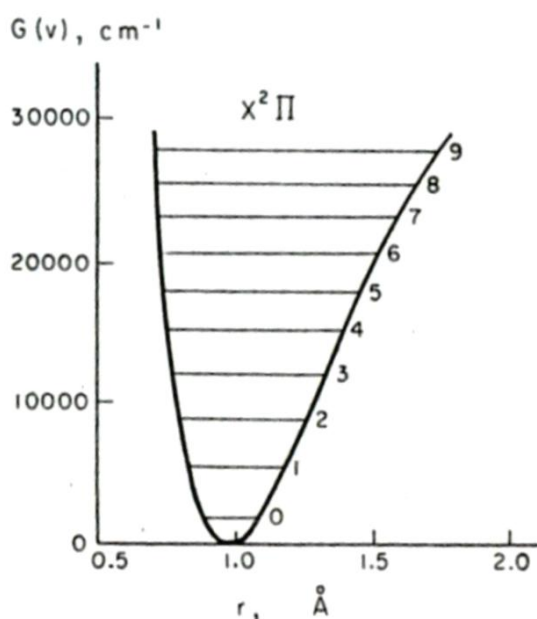
v	eV
9	3.248
8	2.970
7	2.671
6	2.350
5	2.009
4	1.648
3	1.266
2	0.865
1	0.443

Figure 3.16: Potential curve of the ground state of OH using the RKR method presented in Krassovsky *et al.* (1962) with the corresponding vibrational energy levels for $OH^*(v = 1 - 9)$.

Looking at the different energy levels shown it is clear that any downward transitions between two vibrational levels of OH^* will produce photons with energies ranging from approximately $0.3 \, eV$ to $3 \, eV$ given by the difference in energy between the two vibrational levels. $\Delta v = 1$ transitions will release photons with energies of approximately $0.3 \, eV$ and thus with wavelengths of approximately $4 \, \mu m$ falling into the infrared region of the electromagnetic spectrum. Larger transitions such as $\Delta v = 6$ will produce photons with energies of approximately $2 \, eV$ and with wavelengths of approximately $0.6 \, \mu m$ crossing into the visible portion of the electromagnetic spectrum.

Figure 3.17, from Roach and Gordon (1973) (identical to **Figure 3.7** but repeated here for the reader's convenience), shows the entire wavelength range over which vibrational transitions within OH^* occur as well as some additional features of the night sky.
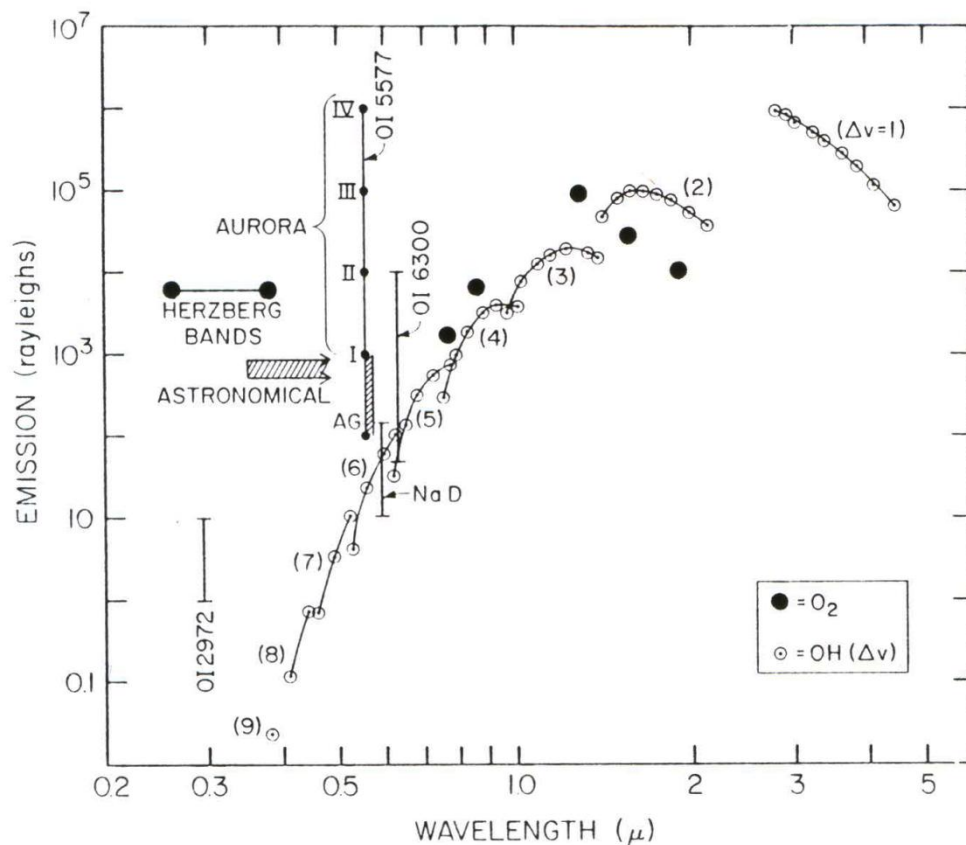
Figure 3.17: Emission intensity as a function of wavelength for the principal upper atmospheric emissions (Roach and Gordon, 1973).

3.5.3 Rotational Energy Levels

Thus far only pure vibrational transitions between different vibrational levels of OH^* have been considered and the possibility of any rotational transitions which may also occur has been ignored. Rotational transitions also occur within OH^* and it is often the case that simultaneous vibration-rotation transitions occur. It is therefore important to understand these transitions despite the fact that the 1-D model developed will not have the capability to distinguish between pure vibration and vibration-rotation transitions. This rotational energy is described by the two remaining degrees of freedom of OH which express the rotation of the molecule about the two axes perpendicular to the internuclear axis.

If the OH molecule is considered, for simplicity, to consist of two masses m_1 and m_2 which are joined by a rigid bar of length R_0 and the whole system rotates about an axis through its centre of mass, the moment of inertia I about this axis is given by

$$I = \mu R_0$$

$$(3.9)$$

where μ is the reduced mass of the system given by

$$\mu = (m_1 m_2)/(m_1 + m_2).$$

$$(3.10)$$

According to classical physics the energy of this system can be determined from

$$\frac{1}{2} I \omega^2$$

$$(3.11)$$

where ω is the angular velocity at which the system rotates. Substituting this potential into the Schrödinger equation leads to solutions for the rotational angular momentum. If J is used to designate the rotational angular momentum quantum numbers, then the allowed values of angular momentum are given by $\sqrt{J(J+1)}\hbar$ or

$$\mathbf{P} = \hbar \mathbf{J}$$

$$(3.12)$$

for integer **J**, as described in Woodgate, (1980), where $\hbar$ has the usual meaning of Planck's constant divided by 2π, $(h \: / \: 2\pi)$. The rotational energy eigenvalues, denoted by E_r, are then given by

$$E_r = \frac{1}{2I}J(J+1)\hbar^2.$$

(3.13)

Given that only certain energy values and angular momenta of the rigid rotor are possible it also follows that only certain frequencies due to changes in rotational states are possible. Furthermore, the allowed emission frequencies are restricted by quantum mechanical selection rules which limit transitions between certain states. This is explained in more detail in Thorne (1988).

3.6   OH* Spectra

Spectra produced as a result of energy level transitions within atoms and molecules are known to fall into three separate regions of the electromagnetic (EM) spectrum. These three regions namely: the visible, infrared and microwave regions of the spectrum correspond to the three types of energy level transition possible; electronic, vibrational and rotational. Generally it is found that electronic transitions fall into the visible, vibrational transitions fall into the infrared, while rotational transitions fall into the microwave region of the EM spectrum (Thorne, 1988).

Given that differences in the vibrational energy levels are much larger than differences in the rotational energy levels, it follows that vibration-rotation transitions also fall into the infrared region of the EM spectrum. Therefore, each pure vibrational transition is surrounded by a band, known as a vibration-rotation band, in which all possible vibration-rotation transitions are accounted for.

Figure 3.18 from Sheen and Byun (2004) (is a repeat of **Figure 3.8** included here for the convenience of the reader) shows numerous features which fall into the visible range of the EM spectrum in the night sky. On the far right of the figure are the vibration-rotation bands for a number of different OH* transitions spanning a wavelength range from $6000 - 9000$ Å.
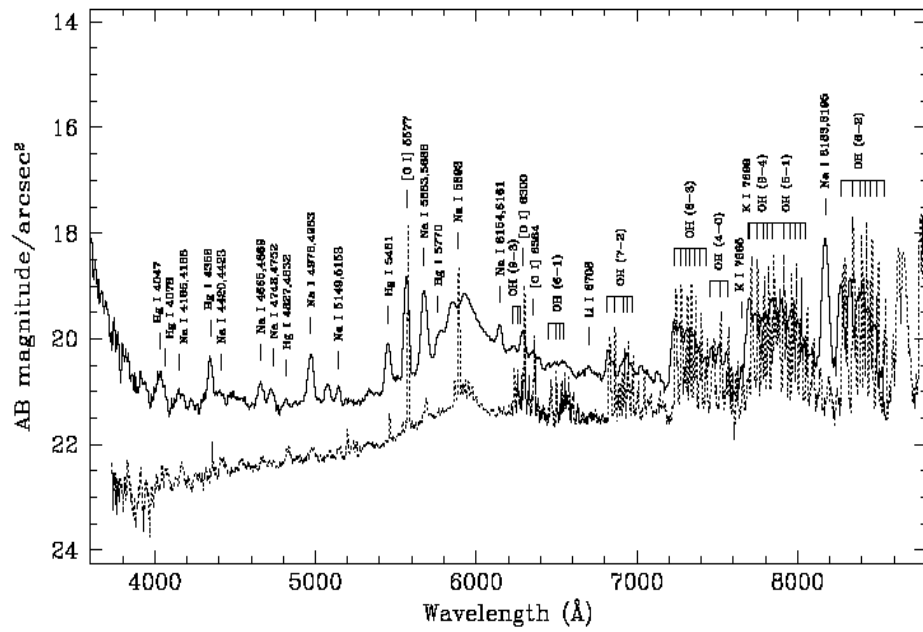
Figure 3.18: Emission intensity as a function of wavelength for the OH* radical at Mount Bohyun (Sheen and Byun, 2004)

Figure 3.19 shows a diagrammatic representation of the first four rotational levels for two separate vibrational states of OH* and can be used to explain these features of the vibration-rotation bands (Thorne, 1988).
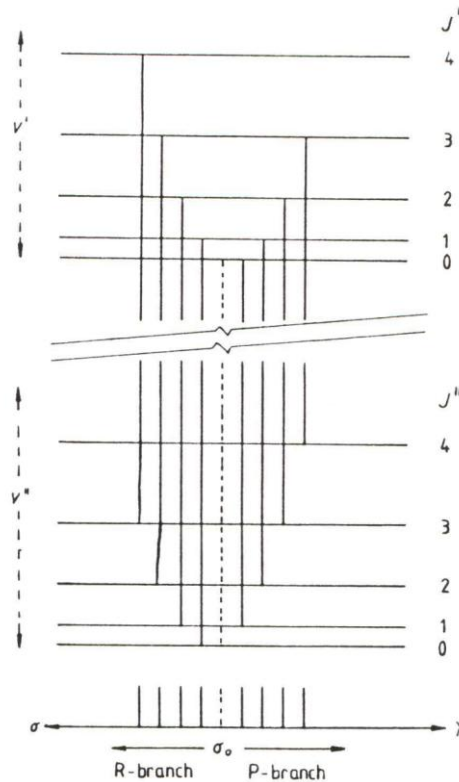
Figure 3.19: Vibration-rotation bands (Thorne, 1988).

134

The v' denotes an upper vibrational initial state and v'' denotes a lower vibrational final state. The numerous J values denote the rotational levels for each of the vibrational states while the vertical lines represent vibration-rotation transitions between the two levels. The dotted vertical line in the central position of the diagram represents the pure vibration transition between the two states. This corresponds to the wavelength characteristic of the difference in energy between the two vibrational states involved in the transition when there is no change in rotational state. At the bottom of this figure a representation of the resulting vibration-rotation band spectra is also displayed.

From **Figure 3.19** it can be seen that on either side of the pure vibration transition there exist a number of possible vibration-rotation transitions. According to quantum mechanics not all transitions between different rotational states are allowed. The selection rule placed on these rotational transitions by quantum theory is given as

$$\Delta J = J' - J'' = 0, \pm 1.$$

(3.14)

Thorne (1988) provides more details on how these selection rules are derived.

With the above selection rule in place three branches within the vibration-rotation band are formed. Each are denoted by a different letter and correspond to the three different possible values of ΔJ. The pure vibration transition resulting in no change of rotational state ($\Delta J = 0$) is referred to as the Q-branch. Vibration-rotation transitions resulting in a $\Delta J = +1$ change in rotational state are referred to as P-branch transitions, while transitions resulting in a $\Delta J = -1$ change in rotational state are referred to as R-branch transitions.

P-branch transitions exhibit slightly lower frequencies than Q-branch transitions and therefore higher wavelengths while R-branch transitions exhibit slightly higher frequencies than Q-branch transitions and lower wavelengths. These features are illustrated in **Figure 3.19**. Furthermore, since the populations of the rotational states follows a Boltzmann distribution this explains the shape of the emission curves displayed in **Figure 3.17**.

3.7 The Dipole Moment

Thus far this discussion has been limited to the different types of transitions that occur to make up the OH^* spectra. A more detailed analysis of the spectra requires a more detailed explanation of the dipole moment and radiative transitions probabilities associated with the OH molecule.

The important role played by the OH radical in various physical and chemical fields has been discussed already. Given its highly reactive nature, experimental studies of this molecule and its characteristics have always proven to be somewhat challenging. In particular, studies designed to determine the exact electronic dipole moment function (EDMF) have proven difficult. These difficulties are related to two particular properties of the OH radical and are explained in detail in Nelson *et al.* (1990). Only a brief summary of these properties will be provided here.

The first property which makes studies of OH^* complicated is the very nature of the OH^* transitions. OH^* exhibits rather intense overtone, or multi-quantum, transitions. This is reflected in the values of the thermally averaged Einstein *A* coefficients of OH^*, the determination of which will be explained in **Section 3.9**. A sample set of these coefficients at 200 K is presented in **Table 3.1** (Mies, 1974).

v'	v'' $= v - 1$	v'' $= v - 2$	v'' $= v - 3$	v'' $= v - 4$	v'' $= v - 5$	v'' $= v - 6$	Total
1	20.15					Units: s^{-1}	20.15
2	25.24	14.07					39.31
3	20.90	39.93	0.920				61.75
4	12.35	72.61	4.29	0.079			89.23
5	4.47	108.4	10.62	0.392	0.050		124.0
6	2.347	141.5	20.99	1.274	0.053		166.3
7	9.142	163.4	37.32	2.907	0.183		213.0
8	25.84	166.8	60.84	5.67	0.569	0.030	259.8
9	50.65	146.6	90.28	10.81	1.189	0.130	299.7

Table 3.1: Thermally averaged Einstein *A* coefficients (s^{-1}) of OH^* derived by Mies (1974).

As shown in **Table 3.1**, OH^* transitions from higher vibrational states are predominately overtone or multi-quantum transitions with $(\Delta v > 1)$. The lower vibrational state transitions are predominately fundamental or single-quantum transitions $(\Delta v = 1)$. This results from the fact that the EDMF has a large curvature in the proximity of the radical's equilibrium bond length, or nuclear separation, before reaching a maximum near the $v = 2$ outer classical turning point of the potential curve (Nelson *et al.,* 1990). Therefore, $\Delta v > 1$ transitions are much stronger than would usually be expected from a typical diatomic molecule.

The second property of OH to make studies arduous is its strong rotational dependence which can be divided into its vibration-rotation interactions as well as its spin uncoupling effects. Both of these strongly modify the transition strengths as a function of rotation Nelson *et al.* (1990).

While it has already been mentioned that OH has a large permanent dipole moment with a value of approximately 1.7 D the vibrational transition dipole moments for OH^* are in fact rather small, with values typically between $0.01 - 0.03$ D. Since the vibration-rotation interaction causes a small amount of the permanent dipole moment to be either added to, or subtracted from, the transition dipole moment even a modest amount of rotation can lead to destructive cancelation of a transition dipole moment. This can substantially alter the intensity of *P* and *R* branch transitions.

Furthermore, since OH has a large rotational constant $(\sim 18.91 \text{ cm}^{-1})$ (Nelson *et al.,* 1990), the spin uncoupling effects, which are very strongly *J* dependent, are large even for low values of *J*. This effect increases with increasing *J* and can be thought of as a transition of the molecules electronic angular momentum coupling scheme. When *J* is low Hund's case A in which spin is strongly coupled to the internuclear axis applies. However, as *J* increases, the behaviour of the molecule changes and an intermediate form of Hund's case A and Hund's case B, in which the spin is completely uncoupled to the internuclear axis, becomes more applicable. These different angular momentum coupling schemes are represented in **Figure 3.20** (Berdyugina and Solanki, 2002).
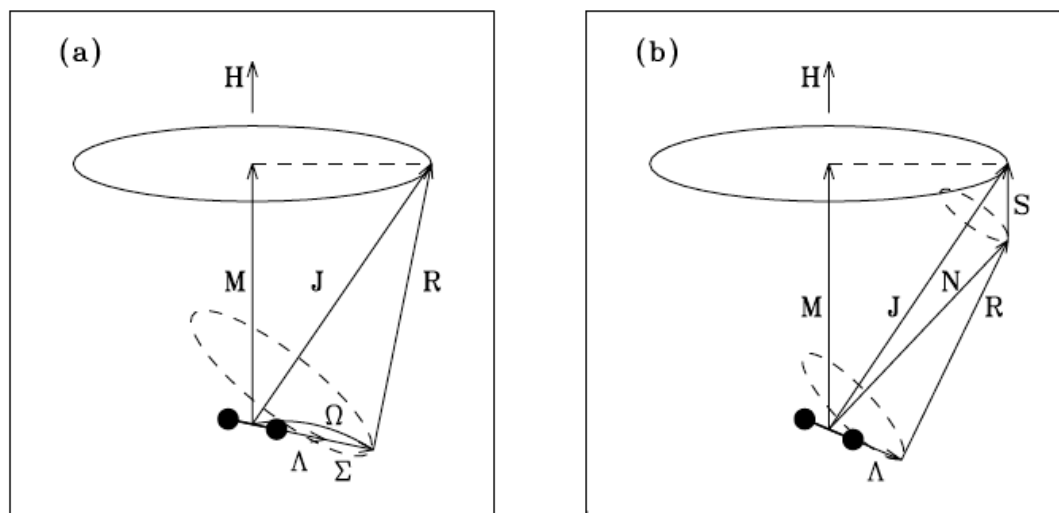
Figure 3.20: Angular momentum schemes described by Hund's case A (a) and Hund's case B (b) for a diatomic molecule within an external magnetic field (Berdyugina and Solanki, 2002).

Within **Figure 3.20** Hund's cases A and B are illustrated when a diatomic molecule is placed in a magnetic field. The molecule itself is represented by the dark dumbbell shape while the direction of the magnetic field is given by H. $\Lambda, S, \Sigma, \Omega, N$, and J all have their usual meanings described in **Section 3.5.1**. The remaining components M and R represent the projection of the total angular momentum J along the magnetic field and the angular momentum of nuclear rotation respectively. Dashed ellipses represent the precession of the individual components making up the total angular momentum vector J. The solid line ellipse represents the rotation of the total angular momentum J when placed in a magnetic field. Further details on Hund's Cases A and B, as well as a more in-depth explanation of the spin uncoupling effects is presented in Herzberg (1989).

The result of these combined effects is a significant alteration of individual vibration-rotation transition probabilities which can vary substantially even within a particular vibrational band. Thus the vibrational bands are, at best, poorly described by a single Einstein A coefficient. Thousands of individual transitions strengths are necessary to fully describe the vibration-rotation bands of OH^*.

3.8   **Determination of the dipole moment**

Despite the difficulties described in the previous section, there have been numerous attempts to accurately calculate the EDMF of OH and the resulting Einstein *A* coefficients. These are necessary factors when attempting to accurately model the behaviour of OH^*.

The first experimental determinations of the OH dipole moment were performed by Garvin (1959), Garvin *et al.* (1960), and Murphy (1971). Both of these groups determined empirical dipole moment functions from the relative intensities of different OH^* transitions originating from the same vibrational level. However, these early efforts ignored the rotational dependence of the transitions. Garvin (1959) and Garvin *et al.* (1960) have since been shown to be in error after conflicts between their data and Krassovsky *et al.* (1962) emerged (Turnbull and Lowe, 1988).

Meyer (1974) and Stevens *et al.* (1974) both calculated theoretical dipole moment functions. Mies, (1974) subsequently employed the function of Stevens *et al.* (1974) to calculate the $\Delta v = 1 - 5\ OH^*$ transition probabilities for vibrational levels $v = 1 - 9$, with rotational levels $J = 0.5 - 15.5$. These transition probabilities were for many years regarded as the "best available values" (Nelson *et al.,* 1990), and are still widely used in studies of OH^*.

Langhoff *et al.* (1986) published new transition probabilities based on the theoretical EDMF of Werner *et al.* (1983) and repeated the process in Langhoff *et al.* (1987) and Langhoff *et al.* (1989). Concurrently, Turnbull and Lowe (1988) presented an empirical dipole moment function determined from measurements of the relative intensities of different OH^* transitions from the same vibrational state $\Delta v = 1$.

Nelson *et al.* (1990) provides what is possibly the most succinct summary of the history of the OH^* electric dipole moment function determinations up to its time, before calculating their own dipole moment function and subsequently Einstein *A* coefficients. The dipole moment function of Nelson *et al.* (1990) was later utilised by Goldman *et al.* (1998) to both extend and update these individual line parameters after developments and advances in the technology available for the study of energy level transitions and intensities.

More recently, Cherepanov (2003) presents a new electronic dipole moment function for the OH radical in the form of a piecewise continuous function which compares very well to the calculations of Langhoff *et al.* (1986), Langhoff *et al.* (1989).

The determination of the OH electric dipole moment function is by no means a completed task despite the obvious similarities between many of the previously calculated functions shown in **Figure 3.21**. This figure compares the EDMF functions of Turnbull and Lowe (1988) (solid line) with those of Stevens *et al.* (1974) and Werner *et al.* (1983).
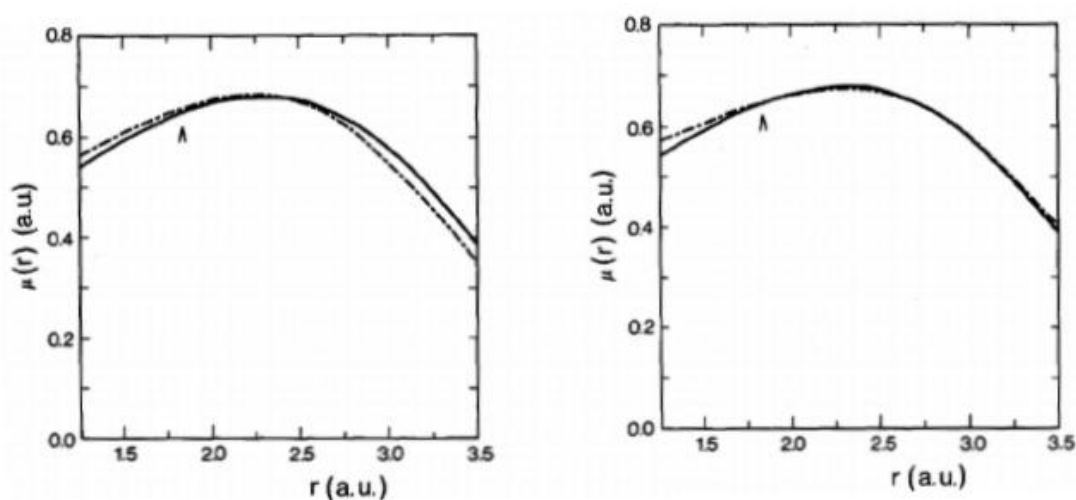
Figure 3.21: Comparison of the dipole moment functions of Turnbull and Lowe (1988) (solid line) with those of Steven *et al.* (1974) (left) and with Werner *et al.* (1983) (right).

Further work remains to be completed as even slight variations in the EDMF can lead to large variations in the calculated Einstein *A* coefficients.

3.9 Determination of the Einstein A Coefficients

Having determined the electronic dipole moment function, the Einstein *A* coefficient for a particular transition between two vibration-rotation levels can be calculated from

$$A_{v'J'}^{v''J''} = \frac{64\pi^4 \nu^3}{3h(2J'+1)} \left| R_{v''J''}^{v'J'} \right|^2 S_{J'J''}$$

(3.15)

where $\left| R_{v''J''}^{v'J'} \right|$ is a matrix element and is the integral of the product of the vibration-rotation wavefunctions of the initial and final molecular states and the EDMF (Turnbull, 1987). This is given as

$$R_{v''J''}^{v'J'} = \int \varphi_{v'J'}(r)\mu(r)\varphi_{v''J''}(r)dr$$

(3.16)

and is often represented by

$$|\langle v''J''|\mu(r)|v'J'\rangle|$$

(3.17)

in various publications including Langhoff *et al.* (1986), Turnbull (1987), and Turnbull and Lowe (1989). (v',J') and (v'',J'') represent the vibrational and rotational quantum numbers of the upper and lower states respectively, while v represents the wavenumber of the transition. $\mu(r)$ is the EDMF and $S_{J'J''}$ is a line strength factor.

This line strength factor is based on the concepts presented in Hill and Van Vleck (1928) who established the theory for determining the line strengths for doublet transitions in which the electronic angular momentum coupling scheme is an intermediate form of Hund's case A and Hund's case B. The factors involved were calculated by Kovacs (1960) and were further modified by Turnbull (1987), for ease of use after Langhoff *et al.* (1986), showed that the theory was accurate for the six principal branches of the Meinel system.

The Einstein *A* coefficients for vibration-rotation transitions of OH^* using the various published forms of the EDMF have been calculated numerous times (Mies, 1974; Langhoff *et al.,* 1986; Turnbull and Lowe, 1989; Nelson *et al.,* 1990; Goldman *et al.,* 1998). Despite these attempts substantial differences in the published figures of Einstein *A* coefficients still remain.

In all cases, as a result of the strong rotational dependence described previously, the transitional probabilities within individual vibrational bands vary significantly. The transition probabilities therefore cannot be represented as the product of a vibrational band strength and rotational line strength necessitating the "voluminous" tables presented in each publication (Turnbull, 1987).

To expect a 3-D model to calculate for thousands of individual vibration-rotation transitions, each with different transition probabilities, would be foolhardy. It is therefore necessary to limit the scope of this thesis to the comparison of individual vibrational band strengths and lifetimes only. This is accomplished through the use of thermally averaged Einstein *A* coefficients, which can accurately describe the behaviour of the different vibrational bands.

Using the individual transition probabilities for the vibration-rotation transitions, while assuming a Boltzmann distribution exists in the populations of the rotational states, and defining a rotational temperature, denoted by T_{rot} the thermally averaged transition probabilities for individual vibrational bands $v' - v''$ can be calculated as

$$A_{v'-v''} = \sum_{J'-J''} A_{v''J''}^{v'J'} \frac{2(2J'+1)}{Q_{v'}(T_{rot})} \exp\left(\frac{-hcE_{v'}(J')}{kT_{rot}}\right)$$

(3.18)

where

$$Q_{v'}(T_{rot}) = \sum 2(2J'+1) \exp\left(\frac{-hcE_{v'}(J')}{kT_{rot}}\right)$$

(3.19)

and is defined as the rotational partition function for the v'th level (Turnbull, 1987). The thermally averaged Einstein *A* coefficients are presented in the right hand column of **Table 3.1**.

Relating all of the above back to the initial question "why is OH^* such a dominant emitter in the night sky?" it can be seen that this is the result of both the altitudinal distribution of OH^*, governed principally by the concentration of atomic oxygen, and the large EDMF associated with OH^*, which leads to high transition rate probabilities in the Einstein *A* coefficients.

3.10   Diurnal Variations in OH^*

Since their discovery the Meinel bands have been probed through the use of ground based observations (Takahashi and Batista, 1981; Johnston and Broadfoot, 1993; Mulligan *et al.,* 1995) rocket measurements, (Krassovsky, 1962; McDade *et al.,* 1987b;

Lopez-Moreno *et al.,* 1988) and satellite observations (Le Texier *et al.,* 1987; Conway *et al.,* 2000; Pickett *et al.,* 2006; Baker *et al.,* 2007; Englert *et al.,* 2008; Gao *et al.,* 2011; Xu *et al.,* 2012) to name but a few.

Concurrently, a number of theoretical models have emerged which attempt to explain the properties of, and variations in, the OH^* nightglow profiles recorded by these various experiments. The 1-D, time dependant, model of Battaner and Lopez-Moreno (1979) is one such model and has been used to deduce average properties in the OH^* airglow layer as well as to investigate average diurnal variations in the emissions of the first 9 vibrational levels of OH^*. Results from this model have been shown to be in good agreement with results from rocket measurements of OH^* emissions presented in Krassovsky (1962).

Figure 3.22 shows a typical diurnal variation in the first 9 vibrational levels of OH^* as predicted by this basic model.
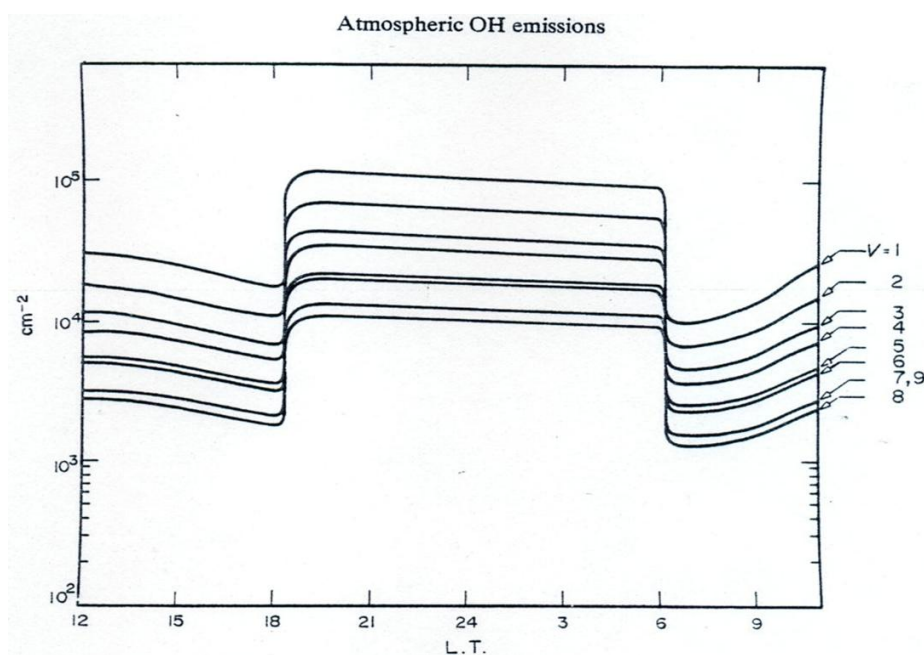
Figure 3.22: Concentration of OH^* in cm^2 columns for vibrational levels $v = (1 - 9)$ versus local time (Battaner and Lopez-Moreno, 1979).

The sharp increase in emissions from all nine vibrational levels at approximately 18 hrs local time can be attributed to increased OH^* production after sunset. This increased production is possible because photolysis of O_3 ceases at dusk due to the drop in incoming solar radiation within the Hartley band $(200 - 305$ nm$)$. Since there is no

photolysis of O_3 during the night, more ozone becomes readily available for OH^* production as atomic oxygen and molecular oxygen recombine.

The absence of incoming solar radiation during the night also impacts the rate of O_2 photolysis and without continued photolysis of O_2 the concentration of O starts to decrease as it produces OH^*. The same can be said for the photolysis of H_2O and the concentration of H. The rate of OH^* production over the course of the night therefore slowly decreases and the number of emissions from the different vibrational levels starts to drop as the population of the different vibrational levels slowly decrease over time.

At dawn, and with the return of incoming solar radiation, the photolysis of ozone once again competes with, and takes precedence over, the production of OH^* and the population of the different vibrational levels decreases significantly at approximately 6 hrs local time. The reduced levels of emissions from OH^* between the hours of dawn and dusk can then be attributed to the competing processes of O_3 photolysis and OH^* production for which the photolysis of O_3 has a much faster reaction rate coefficient.

While the above is broadly representative of the diurnal variation in OH^* emissions, it should be noted that an increase in the emissions from OH^* after local midnight has also often been observed (Wiens and Weill, 1973). This has been attributed to a number of atmospheric features including variations in the atomic oxygen concentrations (Battaner *et al.,* 1977) and atmospheric tides (Petitdidier and Teitelbaum, 1977).

More recently, as a result of highly advanced satellite limb scanning techniques, more insight into the diurnal variations of OH^* has been achieved which has enabled significant improvement of computational models of the mesopause region. In particular Ward (1999) presents a simple model for simulating the diurnal variations in the nightglow based on measurements from the Wind Imaging Interferometer (WINDII) instrument onboard NASA's Upper Atmosphere Research Satellite (UARS). This model attributes the diurnal variations in OH^* intensities to dynamical effects associated with the migrating diurnal tide.

Figure 3.23 shows results from the model of Ward (1999) in predicting the volume emission rate of the $OH^*(9-8)$ band at various local times over the course of a single night during equinox conditions. It can be seen that, at the equator, a maximum in the

OH^* emission is achieved shortly after dusk, in line with the more basic model of Battaner and Lopez-Moreno (1979). It can also be seen that this maximum in the OH^* emissions near the equator in the early evening subsequently evolves into two maxima in the early morning at the mid-latitude regions. This offers an explanation for the various measurements of peak emissions occurring after local midnight.
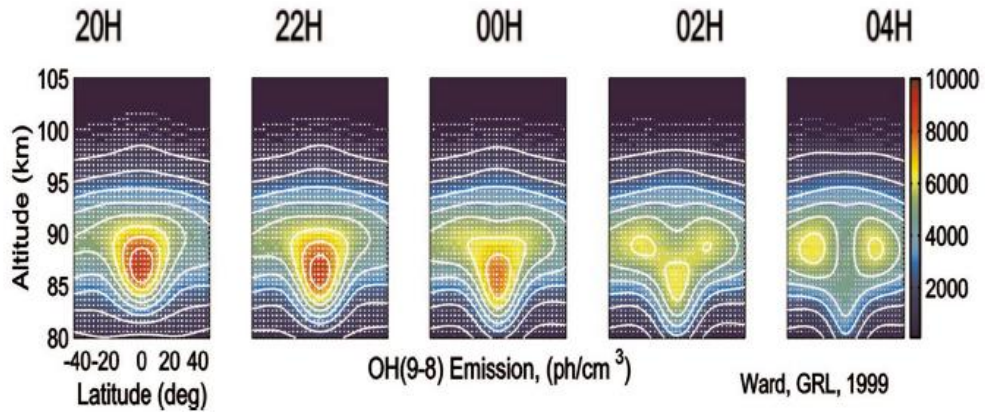
Figure 3.23: Height and latitude cuts at different local times of the $OH^*(9-8)$ diurnal nightglow signatures for equinox conditions (Ward, 1999).

While this model is successful in explaining the broad features from the $OH^*(9-8)$ band transitions observed by the WINDII instrument it should be noted that this model encounters problems calculating day-time volume emission rates (ver). **Figure 3.24** shows the emission rates from this band calculated by the model over a 24 hour period. There are additional peaks in the emission during the day-time at mid-latitudes which have been deemed "unrealistic" as the photolysis of ozone during the day-time results in significant reduction in the intensity of this airglow mechanism (Ward, 1999).
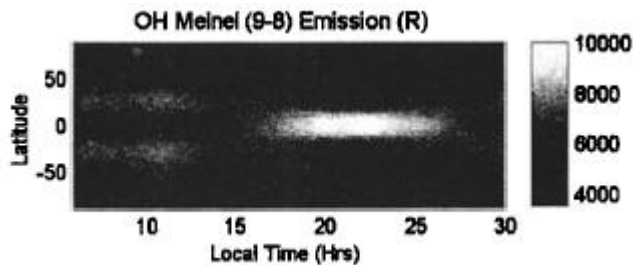
Figure 3.24: Latitude and local time cut of height integrated diurnal nightglow signatures from the $OH^*(9-8)$ band (Ward, 1999).

Marsh *et al.* (2006) expanded the investigation into the effects of the migrating diurnal tide on OH^* emissions using data gathered from the SABER instrument over the course

of 55 days surrounding the March equinox of 2002 and using the ROSE 3-D chemical transport model. By comparing the model predictions of ROSE with observational data recorded by SABER, Marsh *et al.* (2006) were able to show that the migrating diurnal tide produced a significant enhancement in the equatorial emissions of OH^* as also seen in Baker *et al.* (2007).

Figure 3.25 shows averaged VER profiles for OH^* emissions in the $2.0\,\mu$m range covering the $OH^*(9-7)$ and $OH^*(8-6)$ bands at two local times as well as the corresponding temperature profiles at altitudes between $70-110\,$km. The strong variability in the two OH^* profiles highlights the diurnal variation in emissions and the importance of using data recorded at the same local time when attempting to detect seasonal variations in OH^* emissions. This will be discussed in more detail throughout **Chapter 5**.
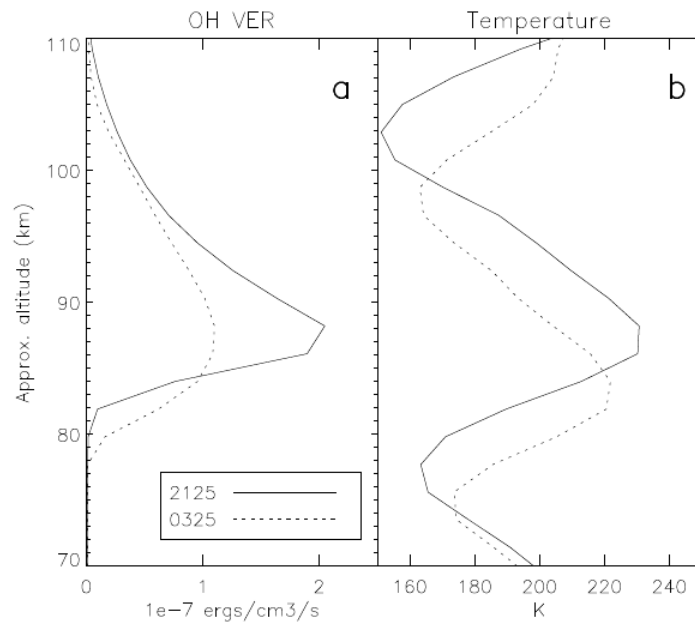
Figure 3.25: SABER OH^* and temperatures profiles averaged from March 26th to May 19th, 2002 at 2.5° N. Profiles are shown for $21\!:\!25$ hrs local time (solid lines) and $03\!:\!25$ hrs local time (dashed lines) (Marsh *et al.,* 2006).

Figures 3.26 and **3.27** compare observational data from SABER (**Figure 3.26**) and model data as predicted by the ROSE model (**Figure 3.27**) over the course of a single night, near equinox, and at altitudes of 88 and 99 km. A number of similar features can be identified in both figures.
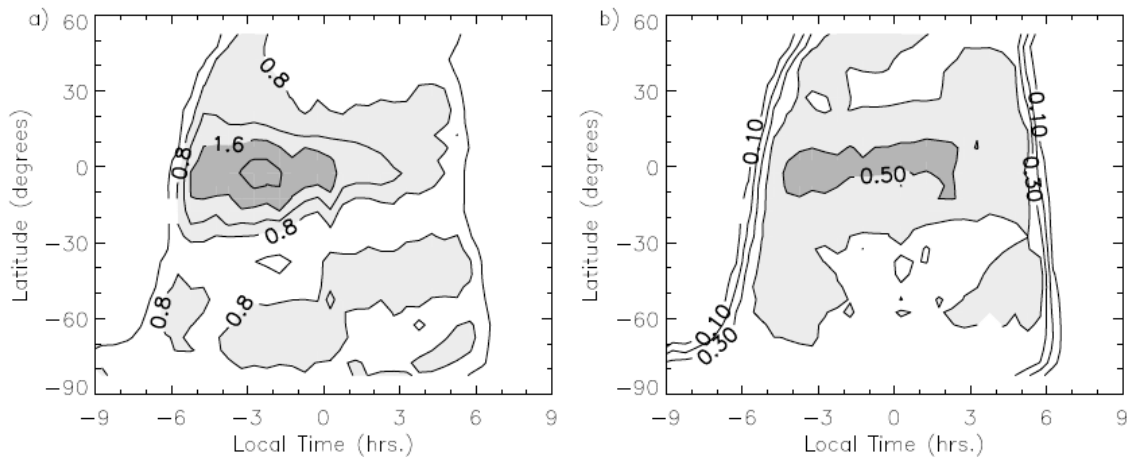
Figure 3.26: SABER OH^* volume emission rate ($1e^{-7}$ ergs/cm^3/s) at 88 km (left panel) and 99 km (right panel).
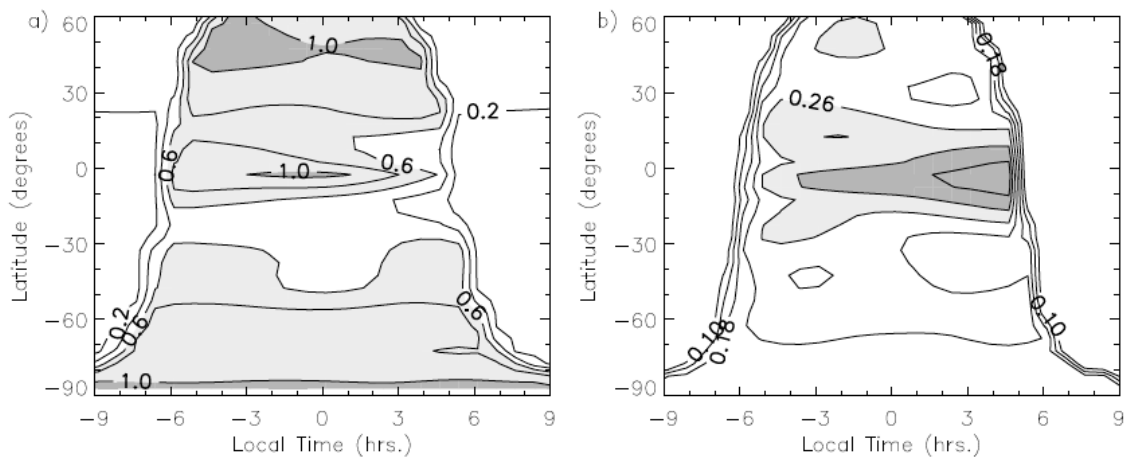
Figure 3.27: ROSE model simulations of the OH^* emission ($1e^{-7}$ ergs/cm^3/s) at 88 km (left panel) and 99 km (right panel) on 22nd April, 2002 (Marsh *et al.,* 2006).

It can be seen that the emission rate is significantly higher during the night-time as previously predicted in the models of both Battaner and Lopez-Moreno (1979) and Ward (1999). There is a clear enhancement in the night-time emission rates at the equator and local minima in the emissions at $\pm 30°$ latitude. It can further be seen in the SABER observations that the sharp increase in emissions soon after dusk leads into a gradual decline in emissions after midnight. This is due to the decreasing amounts of atomic oxygen available for OH^* production. This feature is not captured in the current version of the ROSE model.

Marsh *et al.* (2006) attributed the equatorial enhancement in emissions to changes in the atomic oxygen concentrations resulting from vertical transport at 88 km. At 99 km the variation in emissions was attributed to changes in temperature and atmospheric density, again as a result of vertical transport. It was concluded that the migrating diurnal tide is the dominant cause of nocturnal variations in the emissions of OH^* as the vertical transport results from tidal effects.

Studies of tidal features have shown that the diurnal tide is strongest during equinox and weakest during solstice as well as stronger during the vernal equinox as opposed to the autumnal (Fritts and Isler, 1994; Burrage *et al.,* 1995; Xu, 2004) showing correlation with features from the OH^* emissions.

Gao *et al.* (2011) expanded the original data set of Marsh *et al.* (2006) and looked at the nocturnal variation in the OH^* intensities as measured by SABER over the course of 8 years. In **Figure 3.28** the nocturnal variation in the OH^* emissions in both the $OH^*(9 - 7$ and $OH*8-6$ bands, at equinox and solstice conditions, are presented. The dashed white lines are representative of sunset and sunrise at an altitude of 100 km.
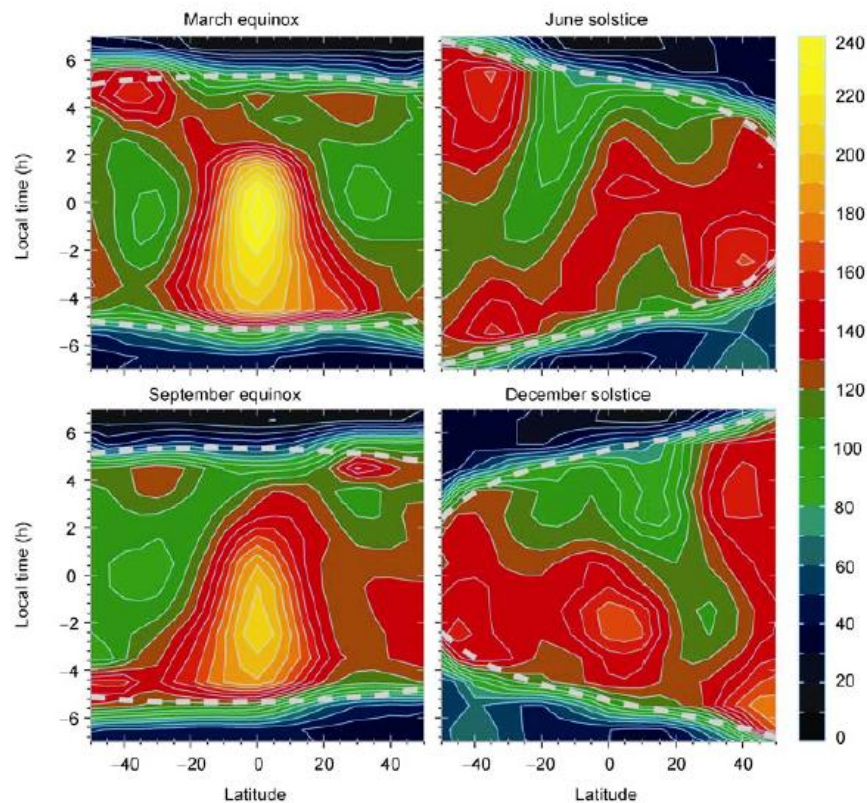
Figure 3.28: Local time and latitude distributions of the OH^* nightglow intensities in kilo Rayleighs (Gao *et al.,* 2011).

In **Figure 3.28** there is a sharp increase in the intensity of the OH^* emissions after sunset and a sharp decline in the OH^* emissions at sunrise. This is consistent with what has been presented previously. During the March equinox there is a clear similarity between what has been recorded by the SABER instrument and in the model predictions of Ward (1999). At the equator there is a sharp increase in the amount of OH^* emissions immediately after sunset which reaches a peak at midnight. As the amount of OH^* emissions at the equator decreases after midnight, two new peaks in the mid-latitude regions ($\pm 30°$) emerge at approximately $4\,\mathrm{hrs}$ (LT). The similarities between the observations of SABER and the model predictions of Ward (1999) are enhanced when looking at the September equinox. The peak in the OH^* intensities at the equator occurs approximately $3\,\mathrm{hrs}$ preceding local midnight before gradually decreasing over the course of the night until dawn. At this time there is a sharp decline in emissions.

From these model predictions and satellite observations, the basic diurnal profile can be attributed to the competing processes of OH^* production, and O_3 photolysis during the day-time. The absence of O_3 photolysis at night allows for increased concentrations of, and emissions from, the first nine vibrational levels of OH^*. The more advanced features of the diurnal variation over the course of the night are accounted for by the introduction of the migrating diurnal tide and its effects on the chemistry and dynamics within the mesopause. It is believed therefore that the tides account for the variations in the nocturnal emissions from OH^* at different latitudes .

3.11   Seasonal Variations in OH^*

Seasonal variations in the OH^* emissions have been studied at great length (Takahashi *et al.* 1977; LeTexier *et al.,* 1989; Abreu and Yee*,* 1989; Lopez-Gonzalez *et al.,* 2004; Gao *et al.,* 2011). Significant difficulties exist in the investigation of these seasonal variations. For example, due to the diurnal variation in emissions, it is necessary to carry out measurements at the same local time when looking for seasonal signatures. This, combined with the latitudinal variation in emissions, effectively eliminates the possibility of using rocket measurements to investigate these features. Ground and satellite based observations are therefore necessary, both of which have their own limitations related to taking measurements *ex infra* and *ex supra*. LeTexier *et al.* (1987) and LeTexier *et al.* (1989) investigated the seasonal variation in OH^* emissions using a

2-D dynamical and photochemical coupled numerical model as well as satellite measurements from the Solar Mesosphere Explorer (SME) satellite. The seasonal variations in the emissions predicted by this model were too weak when compared to measurements. A low signal-to-noise ratio further limited the scope of satellite observations to within 20° of the equator (Marsh *et al.*, 2006).

Since the late 1980's ground and satellite based technology has advanced to the point where seasonal observations can be studied in-depth. These advances have allowed for detailed observations of the seasonal variations in OH^* emissions.

One of the primary contributors to this wealth of data is the SABER instrument onboard NASA's TIMED satellite. **Figure 3.29** from Marsh *et al.* (2006) shows the seasonal variations in OH^* emissions from the $OH^*(9-7)$ and $OH^*(8-6)$ bands at two local times over the course of a 3 year period. The data presented here are monthly means which have been binned according to local time and latitude.
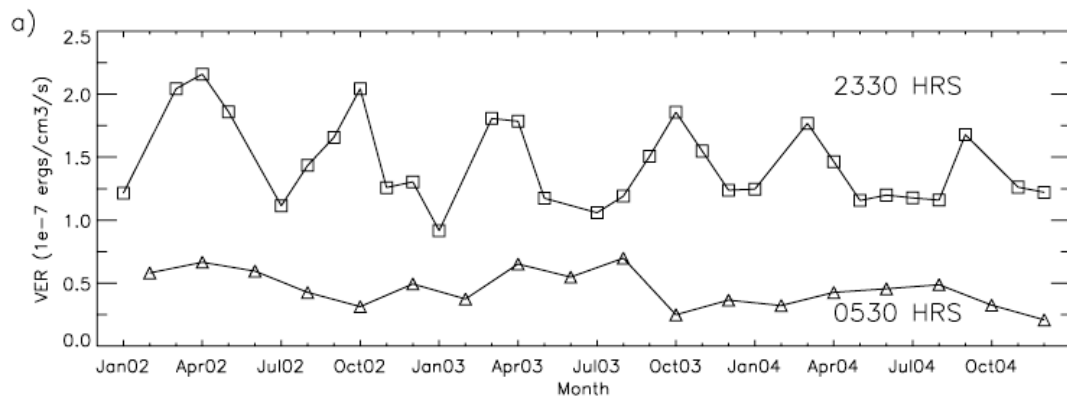
Figure 3.29: Observed seasonal variation in the OH^* emission rate at 89 km for latitudes within 7.5° of the equator. Data are monthly means of all observations that fall within 30 mins of 2330 hrs (squares) and 0530 hrs (triangles) local time (Marsh *et al.*, 2006).

A semi-annual variation is visible at a local time of 2330 hrs with peaks in the emission appearing during equinox, and minima appearing during solstice. This variation is not visible at 0530 hrs emphasising once again the importance of using observational data at the same local time when searching for seasonal signatures.

Given the local time variation in emission strengths, in conjunction with the seasonal variation, Marsh *et al.* (2006) concluded that the variations in the OH^* emissions were

the result of changes in the migrating diurnal tides with local time and season as opposed to changes in vertical diffusion resulting from seasonal variations in gravity wave dissipation as had been previously proposed by LeTexier *et al.* (1987). This earlier proposal cannot easily explain the features observed. This conclusion is further supported in more recent works such as Grgalashvyly *et al.* (2014).

Studies of tidal features have shown that the diurnal tide is strongest during equinox, weakest during solstice and stronger during the vernal equinox as opposed to the autumnal (Fritts and Isler, 1994; Burrage *et al.*, 1995; Xu, 2004). This mirrors features in the OH* emissions.

Figure 3.30 shows plots of the seasonal variation in emissions at the same local times but at 58° S of the equator.
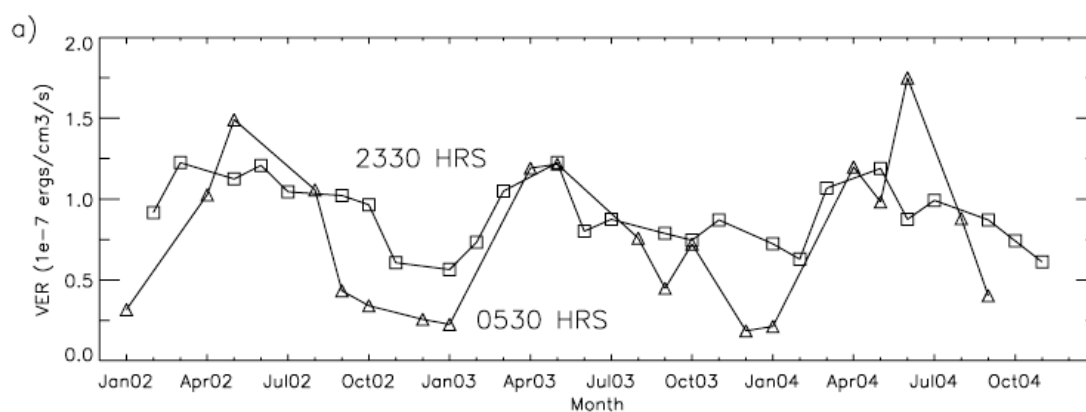
Figure 3.30: Observed seasonal variation in the OH* emission rate at 89 km for latitudes surrounding 58° S. Data are monthly means of all observations that fall within 30 mins of 23:30 hrs (squares) and 05:30 hrs (triangles) local time (Marsh *et al.,* 2006).

The variation in emissions is quite similar at both local times. At these latitudes an annual variation in the emission, rather than a semi annual variation, exists with peaks occurring during May and minima occurring during December. The differences between the two profiles from October to January within each year can be attributed to increased rates of O_3 photolysis after sunrise in the early mornings of the Southern hemisphere's summer.

Profiles of the emission at 58° N are quite similar to the profiles in **Figure 3.30** except that they are shifted by 6 months as would be expected for the Northern hemisphere summer.

In these profiles the tidal features observed in **Figure 3.29** are less evident. This is not unexpected as the amplitude of the diurnal tide drops significantly at higher latitudes (Marsh *et al.,* 2006; Smith *et al.,* 2010). An annual variation in the emissions is observed and can be attributed to the mean meridional circulation. During the winter the downward component of this circulation forces atomic oxygen from the thermosphere down into the mesopause. Given that the production of OH^* depends heavily on the concentration of O within the mesopause it therefore stands to reason that with increased concentrations in O there is more OH^* production and subsequently more OH^* emissions (Marsh *et al.,* 2006).

The overall seasonal variations in OH^* emissions resulting from the combined annual and semi-annual variations described can be seen in **Figure 3.31** (Gao *et al.,* 2011).
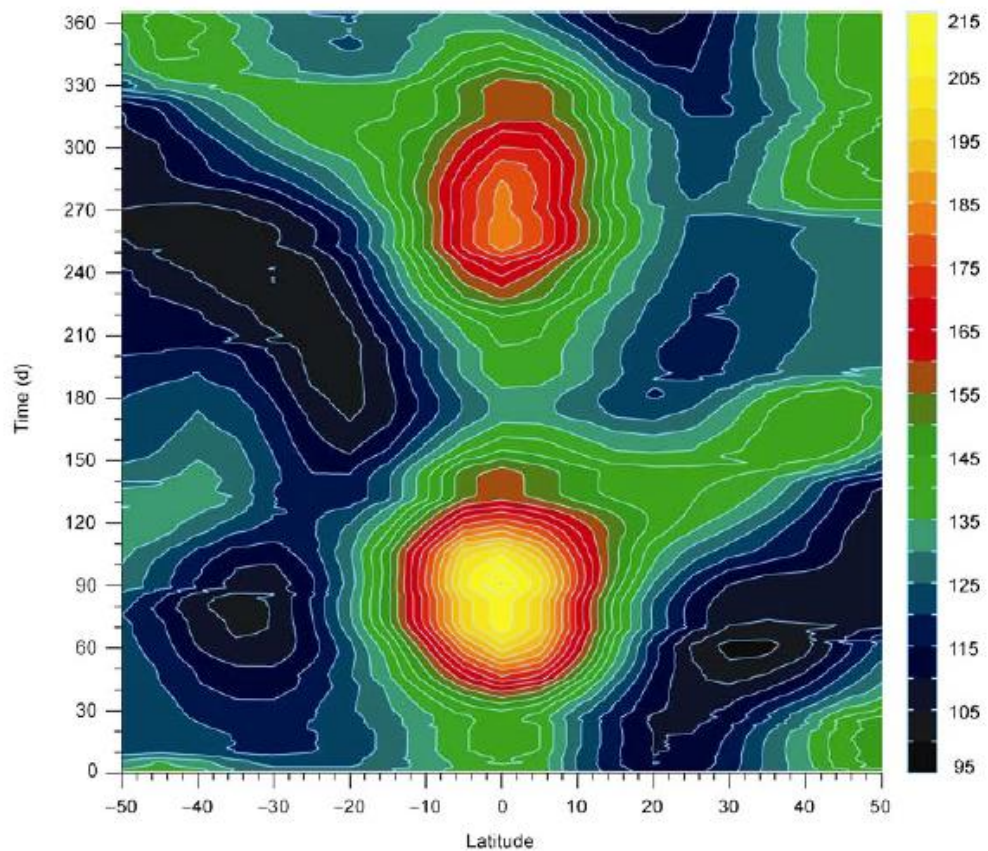
Figure 3.31: Seasonal variations in OH^* nightglow intensities between 50° S and 50° N latitudes in kilo Rayleighs (Gao *et al.,* 2011).

The data presented are averaged emission profiles binned according to local times between -2.5 and 2.5 hrs and integrated over altitudes between $75 - 100$ km. The emissions are strongest at the equator over the course of the year. Within the surrounding tropical region, the combined annual and semi-annual variations, produce strong emissions during the spring equinox. This corresponds to the approximate location at which both the annual and semi-annual variations have their respective peaks. A second strong emission peak emerges during the autumnal equinox. However, the magnitude of this peak is smaller as it corresponds only to a peak within the semi-annual variation in emissions. Both of these peaks subsequently extend into the summer hemisphere when approaching solstice up to approximately $50°$ in latitude. These extensions should not be confused with the secondary peaks in the winter hemisphere attributed to the annual variation in OH^* emissions.

As the SABER instrument only gathers continuous year round data for regions within approximately $\pm 55°$ latitude, (Gao *et al.*, 2011), the scope of these observations is limited to latitudes between 50°N and 50°S. This means that the effects of the semi-annual variation are still visible at the outer boundaries of this plot but the annual variation depicted in Marsh *et al.* (2006) is not completely visible within these data. The emergence of secondary peaks at approximately $50°$ S, surrounding days $110 - 140$, and subsequently $50°$ N, after day 270, is suggestive of this annual variation.

The asymmetry within the seasonal profiles of both hemispheres should be noted. Within the latitude range covered by these observations the mean intensity in the Southern hemisphere is at all times less than the mean intensity over the Northern hemisphere. This can be seen in the peaks previously mentioned at $50°$ N and $50°$ S with the peak in the Northern hemisphere significantly broader and more intense than the peak in the Southern hemisphere. This asymmetry can again be seen in **Figure 3.32** from Gao *et al.* (2011) in which the latitude range of the June solstice profile has been inverted. The purpose of this inversion is to align the seasons within each profile as opposed to latitude.
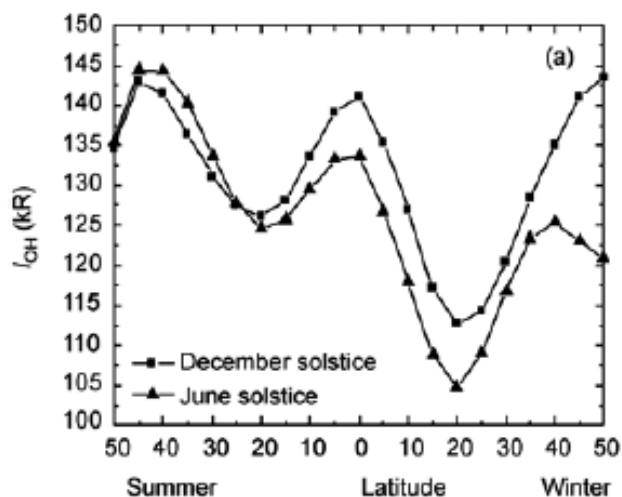
Figure 3.32: Latitude distribution of OH* nightglow intensities at the June solstice and December solstice. The June curves have been reversed so that from left to right the latitude axis indicates 50° S to 50° N for the December curves and 50° N to 50° S for the June curves (Gao *et al.,* 2011).

This asymmetry within these profiles can be attributed to the asymmetry in the temperature profiles of the different hemispheres and subsequently the asymmetry in the O and O_3 profiles. More details of these asymmetries can be found in Shepherd *et al.* (2004) and Xu *et al.* (2007).

3.12   Global Variations in OH*

It remains to discuss the global variations in OH* emissions with respect to both altitude, latitude and longitude. Global studies of the emissions depend entirely on satellite technology. The first global measurements of OH* were performed by the SME satellite (LeTexier *et al.,* 1989). The observations of this satellite have been discussed earlier together with the limitations on the observational data provided by this satellite.

Since the SME observations a wealth of data in global measurements has been recorded by:

1) WINDII (Wind Imaging Interferometer) onboard NASA's UARS (Upper Atmospheric Research Satellite) (Melo *et al.,* 2000; Russell and Lowe, 2003; Russell *et al.,* 2005).

2) MLS (Microwave Limb Sounder) onboard NASA's Aura satellite (Pickett *et al.,* 2006).

154

3) SCIAMACHY (SCanning Imaging Absorption spectroMeter for Atmospheric CHartographY) onboard ESA's (European Space Agency) ENVISAT (Environmental Satellite) (Kaufmann *et al.,* 2007; von Savigny *et al.,* 2012b).

4) SABER (Sounding of the Atmosphere using Broadband Emission Radiometry) onboard NASA's TIMED (Thermosphere-Ionosphere-Mesosphere Energetics and Dynamics) satellite (Marsh *et al.,* 2006; Baker *et al.,* 2007; Gao *et al.,* 2011; Xu *et al.,* 2012).

5) SHIMMER (Spatial Heterodyne Imager for Mesospheric Radicals) onboard the United States NRL (Naval Research Laboratory) STPSat-1 (Space Test Programme Satellite 1) (Englert *et al.,* 2008).

Table 3.2 provides a summary of these satellites linking the name of the instrument used in OH measurements to the relevant satellite, their observations and papers providing descriptions of their operation.

Instrument	Satellite	Observation	Paper	Details
SABER	TIMED	$OH^*(9-7)$ $OH^*(8-6)$ $OH^*(5-3)$ $OH^*(4-2)$	Baker *et al.* (2007)	2002-present 60-180 km 53° $-82°$ latitude
SCIAMACHY	ENVISAT	$OH^*(8-3)$ $OH^*(6-2)$ $OH^*(3-1)$	Kaufmann *et al.* (2007)	2002-2012 72-150 km 10°S $-20°$N (consistent)
WINDII	UARS	$OH^*(8-3)$	Russell *et al.* (2005)	1991-2004 80-300 km 42° $-72°$ latitude
MLS	Aura	OH ground state	Pickett *et al.* (2006)	2004-present 0-90 km $\pm82°$
SHIMMER	STPSat-1	OH ground state	Englert *et al.* (2008)	2007-2009 40-100 km $\pm57°$ latitude

Table 3.2: Summary table linking instruments and satellites associated with OH measurements discussed in this thesis.

For the purposes of this thesis, the SABER instrument provides the majority of the observational data used in model data comparisons presented in **Chapter 4** and **Chapter 5**. The observations of WINDII and SCIAMACHY will also be discussed.

Figure 3.33 from Zhang and Shepherd (1999) shows the results of measurements of the $OH^*(8-3)$ band emissions surrounding the March equinox (first row) and the December solstice (second row) at 5 local times during 1992 obtained from WINDII.
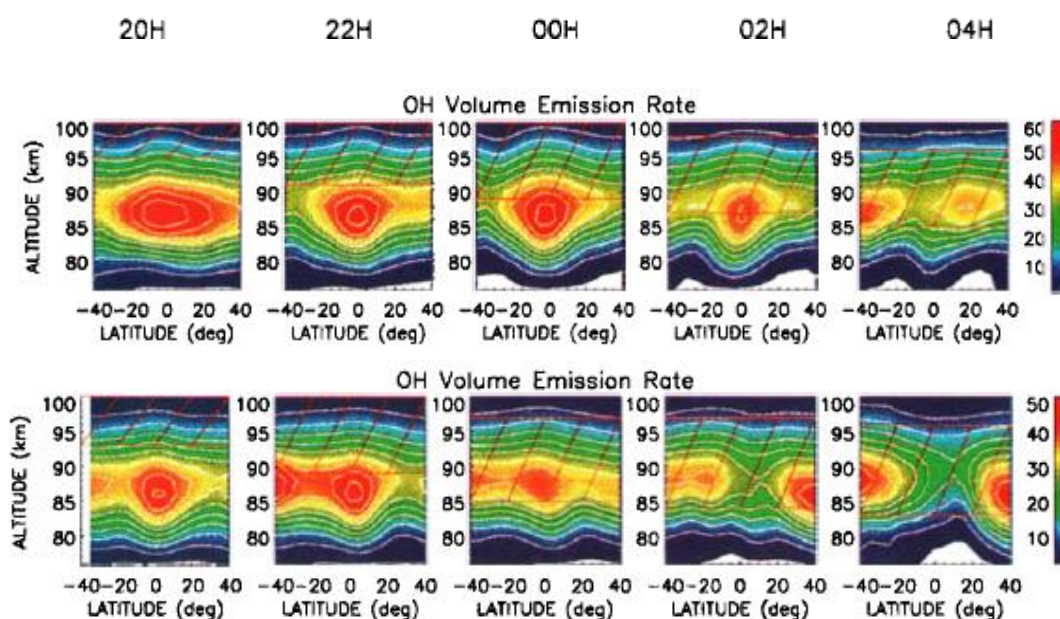
Figure 3.33: WINDII observations of the zonally averaged latitudinal and vertical distributions at $20, 22, 00, 02, 04$ hrs local time of the OH^* volume emission rates in photons/cm^3/s for March/April 1992 (top row) and December to February 1993 (second row) (Zhang and Shepherd, 1999).

The structure of the emission layer is similar to the model predictions of Ward (1999), despite the different vibrational bands considered. During equinox, a peak in the emissions develops within the tropical regions in the early evening at altitudes surrounding 87 km. The emissions subsequently diminish over the course of the night until late morning where the earlier equatorial peak evolves into two separate peaks in the mid-latitudes. The altitude of the layer remains relatively constant over the course of the night.

Broadly speaking, similar features are observed during the December solstice. The peak emissions again occur initially at the equator in the early evening. However, the

magnitude of the emission is lower. During solstice, the peak emission occurs at approximately midnight before diminishing more rapidly and evolving into two separate peaks in the mid-latitude regions at an earlier local time than at equinox. Only a slight variation in altitude is observed at solstice with a magnitude of about 1 km between the peak emissions in the southern and Northern hemisphere during the early morning.

Figure 3.34 shows the altitude latitude cross section of the $OH^*(9-6)$ limb radiances approaching December solstice conditions for 2005 as recorded by SCIAMACHY and presented in Kaufmann *et al.* (2007). The plot covers the Northern hemisphere up to a latitude of 80° and measures the limb radiance in units of photons/m^2 s m sr.
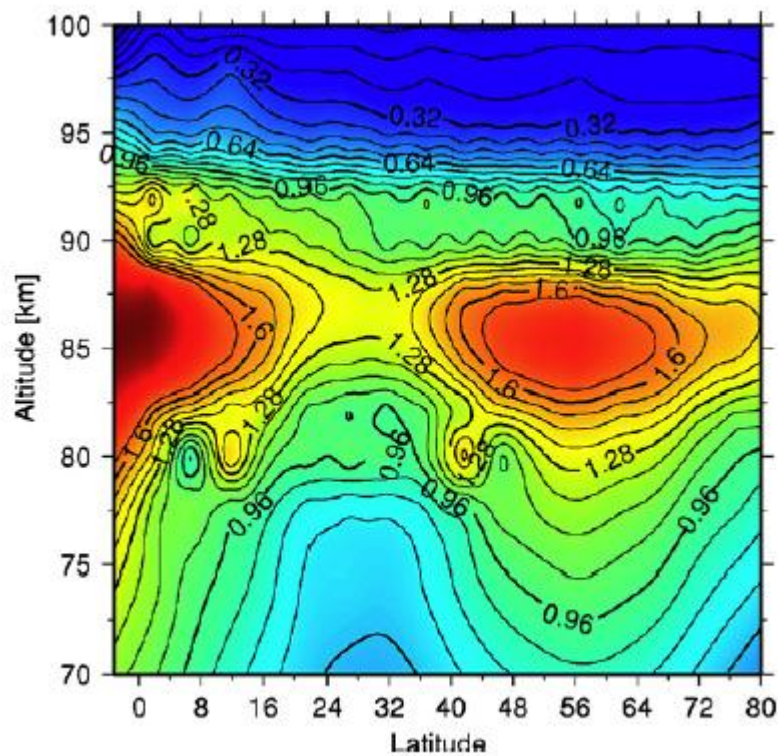
Figure 3.34: Latitude and altitude cross section of the $OH^*(9-6)$ limb radiances for the period 19th November to 21st December 2005 in units of photons/m^2 s m sr (Kaufmann *et al.* 2007).

Similar features to those described previously are evident within the observations of SCIAMACHY. The peak in radiance occurs over the equator and a secondary peak occurs over the mid-latitudes. However, while these peaks are shown to be concurrent features in the nightglow radiance, previous plots from Zhang and Shepherd (1999) show these features to occur at different local times. As **Figure 3.34** plots

SCIAMACHY data, which has not been binned with respect to local time, concurrent features within this plot are to be expected.

The overall global features in OH^* emissions are probably best presented in Gao *et al.* (2011). **Figure 3.35** shows observational data on the altitude and latitude distribution of OH^* emissions during both equinox and solstice conditions. These data have been binned according to local time between -2.5 and 2.5 hrs and averaged over a period of 8 years.
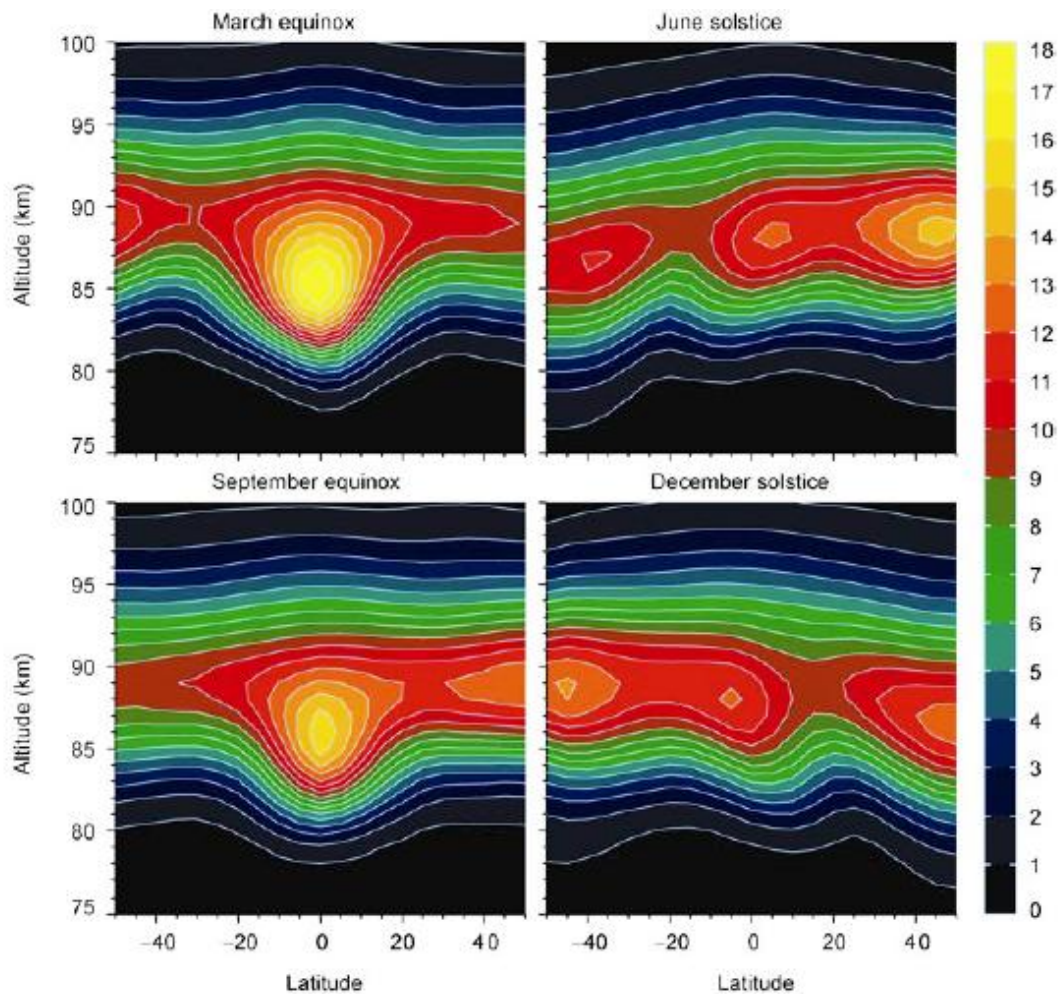
Figure 3.35: Altitude latitude distribution of OH^* nightglow emission rates in 10^4 photons/cm^3/s (Gao *et al.,* 2011).

The largest peak in OH^* emissions can be seen, once again, to occur during equinox conditions with the vernal equinox exhibiting somewhat more intense peaks than the autumnal equinox. This can be attributed to annual and semi-annual variations on the OH^* emissions discussed in the previous section. The extensions of these peaks into the

summer hemispheres up to latitudes of approximately 50° are visible as are the secondary peaks starting to form at high-latitudes within the winter hemisphere.

At all times the altitude range of the emissions covers approximately 15 km between $80 - 95$ km. The peak emissions at the equator during equinox occur at slightly lower altitudes than at other latitudes. During equinox the altitude of the layer remains somewhat constant with latitude, while at solstice there is a clear difference in the altitude of the layer with respect to latitude. This can be explained as the result of a combined effect of mesopause photochemistry and the mean meridional circulation introduced in **Chapter 1**.

Within the summer hemisphere, increased levels of incoming solar radiation leads to adiabatic cooling of the mesopause as it is forced into higher altitudes. At these heights the atomic oxygen concentration profile increases with altitude up to approximately 100 km. Therefore, there is an increase in the amount of OH^* production and hence more OH^* emissions. Within the winter hemisphere the mean meridional circulation forces atomic oxygen from the theremosphere down into the mesopause, causing adiabatic heating of the meospause as it descends to lower altitudes. This results in increased concentrations of atomic oxygen within the mesopause region and hence more OH^* production and OH^* emissions.

These features can be identified in the June and December plots as the peak in emissions at the equator extends itself into the summer hemisphere and to higher altitudes. Within the winter hemisphere a separate peak evolves at lower altitudes.

The longitudinal features in the emissions can be best summarised in **Figures 3.36** and **3.37** from Baker *et al.* (2007). **Figure 3.36** plots the 7 day average of the global emissions from the $OH^*(5-3)$ and $OH^*(4-2)$ bands surrounding the spring equinox of 2005. The average local time corresponding to measurements is 0113 hrs. **Figure 3.37** plots the corresponding global peak altitudes of the emissions from these bands. A peak in the global emission can be seen to exist at the equator. The emission rate drops with increasing latitude until the mid-latitudes where there is a small increase in the level of emissions. In the equatorial regions a wavenumber 2 feature is evident while in the southern regions a small wavenumber 1 feature is visible instead. Since the local time of these emissions correspond roughly to 0113 hours, these wavelike features can

attributed to tidal effects, primarily the non-migrating tides. These features are also shown in Xu *et al.* (2010) in much more detail and will be discussed in **Chapter 5**. From **Figure 3.37** it can be seen that there is an inverse relationship between peak emission rates and peak emission heights. Peak emission rates occur at lower altitudes shown to be approximately 82 km at the equator and approaching 89 km in the mid- to high-latitudes, especially in the Northern hemisphere during the spring equinox.
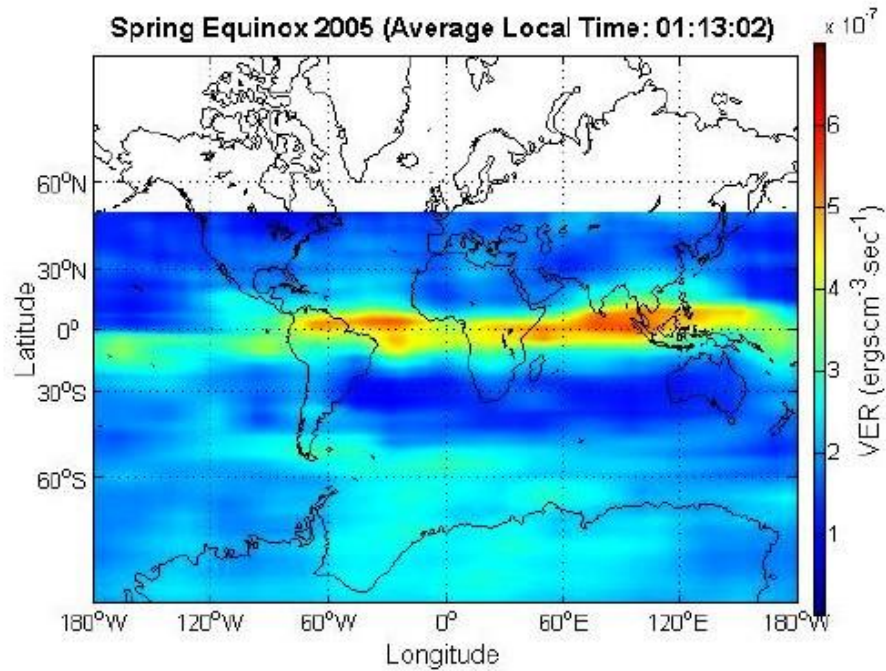
Figure 3.36: Peak OH* mesospheric VER night-time airglow global distribution, 7 day average at the 2005 spring equinox from SABER IR sensor (Baker *et al.,* 2007).
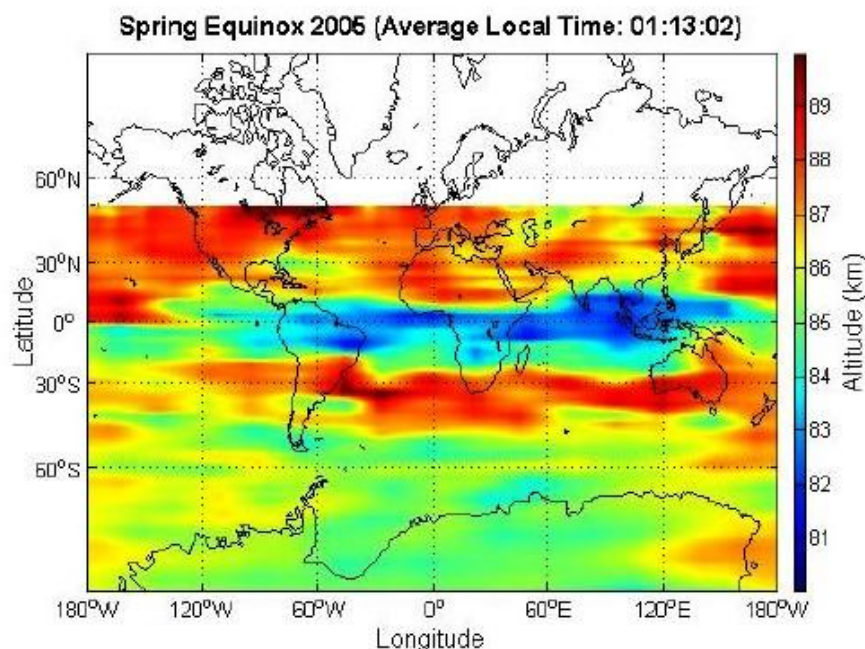
Figure 3.37: Altitude distribution of the peak OH^* mesospheric night-time global airglow VER from SABER IR sensor, 7 day average at the 2005 spring equinox (Baker *et al.*, 2007).

3.13   Chapter 3 Summary

In this chapter the hydroxyl radical has been discussed. In the opening sections a brief outline on the importance of OH in the atmosphere was given which was followed by a short discussion of the radical and the different roles it plays in the different atmospheric layers. The focus was then turned on the mesopause layer of the atmosphere and a distinction was made between OH in the ground state and OH^* in vibrationally excited states in line with the work of Pickett *et al.* (2006). The different behaviour of the radical in these two states was explained. From these discussions two questions emerged.

1)   Why is there an OH^* layer at these particular altitudes?

2)   Why is OH^* such a dominant emitter in the night sky?

Question 1 was answered through consideration of the production and loss terms associated with OH^* and the concentrations of O, O_2 and N_2 within the mesopause. It was shown that OH^* forms within the atomic oxygen layer in which the concentration of O is increasing while the concentration O_2 and N_2 drops at an exponential rate with

atmospheric density. The OH^* is sensitive to O concentrations at the lower boundary and to O_2 and N_2 concentrations at the upper boundary.

Question 2 was answered through detailed consideration of the energetics of the molecule as well as the quantum mechanical selection rules. A description of the determination of the radicals EDMF was provided which was followed by the associated Einstein *A* coefficients. As OH^* has a large dipole moment it was shown that this leads to large radiative transition probabilities accounting for the high levels of emissions.

In the final sections of this chapter investigations of the diurnal, seasonal and global variations are presented which show that the strongest variations in the nocturnal OH^* emissions are attributed to atmospheric tides and in particular the migrating diurnal tide. Both ground based studies (Fritts and Isler, 1994), and satellite observations (Xu *et al.,* 2009) show that these tides are strongest at equinox and weakest at solstice. These studies have also shown that the amplitude of these tides is larger during the vernal equinox than at the autumnal. The strongest features observed in the OH^* emissions therefore follow from diurnal, seasonal and latitudinal variations in the amplitudes of these tides. The tides are capable of strongly modulating the OH^* emission as a direct result of their effect on temperature, atmospheric density, the atomic oxygen mixing ratio and transport within the mesopause region (Ward, 1999; Marsh *et al.,* 2006; Gao *et al.,*2011).

Chapter 4

The One Dimensional (1-D) Model of Vibrationally Excited Hydroxyl

4.1   Introduction

In **Chapter 3** the hydroxyl radical was discussed. This discussion made a distinction between OH and OH^* and was followed by a description of the molecule's energy levels and quantum mechanical selection rules. Details of the history of the EDMF determinations and subsequent inverse radiative lifetimes obtained were provided. The general features of the resulting airglow emissions which this thesis attempts to model were subsequently described.

The 1-D model of vibrationally excited hydroxyl developed as part of this thesis was designed to calculate the concentration of the nine lowest vibrational levels of OH^* within the mesosphere for a given set of geophysical conditions, at a given location, at a given local time. It is similar in many respects to the 1-D models of OH^* previously developed and described in the papers of Makhlouf *et al.* (1995), Pickett *et al.* (2006) and von Savigny *et al.* (2012b) although several differences in the model assumptions, chemical schemes, reaction rates, and initial conditions considered by these models do exist. The reasons for these differences will become clear as the chapter progresses.

In this chapter the 1-D model, which will be referred to as the Maynooth 1-D (M1-D) model, will be described. The results of this model will be compared to results from the Makhlouf model, and the von Savigny model as well as SCIAMACHY and SABER observational data. **Table 4.1** provides a summary, with relevant details, of the 1-D models discussed in this chapter.

Name	Type of Model	Paper	Details
M1-D Model	Photochemical model		Model developed for this thesis.
Makhlouf Model	Photochemical-dynamical model	Makhlouf *et al.* (1995)	Model for investigating OH* response to gravity waves.
McDade Model	Photochemical model	McDade (1991)	Model for investigating altitudinal variations in OH* layers.
von Savigny Model	Photochemical model	von Savigny *et al.* (2012b)	Extension of McDade model.
NRL-CHEM1D Model	Photochemical model	Englert *et al.* (2008)	Investigations of ground state OH.
Caltech 1-D Model	Photochemical model	Pickett *et al.* (2006)	Investigations of ground state OH.

Table 4.1: Summary of 1-D models discussed in this thesis with relevant papers providing descriptions and their objectives in relation to OH.

The vertical range of the model covers 31 levels set at 1 km intervals from $75 - 105$ km. This altitudinal range covers the full extent of the OH* airglow emission layer of interest. Given that this is a relatively narrow range of altitudes it is possible to work with a high model resolution, without the requirements of extensive processing power and time typically necessary for model runs.

Within the M1-D model the concentrations of the nine lowest vibrational states of OH*, OH*$(v \leq 9)$, are calculated by solving the production and loss terms for each individual level. These chemical species all have short lifetimes and undergo chemical, quenching and radiative processes quicker than diffusive processes. Therefore, photochemical equilibrium can be assumed within the model and the concentration of the individual species can be calculated from the production and loss terms alone.

The determination of the concentration of a species in this manner can be described simply by **Equation 4.1**,

$$\frac{\partial N_v}{\partial t} = P_v - L_v N_v$$

<div align="right">(4.1)</div>

where N_v is the concentration of the species in the vth vibrational level. P_v denotes the sum of all production terms and L_v denotes the sum of all loss terms (Dobbin, 2005). This production and loss of OH^* in the different vibrational levels is principally due to the atmospheric photochemistry discussed in **Chapter 3.**

Initial conditions for the model are provided by a number of sources. The start up climatological profiles of the major atmospheric species N_2 and O_2 as well as the atmospheric neutral temperatures are from the Mass Spectrometer and Incoherent Scatter (MSISE-90) empirical model (Hedin, 1991). Initial concentrations for the minor atmospheric species atomic oxygen, O, and atomic hydrogen, H, are also provided by MSIS. The MSISE-90 model was the obvious choice for this data as it provides the concentrations of the majority of precursor species required. More importantly, it provides global coverage of these species at all local times.

Additionally, MSISE-90 provides initial concentrations of the same chemical species to the CMAT2 model and it is this model into which the M1-D model will be incorporated.

The concentrations of ozone, O_3, are obtained directly from the CMAT2 model which uses the UK Universities Global Atmospheric Modelling Programme (UGAMP) Global Ozone Climatology as its source (Dobbin, 2005). While more recent profiles of ozone are available, (for example from the GOMOS instrument onboard the European Space Agency's ENVISAT Satellite), detailed in Bertaux *et al.* (2004) and subsequent works, these profiles have not, at the time of writing, been incorporated into the CMAT2 model. In order to keep the data sets within each model consistent the older ozone profiles are employed. Furthermore, adopting the same profiles allows reasonable predictions of the effectiveness of the M1-D model within CMAT2 to be made.

For comparisons with more recent models, ozone data sets retrieved from the Cospar International Reference Atmosphere (CIRA) Trace Constituent Reference Model (Keating *et al.,* 1996) and SABER instrument will also be employed. In such cases the source of ozone data will be highlighted.

<div align="center">165</div>

4.2   Basic Equations of the M1-D Model

Given the start up concentration profiles described above as initial conditions, the M1-D model can proceed to calculate the concentration of each of the nine lowest vibrational states of OH^*. The production and loss terms for each level are calculated and at each time step the constituent profiles of the minor species are updated. The major atmospheric constituents, O_2 and N_2, are assumed to remain constant. This process is then repeated until the model reaches convergence at all vibrational levels. Convergence can be defined as the point at which the concentration of the vibrational level reaches a steady state.

Assuming that there exists only negligible amounts of OH^* in vibrational levels higher than $OH^*(v = 9)$, it is appropriate to calculate the concentration of this level first. This assumption is reasonable as the 3.49 eV required for production of $OH^*(v = 10)$ is unavailable through the reaction of hydrogen and ozone. Once the population of the ninth level has been determined, the concentration of the subsequent level, $OH^*(v = 8)$, can be calculated and so forth, until the concentrations of all vibrational states, $(v = 1 - 9)$, have been determined.

The population of $OH^*(v = 9)$ is also the easiest to determine as there is only one chemical source of production. Cascade effects from higher vibrational levels augmenting its population through collisional deactivation or radiative emissions need not be considered.

The concentration of $OH^*(v = 9)$ can be determined using

$$n_9 = \frac{P_9}{C_9 + A_9 + L_9}$$

(4.2)

which is an adapted, and simplified, form of the equation presented in Russell and Lowe (2003). n_9 is the population of the $OH^*(v = 9)$, P_9 denotes production into this vibrational level, C_9 is loss of $OH^*(v = 9)$ through collisional deactivation and quenching with O_2, N_2, and O. A_9 is loss by radiative emission and L_9 is loss through chemical reactions, the primary reaction of which is with atomic oxygen.

166

Once the concentration of the $OH^*(v = 9)$ level has been determined it is possible to calculate the population of the next level, $OH^*(v = 8)$ using:

$$n_8 = \frac{P_8 + n_9\left(C_{9,8} + A_{9,8}\right)}{C_8 + A_8 + L_8}.$$

$$(4.3)$$

Equation 4.3 is also adapted, and simplified, from Russell and Lowe (2003) and each symbol has the same meaning as in **Equation 4.2**. The additional production term given by $n_9(C_{9,8} + A_{9,8})$ is production of $OH^*(v = 8)$ via single quantum deactivation of $OH^*(v = 9)$ through collisions with O_2, N_2, and O, and single quantum radiative emission.

Similar equations are developed for each of the lower vibrational levels down to OH in the ground state. The equations for production of $OH^*(v = 5)$ and $OH(v = 0)$ will be discussed here.

$OH^*(v = 5)$ production is given by

$$n_5 = \frac{n_9\left(C_{9,5} + A_{9,5}\right) + n_8\left(C_{8,5} + A_{8,5}\right) + n_7\left(C_{7,5} + A_{7,5}\right) + n_6(C_{6,5} + A_{6,5})}{C_5 + A_5 + L_5}.$$

$$(4.4)$$

In **Equation 4.4** the production term P_v, where v denotes the particular vibrational level, is absent as the reaction of hydrogen and ozone preferentially produces OH^* in the $(v = 9)$ and $(v = 8)$ levels. Smaller amounts are produced in the $(v = 7)$ and $(v = 6)$ levels and there is no significant production of OH^* within lower vibrational levels (Klenerman and Smith, 1987).

It should be noted at this point that the proposed secondary production mechanism of OH^*, given by the reaction of perhydroxyl and oxygen as

$$HO_2 + O \rightarrow OH^*(v \leq 6) + O_2$$

$$(R4.13)\ (from\ Table\ 4.1)$$
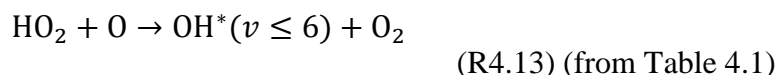
is not considered to be a significant contributing factor to the overall concentrations of OH^*, even in the lower vibrational levels. This reaction has been included in the M1-D model as a source of ground state OH only.

This implies that the production of $\mathrm{OH}^*(v = 5)$, and each subsequent vibrational level $\mathrm{OH}^*(v < 5)$, is entirely attributed to the collisional and radiative transitions originating from the higher vibrational levels falling into the lower vibrational levels. Thus the P_v term disappears from the equations relating to the production of all $\mathrm{OH}^*(v \leq 5)$.

$\mathrm{OH}(v = 0)$, or ground state hydroxyl, production is given by

$$n_0 = \frac{\begin{pmatrix} P_0 + n_9\left(C_{9,0} + A_{9,0}\right) + n_8\left(C_{8,0} + A_{8,0}\right) + n_7\left(C_{7,0} + A_{7,0}\right) \\ + n_6\left(C_{6,0} + A_{6,0}\right) + n_5\left(C_{5,0} + A_{5,0}\right) + n_4\left(C_{4,0} + A_{4,0}\right) \\ + n_3\left(C_{3,0} + A_{3,0}\right) + n_2\left(C_{2,0} + A_{2,0}\right) + n_1\left(C_{1,0} + A_{1,0}\right) \end{pmatrix}}{C_1 + A_1 + L_1}.$$

$$(4.5)$$

Here the production term P_v reappears. This is due to the fact that there are multiple chemical reactions and other processes which produce OH in its ground state within the mesosphere. The majority of these reactions are considered by the M1-D model; however, a small number, for which the overall contribution to OH concentrations is negligible, are ignored.

4.3 Production and Loss Equations of the M1-D Model

The equations described up to this point are relatively simple interpretations of the chemical, radiative, and quenching processes involved in the chemistry of the M1-D model of OH^*. More precise equations for the exact number density of the OH^* vibrational levels calculated by the model are displayed below. In this case the equations for each individual vibrational level are presented in order.

$$[\mathrm{OH}^*(v = 9)] = \frac{b(9)k_1(T)[\mathrm{H}][\mathrm{O}_3]}{\sum_{v'=0}^{8} A_{9,v'} + \sum_{v'=0}^{8} k_2^{9,v'}[\mathrm{O}_2] + k_3^{9,8}[\mathrm{N}_2] + k_4^{9}[\mathrm{O}] + k_5^{9,0}[\mathrm{O}]}$$

$$(4.6)$$

$$[\mathrm{OH}^*(v = 8)] = \frac{b(8)k_1(T)[\mathrm{H}][\mathrm{O}_3] + [\mathrm{OH}^*(v = 9)]\left\{A_{9,8} + k_2^{9,8}[\mathrm{O}_2] + k_3^{9,8}[\mathrm{N}_2]\right\}}{\sum_{v'=0}^{7} A_{8,v'} + \sum_{v'=0}^{7} k_2^{8,v'}[\mathrm{O}_2] + k_3^{8,7}[\mathrm{N}_2] + k_4^{8}[\mathrm{O}] + k_5^{8,0}[\mathrm{O}]}$$

$$(4.7)$$

$$[\text{OH}^*(v=7)]$$
$$= \frac{b(7)k_1(T)[\text{H}][\text{O}_3] + \left\{ \begin{array}{c} \sum_{v=8}^{9} A_{v,7}[\text{OH}^*(v)] + \sum_{v=8}^{9}\left(k_2^{v,7}[\text{O}_2][\text{OH}^*(v)]\right) + \\ \left(k_3^{8,7}[\text{N}_2][\text{OH}^*(v)]\right) \end{array} \right\}}{\sum_{v'=0}^{6} A_{7,v'} + \sum_{v'=0}^{6} k_2^{7,v'}[\text{O}_2] + k_3^{7,6}[\text{N}_2] + k_4^{7}[\text{O}] + +k_5^{7,0}[\text{O}]}$$

$$(4.8)$$

$$[\text{OH}^*(v=6)]$$
$$= \frac{b(6)k_1(T)[\text{H}][\text{O}_3] + \left\{ \begin{array}{c} \sum_{v=7}^{9} A_{v,6}[\text{OH}^*(v)] + \sum_{v=7}^{9}(k_2^{v,6}[\text{O}_2][\text{OH}^*(v)]) + \\ \left(k_3^{7,6}[\text{N}_2][\text{OH}^*(v)]\right) \end{array} \right\}}{\sum_{v'=0}^{5} A_{6,v'} + \sum_{v'=0}^{5} k_2^{6,v'}[\text{O}_2] + k_3^{6,5}[\text{N}_2] + k_4^{6}[\text{O}] + k_5^{6,0}[\text{O}]}$$

$$(4.9)$$

$$[\text{OH}^*(v=5)] = \frac{\left\{ \begin{array}{c} \sum_{v=6}^{9} A_{v,5}[\text{OH}^*(v)] + \sum_{v=6}^{9}(k_2^{v,5}[\text{O}_2][\text{OH}^*(v)]) + \\ \left(k_3^{6,5}[\text{N}_2][\text{OH}^*(v)]\right) \end{array} \right\}}{\sum_{v'=0}^{4} A_{5,v'} + \sum_{v'=0}^{4} k_2^{5,v'}[\text{O}_2] + k_3^{5,4}[\text{N}_2] + k_4^{5}[\text{O}] + k_5^{5,0}[\text{O}]}$$

$$(4.10)$$

$$[\text{OH}^*(v=4)] = \frac{\left\{ \begin{array}{c} \sum_{v=5}^{9} A_{v,4}[\text{OH}^*(v)] + \sum_{v=5}^{9}(k_2^{v,4}[\text{O}_2][\text{OH}^*(v)]) + \\ \left(k_3^{5,4}[\text{N}_2][\text{OH}^*(v)]\right) \end{array} \right\}}{\sum_{v'=0}^{3} A_{4,v'} + \sum_{v'=0}^{3} k_2^{4,v'}[\text{O}_2] + k_3^{4,3}[\text{N}_2] + k_4^{4}[\text{O}] + k_5^{4,0}[\text{O}]}$$

$$(4.11)$$

$$[\text{OH}^*(v=3)] = \frac{\left\{ \begin{array}{c} \sum_{v=4}^{9} A_{v,3}[\text{OH}^*(v)] + \sum_{v=4}^{9}(k_2^{v,3}[\text{O}_2][\text{OH}^*(v)]) + \\ \left(k_3^{4,3}[\text{N}_2][\text{OH}^*(v)]\right) \end{array} \right\}}{\sum_{v'=0}^{2} A_{3,v'} + \sum_{v'=0}^{2} k_2^{3,v'}[\text{O}_2] + k_3^{3,2}[\text{N}_2] + k_4^{3}[\text{O}] + k_5^{3,0}[\text{O}]}$$

$$(4.12)$$

$$[\text{OH}^*(v=2)] = \frac{\left\{ \begin{array}{c} \sum_{v=3}^{9} A_{v,2}[\text{OH}^*(v)] + \sum_{v=3}^{9}\left(k_2^{v,2}[\text{O}_2][\text{OH}^*(v)]\right) + \\ \left(k_3^{3,2}[\text{N}_2][\text{OH}^*(v)]\right) \end{array} \right\}}{\sum_{v'=0}^{1} A_{2,v'} + \sum_{v'=0}^{1} k_2^{2,v'}[\text{O}_2] + k_3^{2,1}[\text{N}_2] + k_4^{2}[\text{O}] + k_5^{2,0}[\text{O}]}$$

$$(4.13)$$

$$[\text{OH}^*(v=1)] = \frac{\left\{ \begin{array}{c} \sum_{v=2}^{9} A_{v,1}[\text{OH}^*(v)] + \sum_{v=2}^{9}(k_2^{v,1}[\text{O}_2][\text{OH}^*(v)]) + \\ \left(k_3^{2,1}[\text{N}_2][\text{OH}^*(v)]\right) \end{array} \right\}}{A_{1,0} + k_2^{1,0}[\text{O}_2] + k_3^{1,0}[\text{N}_2] + k_4^{1}[\text{O}] + k_5^{1,0}[\text{O}]}$$

$$(4.14)$$

$$[\text{OH}(v=0)] = \frac{P_{\text{OH}}}{L_{\text{OH}}} + \frac{\left\{ \begin{array}{c} \sum_{v=1}^{9} A_{v,0}[\text{OH}^*(v)] + \sum_{v=1}^{9}(k_2^{v,0}[\text{O}_2][\text{OH}^*(v)]) + \\ \left(k_3^{1,0}[\text{N}_2][\text{OH}^*(v)]\right) + \sum_{v=1}^{9}(k_5^{v,0}[\text{O}][\text{OH}^*(v)]) \end{array} \right\}}{L_{\text{OH}}}.$$

$$(4.15)$$

Equations 4.6 to **4.15** represent the full extent of the OH^* photochemistry incorporated into the M1-D model. Constituent concentrations are represented in square brackets, e.g. $[\mathrm{OH}^*(v)]$ represents the concentrations of OH^* in the vth level, while the branching ratios of the primary OH^* production reaction are represented by $b(v)$. Reaction rate coefficients are represented by $k_x^{v,v'}(T)$ where k_x represents the reaction rate associated with a particular reaction x, (T) represents any temperature dependent factor related to this reaction rate and v, v' represents any vibrational level dependence factor associated with the de-excitation of OH^* from level v to level v'. The Einstein A coefficients, or inverse radiative lifetimes, associated with radiative emissions are represented by $A_{v,v'}$ where v represents the initial vibrational level and v' represents the final vibrational level into which the OH^* radical has decayed.

The two loss reactions attributed to atomic oxygen account for both chemical loss and quenching loss which are considered separately. $\frac{P_{\mathrm{OH}}}{L_{\mathrm{OH}}}$ in **Equation 4.15** for ground state OH represents production and loss of ground state OH which is not attributed to interactions with OH^*. The chemistry behind these equations is presented in **Table 4.1**.

The following equations represent the production and loss terms of the remaining atmospheric species, including atomic oxygen, ozone, atomic hydrogen, perhydroxyl, and the remaining ground state hydroxyl chemistry, which have been incorporated into the M1-D model i.e. they represent the remaining photochemistry considered. As stated in **Section 4.2** the concentrations of the major atmospheric constituents, molecular nitrogen and molecular oxygen, are assumed to remain constant.

These equations (**Equations 4.16 – 4.20**) have been derived in a similar fashion to the equations governing OH^* photochemistry described previously.

$$[\mathrm{O}] = \frac{1}{\sum_{v=0}^{9} k_4^v [\mathrm{OH}(v)] + k_6(T)[\mathrm{O}_3] + k_7(T)[\mathrm{O}][\mathrm{M}] + k_8(T)[\mathrm{O}_2][\mathrm{M}] + k_9[\mathrm{HO}_2]}$$

$$(4.16)$$

$$[\mathrm{O}_3] = \frac{k_8(T)[\mathrm{O}][\mathrm{O}_2][\mathrm{M}]}{k_1(T)[\mathrm{H}] + k_6(T)[\mathrm{O}] + k_{10}(T)[\mathrm{OH}] + k_{11}(T)[\mathrm{HO}_2]}$$

$$(4.17)$$

$$[\mathrm{H}] = \frac{\sum_{v=0}^{9} k_4^v [\mathrm{OH}(v)][\mathrm{O}]}{k_1(T)[\mathrm{O_3}] + k_{12}(T)[\mathrm{O_2}][\mathrm{M}] + k_{13}[\mathrm{HO_2}]}$$

(4.18)

$$[\mathrm{HO_2}] = \frac{k_{10}(T)[\mathrm{O_3}][\mathrm{OH}] + k_{12}(T)[\mathrm{H}][\mathrm{O_2}][\mathrm{M}]}{k_9[\mathrm{O}] + k_{11}(T)[\mathrm{O_3}] + k_{13}[\mathrm{H}]}$$

(4.19)

$$[\mathrm{OH}(v = 0)] = \frac{k_9[\mathrm{O}][\mathrm{HO_2}] + k_{11}(T)[\mathrm{O_3}][\mathrm{HO_2}] + 2k_{13}[\mathrm{H}][\mathrm{HO_2}] + C_{\mathrm{OH}}}{k_4^0[\mathrm{O}] + k_{10}(T)[\mathrm{O_3}]}.$$

(4.20)

In each of the above equations the symbols have their usual meanings as described previously while C_{OH} represents the contribution to the ground state OH concentrations resulting from the OH^{*} chemistry.

For reference, the combined equation takes the form:

$$[\mathrm{OH}(v = 0)] = \frac{\left\{ \begin{array}{l} \sum_{v=1}^{9} A_{v,0}[\mathrm{OH}^*(v)] + \sum_{v=1}^{9}(k_2^{v,0}[\mathrm{O_2}][\mathrm{OH}^*(v)]) + \\ \sum_{v=1}^{9}(k_3^{v,0}[\mathrm{N_2}][\mathrm{OH}^*(v)]) + \sum_{v=1}^{9}(k_5^{v,0}[\mathrm{O}][\mathrm{OH}^*(v)]) \end{array} \right\}}{k_4^0[\mathrm{O}] + k_{10}[\mathrm{O_3}]}$$
$$+ \frac{k_9[\mathrm{O}][\mathrm{HO_2}] + k_{11}[\mathrm{O_3}][\mathrm{HO_2}] + 2k_{13}[\mathrm{H}][\mathrm{HO_2}]}{k_4^0[\mathrm{O}] + k_{10}[\mathrm{O_3}]}.$$

(4.21)

The full set of reactions governed by these equations is summarised in **Table 4.2** below.

	OH^* Production			**Additional Chemistry**
(R4.1)	$H + O_3 \rightarrow OH^*(v = 6 - 9)$	(R4.7)		$O + O_2 + M \rightarrow O_3 + M$
		(R4.8)		$O + O + M \rightarrow O_2 + M$
	OH^* Loss	(R4.9)		$O + O_3 \rightarrow O_2 + O_2$
(R4.2)	$OH^*(v) + N_2 \rightarrow OH^*(v') + N_2$	(R4.10)		$H + O_2 + M \rightarrow HO_2 + M$
(R4.3)	$OH^*(v) + O_2 \rightarrow OH^*(v') + O_2$	(R4.11)		$H + HO_2 \rightarrow OH + OH$
(R4.4)	$OH^*(v) + O \rightarrow OH^*(v') + O$	(R4.12)		$OH + O_3 \rightarrow HO_2 + O_2$
(R4.5)	$OH^*(v) + O \rightarrow H + O_2$	(R4.13)		$HO_2 + O \rightarrow OH + O_2$
(R4.6)	$OH^*(v) \rightarrow OH^*(v') + hv$	(R4.14)		$HO_2 + O_3 \rightarrow OH + 2O_2$

Table 4.2: Summary of chemical reactions related to OH^* chemistry encoded within the M1-D model.

While the reactions described here in no way give a complete account of the chemistry within the mesopause region, they do take account of the major chemistry required for modelling of OH^*.

A small number of additional reactions have been incorporated into the M1-D model, such as

$$H + HO_2 \rightarrow H_2 + O_2$$

(R4.15)

$$H + HO_2 + H_2O + O.$$

(R4.16)

However, given that these reactions play only a minor role in the chemistry of the mesopause, and that the inclusion of these reactions requires the activation of a further two atmospheric species; namely (H_2) and (H_2O), these reactions are "switched off" within the model.

4.4   Study 1: Initial Testing of the M1-D Model

Upon development of the M1-D model a number of tests were performed to determine how well it compares to other previously developed, and well established, 1-D models. The 1-D kinetic model of Makhlouf *et al.* (1995) was chosen for the initial comparison. This model uses the previously developed model of Winick *et al*. (1985) to determine the initial number density profiles of reactive minor species within the atmosphere. The major species and neutral temperatures are determined from the trace constituent climatological model of Summers (1993). These data are given as input to the 1-D kinetic model which calculates the number densities of the individual vibrational levels of OH^*.

It should be noted that Makhlouf *et al.* (1995) adopt a "fast atomic oxygen quenching rate" of 2.5×10^{-10} cm^3/s for $OH^*(v = 3 - 9)$. Slower rates of 1.05×10^{-10} cm^3/s and 3.9×10^{-11} cm^3/s are adopted for $OH^*(v = 2)$ and $OH^*(v = 1)$ respectively. These quenching rates are attributed to the reaction

$$OH^*(v) + O \rightarrow H + O_2.$$

<div align="right">(R4.5)</div>

Within the M1-D model this reaction describes a chemical loss reaction rather than a quenching loss reaction as ground state OH is not produced. Therefore, there is a significant difference in what this thesis describes as quenching and what is described as quenching in Makhlouf *et al.* (1995). As such, each model utilises "quenching rates with atomic oxygen" which, on comparison, are significantly different from one another.

Reaction R4.5 is included in the M1-D model as a contributor to the chemical loss of OH^*, rather than as loss through quenching, while quenching of OH^* with atomic oxygen is accounted for by the reaction

$$OH^*(v) + O \rightarrow OH(v = 0) + O.$$

<div align="right">(R4.4)</div>
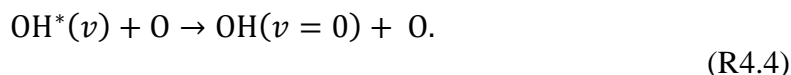
This reaction has a much lower reaction rate of 2.0×10^{-13} cm^3/s (Winick *et al.*, 1983). The above is mentioned so that confusion between what the Makhlouf model describes as "quenching with atomic oxygen" and what the M1-D model describes as

similar quenching can be avoided. The inclusion of this quenching reaction (**Reaction R4.4**) into the M1-D model, a reaction which is not incorporated into the Makhlouf model, is one factor which contributes to a number of differences in the results obtained from both models.

Figure 4.1 shows a digitised version of the results presented in *Figure 4* of Makhlouf *et al.* (1995). The model was run using input profiles generated for local midnight on day 165 of the year (June 14th) and at co-ordinates 30°N, 105.8°W, corresponding to the location of the White Sands Missile Range Tracking Station in Sacramento Peak, New Mexico.

Figure 4.2 shows the concentrations of OH^* generated by the M1-D model for comparison. Initial concentrations of the major species N_2, O_2 and O as well as the minor species H and neutral temperatures were determined from the MSISE-90 database (Hedin, 1991). Initial concentrations for ozone were determined from the CIRA trace constituent reference model (Keating *et al.,* 1996), published at approximately the same date as the Makhlouf *et al.* (1995) paper. Concentrations of OH and HO_2 were determined from the profiles presented in *Figure 2* of Makhlouf *et al.* (1995) as calculated by the model of Winick *et al*. (1985). All profiles were generated for the same time of day (local midnight), same day of the year (day 165), approaching solstice conditions, and at the same location (30°N, 105.8°W) as those employed by the Makhlouf model.

A detailed comparison of the results of the two models follows.
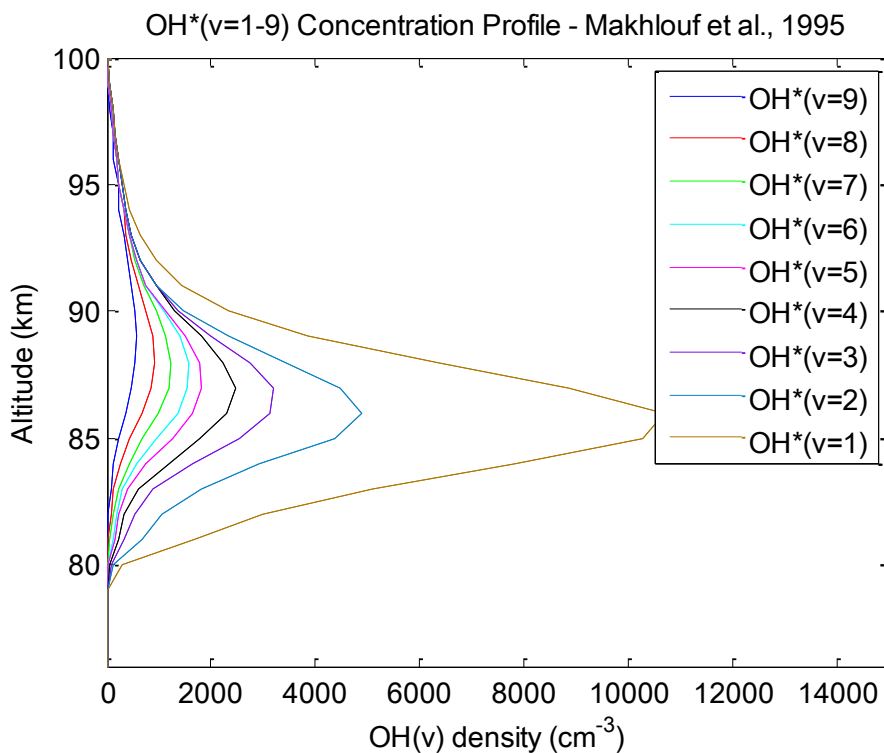
Figure 4.1: Photochemical equilibrium altitude profiles of $\mathrm{OH}^*(v = 1 - 9)$ generated by Makhlouf model using input profiles for day 165, midnight, 30° N (Makhlouf *et al.,* 1995).
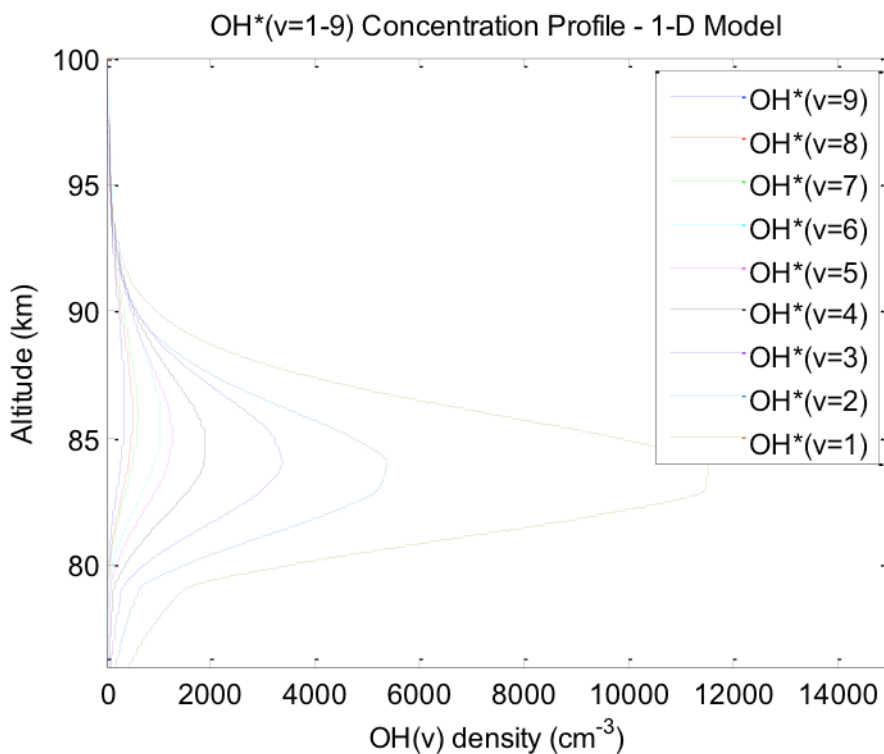
Figure 4.2: Photochemical equilibrium altitude profiles of $\mathrm{OH}^*(v = 1 - 9)$ generated by M1-D model using input profiles for day 165, midnight, 30° N.

It is clear that the profiles generated by the two models are in good general agreement with one another. Both models predict a large increase in OH* concentrations above approximately an altitude of 80 km as well as a sharp decline in the concentrations before reaching an altitude of 90 km. The altitudinal extent of each individual OH* layer predicted by both models is in very close agreement.

The magnitude of the different OH* concentration levels are also in close agreement with one another. However, the M1-D model tends to predict slightly higher concentrations than the Makhlouf model within the lower vibrational levels and slightly lower concentrations than the Makhlouf model within the higher vibrational levels. This can be attributed, at least in part, to differences in the upper level concentrations due to the inclusion of the quenching reaction

$$OH^*(v) + O \rightarrow OH(v = 0) + O$$
$$\text{(R4.4)}$$
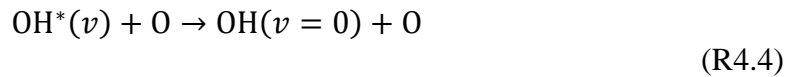
which, as mentioned previously, is not incorporated into the model of Makhlouf. As a chemical quenching reaction this has the effect of decreasing the amount of OH*.

Differences in the concentrations of the lower vibrational levels can be attributed to differences in the initial atomic oxygen concentration profiles used by both models. Between 80 and 85 km the Makhlouf model uses atomic oxygen concentrations slightly lower than those used by the M1-D model. This results in reduced production of OH* at these altitudes decreasing the overall concentrations. The difference in the atomic oxygen concentration increases to a full order of magnitude below 80 km and to four orders of magnitude by 75 km significantly hampering any OH* production at these altitudes.

A small amount of OH* is produced by the Makhlouf model through the inclusion of the reaction

$$HO_2 + O \rightarrow OH^*(v \leq 6) + O_2$$
$$\text{(R4.13)}$$
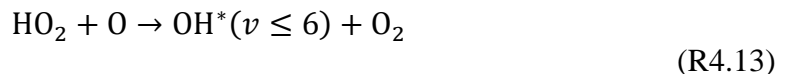
as a secondary source of OH* production. However, on the basis of M1-D model calculations this reaction is not required as an additional source of OH*, even at low

vibrational levels, as significantly more low-level OH^* can result from cascade reactions and collisions involving the higher vibrational levels transitioning downwards.

A key difference between the two generated profile sets is the difference in the heights of the peak concentrations of each vibrational level. This arises despite the fact that the OH^* layers predicted by both models have similar depth. **Figure 4.1** shows that for $OH^*(v = 9)$ the Makhlouf model predicts a peak height of approximately 89 km. The peak height subsequently drops by approximately 0.5 km for each subsequent vibrational level. This leads to successive peaks, at half km intervals, between approximately 85 km and 89 km. The M1-D model predicts a peak height of approximately 87 km for $OH^*(v = 9)$ with a similar decrease of 0.5 km for successive vibrational level peaks, between altitudes of approximately 83 km and 87 km. The results from both models are therefore in close agreement with SCIAMACHY observations and model predictions of von Savigny *et al.* (2012b) which revealed similar altitudinal distributions in OH^* peak heights and are discussed in more detail in **Section 4.6**.

Given that the majority of the initial concentration profiles within the above comparison are obtained from alternate sources, differences in the results such as those described are expected. This provides the opportunity to investigate what effect incorporating the individual constituent profiles from the Makhlouf model into the M1-D model has on the model results in relation to OH^*.

4.5 Study 2: M1-D Model Sensitivity to Initial Conditions

4.5.1 Atomic Oxygen

It was originally thought that the difference in the peak heights observed in the results of both models could be explained by the inclusion of the new quenching reaction (**R4.4**) with atomic oxygen. Given that the concentration of atomic oxygen increases over this particular altitude range, it appeared reasonable to assume that this would lead to significantly more quenching at higher altitudes rather than at lower altitudes, thereby decreasing the concentration of OH^* at higher altitudes and forcing the peak in the layer to occur at lower altitudes.

However, removing the reaction from the model resulted in only a marginal difference in the OH^* concentrations predicted for all vibrational levels as well as a negligible difference in the peak concentration heights. Thus, further investigations were carried out to determine the root cause of the differences between the peak heights obtained from the two models.

Figure 4.3 shows a comparison of the $OH(v = 8)$ profiles obtained from the Makhlouf model and two different profiles generated by the M1-D model. In the first profile (solid line) the atomic oxygen profile from the MSISE-90 database was used as in **Figure 4.2.**. In the second profile (dashed line) the corresponding atomic oxygen profile from **Figure 2** of Makhlouf *et al*. (1995) was used as input in the model run. The $OH(v = 8)$ profile generated by the Makhlouf model is also displayed (dotted line).
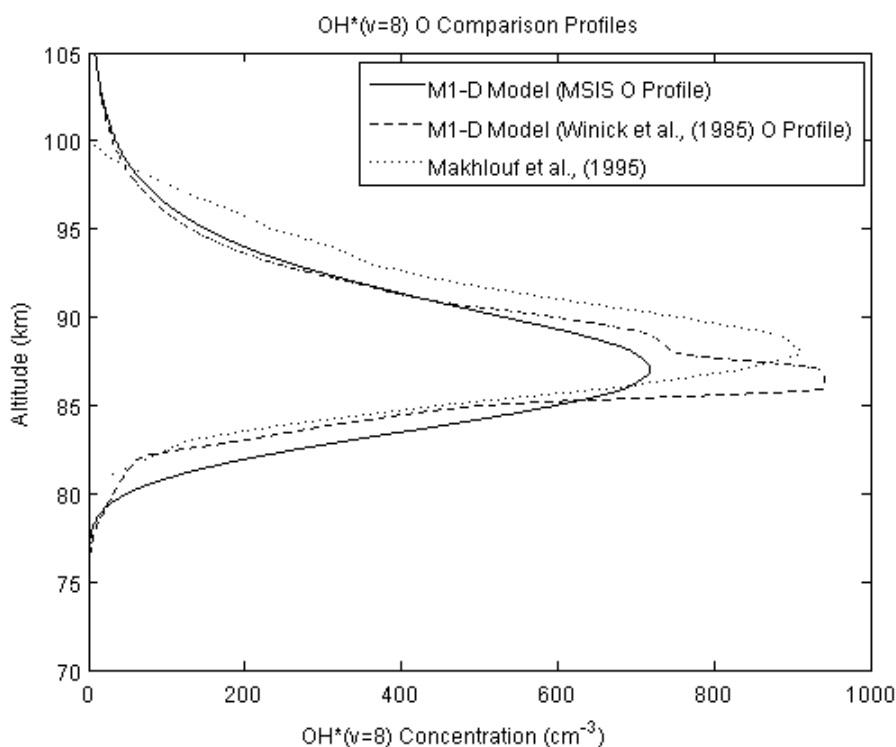
Figure 4.3: M1-D model altitude profiles of $OH^*(v = 8)$ using MSISE-90 O profile (solid line), Winick *et al.* (1985) O profile (dashed line), with Makhlouf model altitude profile (dotted line).

It can be seen that the modified oxygen profile allows for the prediction of concentrations that are in better agreement with the Makhlouf model. However, it does not change the altitude of the peak concentration by an appreciable amount and the peak heights remain approximately 2 km apart. Similar profiles were generated for the

remaining vibrational levels and this trend is consistent. Better agreement between the model results is achieved using the modified atomic oxygen profile with regards to OH* concentrations; however, only negligible changes to the heights of each vibrational level are observed. Based on these data it was concluded that the atomic oxygen profile plays a substantial role in determining the concentrations within the OH* layers although it has less influence on the determination of the peak heights within the individual layers. This is investigated further in **Section 4.6**.

4.5.2   Ozone

Figure 4.4 shows the results of an investigation into the variation in the $OH(v = 8)$ profile when the ozone profile of Winick *et al.* (1985) is adopted as opposed to the original profile obtained from CIRA (Keating *et al.,* 1996).
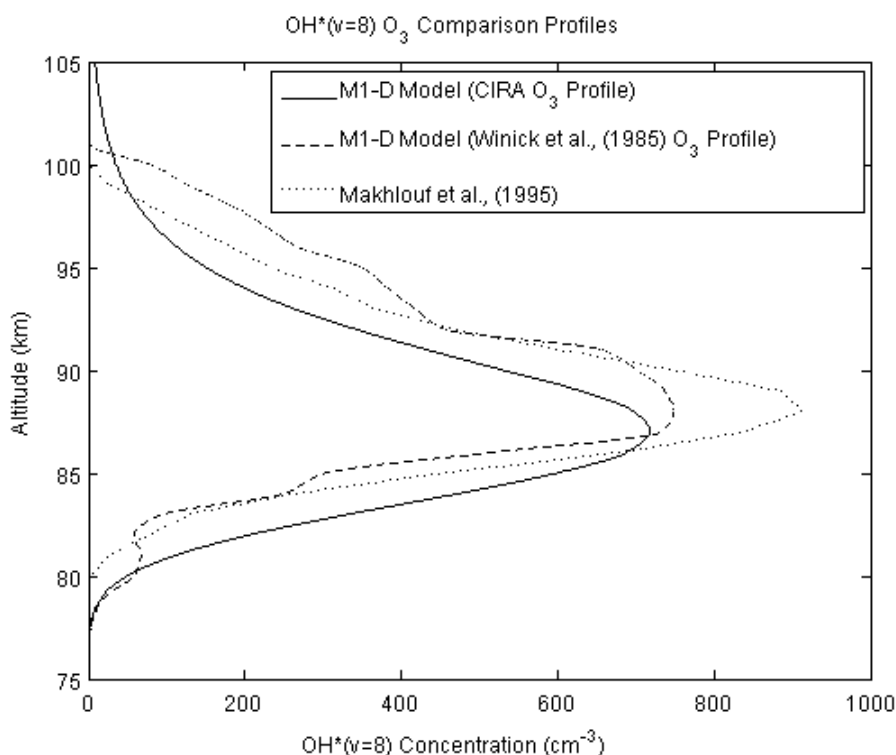
Figure 4.4: M1-D model altitude profiles of $OH^*(v = 8)$ using CIRA O_3 profile (solid line), Winick *et al.* (1985) O_3 profile (dashed line), with Makhlouf model altitude profile (dotted line).

In this case the $OH^*(v = 8)$ layer has ascended by approximately 1 km, bringing it into better agreement with the peak height predicted by the Makhlouf model. However, the peak concentration has not changed significantly, except at heights above 92 km where

there is a clear increase. Again this trend is repeated for each of the vibrational layers, with each exhibiting an upward shift of approximately 1 km in the peak concentration altitude and a slight increase in concentration.

In each case there is also a significant increase in the concentration of OH^* above altitudes of 92 km. These unexpected increases in concentrations may be the result of inaccuracies in determining the exact values of ozone concentrations presented in Makhlouf *et al.* (1995). Given the relatively high concentrations of ozone, when compared to other minor chemical species, and the log scale employed, it was naturally more difficult to determine exact values for the concentration. Repeated attempts to achieve more accurate values eventually led to only marginal differences in the results displayed in **Figure 4.4**.

4.5.3 Atomic Oxygen and Ozone Combined Variation

Figure 4.5 shows the M1-D model results when both the altered atomic oxygen and ozone profiles have been used as initial input. Results from the Makhlouf model are also displayed.
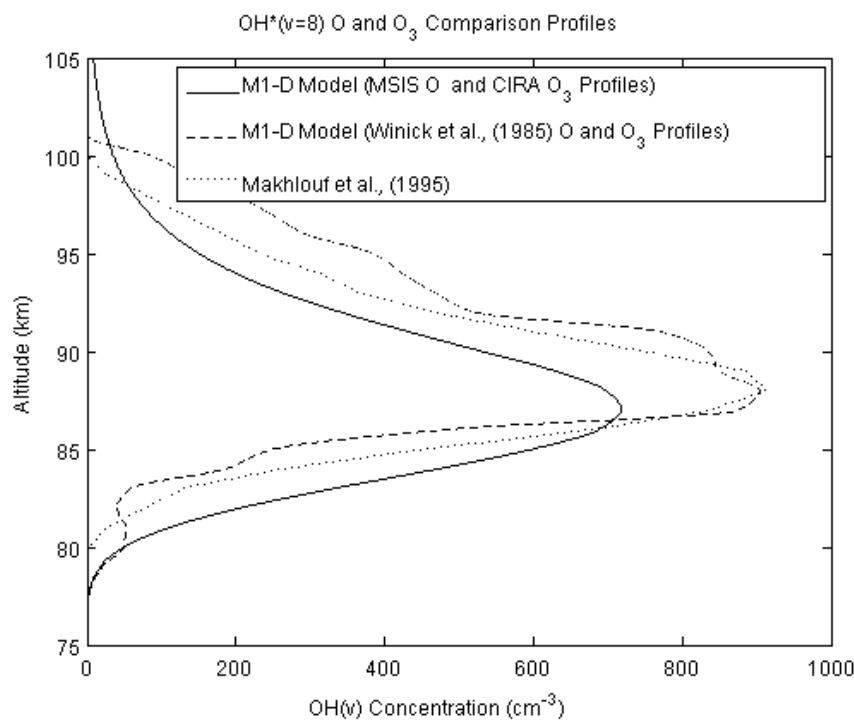
Figure 4.5: M1-D model altitude profiles of $OH^*(v = 8)$ using MSISE-90 O profile and CIRA O_3 profile (solid line), Winick *et al.* (1985) O and O_3 profile (dashed line), with Makhlouf model altitude profile (dotted line).

Both the concentration and peak height of the layer predicted are now in much better agreement with the Makhlouf model. However, the somewhat large increase in the concentration of OH^* above 92 km remains. The concentration peak height remains approximately 1 km lower than that produced by the Maklouf model; while the concentrations below altitudes of approximately 92 km are almost identical.

The concentration of the layer is in much better agreement than in the previous figures and the increase in OH^* concentrations above 92 km has been partially ameliorated. The remaining discrepancies in the results from both models can be attributed to the slightly different chemical routines and reaction rates that both models employ. Given the levels of uncertainty in the initial conditions it is reasonable to conclude that the M1-D model can produce results that are in very good agreement with the Makhlouf model.

4.6   Study 3: M1-D Model Comparison with SCIAMACHY observations and 1-D model of von Savigny *et al.* (2012b)

Studies 1 and **2** in this chapter compare the M1-D model results to the well established model of Makhlouf *et al.* (1995) in respect of OH^* concentrations. The effects of varying the initial conditions of the M1-D model were also investigated and it was shown that with similar initial conditions the M1-D model could effectively reproduce the Makhlouf model results.

The following study focuses on the altitudinal distribution of the OH^* layers. The model results are compared to the more recent 1-D model of von Savigny *et al.* (2012b), which is an extended version of the 1-D model described in McDade (1991). Observational data from the SCIAMACHY instrument on board the ESA's ENVISAT is also used for this comparison. As this study focuses on altitudinal variations, the results of the model runs are normalised with respect to the peak emission rates, as are the observed SCIAMACHY profiles. This enhances the visual impact of altitudinal variations that may not be readily apparent in **Studies 1** and **2**. Further verification of OH^* concentrations will be the subject of **Study 4** in **Section 4.7**.

Figure 4.6 shows normalised monthly and zonally averaged volume emission rate profiles from the $OH^*(3-1)$, $OH^*(6-2)$ and $OH^*(8-3)$ bands measured by the

SCIAMACHY instrument during July 2005. The data are binned into 10° latitude bins between 30° S and 10° N. The local time of the measurements is approximately 22 hours.
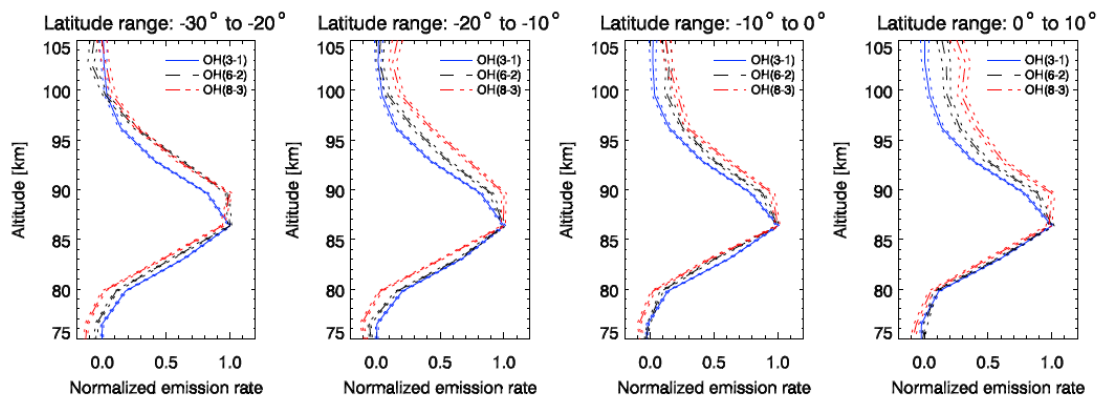
Figure 4.6: Normalised monthly and zonally averaged volume emission rate profiles for the OH*$(3-1)$, OH*$(6-2)$ and OH*$(8-3)$ bands for 10° latitude bins between 30° S and 10° N for July 2005. Dotted lines represent retrieval error based on the standard error of the inverted limb-radiance profiles (von Savigny *et al.* 2012b).

It can be seen that an altitudinal shift exists between the three emission bands in each of the latitudinal bands observed. The peak in the OH*$(8-3)$ emission occurs at the highest altitude while the OH*$(3-1)$ emission occurs at the lowest altitude. The OH*$(6-2)$ emission peaks at an altitude between the other two. In each of the profiles the altitudinal shift between the OH*$(8-3)$ and OH*$(3-1)$ bands is approximately $3-4$ km and occurs between altitudes of $85-90$ km. However, the exact peak height cannot be determined using SCIAMACHY data because of its 2.8 km vertical field of view and 3.3 km tangent height sampling (von Savigny *et al.* 2012b).

These profiles will now be compared to the results from the model of von Savigny *et al.* (2012b) and the M1-D model. Initial concentration profiles for the atmospheric species employed by both models are representative of conditions for July 2005 at 22 hours local time and are obtained primarily from the MSISE-90 empirical model (Hedin, 1991).

Figure 4.7 (left panel) shows the fractional population of OH*$(v = 1 - 9)$ as a function of altitude calculated by the model of von Savigny *et al.* (2012b). The right panel shows the normalised emission rate profiles for the same vibrational levels. The

calculations are based on the assumptions that OH^* emissions follow a Gaussian altitude profile with a mean peak altitude of 87 km and a FWHM of 8 km. More details of the calculations are provided in von Savigny *et al.* (2012b). **Figure 4.8** (left panel) shows the same fractional population calculated by the M1-D model directly from the incorporated chemistry. The right panel shows the associated relative emission rates.
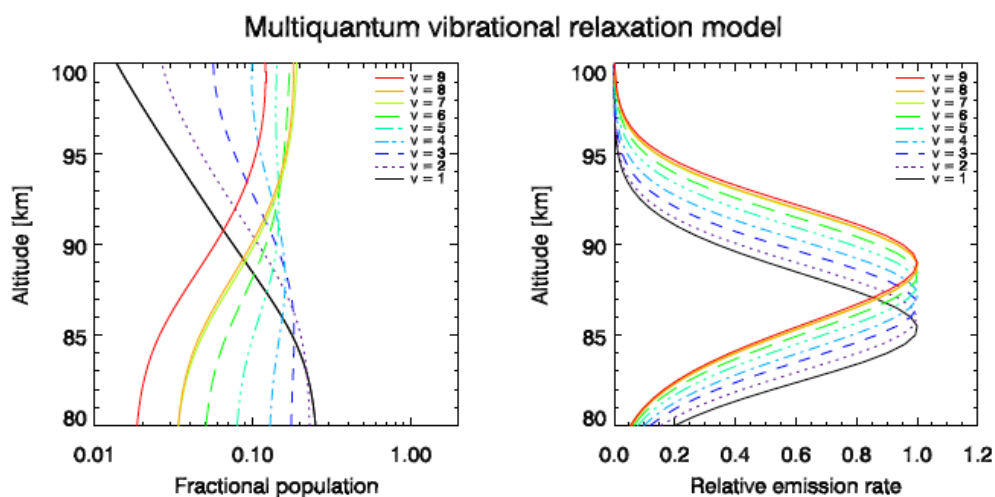
Figure 4.7: (Left panel): Fractional populations of $OH^*(v = 1 - 9)$ for July 2005 as a function of altitude based on model of von Savigny *et al.* (2012b). (Right panel): Normalised emission rate profiles for $OH^*(v = 1 - 9)$ calculated by same model.
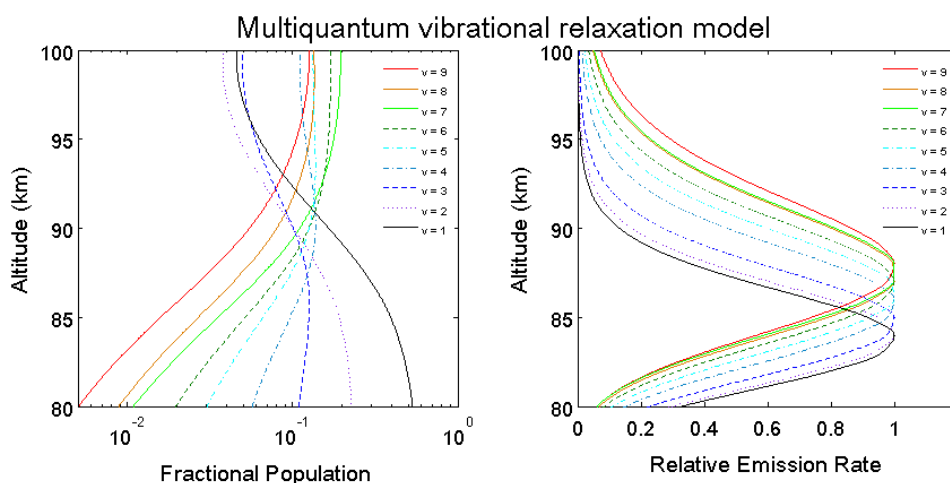
Figure 4.8: (Left panel): Fractional populations of $OH^*(v = 1 - 9)$ for July 2005 as a function of altitude based on the M1-D model (Right panel): Normalised emission rate profiles for $OH^*(v = 1 - 9)$ calculated by same model.

It can be seen that the fractional population distribution of both models is somewhat different; however, the trend produced by both models is quite similar. In both cases

the upper vibrational levels increase their fractional population with increasing altitude while the fractional population of the lower vibrational levels decreases with increasing altitude. Differences in the overall magnitude occur primarily at the upper and lower boundaries of the emission layer and are not unexpected given the different methods used by both models to calculate OH^* emission rates. Of greater importance in this comparison is the altitudinal distribution calculated by both models which can be seen to be almost identical.

The results of both models show a clear altitudinal variation in the emission peaks calculated. Emissions from the higher vibrational levels occur at higher altitudes than the lower vibrational levels. This is accord with the SCIAMACHY observations. The altitudinal variation between the $\mathrm{OH}^*(v=9)$ and $\mathrm{OH}^*(v=1)$ levels predicted by von Savigny *et al.,* (2012b) is approximately $4\,\mathrm{km}$, between $85-89\,\mathrm{km}$, leading to an average peak altitude difference of about $0.5\,\mathrm{km}$ between consecutive OH^* levels. The M1-D model predicts a similar altitudinal variation of $4\,\mathrm{km}$, between $84-88\,\mathrm{km}$, and thereby the same average altitudinal difference of $0.5\,\mathrm{km}$ between consecutive emission layers also in agreement with SCIAMACHY observations. The difference in the altitudinal range produced by both models can be attributed to the assumption of von Savigny *et al.* (2012b) that the average peak emission height occurs at 87 km while the M1-D model predicts this to occur at 86 km. Therefore, it can be seen that both models produce similar altitudinal variations which compare well with SCIAMACHY observations.

In order to further test the M1-D model capabilities, results from both models are presented when the chemical schemes are altered to eliminate quenching by O as a sink of OH^*. **Figure 4.9** shows the model results from von Savigny *et al.* (2012b) when this quenching has been eliminated. **Figure 4.10** shows the results of the M1-D model under the same conditions.
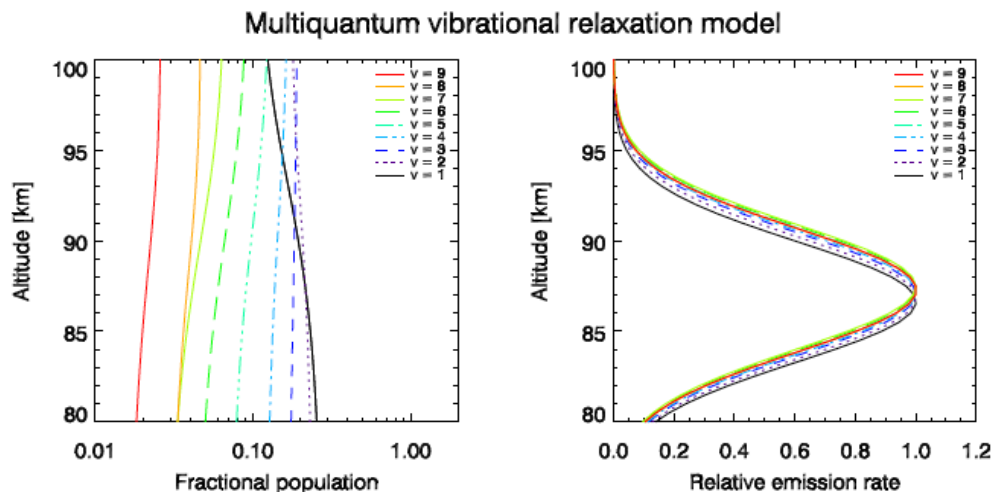
Figure 4.9: (Left panel): Fractional populations of $OH^*(v = 1 - 9)$ for July 2005 as a function of altitude when quenching by O has been neglected, based on model of von Savigny *et al.* (2012b). (Right panel): Normalised emission rate profiles for $OH^*(v = 1 - 9)$ calculated by same model.
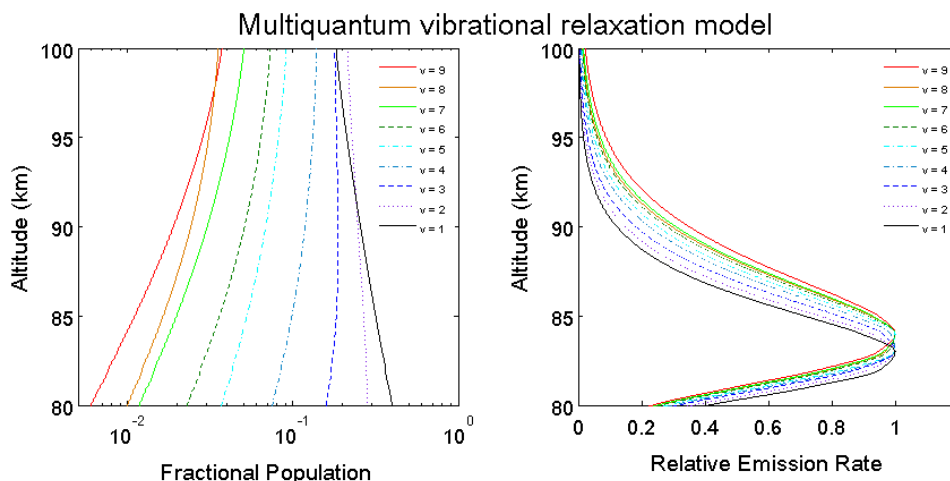
Figure 4.10: (Left panel): Fractional populations of $OH^*(v = 1 - 9)$ for July 2005 as a function of altitude when quenching by O has been neglected, based on M1-D model. (Right panel): Normalised emission rate profiles for $OH^*(v = 1 - 9)$ calculated by same model.

Again it can be seen that the fractional populations produced by both models are different although the trends in the altitudinal variations agree. Vibrational levels $v = 3 - 9$ increase their fractional population over the altitude range while the fractional population of vibrational levels $v = 1, 2$ decreases. This result is produced by both models.

The altitudinal range of the peak emission heights produced by both models can also be seen to be significantly reduced now that quenching by atomic oxygen has been eliminated. Therefore, in line with the results of previously developed models and direct observations of emission layer peak altitudes, the M1-D offers further verification that quenching by atomic oxygen is necessary to reproduce an accurate emission peak altitudinal variation with vibrational level.

Further comparison of the results of both models shows that while the altitudinal range of the emission peaks has been reduced, the M1-D produces an altitudinal variation of approximately 2 km while von Savigny *et al.* (2012b) produces a variation of approximately only 1 km. There is also a significant variation between the average peak height of the emission layers produced by both models. The model of von Savigny produces an average peak emission height of 87 km, as expected based on the model assumptions, while the average peak height of the M1-D model has dropped from 86 km to 83 km.

Given that the OH* emission layer is highly sensitive to variations in [O] at the lower boundary and $[M]^2$ at the upper boundary (Marsh *et al.,* 2006), a drop in average peak emission altitudes is not unexpected. By eliminating quenching by atomic oxygen from the model chemistry more oxygen becomes available for the production of O_3 and hence OH*. The effect of this is more pronounced at lower altitudes, where the concentration of O is increasing, than at upper altitudes where decreasing concentrations of M counteract the effect. The overall result is more OH* production at lower altitudes which reduces the peak emission altitude. This feature of OH* emissions cannot be observed in the model of von Savigny *et al.* (2012b) because it assumes that the mean peak altitude of the emission layer occurs at 87 km.

Figure 4.11 shows the results from the model of von Savigny *et al.* (2012b) when quenching by atomic oxygen has been reintroduced. However, the O quenching rate constant of Smith *et al.* (2010) has been adopted with a correction factor from Xu *et al.* (2012) instead of the rate constant of Alder-Golden (1997) previously employed. Adjusted O_2 quenching rates from Xu *et al.* (2012) have also been adopted. **Figure 4.12** shows model results from the M1-D model after the same alterations to the quenching rates have been adopted.
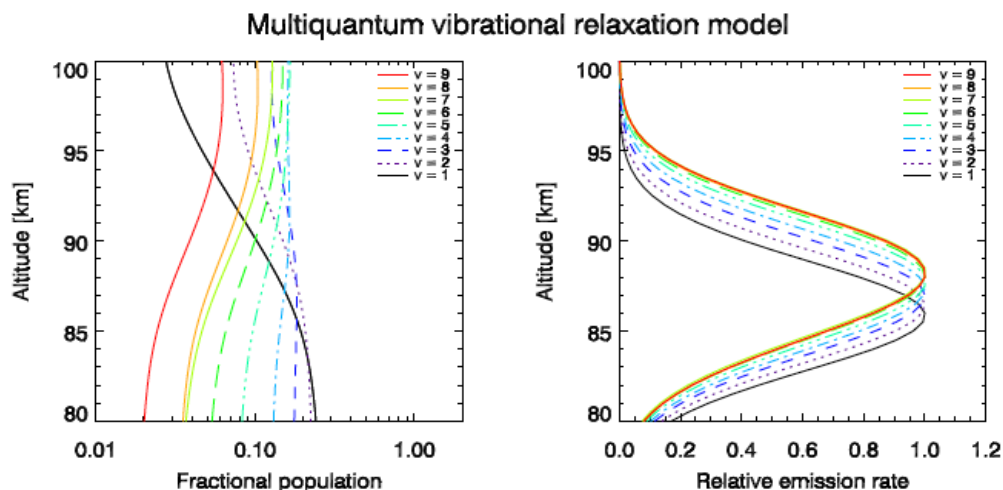
Figure 4.11: (Left panel): Fractional populations of $OH^*(v = 1 - 9)$ for July 2005 as a function of altitude when O quenching constant is taken from Smith *et al.* (2010) in combination with a 1.293 correction factor from Xu *et al.* (2012), based on model of von Savigny *et al.* (2012b). (Right panel): Normalised emission rate profiles for $OH^*(v = 1 - 9)$ calculated by same model.
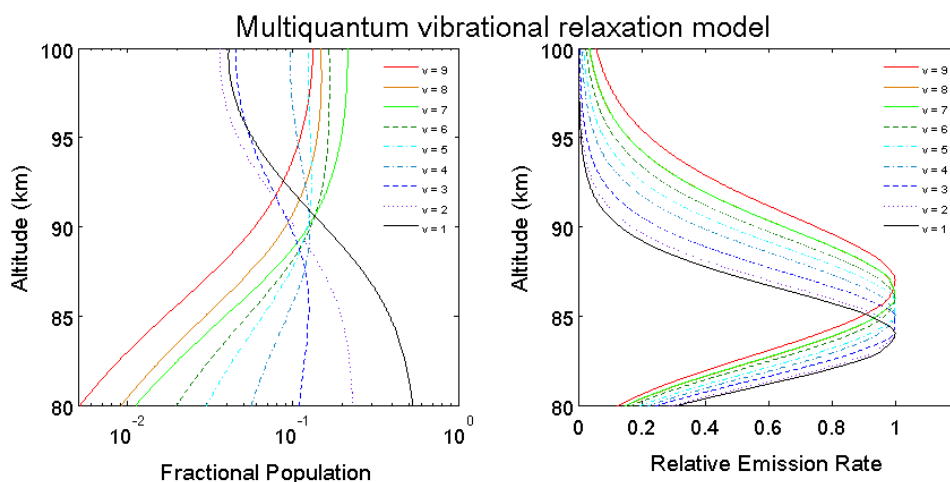
Figure 4.12: (Left panel): Fractional populations of $OH^*(v = 1 - 9)$ for July 2005 as a function of altitude when O quenching constant is taken from Smith *et al.* (2010) in combination with a 1.293 correction factor from Xu *et al.* (2012), based on M1-D model. (Right panel): Normalised emission rate profiles for $OH^*(v = 1 - 9)$ calculated by same model.

In both figures many of the features observed in **Figures 4.8** and **4.9** have been restored. The fractional populations produced by both models are still dissimilar at the layer boundaries although the trends in the populations are the same. Both models show a clear increase in the fractional population of the upper vibrational levels with increasing

altitude while the lower vibrational levels show a decreasing fractional population over the same range.

The altitudinal range of the peak emission heights has also been restored although not to the same extent. The model of von Savigny *et al.* (2012b) now shows an altitude variation of only 3 km surrounding the expected 87 km assumed mean altitude, while the M1-D model shows a 3 km variation centred on a mean altitude of approximately 85.5 km.

The restored features can be attributed almost entirely to the reintroduction of quenching by atomic oxygen since the adjusted O_2 quenching rates produced only minor changes in the results from both models.

In a final comparison with the model of von Savigny *et al.* (2012b) the sensitivity of the M1-D model results to changes in the atomic oxygen concentration profiles are examined. **Figure 4.13** shows results from the von Savigny model when the atomic oxygen concentrations have been scaled by factors of 0.5, 1.0, 5.0 and 10.0 respectively. Note that these scaling factors are substantially larger than variations in O concentrations explored in **Section 4.5.1** and **4.5.3**. **Figure 4.14** shows the M1-D model results using the same scaling factors.
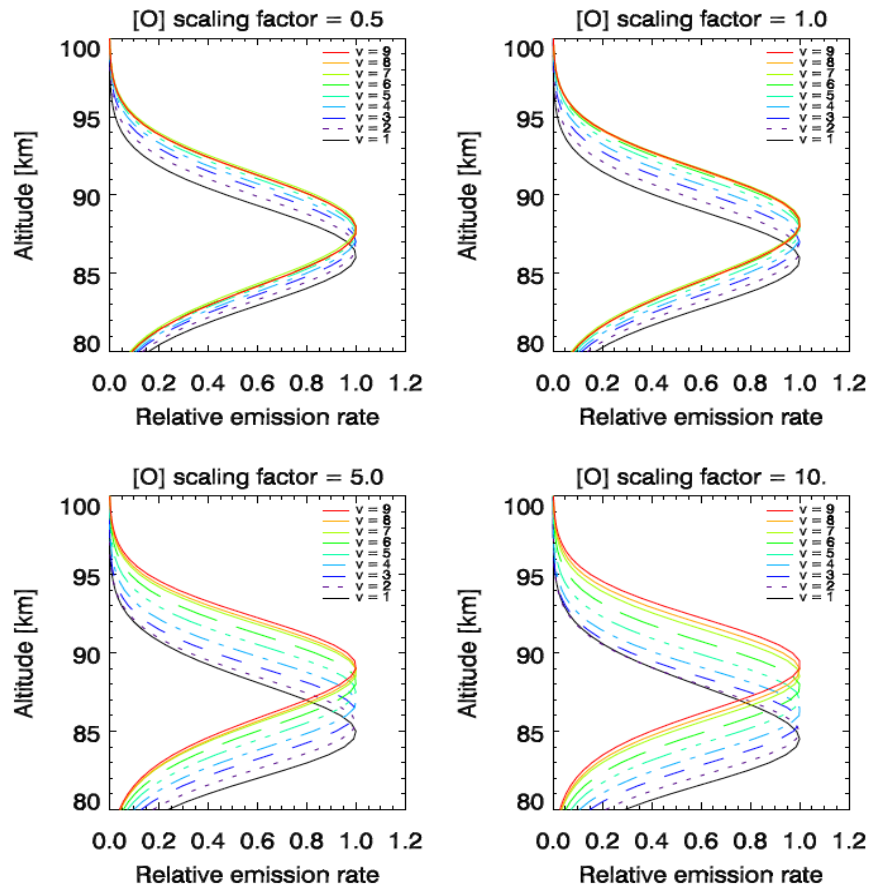
Figure 4.13: Sensitivity of the von Savigny *et al.* (2012b) modelled emission rate profiles to atomic oxygen concentrations. The standard MSISE-90 atomic oxygen profile is scaled with constant factors varying between $0.5 - 10.0$. Rate constants for quenching by atomic oxygen and molecular oxygen are corrected values from Xu *et al.* (2012).
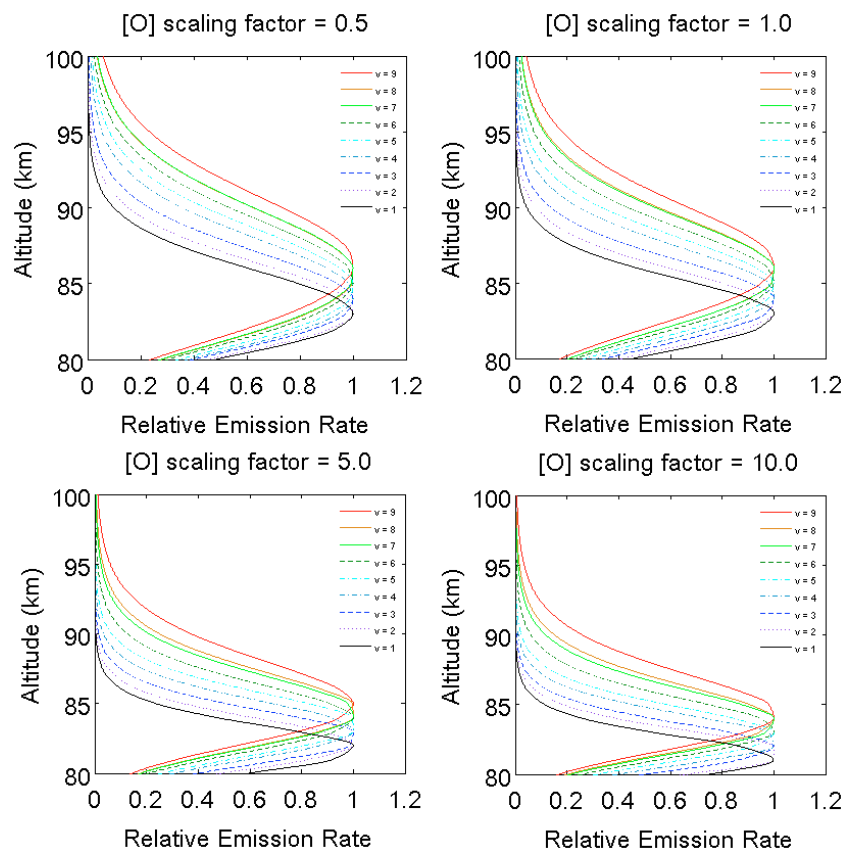
Figure 4.14: Sensitivity of the M1-D modelled emission rate profiles to atomic oxygen concentrations. The standard MSISE-90 atomic oxygen profile is scaled with constant factors varying between $0.5 - 10.0$. Rate constants for quenching by atomic oxygen and molecular oxygen are corrected value from Xu *et al.* (2012).

Figure 4.13 shows that the model of von Savigny produces a significant increase in the emission peak altitude range with increasing atomic oxygen concentrations. However, the M1-D model produces a small decrease in the same emission peak altitude range while the average peak height of the layers also drops in altitude from $85 - 83$ km in **Figure 4.14**.

The sinking of the mean peak altitude within the M1-D model results can once again be attributed to the sensitivity of the lower boundary of the emission layers to changes in atomic oxygen. Increasing the concentration of O over this altitude range results in more O_3 production and hence more OH^*. However, the effect of this is counteracted by the decreasing concentrations of O_2 and N_2 with increasing altitude. Thus more production of OH^* occurs at lower altitudes reducing the peak altitude of the emissions.

Increasing O concentrations further augments the amount of O available for quenching. Below altitudes of 85 km this is a relatively inefficient process (von Savigny *et al.* 2012b) as the concentration of O is still quite low. However, at altitudes above 85 km increasing the concentration of O results in significantly increased quenching by atomic oxygen. This can reduce the emission rates causing a further drop in the altitude of the emission layers.

The difference between the results obtained by both models would appear to arise from the assumption made in von Savigny *et al.* (2012b) that the average peak emission height is confined to an altitude of 87 km. Fixing the peak altitude to 87 km introduces an artificial constraint in the von Savigny model. For example, the concentrations of O_2 and N_2 decrease by approximately 50% between altitudes of 83 and 87 km. Therefore, the values obtained by both models for both single and multiquantum collisions with O_2 and N_2 will be significantly different as a result of this exponential decline in concentrations.

Despite the differences in the modelled results presented in this section it should be remembered that using atmospheric concentration profiles which have been unaltered, and are therefore considered representative of atmospheric conditions, both models produce very similar results which compare favourably to SCIAMACHY measurements.

4.7 Study 4: M1-D Model Sensitivity to Temporal and Spatial Variations

Given the success of the M1-D results thus far, the model was applied to different co-ordinates on the globe, at different times of day, and during different times of year as part of a more extensive test into its ability to predict reasonable concentrations of OH*. The model results were subsequently examined spatially, to determine latitudinal and longitudinal variations, and temporally, to examine variations in both local time and time of year.

Since Makhlouf *et al.* (1995) provides data for only one location and at one time of year, comparisons between these two models were no longer feasible. Furthermore, SCIAMACHY data is limited to low latitudinal regions. However, given the significant

number of publications on OH* emissions and concentrations in recent years, derived from measurements obtained by such instruments as NASA's SABER instrument onboard the TIMED satellite, a wealth of recent observational data is available for comparison.

At this point it should be noted that MSISE-90 profiles for the concentrations of the chemical species O and H are readopted as initial conditions for the M1-D model. Concentrations of O$_3$ and of ground state OH and HO$_2$ are taken directly from the CMAT2 model.

In the following section, profiles of the different vibrational levels, at different locations on the globe, and at different local times are examined. These profiles are produced at three different latitudes, 40°N, 0° and 40°S, for equinox conditions on day 80 of 2003 and allow for changes in the altitudinal and latitudinal distribution of OH* concentrations at this particular time of year to be investigated. The model predictions are compared to profiles derived from direct measurements of OH* emissions made by the SABER instrument onboard the TIMED satellite.

An extensive study in determining OH* concentrations and emission levels from SABER data was conducted by Xu *et al.* (2012). In this study version 1.07 data from the SABER instrument was used to determine temperature and ozone profiles while "unfiltered" 2.0 μm and 1.6 μm airglow emission profiles were used to determine OH* concentrations.

The "unfiltering" of the data was performed as the filter used to measure the Meinel bands onboard SABER is not perfect in a number of ways. Firstly, it does not include all emission lines and secondly the response of the filter is only in the range of 80-100% over the width of the band. More details of the filters limitations can be found in Mlynczak *et al.* (2005) while a detailed description of the unfiltering process can be found in Xu *et al.* (2012). Using this SABER data Xu *et al.* (2012) produced longitudinally averaged night-time OH* profiles over latitude bands 20° wide with which the results of the M1-D model are compared.

4.7.1 Latitudinal Variations at Equinox Conditions

In the first case study Xu *et al.* (2012) presents data from day 80, 2003 corresponding to equinox conditions over three latitude bands centred at 40°N, 0° and 40°S. The profiles produced are for three local times of 0300 hrs, 0130 hrs and 0100 hrs.

In this section a detailed comparison of the M1-D modelled concentrations and the concentrations derived from the SABER measurements are presented. In the first case a comparison at equinox conditions (day 80 of 2003) is made at three separate latitude bands (40°N, 0° and 40°S). This comparison is carried out for two separate vibrational levels $OH^*(v = 8)$ and $OH^*(v = 4)$. These two vibrational levels were selected for the comparison so that data from the two separate channels onboard SABER dedicated to observing OH^* emissions are employed.

4.7.1.1 High Vibrational Levels

Figure 4.15, 4.16 and **4.17,** present M1-D model predictions of the concentrations of $OH(v = 8)$ at local times 0300 hrs, 0130 hrs and 0100 hours respectively.
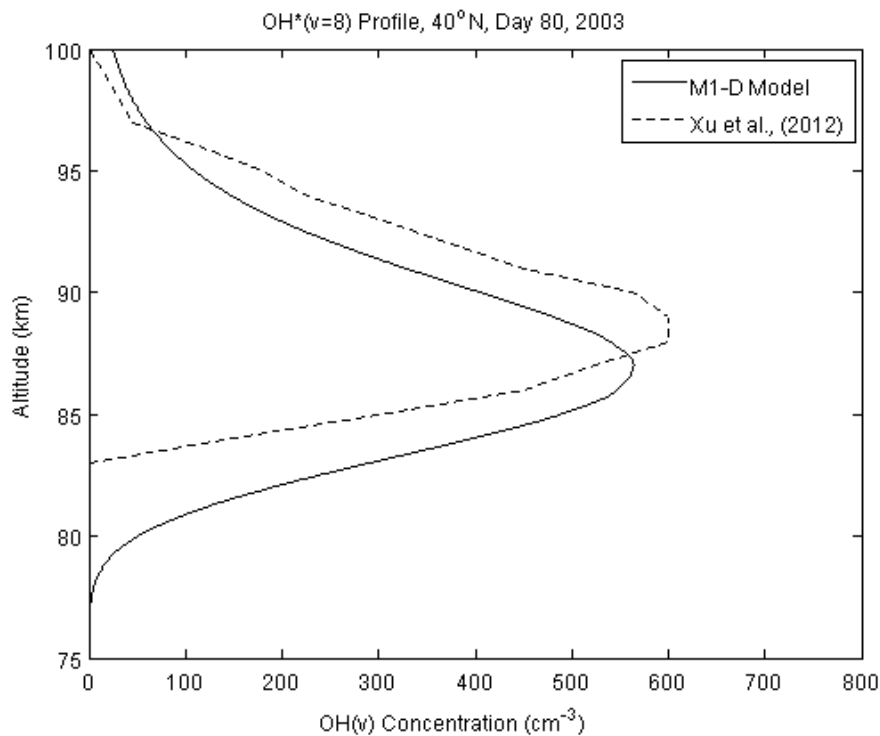
Figure 4.15: Altitudinal profile of $OH^*(v = 8)$ at $40°$ N for day 80 of 2003 at 0300 local time calculated by M1-D model (solid line) and measured by SABER instrument (dashed line) presented in Xu *et al.* (2012).
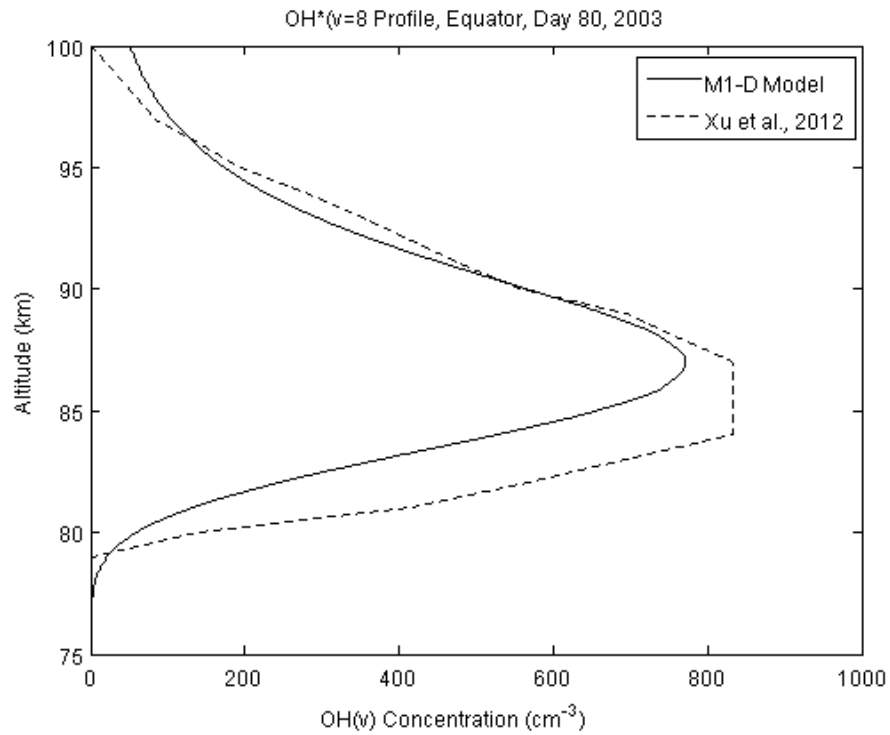
Figure 4.16 Altitudinal profile of $OH^*(v = 8)$ at equator for day 80 of 2003 at 0130 local time calculated by M1-D model (solid line) and measured by SABER instrument (dashed line) presented in Xu *et al.* (2012).
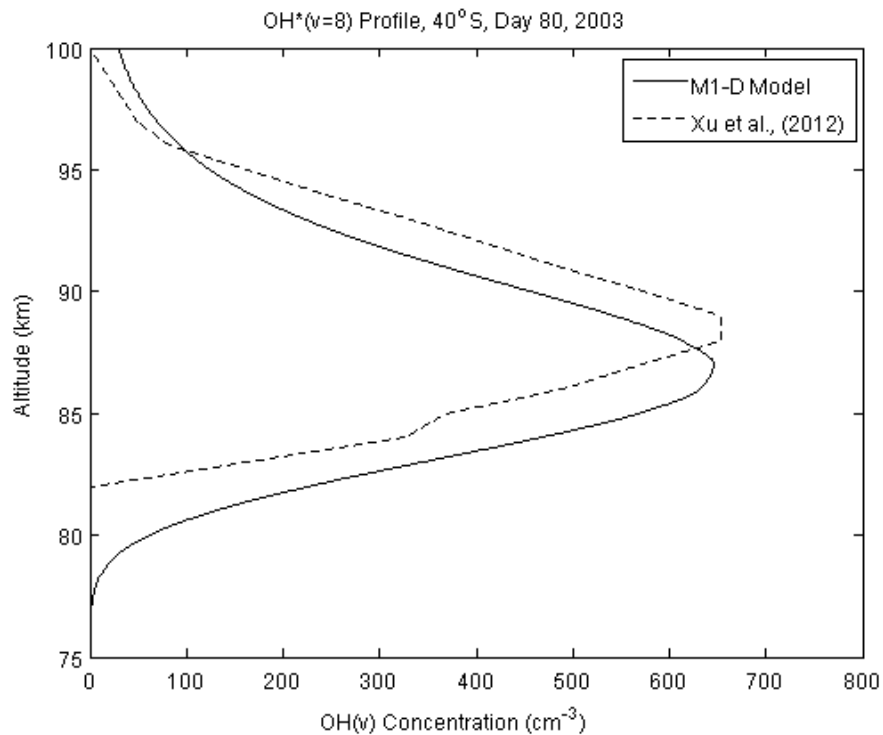
Figure 4.17 Altitudinal profile of $OH^*(v = 8)$ at 40° S for day 80 of 2003 at 0100 local time calculated by M1-D model (solid line) and measured by SABER instrument (dashed line) presented in Xu *et al.* (2012).

194

Within these figures it can be seen that in all cases the M1-D model predicts concentrations that are in very good agreement with the SABER data. The concentrations are only slightly lower than those measured by SABER. The OH^* layer thickness is also in good agreement for **Figures 4.15** and **4.17** at 40° N and 40°S of the equator while in **Figure 4.16**, over the equator, the modelled layer is somewhat thinner than the SABER measurements.

At 40° N and 40° S the peak concentration height varies by approximately 2 km. The M1-D model predicts a peak height of approximately 86 km throughout the year while SABER measures a peak height of 88 km at the higher latitudes. However, there is very good agreement on the peak heights at the equator with both sources showing peak altitudes of 86 km. This implies that the chemistry of the M1-D model is accurate. Differences in the initial conditions, or alternatively atmospheric processes such as tides or gravity waves, which are not accounted for by the M1-D model, could force the peak in OH^* concentrations into higher altitudes at higher latitudes. The effect of these additional atmospheric processes cannot be investigated until the M1-D model has been incorporated into the 3-D CMAT2 model. It is the job of CMAT2 to account for these atmospheric processes.

4.7.1.2 Low Vibrational Levels

A similar comparison was carried out for the remaining vibrational levels and similar features were found to exist in the majority of cases. The main difference between the higher and lower vibrational level predictions is that, while for higher vibrational levels the M1-D model generally predicts concentrations slightly lower than those recorded in SABER data, at lower vibrational levels the M1-D model typically predicts concentrations that are slightly higher than those revealed by SABER measurements. While this is not true in all cases, it is true for the vast majority.

Displayed in **Figures 4.18, 4.19 and 4.20** are profiles for vibrational level $OH^*(v = 4)$ for the same location, time of day and time of year as **Figure 4.15, 4.16 and 4.17.**

Figure 4.18: Altitudinal profile of OH$^*(v = 4)$ at 40° N for day 80 of 2003 at 0300 local time calculated by M1-D model (solid line) and measured by SABER instrument (dashed line) presented in Xu *et al.* (2012).
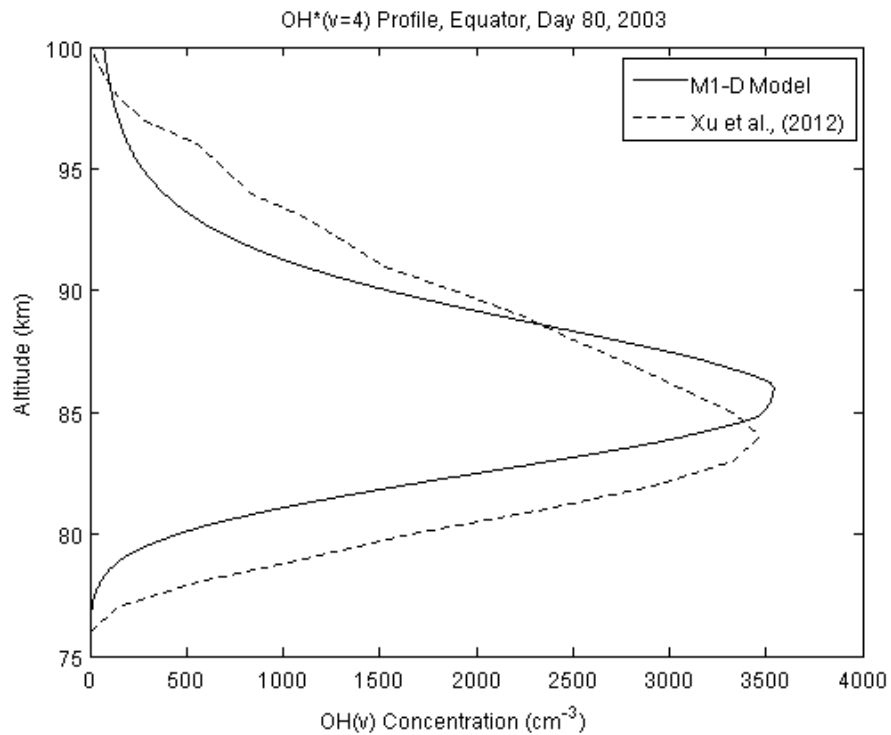
Figure 4.19: Altitudinal profile of OH$^*(v = 4)$ at equator for day 80 of 2003 at 0130 local time calculated by M1-D model (solid line) and measured by SABER instrument (dashed line) presented in Xu *et al.*, (2012).
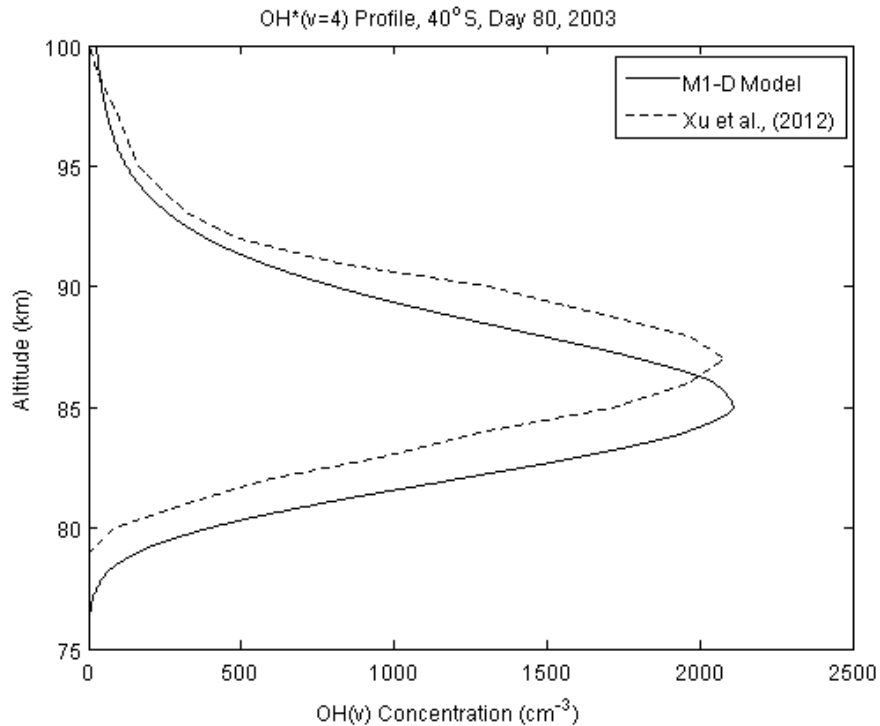
Figure 4.20: Altitudinal profile of $OH^*(v = 4)$ at $40°$ S for day 80 of 2003 at 0100 local time calculated by M1-D model (solid line) and measured by SABER instrument (dashed line) presented in Xu *et al.,* (2012).

Similar features to those described earlier are visible in all three figures. Layer thicknesses are again in good agreement, especially at higher latitudes; although just as before, the M1-D model tends to predict a layer that is somewhat thinner at the equator than the SABER data.

The concentrations are in very close agreement although in most cases the model tends to slightly over-predict the concentrations when compared with the SABER data, especially at higher latitudes.

Peak heights of approximately 85 km are predicted at all three latitudes by the M1-D model while the SABER data shows a variation in peak height of approximately 3 km between the equator and the higher latitudes. This variations extends from 84 km at the equator to 87 km at 40°N and 40°S. This further suggests that while the chemistry may be accurate, atmospheric processes such as tides or gravity waves may be responsible for the variation in peak heights observed.

4.7.1.3   Further Investigations of M1-D Model Sensitivity to Ozone

Based on the results of the initial sensitivity studies of the M1-D model detailed above (in particular **Section 4.6**), it was reasonably assumed that discrepancies within the initial ozone profiles used by the model could explain the differences in the peak altitudes exhibited in **Sections 4.7.1.1 and 4.7.1.2**. Therefore, SABER recorded ozone profiles were adopted as input for the M1-D model in order to examine what effect further variations in ozone concentrations could have on the modelled results.

Figure 4.21 shows the $OH^*(v = 8)$ profile generated by M1-D model using the appropriate ozone profile derived from SABER measurements. For comparison, the $OH^*(v = 8)$ concentration profile determined by SABER is also presented, identical to the profile presented in **Figure 4.15.**
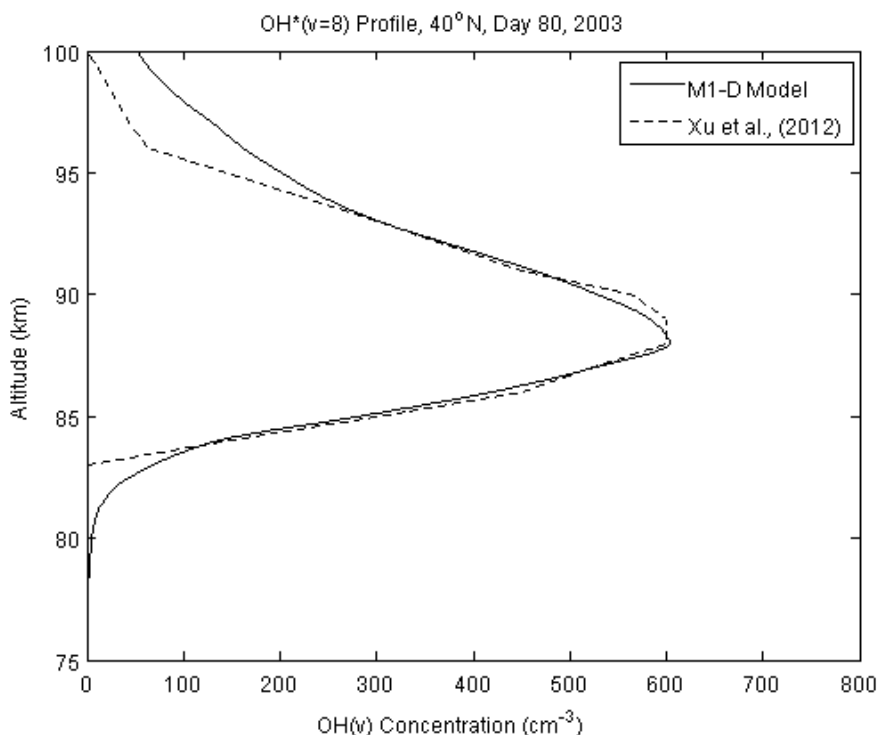
Figure 4.21: Altitudinal profile of $OH^*(v = 8)$ at 40° N for day 80 of 2003 at 0300 local time calculated by M1-D model (solid line) and measured by SABER instrument (dashed line) presented in Xu *et al.* (2012) using SABER retrieved O_3 profiles.

The $OH^*(v = 8)$ profile displayed in **Figure 4.21** shows significant improvement. The concentrations predicted for this vibrational level are improved and the height of the layer has increased in altitude by approximately 2 km. The height of the concentration

peak has also increased by the same amount thereby becoming almost indistinguishable from the SABER measured profile.

This process was undertaken for all vibrational levels and in **Figure 4.22** the effect on the $OH^*(v = 4)$ level is displayed. This profile also exhibits much better agreement with SABER data.

Figure 4.22: Altitudinal profile of $OH^*(v = 4)$ at $40°$ N for day 80 of 2003 at 0300 local time calculated by M1-D model (solid line) and measured by SABER instrument (dashed line) presented in Xu *et al.* (2012) using SABER retrieved O_3 profiles.

The process was repeated for each latitudinal band. Similar results were found for the lower latitude band at 40°S as expected given that the ozone profiles at both locations (40°N and 40°S) are similar (Xu *et al.* 2012). This is shown in **Figure 4.23** for $OH^*(v = 4)$.
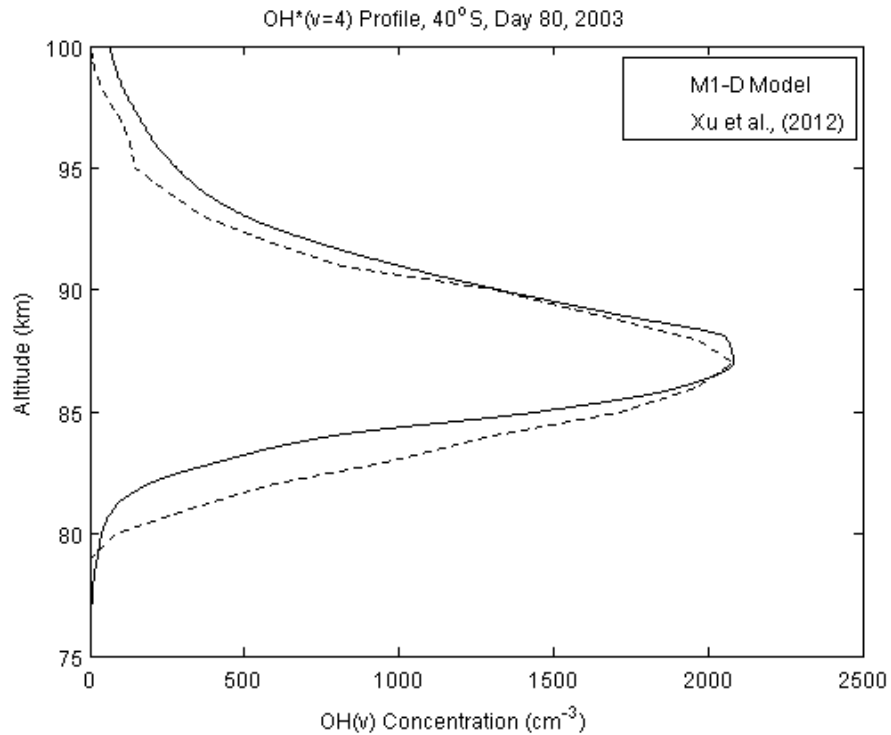
Figure 4.23: Altitudinal profile of $OH^*(v = 4)$ at $40°$ S for day 80 of 2003 at 0100 local time calculated by M1-D model (solid line) and measured by SABER instrument (dashed line) presented in Xu *et al.* (2012) using SABER retrieved O_3 profiles.

The effect of the new ozone profile also improves the comparison of the two data sets at the equator. However, the new ozone profile causes the M1-D model to predict peaks in the OH^* layers at higher altitudes than those measured by the SABER instrument. This is shown for $OH^*(v = 4)$ in **Figure 4.24**.

Figure 4.24: Altitudinal profile of $OH^*(v = 4)$ at equator for day 80 of 2003 at 0130 local time calculated by M1-D model (solid line) and measured by SABER instrument (dashed line) presented in Xu *et al.* (2012) using SABER retrieved O_3 profiles.

This results from the fact that at the equator during equinox, the ozone profile is markedly different from the ozone profiles at the different latitude bands surrounding 40°N and 40°S and exhibits a peak height that has increased in altitude by approximately 5 km from 89 km to 94 km.

4.7.2 Latitudinal Variations at Solstice Conditions

The latitudinal distributions of different OH^* vibrational levels for a number of different latitudes at a number of local times have been discussed. However, the plots given in **Section 4.7.1** are only for one particular day of the year and representative of equinox conditions. A similar comparison, using data from a different time of year (day 180 of 2003, representing solstice conditions) will be presented in this section.

4.7.2.1 Inter Comparison of Makhlouf, SABER, and M1-D Model

Since the first location (at 40° N) is in the vicinity, and at the same time of year (~ day 180) as the results previously shown from the Makhlouf model, a quick comparison on the variation in concentrations predicted by the M1-D model, the Makhlouf model and

201

SABER data from Xu *et al.* (2012) is presented. The results from two different vibrational levels $OH^*(v = 8)$ and $OH^*(v = 4)$ are shown in **Figure 4.25** and **Figure 4.26** respectively. These particular vibrational levels were chosen so that data from both SABER channels dedicated to the observation of the OH^* airglow could be employed. Initial concentrations of ozone are taken from CMAT2.
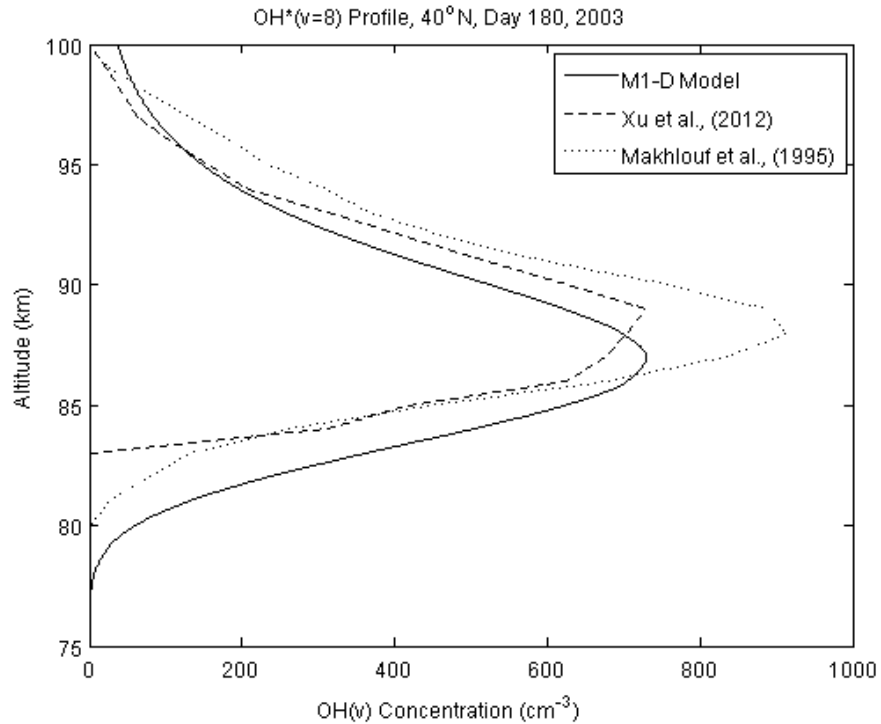
Figure 4.25: Altitudinal profile of $OH^*(v = 8)$ at 40° N for day 180 of 2003 at 0300 local time calculated by M1-D model (solid line) and measured by SABER instrument (dashed line) presented in Xu *et al.*, (2012). Altitudinal profile for $OH^*(v = 8)$ from Makhlouf *et al*. (1995) is also shown for comparison (dotted line).
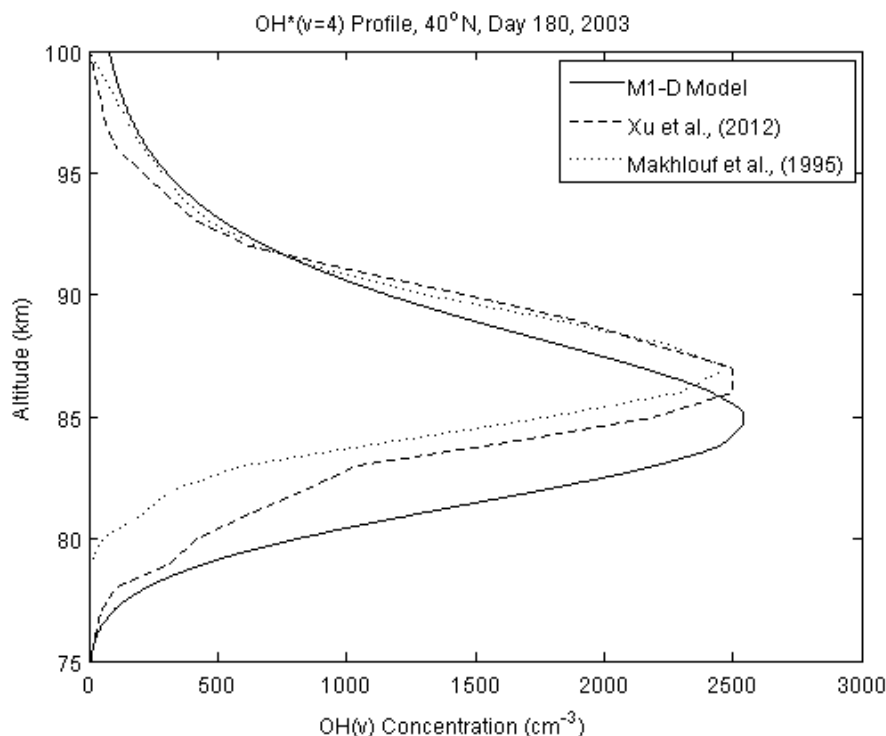
Figure 4.26: Altitudinal profile of $OH^*(v = 4)$ at 40° N for day 180 of 2003 at 0300 local time calculated by M1-D model (solid line) and measured by SABER instrument (dashed line) presented in Xu *et al.,* (2012). Altitudinal profile for $OH^*(v = 4)$ from Makhlouf *et al.* (1995) is also shown for comparison (dotted line).

It can be seen clearly that the M1-D model tends to predict less OH^* at the higher vibrational levels than the Makhlouf model (**Figure 4.25**). However, the M1-D predictions of the higher vibrational level concentrations are in better agreement with the profiles derived from the SABER measurements.

Looking at the peak heights of the layer it can be seen that the Makhlouf model makes a better prediction of the peak height. As discussed previously, the difference in the peak heights produced by the M1-D model can be attributed to variations primarily in the ozone profiles employed in the initial conditions.

Within **Figure 4.26** the M1-D model predicts slightly higher concentrations for the lower vibrational levels than the Makhlouf model. However, the concentrations from both models are still very much in agreement with the data obtained from the SABER observations. The Makhlouf model results show a slightly better agreement with the SABER data measurements, especially between 87 km and 95 km with regards to this

vibrational levels concentrations. The peak heights predicted by the Makhlouf model are also in better agreement with the SABER measurements.

Small variations between the peak heights of all three sources are still visible. SABER measured a peak height of 86 km, the Makhlouf model predicts a peak height of 87 km and the M1-D model predicts a peak height of approximately 85 km. While the M1-D model predicts peak concentrations at lower altitudes at these lower vibrational levels, it predicts an overall layer thickness that is in better agreement with the SABER measurements. The Makhlouf model predictions underestimate the thickness of the layer by about 1 km. This can be attributed to variations in the atomic oxygen profiles adopted by the Makhlouf model which falls sharply below 85 km.

Analyses of the other vibrational levels show similar characteristics to those exhibited in the figures above. For the higher vibrational levels the Makhlouf model predicts higher OH^* concentrations than both the M1-D model and SABER. However, it gives a better prediction of the peak heights. The layer thickness as predicted by all three sources are in very close agreement.

For the lower vibrational levels the concentrations produced by both models are in good agreement with SABER data. However, the Makhlouf model predicts a layer somewhat thinner than that produced by the M1-D model and SABER, while the M1-D model maintains good agreement with SABER measurements of both layer and peak altitudes at lower heights.

In the following section a comparison of the M1-D model results with SABER data will be presented.

4.7.2.2   High Vibrational Levels

Figures 4.27, 4.28 and 4.29 show M1-D model predictions of the concentrations of $OH(v = 8)$ at local times 0300 hrs, 0230 hrs and 0045 hrs respectively. These are shown below and incorporate, yet again, the ozone profiles adopted from CMAT2.
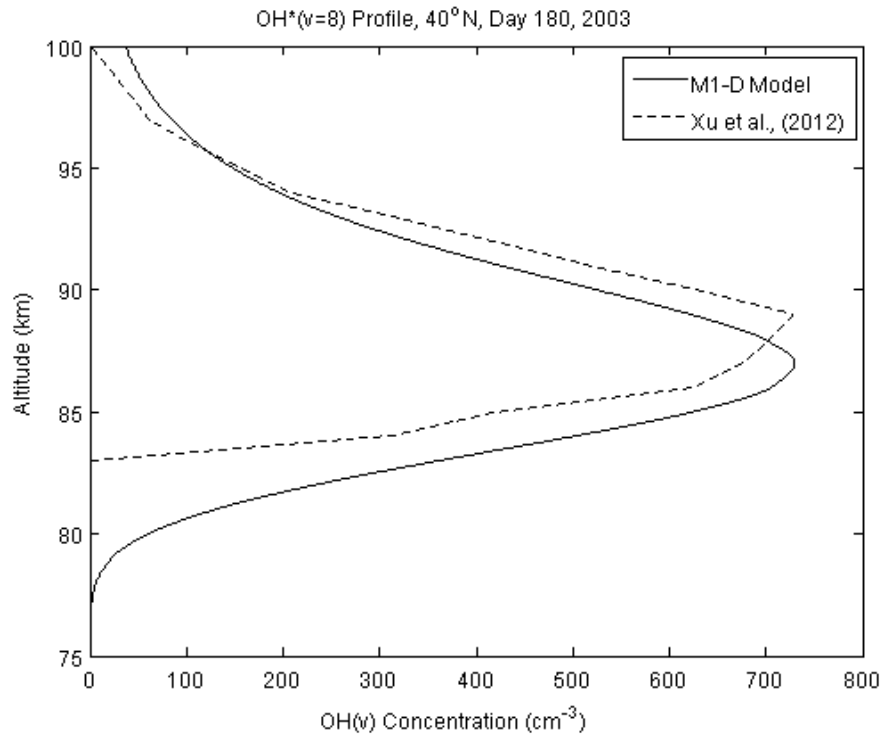
Figure 4.27: Altitudinal profile of $OH^*(v = 8)$ at 40° N for day 180 of 2003 at 0300 local time calculated by M1-D model (solid line) and measured by SABER instrument (dashed line) presented in Xu *et al.* (2012).
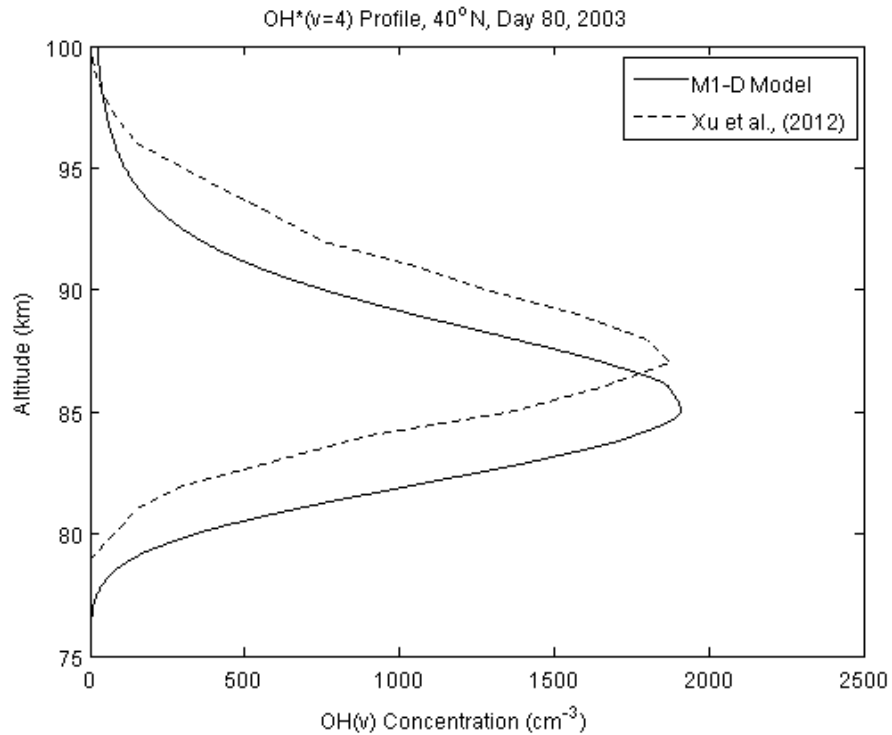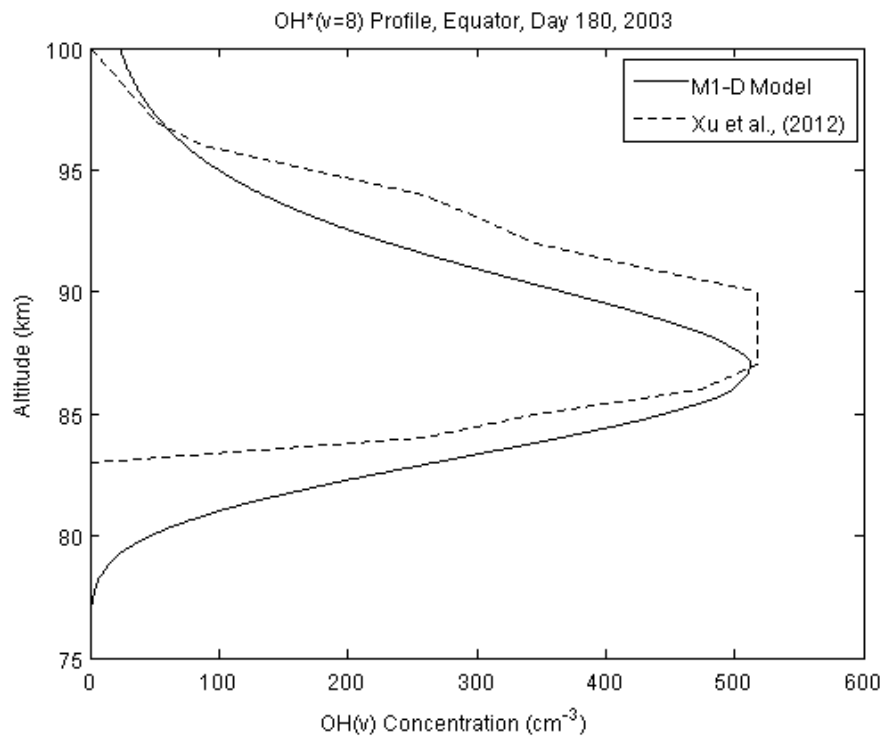

Figure 4.28: Altitudinal profile of $OH^*(v = 8)$ at equator for day 180 of 2003 at 0230 local time calculated by M1-D model (solid line) and measured by SABER instrument (dashed line) presented in Xu *et al.* (2012).
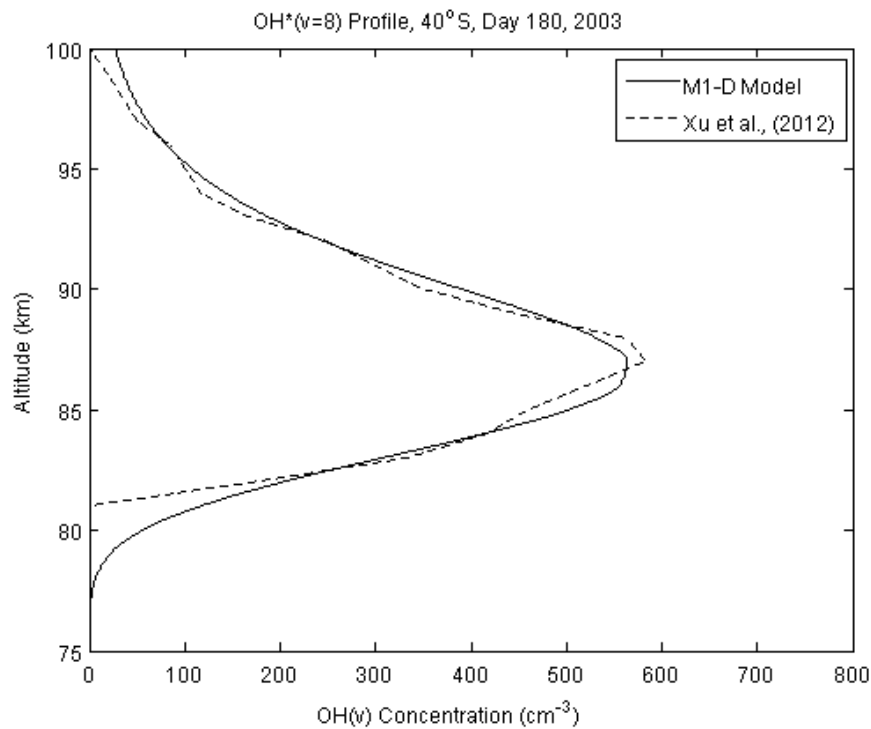
Figure 4.29: Altitudinal profile of $OH^*(v = 8)$ at $40°$ S for day 180 of 2003 at 0045 local time calculated by M1-D model (solid line) and measured by SABER instrument (dashed line) presented in Xu *et al.* (2012).

In the above plots it can be seen that in all cases the M1-D model predicts concentration that are in very good agreement with the SABER data. In **Figures 4.27** and **4.29** the M1-D model predicts concentrations that are slightly lower than those measured by SABER. In **Figure 4.28** the concentrations predicted are slightly higher than those predicted by SABER following the same trends as observed previously. Analyses of other high vibrational levels (e.g. $v = 7$ and 9) show that typically the M1-D model underestimates the concentrations of the higher vibrational states while overestimating the lower vibrational levels (e.g. $v = 1, 2$ and 3) slightly.

The OH^* layer thicknesses are in good agreement for **Figures 4.27** and **4.29** at $40°$ N and especially at $40°$S of the equator while in **Figure 4.28**, over the equator, the model predicted layer is somewhat thinner than the profile retrieved from the SABER measurements.

The peak heights predicted at $40°$ N and at the equator are approximately 2 km lower, at 86 km, than the SABER peak heights at 88 km. This is not surprising given that the ozone profiles from CMAT2 have been readopted.

However, overall there is still very good agreement between the two data sets shown especially in **Figure 4.29**. Here it can be seen that at almost all altitudes, with the exception of the peak itself, there is excellent agreement between the concentrations and altitudinal distribution of OH^* for this particular vibrational level.

4.7.2.3   Low Vibrational Levels

A similar comparison was carried out for the other vibrational levels and similar features and trends were found in the majority of cases. The main difference between higher and lower vibrational levels is, again, that for higher levels the M1-D model predicts concentrations slightly lower than those recorded in SABER data while at lower levels the model predicts concentrations that are slightly higher than those produced by SABER. These features can be seen below in **Figure 4.30, 4.31 and 4.32** for vibrational level $OH^*(v = 4)$ for the same location, time of day and time of year as **Figures 4.27**, **4.28** and **4.29**.
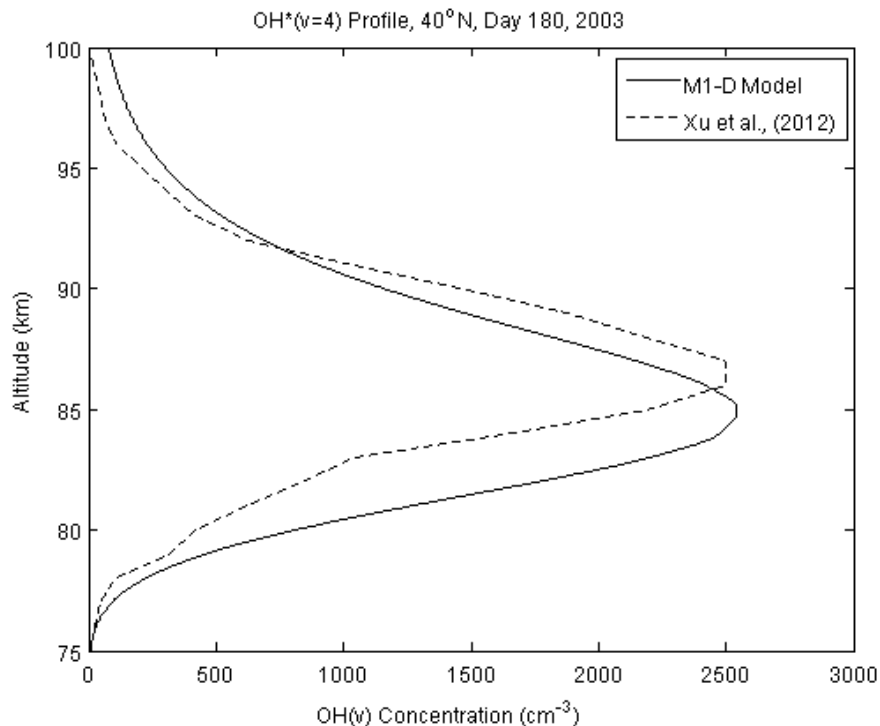
Figure 4.30: Altitudinal profile of $OH^*(v = 4)$ at 40° N for day 180 of 2003 at 0300 local time calculated by M1-D model (solid line) and measured by SABER instrument (dashed line) presented in Xu *et al.* (2012).
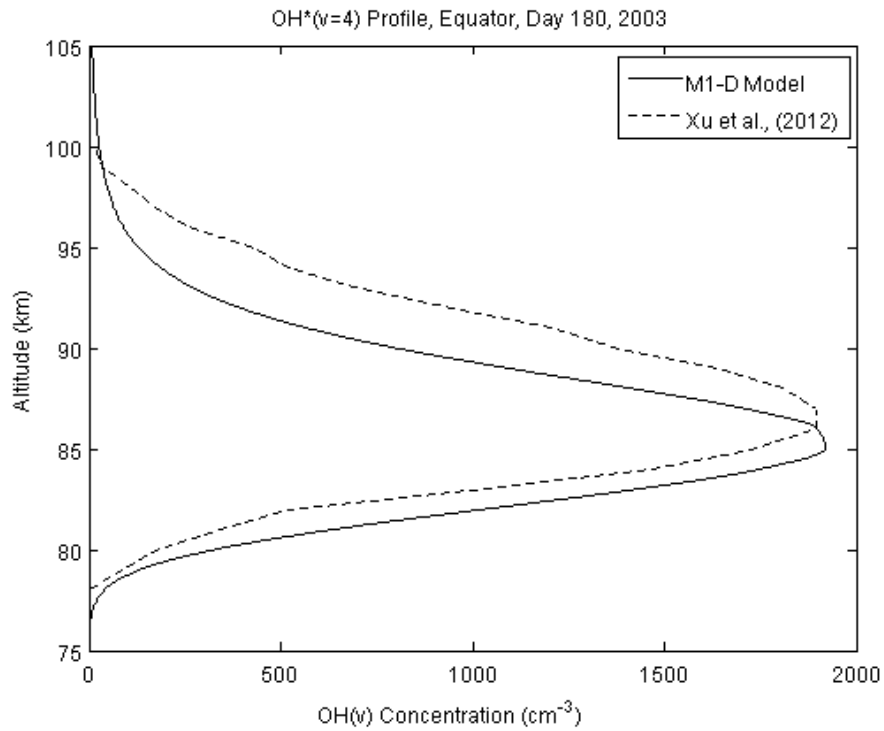
Figure 4.31: Altitudinal profile of OH$^*(v = 4)$ at equator for day 180 of 2003 at 0230 local time calculated by M1-D model (solid line) and measured by SABER instrument (dashed line) presented in Xu *et al.* (2012).
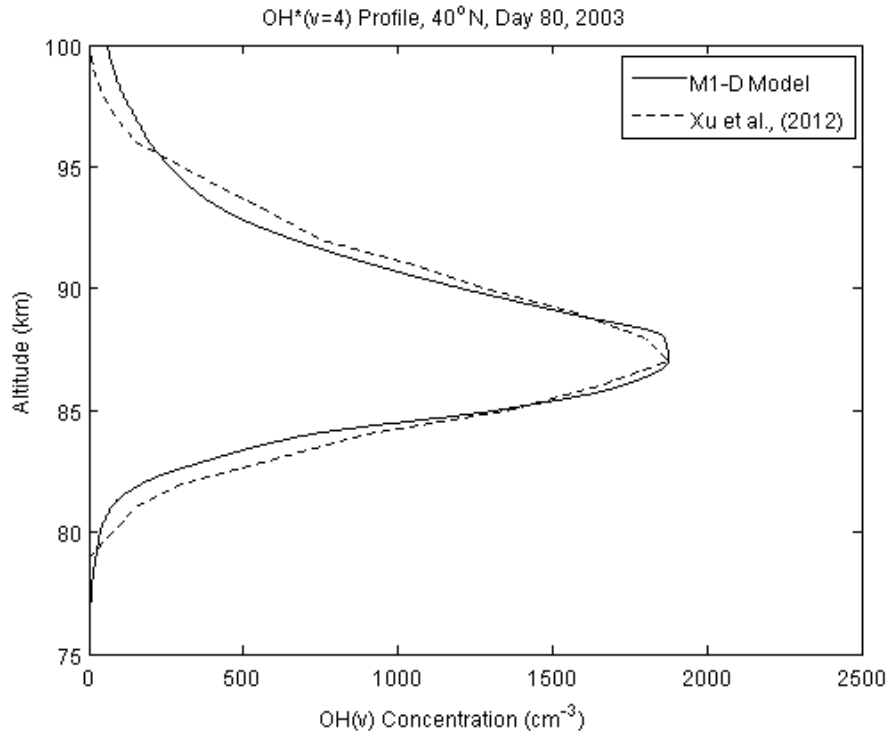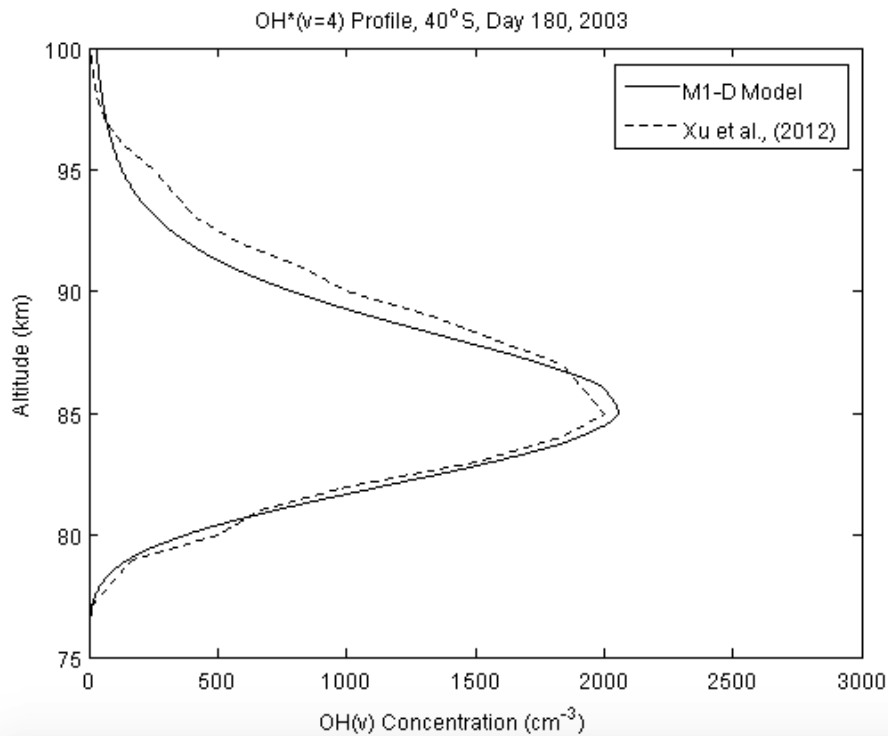

Figure 4.32: Altitudinal profile of OH$^*(v = 4)$ at 40° S for day 180 of 2003 at 0045 local time calculated by M1-D model (solid line) and measured by SABER instrument (dashed line) presented in Xu *et al.* (2012).

4.7.2.4   Further Investigations of M1-D Model Sensitivity to Ozone

The process of adopting ozone profiles from the SABER data for these same locations and local times was again undertaken and the model results with these adapted profiles are displayed below. **Figures 4.33** and **4.34** indicate profiles for $OH^*(v = 8)$ and $OH^*(v = 4)$ respectively showing that with these ozone profiles there is better agreement between the results of the M1-D model and the data retrieved from SABER. The results from two vibrational levels are shown and it can be seen that the agreement is better across for each vibrational level.
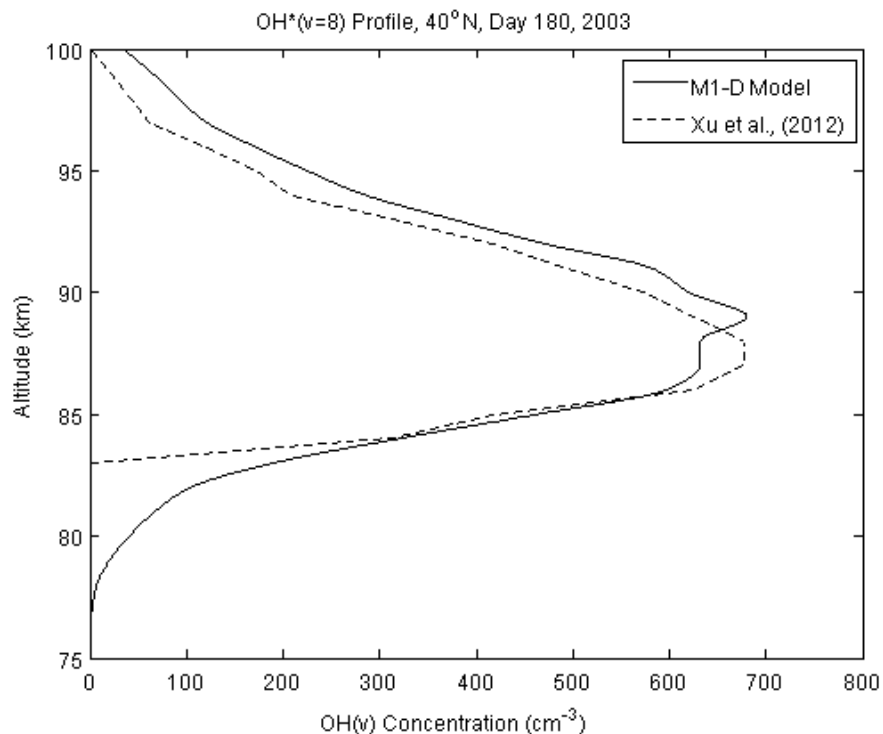
Figure 4.33: Altitudinal profile of $OH^*(v = 8)$ at 40° N for day 180 of 2003 at 0300 local time calculated by M1-D model (solid line) and measured by SABER instrument (dashed line) presented in Xu *et al.* (2012) using SABER retrieved O_3 profiles.
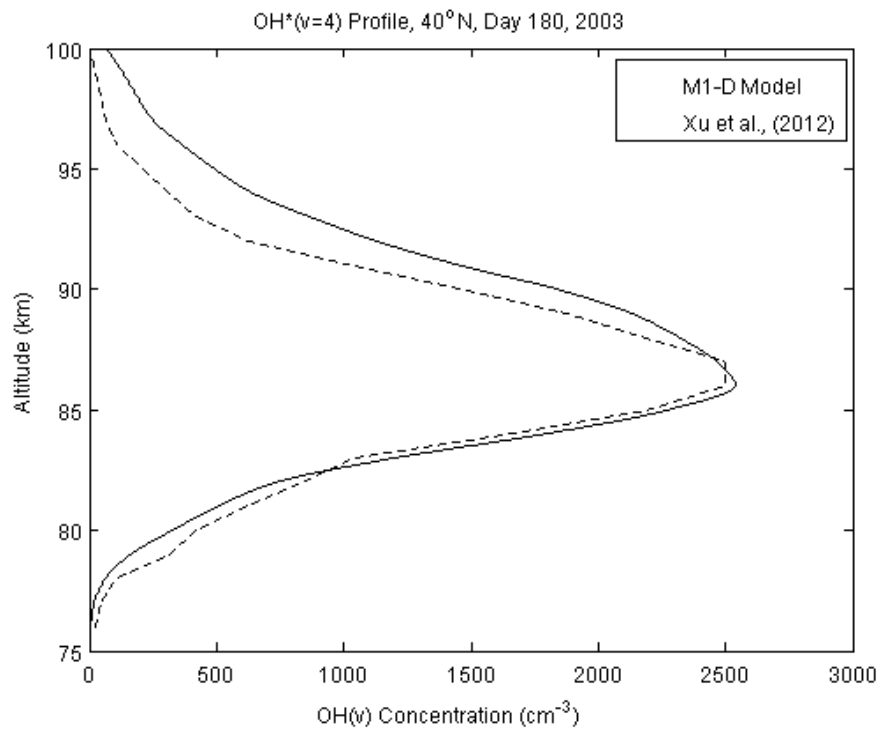
Figure 4.34: Altitudinal profile of $OH^*(v = 4)$ at 40° N for day 180 of 2003 at 0300 local time calculated by M1-D model (solid line) and measured by SABER instrument (dashed line) presented in Xu *et al.* (2012) using SABER retrieved O_3 profiles.

Figures 4.35 and **4.36** show that this agreement also extends to each latitude band.
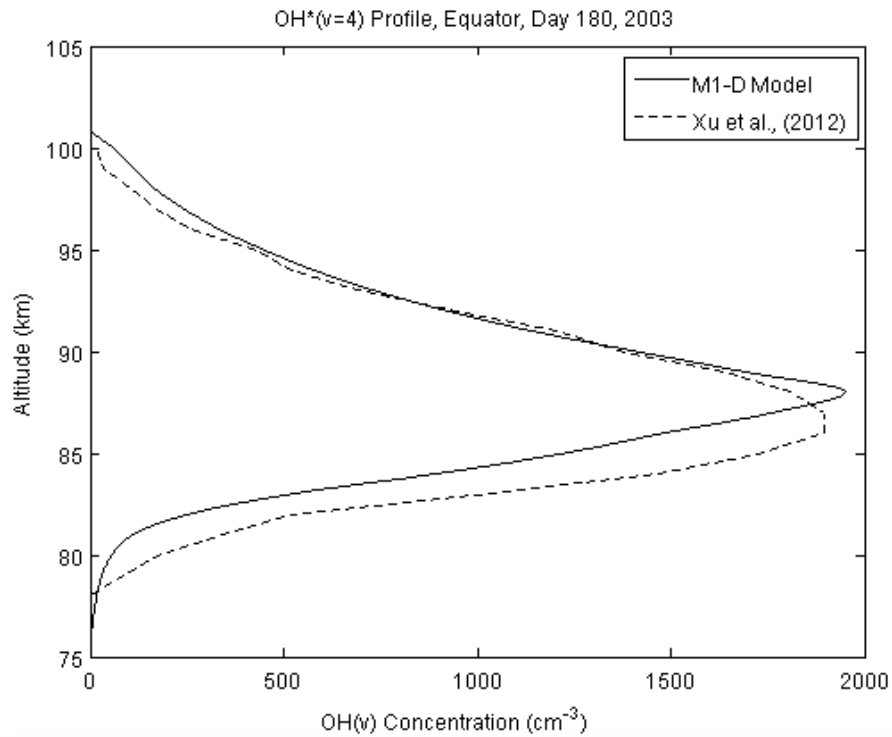
Figure 4.35: Altitudinal profile of $OH^*(v=8)$ at equator for day 180 of 2003 at 0230 local time calculated by M1-D model (solid line) and measured by SABER instrument (dashed line) presented in Xu *et al.* (2012) using SABER retrieved O_3 profiles.
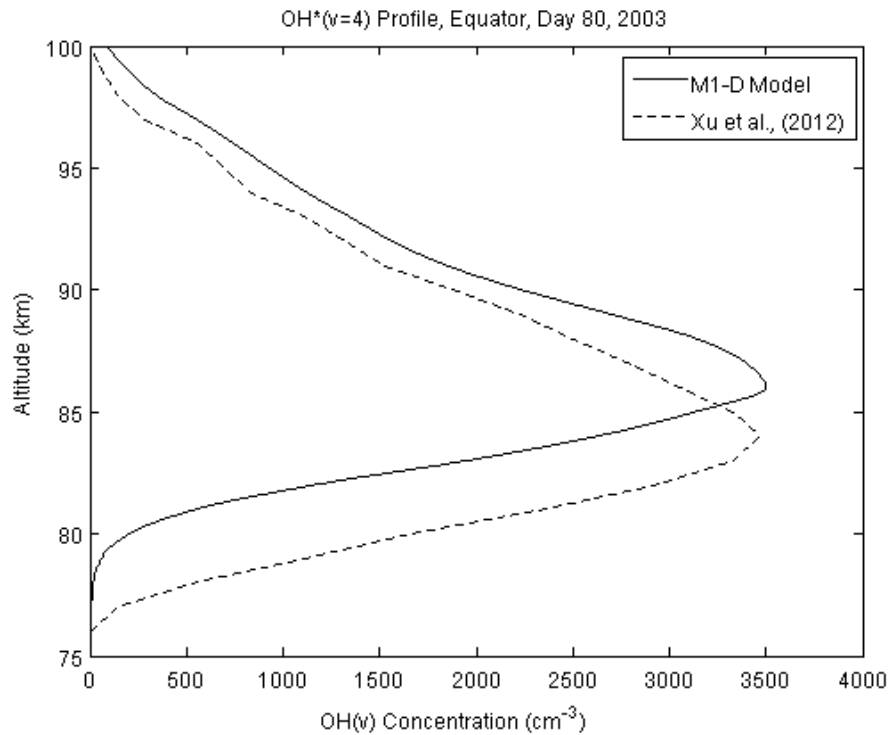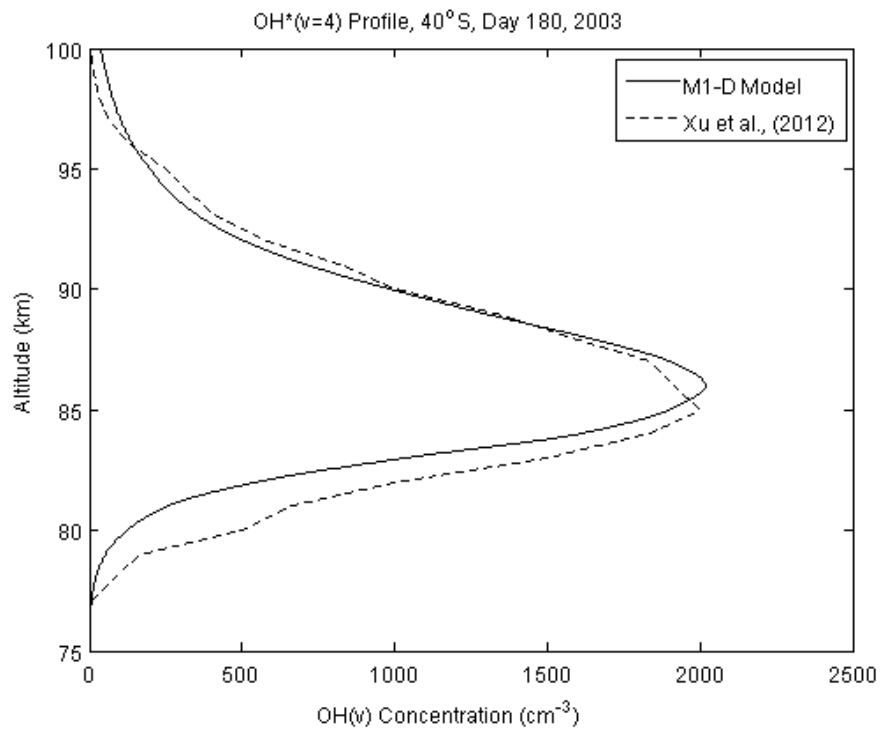

Figure 4.36: Altitudinal profile of $OH^*(v=8)$ at $40°$ S for day 180 of 2003 at 0045 local time calculated by M1-D model (solid line) and measured by SABER instrument (dashed line) presented in Xu *et al.* (2012) using SABER retrieved O_3 profiles.

4.8   Chapter 4 Summary

Within this chapter the development of a 1-D model of OH^* has been described. The results of this model have been compared to the previously developed models of Makhlouf *et al.* (1995) and von Savigny *et al.* (2012b) as well as observational data from the SCIAMACHY instrument on board the ESA's ENVISAT satellite and the SABER instrument on board NASA's TIMED satellite.

It was found that given the appropriate initial conditions the M1-D model can reproduce the results of Makhlouf *et al.* (1995), with only minor variations, without the inclusion of the perhydroxyl reaction as a source of OH^*. This suggests that this reaction does not contribute significantly to the levels of OH^* within the mesopause supporting the conclusions of McDade (1991). Varying the initial concentration profiles of atomic oxygen and ozone show that the OH^* concentrations are highly dependent on O while the peak altitude of the OH^* layers is highly dependent on O_3.

Investigations of the altitudinal distribution of the OH^* layers showed a variation in the peak emission heights of approximately 4 km between $OH^*(v = 9)$ and $OH^*(v = 1)$. The higher vibrational levels were shown to peak at higher altitudes than the lower vibrational levels. An average difference of approximately 0.5 km existed between the peak emission rate heights of consecutive OH^* layers in agreement with both the model of von Savigny *et al.* (2012b) and SCIAMACHY observations. Elimination of quenching by atomic oxygen from both the von Savigny and M1-D models significantly reduced this altitudinal distribution of the emission layers to 1 and 2 km respectively. A drop in the mean altitude of the emission layers from 86 to 83 km was also predicted by the M1-D model and attributed to the increased levels of O available for OH^* production. This feature cannot be observed in the von Savigny model results as long as the mean peak is assumed to exist at 87 km.

Significant variations in the concentrations of O used by both models showed further divergence between the von Savigny and M1-D model results. While the von Savigny model showed a broadening of the emission layers with increasing O concentrations, the M1-D models showed that this effect is counteracted by the sinking of the emission peak altitudes resulting from increased OH^* production at the lower boundary and increased atomic oxygen quenching above 85 km.

Finally, studies of the latitudinal and seasonal response of the M1-D model were investigated and the results were compared to observations from the SABER instrument on board NASA's TIMED satellite. It was found that in almost all cases the M1-D model could accurately predict OH^* concentrations for the individual OH^* layers. However, the agreement between the modelled and observed results improved when ozone profiles adopted from SABER measurements were utilised as part of the initial conditions rather than UGAMP profiles provided by CMAT2.

Chapter 5

The 3-D Model of Vibrationally Excited Hydroxyl (OH^*)

5.1   Introduction

In **Chapter 4** the M1-D photochemical model of OH^* developed as part of this thesis was described. The results of this model were compared to the results of other previously developed models and to observational data from ESA's SCIAMACHY and NASA's SABER instruments. Investigations into the model sensitivity to variations in atomic oxygen and ozone were also carried out.

In this chapter the M1-D photochemical model is extended to calculate for the chemical production and loss of the nine lowest vibrational states of OH^* on a global scale by incorporating it into the CMAT2 GCM code which was run on the Maynooth University HPC facility. The High Performance Computing (HPC) Facility at Maynooth University currently consists of an SGI Altix 8200 ICE cluster (Sioc) with 43 compute nodes. Each node has two Intel(R) Xeon(R) E5462 "HarperTown" quad-core processors, running at 2.80GHz, and 16Gb of memory installed. This totals 344 CPU cores and 688 Gigabytes of memory in the system. It also has 32 Terrabytes of disk storage. The cluster runs SuSE Linux as operating system.

This was accomplished by adding 9 new chemical species, representing the nine lowest vibrational levels of $OH^*(v = 1 - 9)$, into the list of chemical species considered by the CMAT2 model. The incorporation of new chemical species into a GCM is by no means a trivial process and involved significant modification of a number of the CMAT2 core modules, routines and subroutines.

New variables, initial conditions and start-up climatologies for the new chemical species were developed and incorporated into the 'input parameters' and 'climatology' routines of the CMAT2 model. Subsequently, a total of 67 new chemical reactions accounting for production and loss of the different OH^* levels via chemical, collisional and quenching mechanisms were incorporated into a new CMAT2 'chemistry' module.

As CMAT2 had previously not been employed to calculate emissions from atmospheric constituents an entirely new 'emissions' subroutine was developed and incorporated in order to calculate the volume emission rates of the different OH^* species. A total of 37 emission bands from OH^* were incorporated into this subroutine which utilise the Einstein *A* coefficients of Nelson *et al.* (1990). New calls for the calculation of OH^* chemistry and emissions were implemented within the core module and the results of these calculations were output as a number of additional netcdf files.

The result of these modifications significantly impact the CMAT2 model run time. Depending on the complexity of the input parameters, such as the gravity wave or ionospheric routine employed in the model run, the model run time can approach double the amount of time required for a standard model run in which OH^* chemistry is not included.

By incorporating the M1-D model into the 3-D GCM the effects of horizontal and vertical advection are added into the calculations, as well as other atmospheric dynamics such as gravity waves and tides. With the addition of these features a more realistic picture of the overall global distribution in the different OH^* species should be achievable.

In order to test the incorporation of the M1-D model into CMAT2 a number of diagnostic tests were performed. These tests were designed to evaluate the capabilities of the model in respect of other models that have previously been developed such as the ROSE chemical model described in Rose and Brasseur (1989), Marsh *et al.* (2001), Marsh *et al.* (2003).

5.2 Study 1: Diurnal Variations in $OH^*(9-8)$ Emissions

An initial comparison of the CMAT2 results was made with the model results of Ward (1999). This particular model was chosen for the comparison primarily for its

simplicity, calculating the number of emissions within the $OH^*(9-8)$ band during equinox conditions.

This represents the simplest case available as, during equinox, the atmosphere is in its most stable condition while $OH^*(v=9)$ is only produced via

$$H + O_3 \rightarrow OH^* + O_2$$

<div align="right">(R5.1)</div>

and not by any alternative means such as radiative transitions from higher vibrational levels. As such this represents an ideal starting point for the evaluation of the incorporated model's capabilities. **Figure 5.1** shows the model results of Ward (1999). **Figure 5.2** shows the model results of CMAT2. Note that the altitudinal extent of the CMAT2 results is 5 km lower than that of Ward (1999). This is due to the fact that no appreciable emissions are predicted above 100 km by CMAT2. The format of the CMAT2 plot is also altered to increase the level of detail visible in the results.
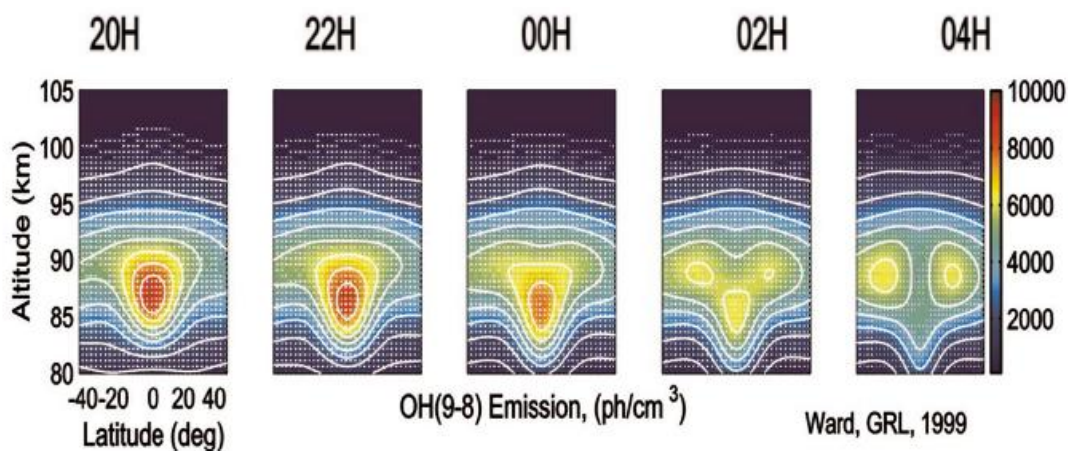
Figure 5.1: Height/latitude cuts at different local times of the $OH^*(9-8)$ diurnal nightglow emission during equinox conditions (Ward, 1999).
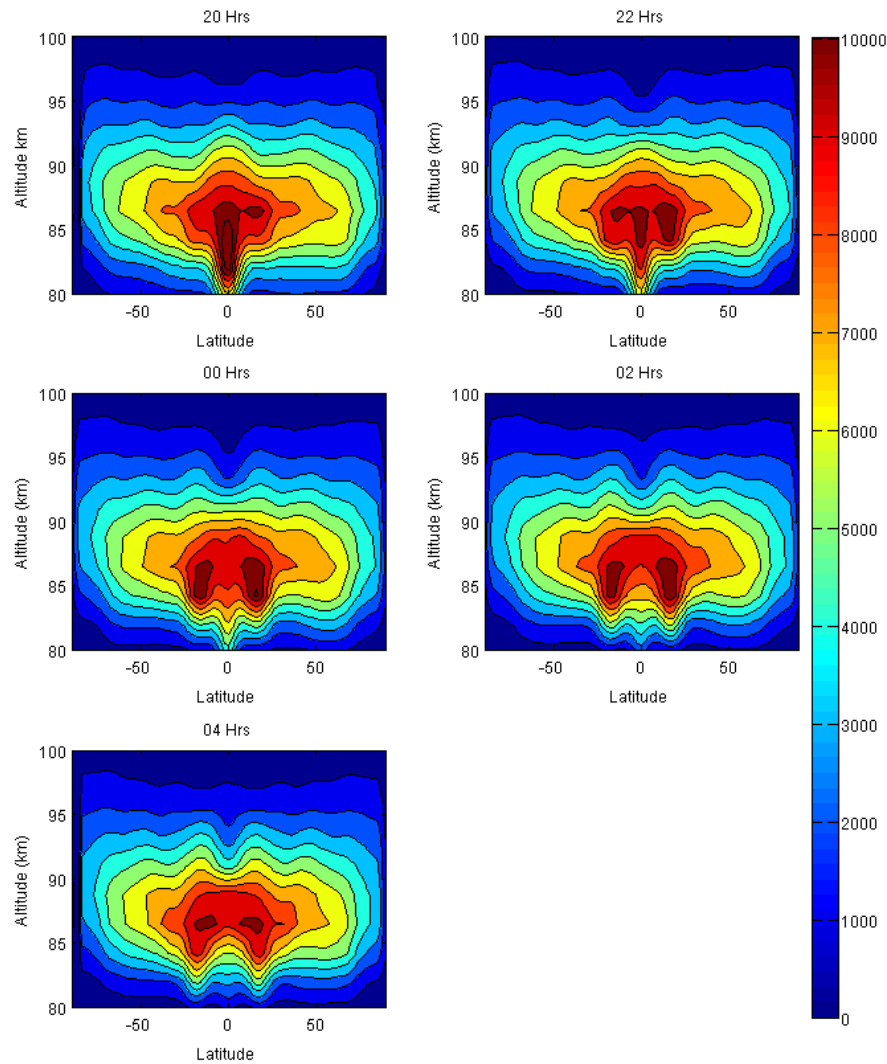
Figure 5.2: Height/latitude cuts at different local times of the $OH^*(9-8)$ diurnal nightglow emission during equinox conditions of 2008 produced by CMAT2.

From **Figures 5.1** and **5.2** it can be seen that the CMAT2 model predicts similar levels of emissions to the model developed by Ward at all latitudes and altitudes. During equinox and at 20 hrs local time both models predict a peak in the emission of $OH^*(9-8)$ at the equator which reaches a total emission of approximately 10,000 photons/cm^3 at a peak altitude at approximately 87 km. This peak is localized at the equator and the altitude of the peak in intensity is somewhat lower at the equator than at other latitudes.

217

At 22 hrs local time both models predict that the magnitude of the peak has dropped slightly and the CMAT2 model starts predicting increased levels of $\text{OH}^*(9-8)$ emissions within the tropical regions, migrating polewards from the equator.

By local midnight the CMAT2 model predicts two distinct peaks in the emission which have migrated polewards from the equator and occupy the tropical regions. The number of emissions at the equator has continued to drop such that the number of emissions from this particular band are now greater in the tropical regions than at the equator. The Ward model also shows a decrease in the level of emission at midnight over the equator; however, it is only now that this model starts to show the emergence of additional peaks within the tropical regions.

Only at 02 hrs are the peaks in the tropical regions clearly evident in the predictions of the Ward model, approximately 2 hours behind the model predictions of CMAT2. By this time it is also evident that there is a disparity in the number of emissions predicted by both models. While CMAT2 predicts lower levels of emissions coming from the tropical regions than earlier in the night, these emissions are still quite strong when compared to the emissions predicted by the Ward model. CMAT2 predicts emissions of approximately $9{,}000 - 10{,}000$ photons/cm^3 while the Ward model predicts levels of approximately $7{,}000$ photons/cm^3.

By 04 hrs both models predict that the number of emissions has decreased further and peaks in the emission are observed in the tropics between $20° - 40°$ N/S of the equator; although there are still some differences in the peak magnitudes.

From **Figures 5.1** and **5.2** the night-time trends in the emissions within the $\text{OH}^*(9-8)$ band can be established; however, for the sake of completeness **Figures 5.3** and **5.4** show the diurnal profile of this emission band over the equator and over the northern tropical region.

Here it can be seen that at sunset there is a large increase in the levels of emissions at both latitudes. However, in **Figure 5.3** (at the equator) the level of emissions reaches a maximum soon after sunset before gradually declining over the course of the night while in **Figure 5.4** (within the tropics) the emission intensity does not reach its peak until approximately 2 hours after local midnight. At these latitudes the emissions start off in the evening at a relatively low level, when compared to the level of emissions at

the equator, before gradually increasing until approximately $02\,\text{hrs}$. The level of emissions subsequently declines until sunrise at which point there is a sharp drop in the levels of emissions at both latitudes.
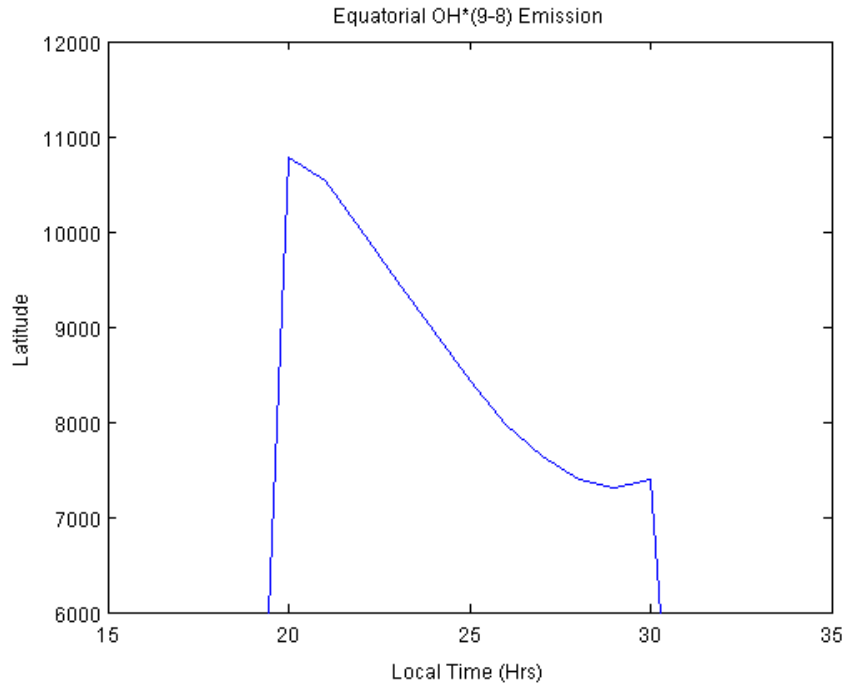
Figure 5.3: Diurnal variation in the night-time emission from the $OH^*(9-8)$ band over the equator during March equinox of 2008, produced by CMAT2.
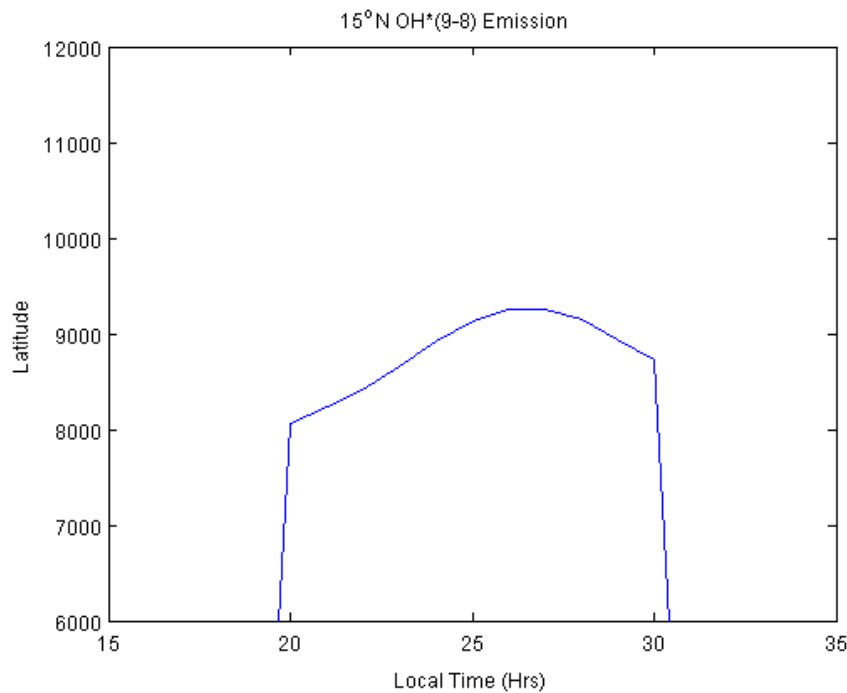
Figure 5.4: Diurnal variation in the night-time emission from the $OH^*(9-8)$ band at 15° N of the equator during March equinox of 2008, produced by CMAT2.

From the results shown in **Figures 5.3** and **5.4** it is evident that the diurnal profiles of these emissions are highly variable, not only in local time, but also latitude and therefore ground based measurements at different locations could not be expected to find similar diurnal variations in the emission. However, the magnitude of emissions should be comparable at least to within a factor of approximately 2. In **Figure 5.5** the diurnal variation of the $OH^*(9-8)$ emission band between latitudes of $\pm50°$ is presented emphasising both the latitudinal and local time variations in the emission.
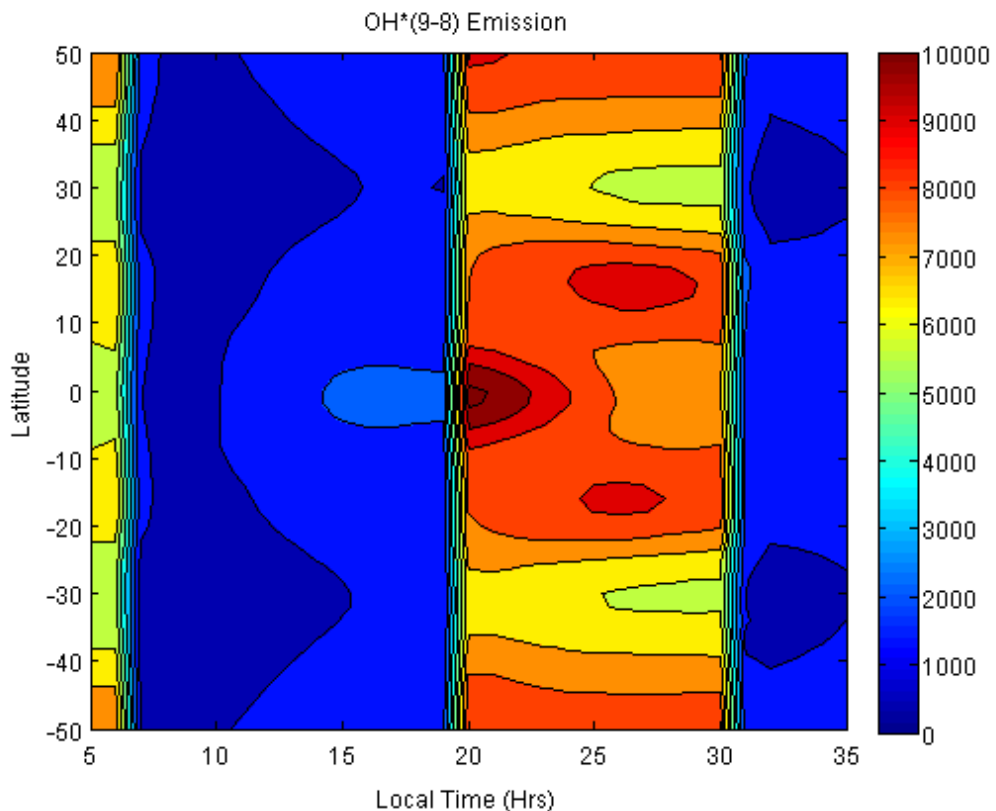
Figure 5.5: Diurnal variation in the night-time emission from the $OH^*(9-8)$ band for latitudes between $\pm50°$ during March equinox of 2008, produced by CMAT2.

Based on the results presented in this section it can be concluded that the CMAT2 model predicts similar levels of emissions for the $OH^*(9-8)$ band to those predicted by the OH^* model presented in Ward (1999) in respect of altitude, latitude and local time. This suggests that the incorporation of the M1-D model into the CMAT2 code has been successful, at least for this particular band. However, this comparison has only looked at one of the nine OH^* species incorporated into the CMAT2 model, $OH^*(v = 9)$, and one of 37 incorporated emission bands, $OH^*(9-8)$. A more rigorous test of the CMAT2 models capabilities is therefore required. For this reason, in the following

sections of this chapter, the study is extended to multiple vibration levels of OH^* and multiple emissions bands.

5.3 Study 2: Seasonal Variations in $OH^*(9-7)$ and $OH^*(8-6)$ Emissions

One of the most extensive investigations of OH^* data from the SABER instrument was performed by Gao *et al.* (2011). Within their paper 8 years of SABER data, from the year 2002 to 2009, were analysed to determine the average features from the $OH^*(9-7$ and $OH*8-6$ band emissions covered by the $OH*-A$ (*2.0* µm) SABER channel between latitudes of $\pm55°$ surrounding the equator. This particular latitude range was chosen so that gaps in the data measured by SABER at high-latitudes could be avoided.

The data were binned into a grid with dimensions of $10°$ latitude $\times$ 1 hr (local time) $\times$ 1 km altitude before being averaged zonally across each grid box. In the latitudinal direction a $5°$ running average was then performed leading to altitudinal profiles of the OH^* emission rates at 21 latitudes between $\pm50°$. Given that it takes approximately 60 days for SABER to complete a full 24 hr local time coverage 30 days of data on either side of the individual equinox or solstice event were also utilised in the analysis. It is assumed that the full 24 hr coverage gathered is representative of the individual day at the centre of the observational range. Following this, the average OH^* nightglow emission rate was determined by averaging the night-time emission between -2.5 and $+2.5$ hrs local time. The results of this analysis, as presented in Gao *et al.* (2011), are shown in **Figure 5.6**.
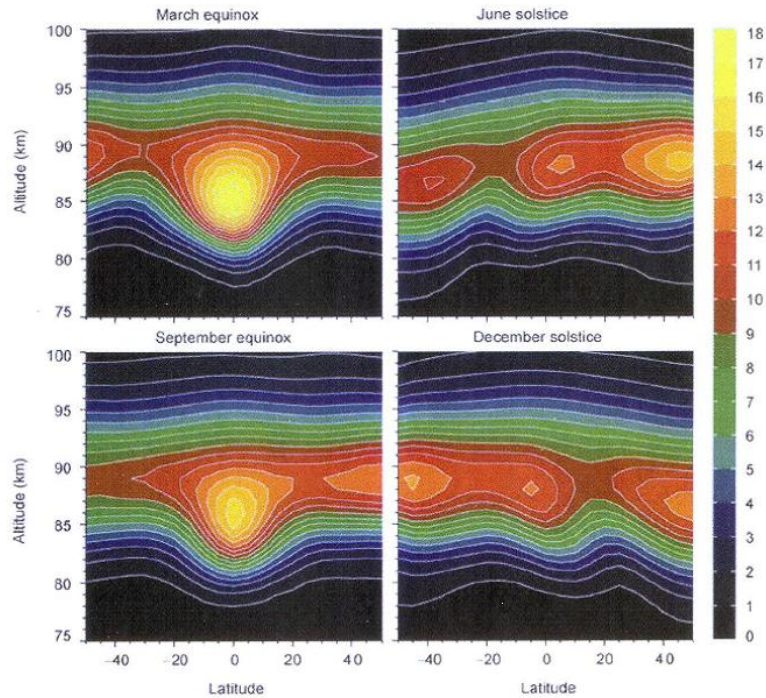
Figure 5.6: Altitude-latitude distribution of $OH^*(9-7)$ and $OH^*(8-6)$ emission rates in 10^4 cm^{-3} s^{-1} for equinox and solstice conditions, 2002-2009 (Gao *et al.,* 2011).

In order to perform a comparison between the data presented in **Figure 5.6** from Gao *et al.,* (2011) and the CMAT2 model, four CMAT2 runs were performed at equinox and solstice conditions for the year 2008. Within each model run the concentration of the nine individual vibrational states of OH^* were determined and from these concentrations the number of emissions in each band were calculated. In a similar fashion to what is described in Gao *et al.* (2011), these night-time emissions were subsequently averaged between -2.5 and $+2.5$ hrs local time.

The results of these four CMAT2 model runs are presented in **Figures 5.7** through **5.22**. In each case the individual emission profile from the $OH^*(9-7)$ and $OH^*(8-6)$ emission bands are displayed separately before being combined to produce a composite emission profile made up of the emissions from both bands. These combined emission profiles are subsequently compared to emission profiles recorded by the SABER instrument. In order to facilitate this comparison the work of Gao *et al.* (2011) establishing the above profiles has been repeated. However, only SABER data from the year 2008 has been utilised. The latitudinal range of the model results has also been limited to within $\pm 50°$ latitude for ease of comparison, although it should be remembered that CMAT2 predications are available at the full range of latitudes (90° S to 90° N).
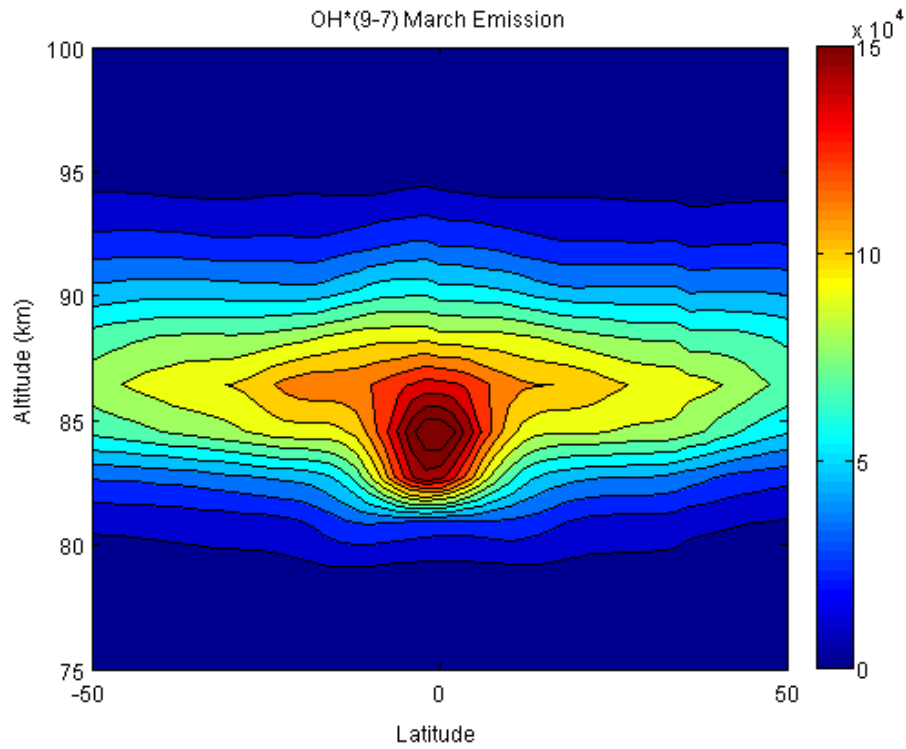
Figure 5.7: CMAT2 altitude-latitude distribution of $OH^*(9-7)$ nightglow emission rate in $cm^{-3} \, s^{-1}$ at 00 hrs local time for March 21st, 2008.
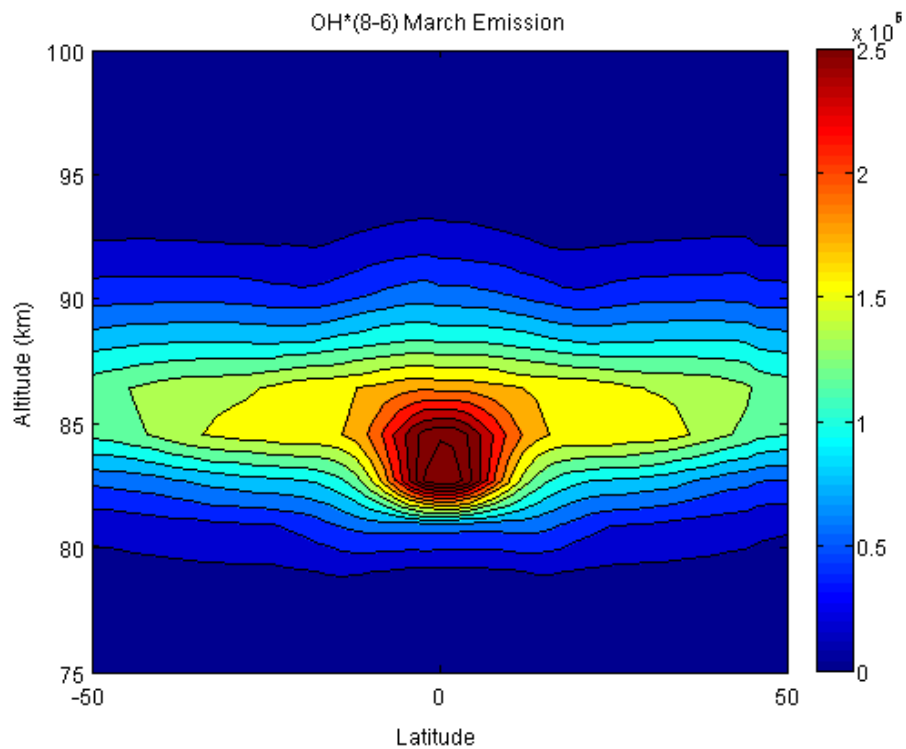
Figure 5.8: CMAT2 altitude-latitude distribution of $OH^*(8-6)$ nightglow emission rate in $cm^{-3} \, s^{-1}$ at 00 hrs local time for March 21st, 2008.

Figure 5.9: CMAT2 altitude-latitude distribution of the combined $OH^*(9-7)$ and $OH^*(8-6)$ nightglow emission rate in $cm^{-3}\ s^{-1}$ at 00 hrs local time for March 21st, 2008.

Figure 5.10: SABER altitude-latitude distribution of the combined $OH^*(9-7)$ and $OH^*(8-6)$ nightglow emission rate in $cm^{-3}\ s^{-1}$ at 00 hrs local time for March 21st, 2008.

Figures 5.7 to **5.9** show the CMAT2 model results for March equinox conditions of 2008. **Figure 5.10** shows the observational data for the same period gathered by the SABER instrument. Both the $OH^*(9-7)$ and the $OH^*(8-6)$ emission profiles show a peak in the level of emissions at the equator with the peak in the $OH^*(8-6)$ band exhibiting slightly stronger features than the $OH^*(9-7)$ band due to its slightly higher concentration. A minor difference in the altitude of the peak emission also exists within the profiles with the peak in the $OH^*(9-7)$ band occurring at 85 km while the peak in the $OH^*(8-6)$ band occurs at the lower altitude of 84 km. Given that these emissions originate from two separate OH^* species an altitude difference in the emission is expected although the altitudinal difference predicted here is slightly larger than that predicted by both the M1-D model and by von Savigny *et al.* (2012b) as detailed in **Chapter 4**. It should be remembered that CMAT2 has a vertical resolution of approximately 2 km at mesopause altitudes and therefore cannot be expected to reproduce the altitudinal distribution of the OH^* layers exactly in line with the M1-D model or von Savigny *et al.* (2012b).

It can be seen that the $OH^*(9-7)$ layer extends over a larger altitude range from $80-94$ km while the $OH^*(8-6)$ band extends from $80-93$ km. The combined emission profile from both bands is presented in **Figure 5.9** and compares well with the SABER observational data presented in **Figure 5.10**. Both figures exhibit a strong peak in the OH^* emissions at the equator. However, CMAT2 predicts a magnitude in the emission that is approximately a factor of two larger than that shown in the SABER data. It is a known feature of the version of CMAT2 utilised in this project that model runs tend to over-predict the amount of atomic oxygen within the atmosphere by approximately a factor of two (Dobbin, 2008). The unexpectedly high OH^* emissions predicted by CMAT2 is attributable to this previously documented atomic O problem.

Despite this difference the morphology of the emission layer in both figures is quite similar with both exhibiting a similar emission layer thickness, (extending from $80-95$ km); although low levels of emissions can be seen to extend up to almost 100 km in the observational data. The altitude of the peak emission is in very close agreement at 84 km.

The emergence of a secondary peak in the emission shown in **Figure 5.10** at approximately 50° S of the equator is not evident in the CMAT2 profiles. This may be

an additional feature of the OH^* emission during equinox. Given that the observational data used to produce this graph utilises data up to and over a month prior to equinox it may also be possible that this is the remnant of the mid-latitude winter maximum in the emission displayed later in **Figures 5.19** to **5.22**.
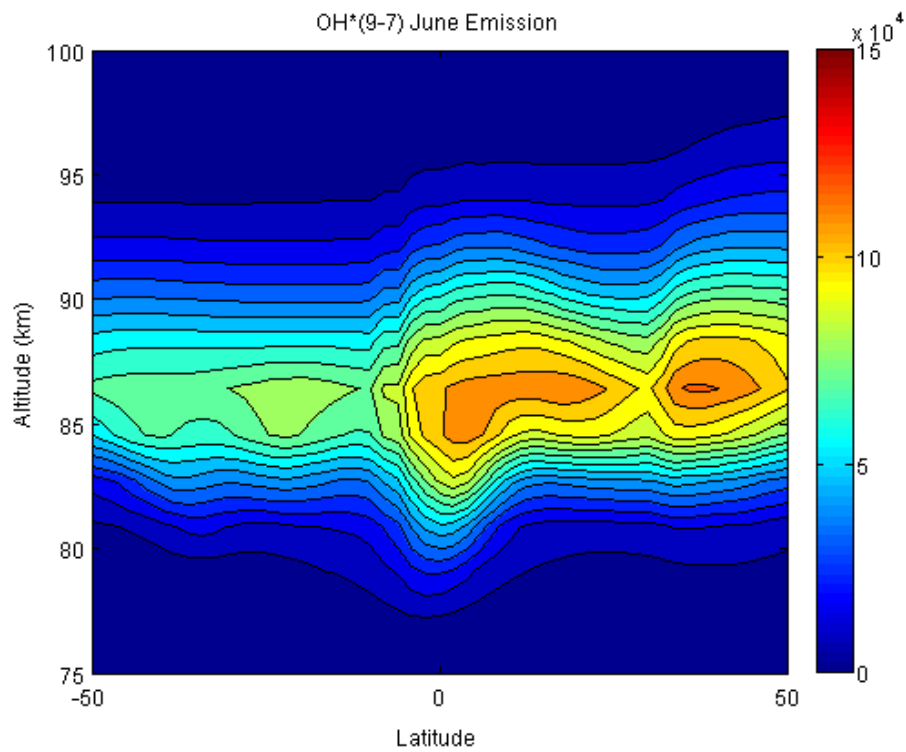
Figure 5.11: CMAT2 altitude-latitude distribution of OH$^*(9-7)$ nightglow emission rate in cm^{-3} s^{-1} at 00 hrs local time for June 21st, 2008.
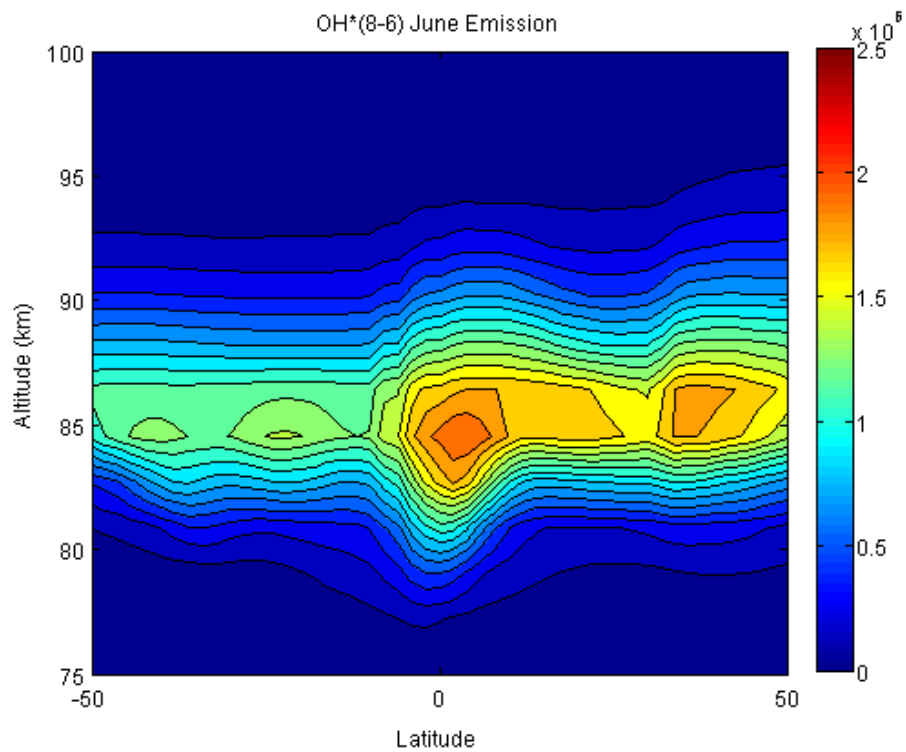
Figure 5.12: CMAT2 altitude-latitude distribution of OH$^*(8-6)$ nightglow emission rate in cm^{-3} s^{-1} at 00 hrs local time for June 21st, 2008.
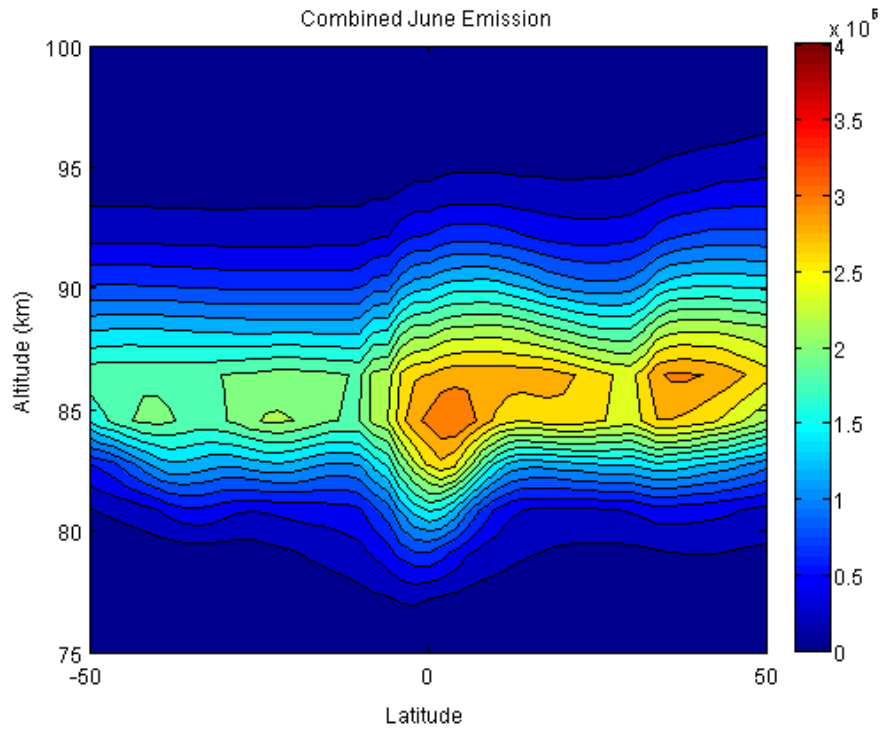
Figure 5.13: CMAT2 altitude-latitude distribution of the combined $\text{OH}^*(9-7)$ and $\text{OH}^*(8-6)$ nightglow emission rate in $\text{cm}^{-3}\,\text{s}^{-1}$ at $00\,\text{hrs}$ local time for June 21$^{\text{st}}$, 2008.
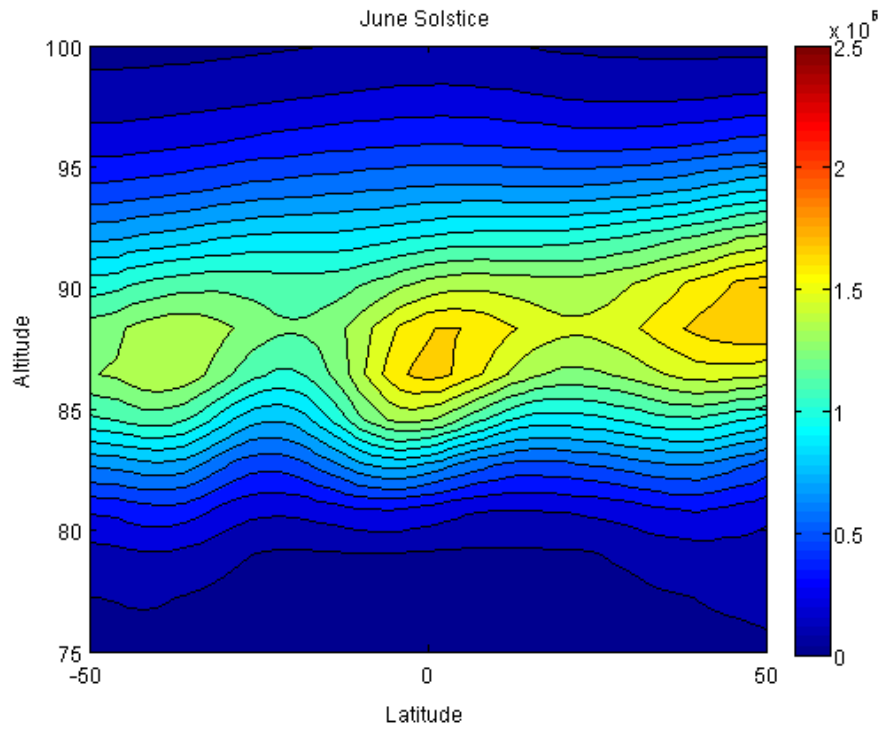
Figure 5.14: SABER altitude-latitude distribution of the combined $\text{OH}^*(9-7)$ and $\text{OH}^*(8-6)$ nightglow emission rate in $\text{cm}^{-3}\,\text{s}^{-1}$ at $00\,\text{hrs}$ local time for June 21$^{\text{st}}$, 2008.

Figures 5.11 to **5.13** show the model results for the same emission bands during June solstice conditions. The morphology of both emission bands is quite similar although the magnitude of the $OH^*(8-6)$ band emission is shown to be slightly higher than the $OH^*(9-7)$ band emission at all latitudes. There is a minor difference in the altitude of the peak emission although it is still in close agreement with the predictions of von Savigny *et al.,* (2012b) as the altitudinal peak in the $OH^*(9-7)$ band is located at 87 km while the peak in the $OH^*(8-6)$ is located at approximately 86 km.

The morphology of **Figures 5.11** and **5.12** are very similar although minor differences can be observed. These minor differences can be explained by the additional sources of production available to the lower vibrational levels of OH^* which result from collisional deactivation with the major atmospheric species. Given that $OH^*(v=9)$ has only one source of production while $OH^*(v=8)$ has five,

$$H + O_3 \rightarrow OH^*(v=8) + O_2$$

$$\text{(R5.2)}$$

$$OH^*(v=9) + O \rightarrow OH^*(v=8) + O$$

$$\text{(R5.3)}$$

$$OH^*(v=9) + O_2 \rightarrow OH^*(v=8) + O_2$$

$$\text{(R5.4)}$$

$$OH^*(v=9) + N_2 \rightarrow OH^*(v=8) + N_2$$

$$\text{(R5.5)}$$

$$OH^*(v=9) \rightarrow OH^*(v=8) + h\nu$$

$$\text{(R5.6)}$$
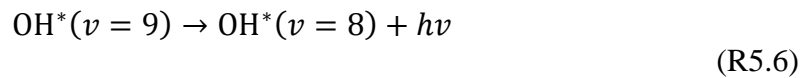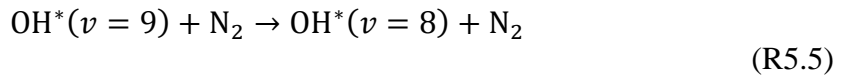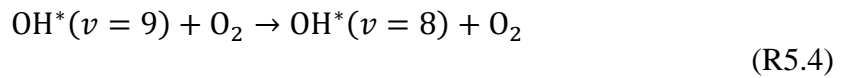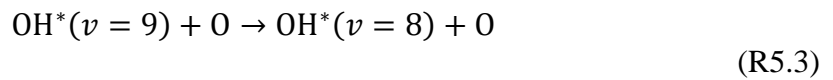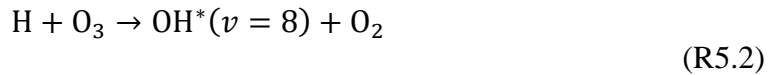
slight differences in the morphology are expected as some of these processes compete with one another. The most prominent difference between the two profiles is that the peak in emission from the $OH^*(9-7)$ which occurs at approximately 40° N does not correspond to the peak in the emission of the $OH^*(8-6)$ band which is still located at the equator, although the difference in magnitudes of these local peaks is quite small. This suggests that within the CMAT2 model excess production of the $OH^*(8-6)$ emission is occurring at the equator during solstice.

The increased level in emissions within the Northern hemisphere of **Figures 5.11** and **5.12** may be attributed to increased concentrations of atomic oxygen in this hemisphere at this time of year which result from the increased levels of O_2 photo-dissociation during the longer summer days. Furthermore, given that O is one of the principal quenchers of OH^* it is possible that increased collisional deactivation of $OH^*(v = 9)$ leads to increased production of $OH^*(v = 8)$ within the Northern hemisphere augmenting emissions from this vibrational level. Since $OH^*(v = 9)$ has only one chemical source of production these effects would not be observed in the $OH^*(9 - 7)$ emission band.

The increasing altitude of the peak emission with latitude in **Figures 5.11** and **5.12** is also a significant feature of the emission and suggests that the CMAT2 model is, at least in part, able to predict certain effects attributed to the mesospheric circulation within the atmosphere. As described in **Chapter 1** this circulation results in a mesopause that exists at higher altitudes and exhibits colder temperatures during the summer months, and lower altitudes exhibiting warmer temperatures during the winter months.

Figure 5.13 shows the combined $OH^*(9 - 7)$ and $OH^*(8 - 6)$ emission profile for comparison with **Figure 5.14** which shows SABER observational data from the same period. As with equinox conditions it can be seen that the morphology of the two figures is quite similar although CMAT2, as expected, again over-predicts the number of emissions at all latitudes by approximately a factor of 2.

There are clearly two additional peaks in the emission at latitudes of approximately $\pm 40°$. The Northern hemisphere peak is shown by both SABER and CMAT2 to have a larger magnitude than the Southern hemisphere peak. However, CMAT2 also predicts high levels of emissions at the equator which are larger than the minor emission peak revealed by the SABER observations. These increased emissions at the equator obscure the smooth transition in the number of emissions displayed in **Figure 5.14**.

The altitudinal variation in peak emission heights with latitude is also visible in both figures and both figures show approximately the same variation.
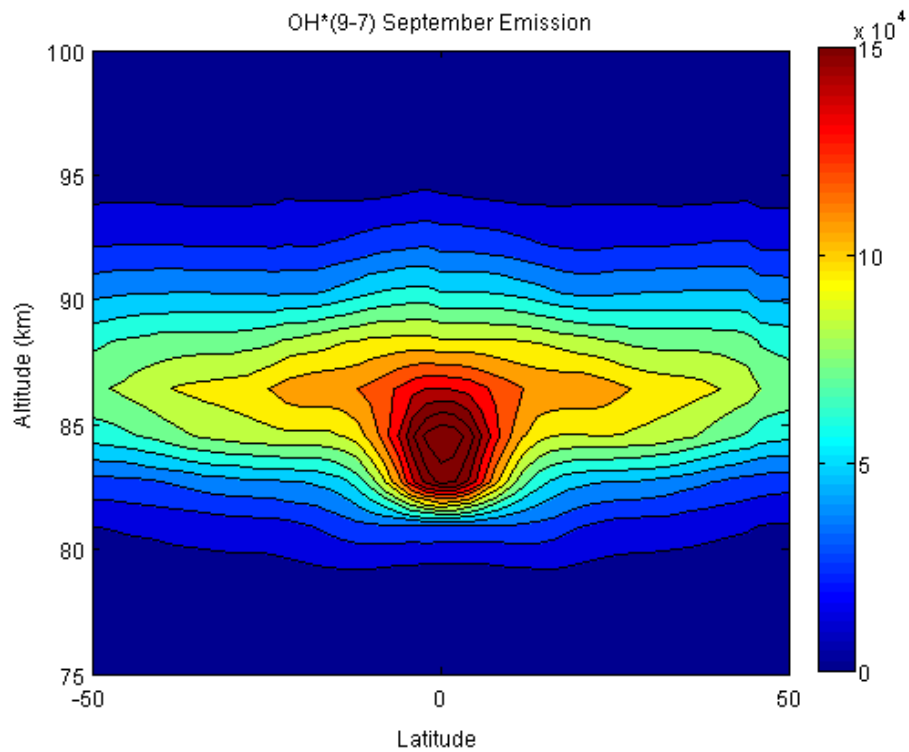
Figure 5.15: CMAT2 altitude-latitude distribution of $OH^*(9-7)$ nightglow emission rate in $cm^{-3} s^{-1}$ at 00 hrs local time for September 21st, 2008.
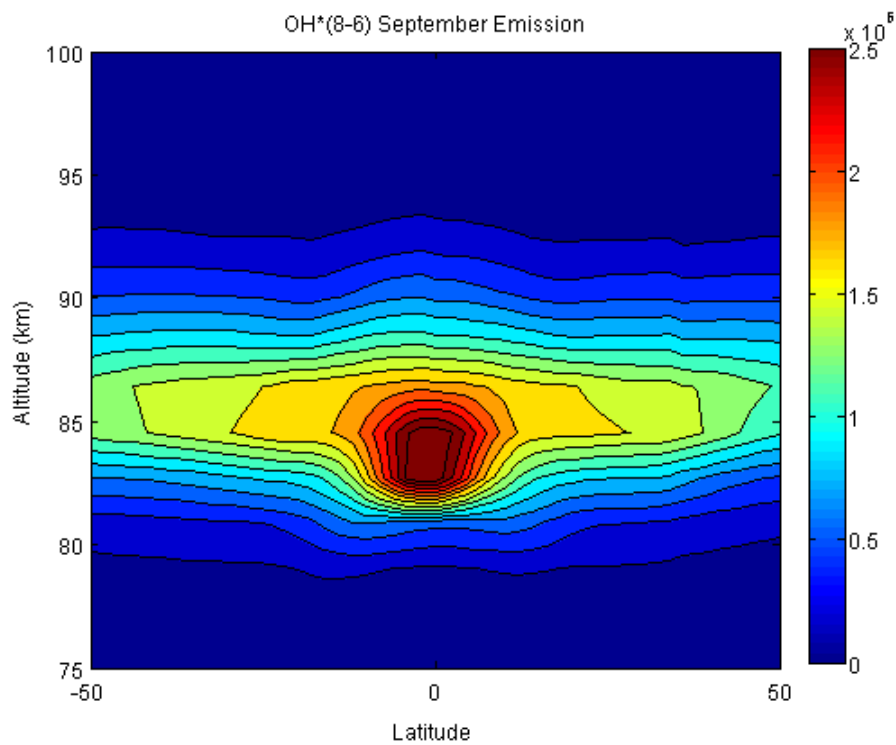
Figure 5.16: CMAT2 altitude-latitude distribution of $OH^*(8-6)$ nightglow emission rate in $cm^{-3} s^{-1}$ at 00 hrs local time for September 21st, 2008.
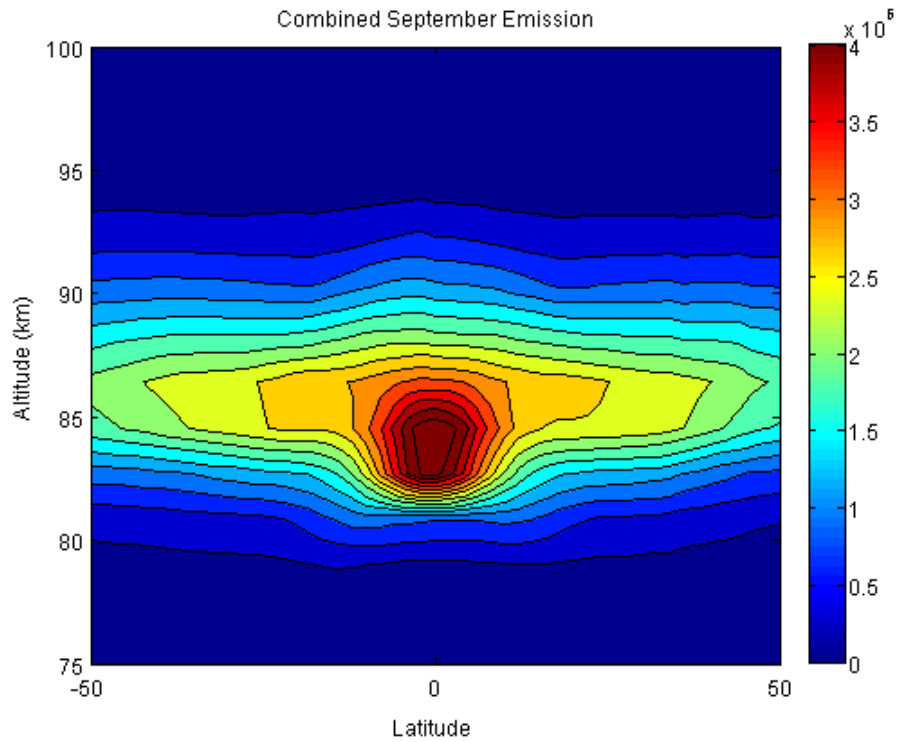
Figure 5.17: CMAT2 altitude-latitude distribution of the combined OH*(9 − 7) and OH*(8 − 6) nightglow emission rate in cm^{-3} s^{-1} at 00 hrs local time September 21st, 2008.
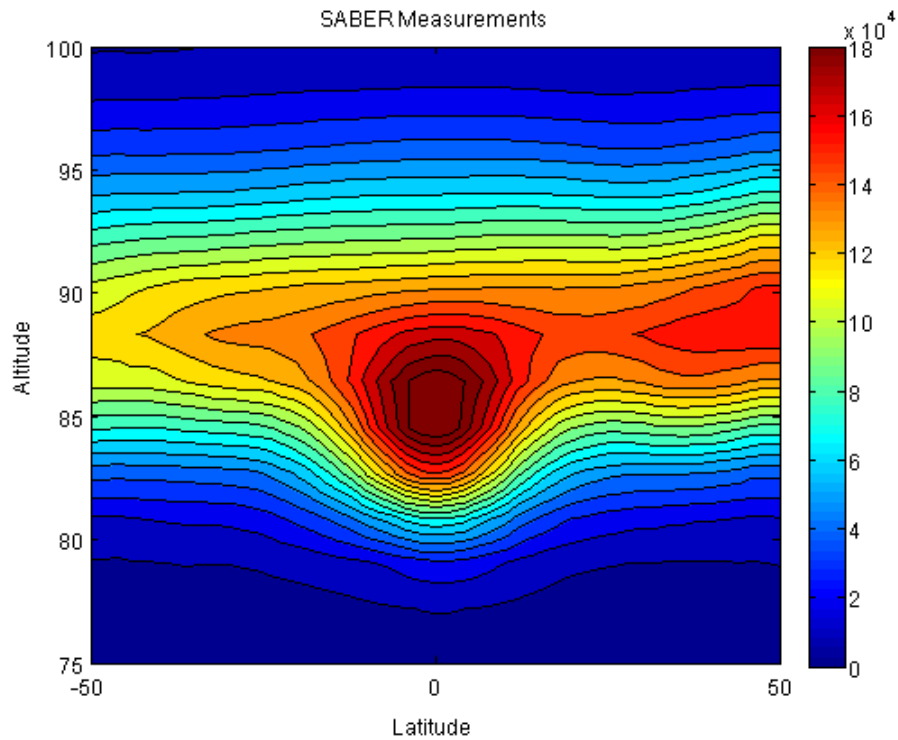
Figure 5.18: SABER altitude-latitude distribution of the combined OH*(9 − 7) and OH*(8 − 6) nightglow emission rate in cm^{-3} s^{-1} at 00 hrs local time for September 21st, 2008 recorded by SABER instrument.

Figures 5.15 to **5.17** show the model results for the emission bands during the September equinox. The results for the different bands are quite similar with the $OH^*(8-6)$ band exhibiting the same global features as the $OH^*(9-7)$ band with only a slightly higher magnitude. As expected during equinox, the peak emission has returned to the equator for both bands and the additional mid-latitude peaks observed during solstice have faded away.

In both the $OH^*(9-7)$ and the $OH^*(8-6)$ emission profiles there exists a peak in the level of emissions at the equator with the peak in the $OH^*(8-6)$ band exhibiting slightly stronger features than the $OH^*(9-7)$ band due to its slightly higher concentration. A minor difference in the altitude of the peak emission also exists within the profiles with the peak in the $OH^*(9-7)$ band occurring at approximately 85 km while the peak in the $OH^*(8-6)$ band occurs at the lower altitude of 84 km in close agreement with the results described in von Savigny *et al.* (2012b) and discussed in detail in **Chapter 4**.

The $OH^*(9-7)$ layer extends over a larger altitude range from $80-94$ km while the $OH^*(8-6)$ band extends from $80-93$ km. The combined emission profile from both bands is presented in **Figure 5.17** and compares favourably with the observational data presented in **Figure 5.18**.

Both figures exhibit a strong peak in the OH^* emissions at the equator, although CMAT2 predicts a magnitude in the emission that is approximately a factor of two stronger than that shown in the SABER data. As with the previous cases, this can attributed to the increased levels of atomic oxygen predicted by the current version of CMAT2.

Despite this difference the morphology of the emission layer in both figures is quite similar with both figures exhibiting a similar emission layer thickness, (extending from $80-95$ km) although low levels of emissions can be seen to extend up to almost 100 km in the observational data. The altitude of the peak emission predicted by CMAT2 at 84 km is in very close agreement with SABER measurements.

The emergence of the secondary peak in the emission shown in **Figure 5.18** now at approximately $50°$ N of the equator is again not evident within any of the CMAT2 profiles. This may be an additional feature of the OH^* during equinox. Given that the

observational data used to produce this graph utilises data up to and over a month prior to equinox it may also be possible that this is a remnant of the summer maximum in the emission displayed earlier in **Figures 5.11** through **5.14**.
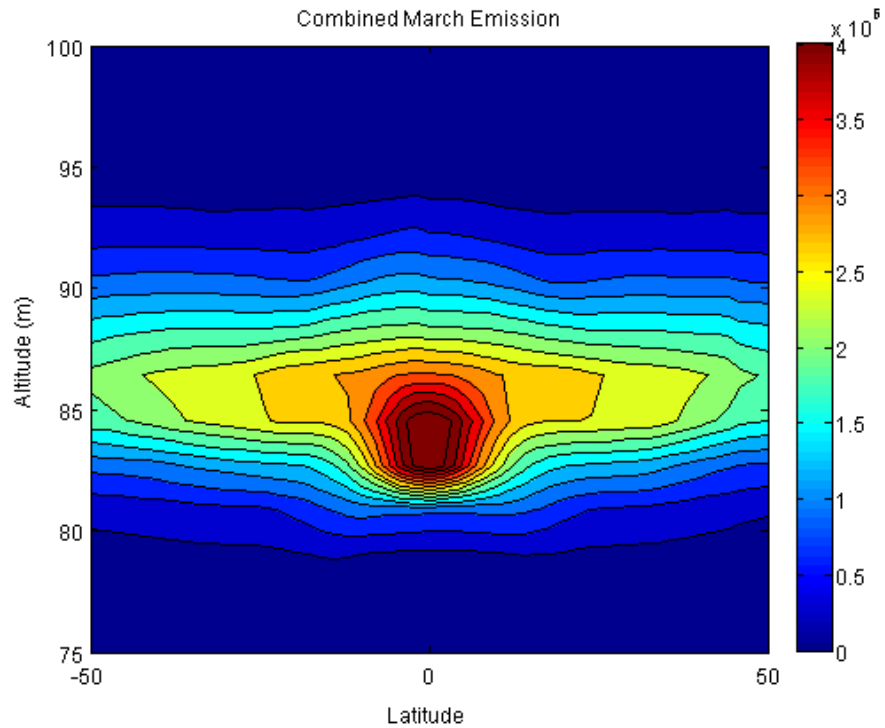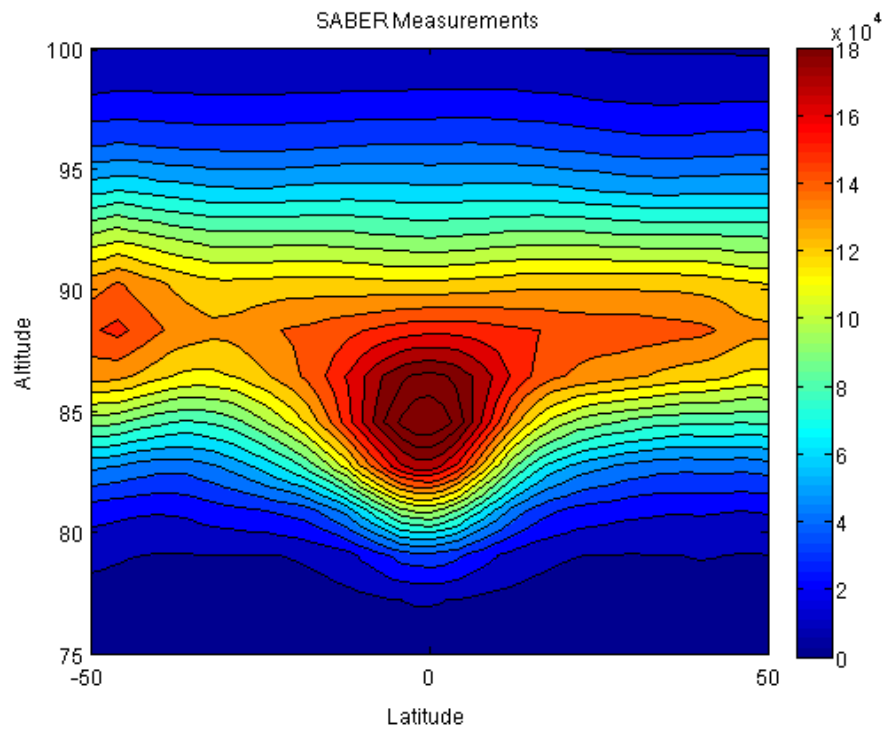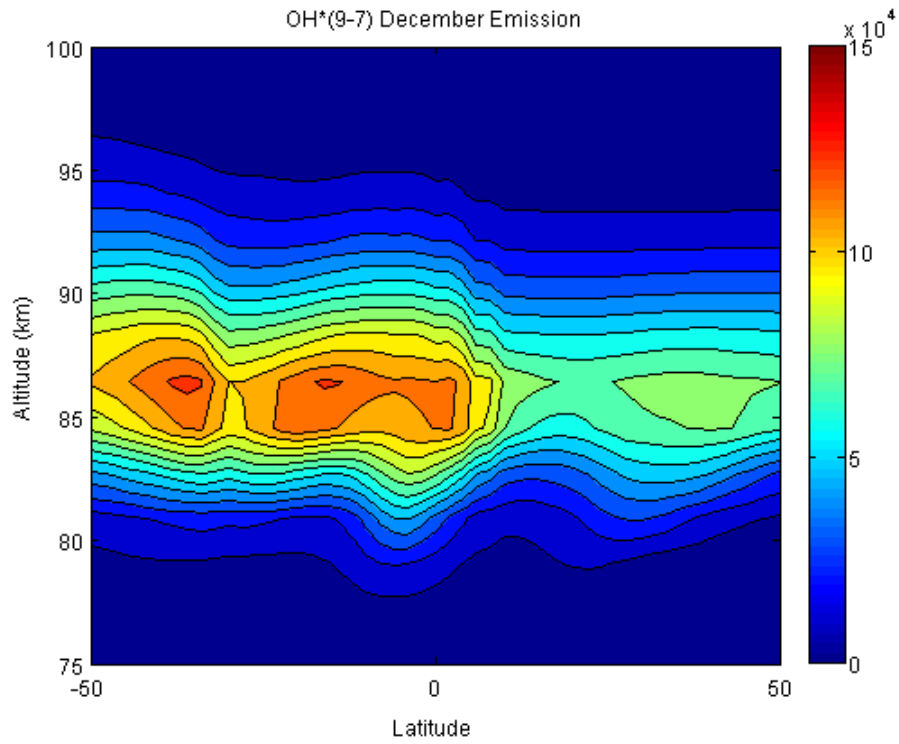
Figure 5.19: CMAT2 altitude-latitude distribution of $OH^*(9-7)$ nightglow emission rate in $cm^{-3} \, s^{-1}$ at 00 hrs local time for December 21st, 2008.
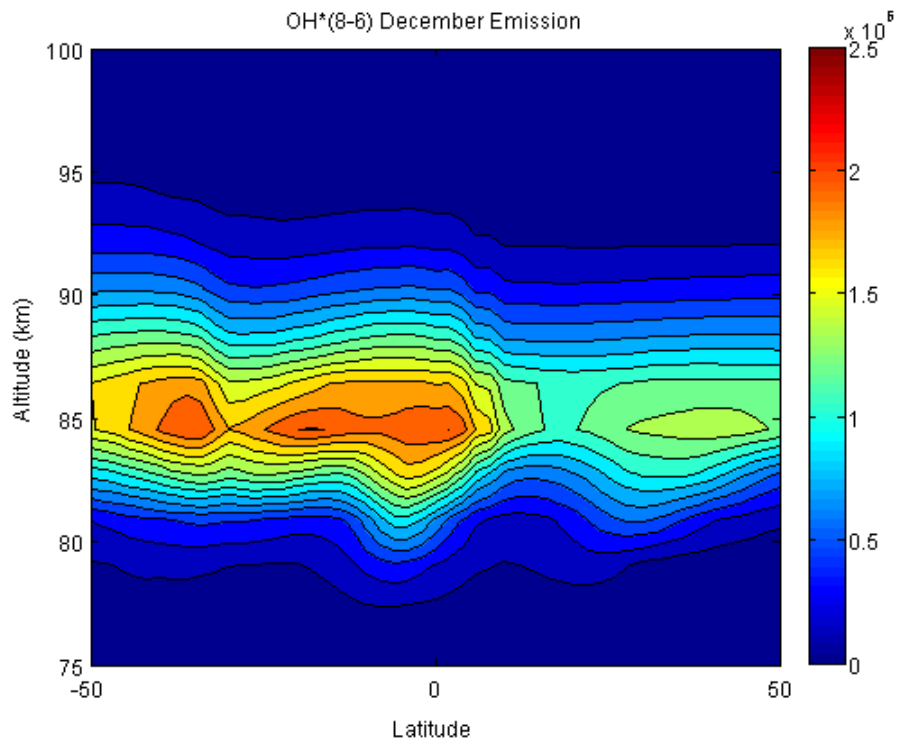
Figure 5.20: CMAT2 altitude-latitude distribution of $OH^*(8-6)$ nightglow emission rate in $cm^{-3} \, s^{-1}$ at 00 hrs local time for December 21st, 2008.
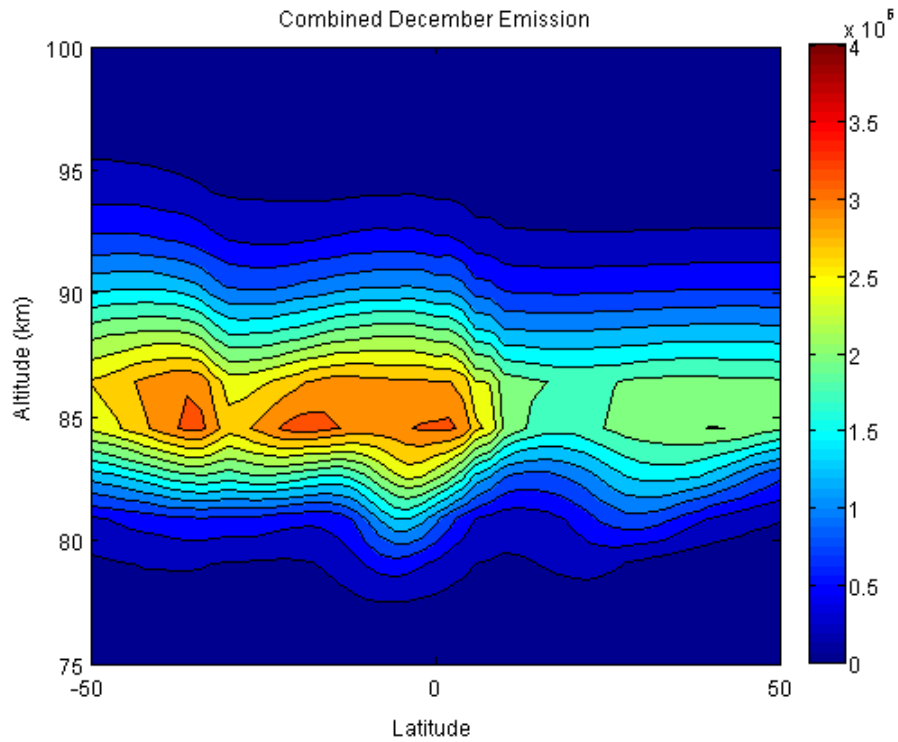
Figure 5.21: CMAT2 altitude-latitude distribution of the combined OH$^*(9-7)$ and OH$^*(8-6)$ nightglow emission rate in cm^{-3} s^{-1} at 00 hrs local time December 21st, 2008.
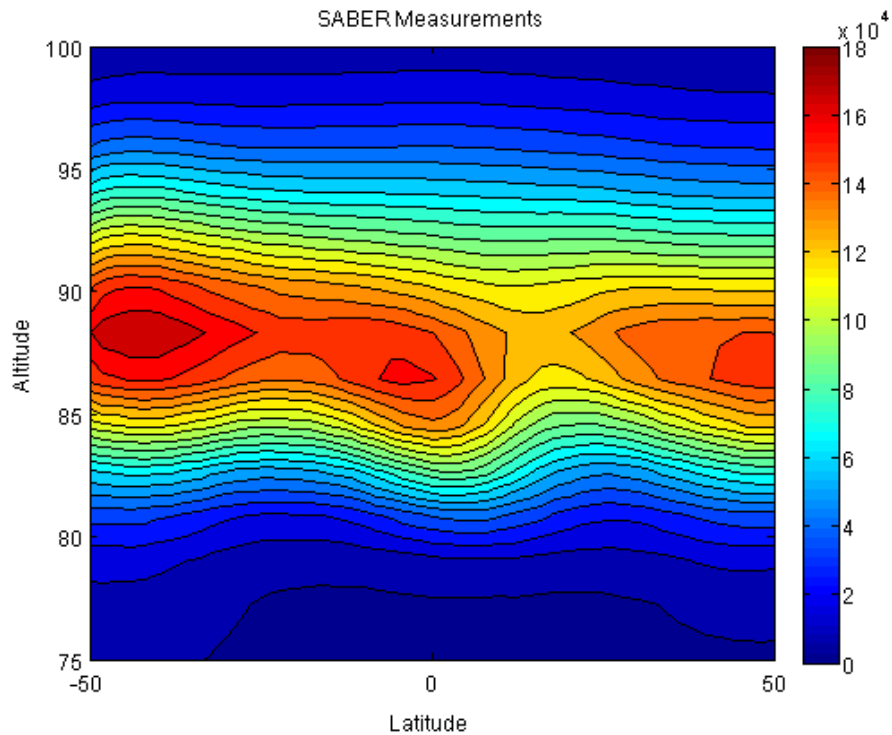
Figure 5.22: SABER altitude-latitude distribution of the combined OH$^*(9-7)$ and OH$^*(8-6)$ nightglow emission rate in cm^{-3} s^{-1} at 00 hrs local time for December 21st, 2008 recorded by SABER instrument.

Figures 5.19 to **5.21** show the model results of the emission band for December solstice conditions. It can be seen that the morphology of both emission bands is quite similar although the magnitude of the $OH^*(8-6)$ band emission is shown to be slightly higher than the $OH^*(9-7)$ band emission at all latitudes. There is a minor difference in the altitude of the peak emission which is still in close agreement with the predictions of von Savigny *et al.* (2012b) as the altitudinal peak in the $OH^*(9-7)$ band is located at 87 km while the peak in the $OH^*(8-6)$ is now located at approximately 86 km.

The morphology of **Figures 5.19** and **5.20** are again very similar although minor difference can be observed. These minor differences can be attributed to the additional sources of production available to the lower levels of OH^* which result from collisional deactivation with the major atmospheric species shown by **Reactions R5.2** to **R5.6**. As stated earlier, given that $OH^*(v=9)$ has only one source of production while $OH^*(v=8)$ has five slight differences in the morphology are expected as these processes compete.

The increased level in emissions within the Southern hemisphere of **Figures 5.19** and **5.20** may be attributed to increased concentrations of atomic oxygen in this hemisphere at this time of year which result from the increased levels of O_2 photo-dissociation during the longer summer days. Furthermore, given that O is one of the principal quenchers of OH^* it is possible that increased collisional quenching of $OH^*(v=9)$ leads to increased production of $OH^*(v=8)$ within the Southern hemisphere augmenting emissions from this vibrational level. Since $OH^*(v=9)$ has only one chemical source of production these effects would not be observed in the $OH^*(9-7)$ emission band.

The increasing altitude of the peak emission with latitude in **Figures 5.19** and **5.20** is a significant feature of the emission showing that once again, the CMAT2 model is at least in part able to predict certain effects attributed to the mesospheric circulation within the atmosphere. This circulation results in a mesopause that exists at higher altitudes and exhibits colder temperatures during the summer months, and lower altitudes exhibiting warmer temperatures during the winter months as is visible within the above figures as detailed in **Chapter 1**.

Figure 5.21 shows the combined $\mathrm{OH}^*(9-7)$ and $\mathrm{OH}^*(8-6)$ emission profile for comparison with **Figure 5.22** which shows SABER observational data from the same period. As with the other three cases it can be seen that the morphology of the two figures is quite similar although CMAT2, as expected, over-predicts the number of emissions at all latitudes by approximately a factor of 2.

Two additional peaks in the emission occur at latitudes of approximately $\pm 40°$. The Southern hemisphere peak is shown by both SABER and CMAT2 to have a larger magnitude than the Northern hemisphere peak. However, CMAT2 does not predict the smooth emission band joining both the southern latitude and equatorial peaks, but establishes instead a minor peak at approximately $20°\,\mathrm{S}$. Once again increased levels of emissions at the equator obscure the smooth transition in emissions displayed in the SABER data in **Figure 5.22**.

The altitudinal variation in peak emission heights is also visible in both figures and both figures show approximately the same variation in the peak emission heights.

Utilising data from **Figures 5.9**, **5.13**, **5.17** and **5.21**, **Figure 5.23** plots the overall seasonal variation in the combined $\mathrm{OH}^*(9-7)$ and $\mathrm{OH}^*(8-6)$ emission with time of year. Two local times were selected so that the variation could be compared to observed features in the seasonal variation recorded by the SABER instrument and presented in Marsh *et al.* (2006). **Figure 5.24** shows the seasonal variation in emissions for the years $2002-2004$ derived from SABER measurements.
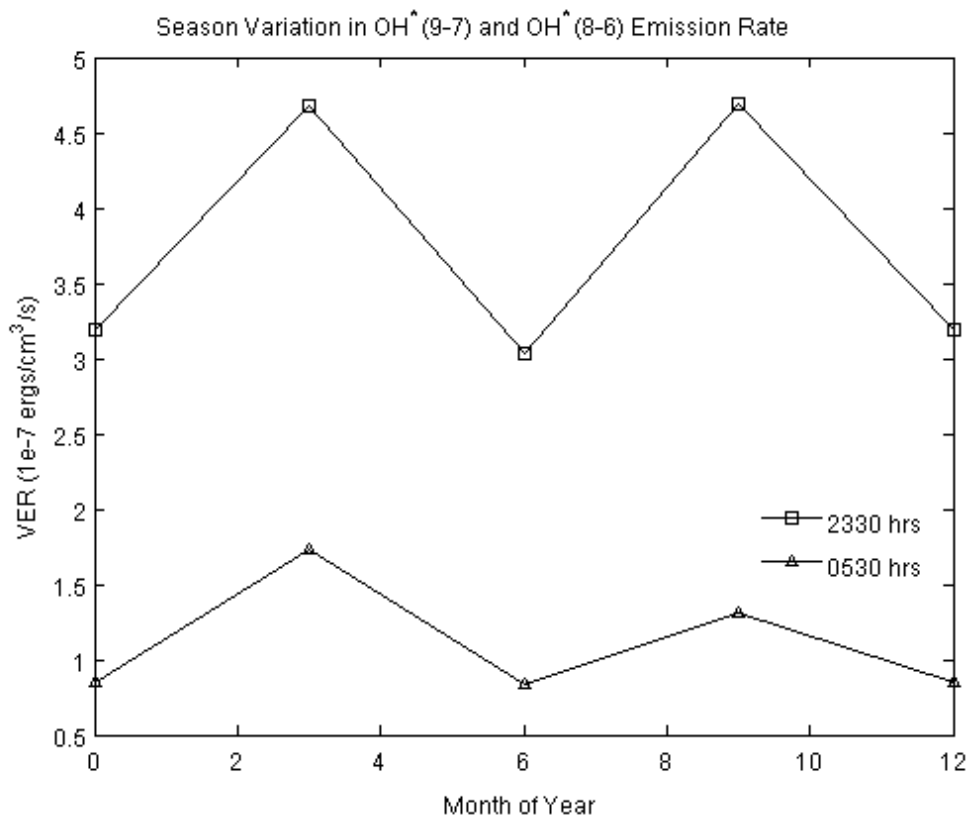
Figure 5.23: Seasonal variation in the combined $OH^*(9-7)$ and $OH^*(8-6)$ volume emission rates produced by the CMAT2 model for local times of 2330 hrs (squares) and 0530 hrs (triangles) 2008.
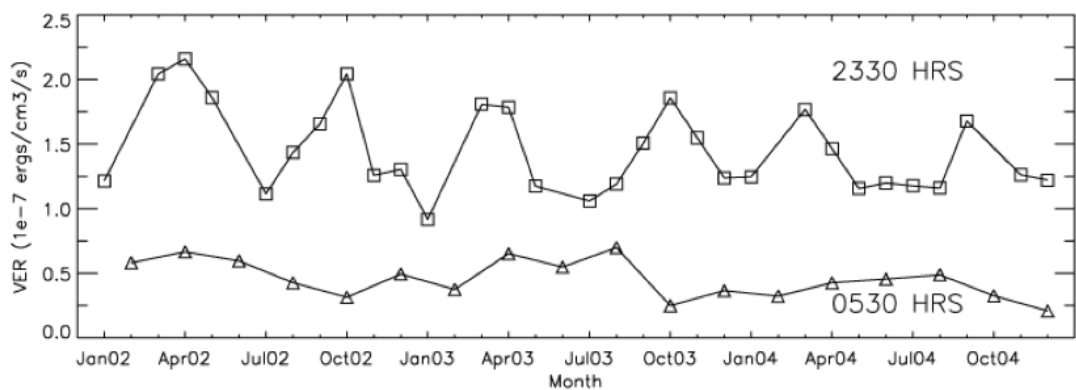
Figure 5.24: Seasonal variation in the combined $OH^*(9-7)$ and $OH^*(8-6)$ volume emission rates observed by the SABER instrument for local times of 2330 hrs (squares) and 0530 hrs (triangles) from years $2002-2004$ (Marsh *et al.,* 2006).

While these data presented in **Figures 5.23** and **5.24** are from different years (CMAT2 data is predicted for year 2008) the trend in the seasonal variation produced by the

CMAT2 model is similar to the features recorded by SABER and repeated annually. At 2330 hrs, during the March equinox, the emission reaches a maximum before dropping to a minimum at the June solstice. The emission levels subsequently increase reaching a second maximum during the autumnal equinox before decreasing again in the run up to the December solstice. This feature is observed in each year of SABER data.

At 0530 hrs CMAT2 predicts that the variation in the emission has been substantially reduced, although a certain amount of variation is still evident. Peaks in the emissions still occur during equinox and minima are predicted at solstice. SABER data also reveals a significant drop in the variability of the emission rate at this time. However, the magnitude of SABER variability is lower than that predicted by CMAT2 suggesting that the model over-predicts the variability at this local time.

While this is a basic seasonal comparison, it can be seen that CMAT2 does predict the season variability in the OH^* emission observed in the SABER data. The magnitude of the variability is similar at 2330 hrs with a value of approximately 1×10^{-7} ergs/ cm^3/s observed in both model results and SABER data. However, the magnitude of the variability predicted by CMAT2 at 0530 hrs is approximately a factor of two higher than observed in the SABER data. It can also be seen that at all times of year CMAT2 typically predicts emission rates that are a factor of two higher than those observed in the SABER measurements.

5.4 Study 3: Seasonal Variations in $\mathbf{OH}^*(5-3)$ and $\mathbf{OH}^*(4-2)$ Emissions

In many previous studies authors have limited the analyses of model results and observational data to just one channel of the SABER instrument, typically the channel dedicated to the higher vibrational level emissions. Given that this thesis attempts to model all emissions from the different vibrational state of OH^* it is also necessary to compare the model results in respect of the lower band. While the general features of the emissions at lower levels are similar to emissions from the higher vibrational levels, the multiple sources of production and loss associated with the lower levels make this an important comparison. From these results it can be determined how well the CMAT2 model represents the collisional deactivation and quenching reactions of the upper vibrational states which produce the lower vibrational states.

For this comparison, individual emission profiles for the $\mathrm{OH}^*(5-3)$ and $\mathrm{OH}^*(4-2)$ bands will not be presented as the morphology of each band shows only minor differences. The magnitudes of the emissions are the only significant alteration to the profiles. This was shown previously for the upper vibrational levels ($\mathrm{OH}^*(9-7)$ and $\mathrm{OH}^*(8-6)$) in **Section 5.3**. Only the combined profiles are presented for comparison with SABER data.
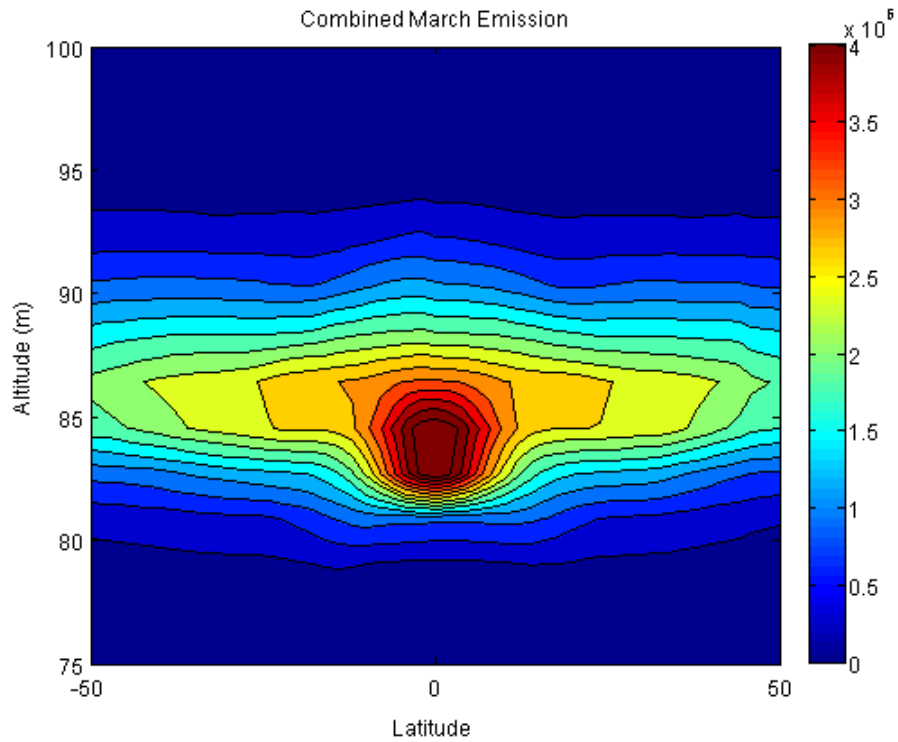
Figure 5.25: CMAT 2 altitude-latitude distribution of the combined $OH^*(5-3)$ and $OH^*(4-2)$ nightglow emission rate in $cm^{-3}\ s^{-1}$ at 00 hrs local time for March 21st, 2008.
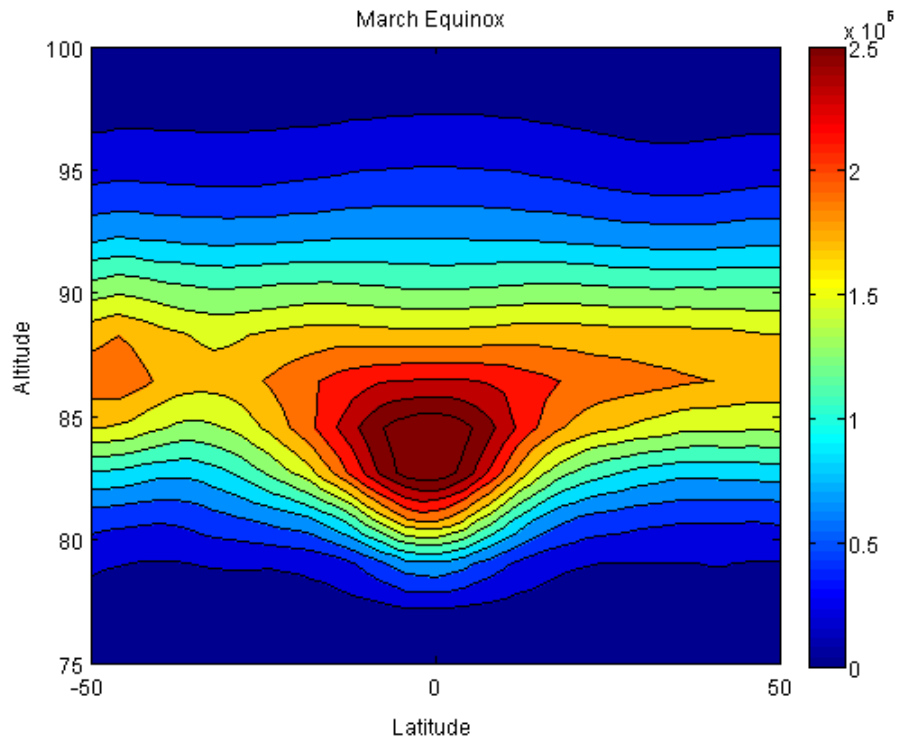
Figure 5.26: SABER altitude-latitude distribution of the combined $OH^*(5-3)$ and $OH^*(4-2)$ nightglow emission rate in $cm^{-3}\ s^{-1}$ at 00 hrs local time for March 21st, 2008 recorded by SABER.

Figure 5.25 shows the modelled emission from the $OH^*(5-3)$ and $OH^*(4-2)$ bands for the March solstice between $\pm 50°$ latitude. **Figure 5.26** shows the observed emissions from the SABER instrument for the same period. As with the analysis of the previous SABER channel it can be seen that CMAT2 successfully models the overall general features of the emission during equinox; although the modelled emissions are now typically stronger by a factor of 1.5 compared with a factor of 2 for the high vibrational levels.

In both the modelled and observed figures a peak in the emission occurs over the equator at an altitude of 84 km which is in agreement with the altitudinal predictions of von Savigny *et al.* (2012b). At higher latitudes the peak in the emission rises to approximately 86 km in both the Northern and Southern hemispheres showing a clear altitudinal variation in the peak emission with latitude. It can also be seen that the modelled emission layer is somewhat thinner than the observed emission layer extending from $80-94$ km rather than the observed $78-96$ km. It is worth noting here that the level of emissions below 80 km and above 92 km, in both profiles, contribute only slightly to the overall total emission. The majority of emissions occur in a 10 km layer surrounding the altitudinal peak.

A secondary peak in the observed emission profile appears in the mid-latitudes which is not predicted by the CMAT2 model. This is not entirely unexpected as the SABER data used to compile **Figure 5.26** includes data from over a month prior to the actual date of the equinox. These data are therefore likely to include some features from the previous December solstice mid-latitude maximum in the emission which occurs at the same latitude as the secondary peak.

Baker *et al.* (2007) further investigates emissions from the $OH^*(5-3)$ and $OH^*(4-2)$ bands during spring equinox conditions. **Figure 5.27** shows the global distribution of a seven-day average in the magnitude of the peak VER (volume emission rate) as recorded by SABER during the spring equinox of 2005. **Figure 5.28** shows the global distribution of the corresponding altitudes of the peak VER's.
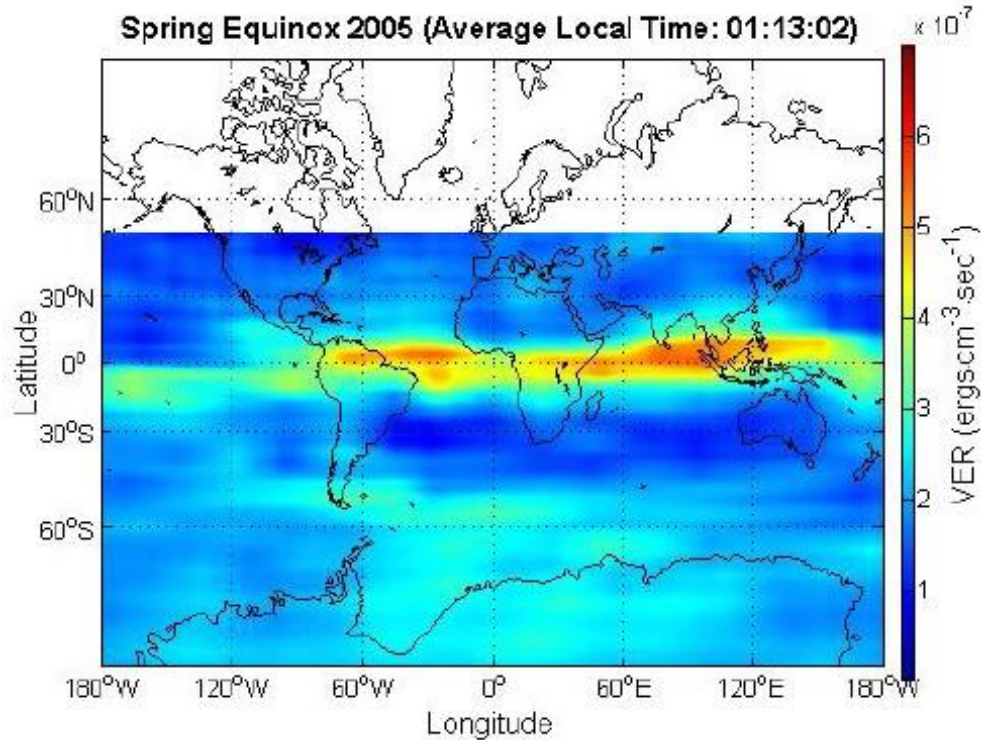
Figure 5.27: Peak $OH^*(5-3)$ and $OH^*(4-2)$ mesospheric VER night-time airglow global distribution, 7 day average at the 2005 spring equinox from SABER (Baker *et al.*, 2007).
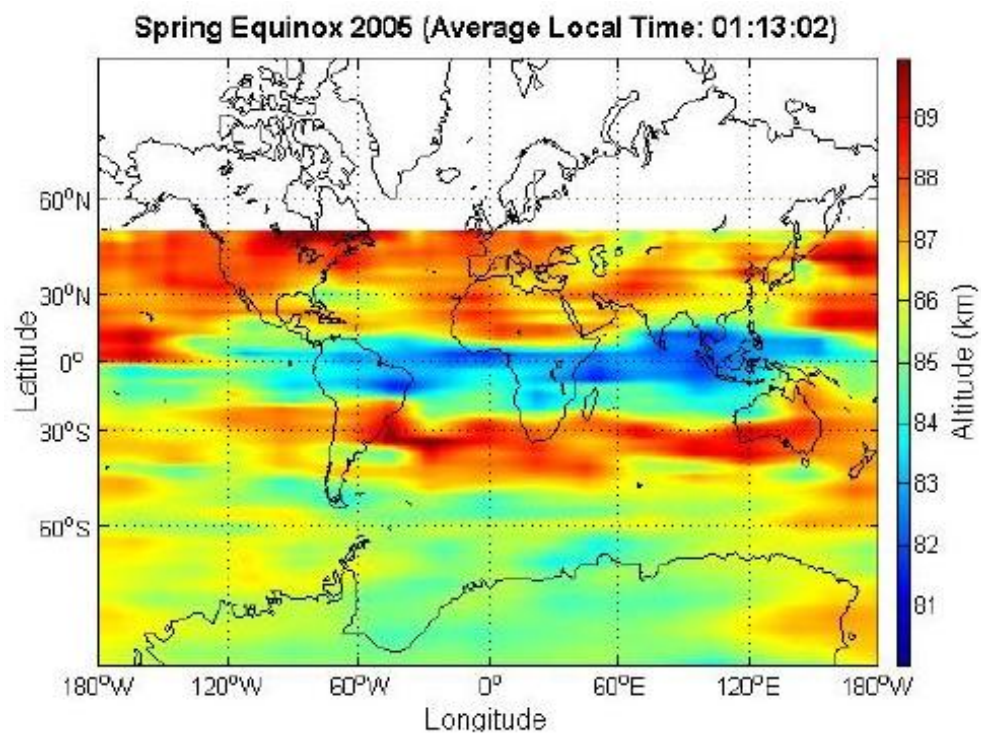
Figure 5.28: Altitudinal distribution of the peak $OH^*(5-3)$ and $OH^*(4-2)$ mesospheric VER night-time airglow global distribution, 7 day average at the 2005 spring equinox from SABER (Baker *et al.*, 2007).

A direct comparison of **Figures 5.25** and **5.26** with **Figures 5.27** and **5.28** is not possible for reasons outlined below and in much greater detail in **Section 5.6**; however, a number of similar and corresponding features can be identified. Firstly, **Figure 5.27** shows a clear equatorial peak in the emission rate at all longitudes. This corresponds to the equatorial peaks in both **Figures 5.25** and **5.26**. The latitudinal extent of these peaks can also be seen to be identical, confined within latitudes of approximately $\pm 15°$. A minor secondary peak in the emission at mid- to high-latitudes is observed between longitudes of 60° W and 60° E of **Figure 5.27** which correspond to the secondary mid-latitude peak in **Figure 5.26**. Beyond these longitudes no appreciable secondary peak in the emission is observed as suggested in the CMAT2 predictions in **Figure 5.25**. The variation in the emissions at mid- to high-latitudes appear to follow a wave feature with a wavenumber 1. This will be further investigated in **Section 5.6**.

Looking at the altitudinal heights of the peak VER's displayed in **Figure 5.28** it can be seen that equatorial peaks occur at altitudes lower than at other latitudes at all longitudes. This is in complete agreement with the CMAT2 results in **Figure 5.25** which shows an altitudinal difference of approximately 4 km between the emission peak at the equator and the emission peak at $\pm 50°$. This is also in agreement with the SABER data which shows that the peak VER varies typically between approximately 83 and 88 km.

A more extensive comparison between the CMAT2 results and the results presented in Baker *et al.* (2007) would be desirable. However, as will be discussed in **Section 5.6** and further in **Chapter 6**, CMAT2 is not designed for detailed studies of longitudinal variations at a fixed local time. Any attempt to produce a figure similar to **Figure 5.27** from CMAT2 results would be further complicated by the altitudinal variance in the peak emissions displayed in **Figure 5.28** making such an effort difficult to justify. Therefore, this comparison with Baker *et al.,* (2007) results is presented here and only briefly in **Section 5.6**.
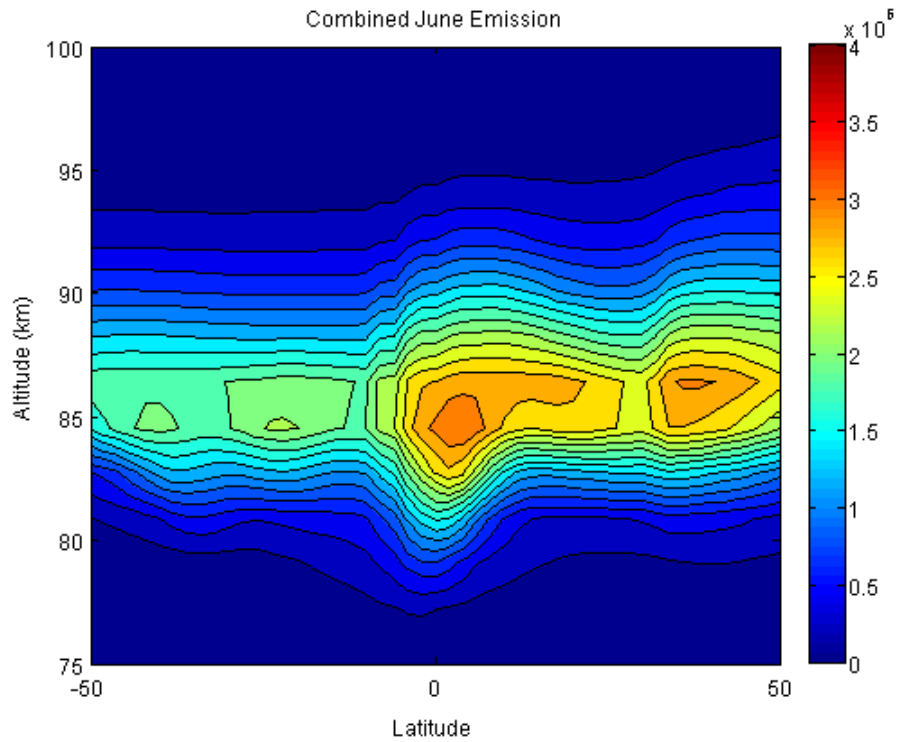
Figure 5.29: CMAT2 altitude-latitude distribution of the combined $OH^*(5-3)$ and $OH^*(4-2)$ nightglow emission rate in $cm^{-3} s^{-1}$ at 00 hrs local time for June 21st, 2008.
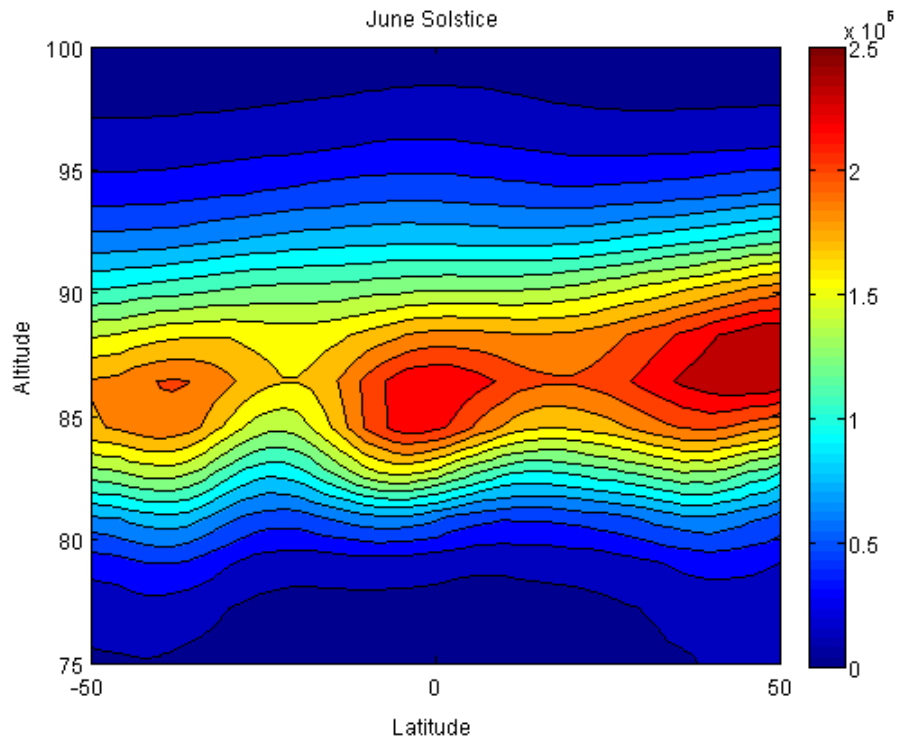
Figure 5.30: SABER altitude-latitude distribution of the combined $OH^*(5-3)$ and $OH^*(4-2)$ nightglow emission rate in $cm^{-3} s^{-1}$ at 00 hrs local time for June 21st, 2008 recorded by SABER.

Figure 5.29 shows the combined modelled emissions for the $OH^*(5-3)$ and $OH^*(4-2)$ bands during the June solstice of 2008 while **Figure 5.30** shows the observed emissions for the same period. Once again it can be seen that CMAT2 successfully models the general features of the emission although the strength of the emission is still approximately 1.5 times stronger than the observed emission at most latitudes, although somewhat less so within the Southern hemisphere.

Both CMAT2 and SABER reveal a number of peaks in the emissions at the equator and at approximately $\pm40°$ latitude. In both cases the strongest peak is located at $40°\,N$ although the equatorial peak in the CMAT2 emissions is only marginally less than the northern peak. In both cases the southern peak is the weakest. Looking at the latitudinal variation in the emissions CMAT2 shows an overall larger variation which is less smooth than that demonstrated in the observed emissions. As with the analysis of the upper vibrational levels it appears that during solstice, CMAT2 predicts increased levels of OH^* production at the equator. This obscures the smooth transition in the emission profile with latitude shown in the SABER measurements.

A clear altitudinal variation in the emission is visible in both profiles with emissions in the Northern hemisphere peaking at altitudes surrounding $87\,km$. The altitudinal gradient predicted by CMAT2 is steeper than the observed gradient as the modelled emissions in the Southern hemispheric peak is located at approximately 85 km while the observed emission profile shows a peak at 86 km. As with the previous analysis this variation in peak altitudes can be directly related to the mesospheric circulation described in **Chapter 1**.
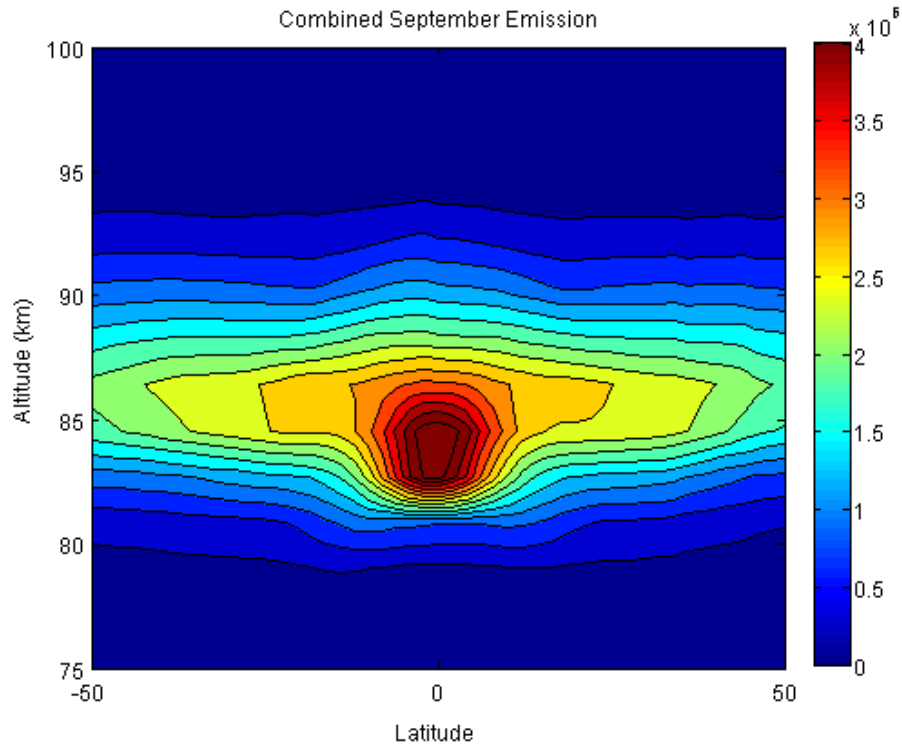
Figure 5.31: CMAT2 altitude-latitude distribution of the combined $OH^*(5-3)$ and $OH^*(4-2)$ nightglow emission rate in $cm^{-3}\,s^{-1}$ at 00 hrs local time for September 21st, 2008.
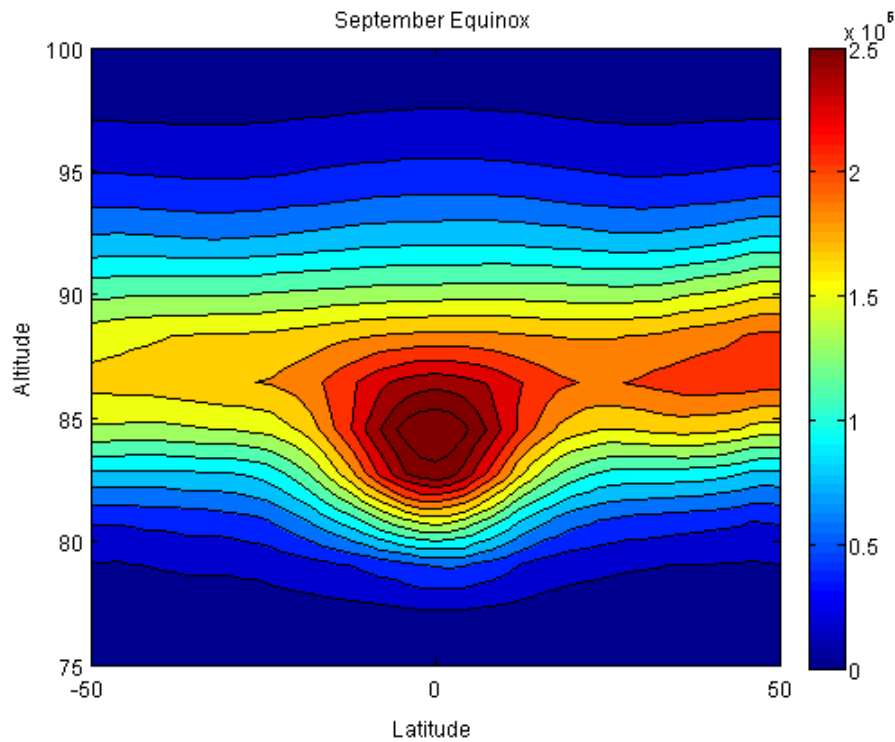
Figure 5.32: SABER altitude-latitude distribution of the combined $OH^*(5-3)$ and $OH^*(4-2)$ nightglow emission rate in $cm^{-3}\,s^{-1}$ at 00 hrs local time for September 21st, 2008 recorded by SABER.

Figure 5.31 shows the modelled emission from the $OH^*(5-3)$ and $OH^*(4-2)$ bands for the September equinox between $\pm 50°$ latitude. **Figure 5.32** shows the observed emissions from the SABER instrument for the same period. As with the analysis of the $2\,\mu$m channel ($OH^*(9-7)$ and $OH^*(8-6)$) it can be seen that CMAT2 successfully models the overall general features of the emission during the equinox although the modelled emissions are now typically stronger by a factor of 1.5.

In both the modelled and observed figures, a peak in the emission occurs over the equator at an altitude of 84 km which is in agreement with the altitudinal predictions of von Savigny *et al.* (2012b). At higher latitudes the peak in the emission rises to approximately 86 km in both the Northern and Southern hemispheres showing a clear altitudinal variation in the peak emission with latitude. The modelled emission layer is somewhat thinner than the observed emission layer extending from $80-94$ km rather than the observed $78-96$ km. It is again worth noting here that the level of emissions below 80 km and above 92 km, in both profiles, contribute only slightly to the overall total emission. The majority of emissions occur in a 10 km layer surrounding the altitudinal peak.

The secondary peak in the observed emission profile once again appears in the mid-latitudes and is not predicted by the CMAT2 model. Again this is not entirely unexpected as the SABER data used to compile **Figure 5.31** includes data from over a month prior to the actual date of the equinox. These data are therefore likely to include some features from the previous June solstice maximum in the emission which occurs at the same latitude as the secondary peak.
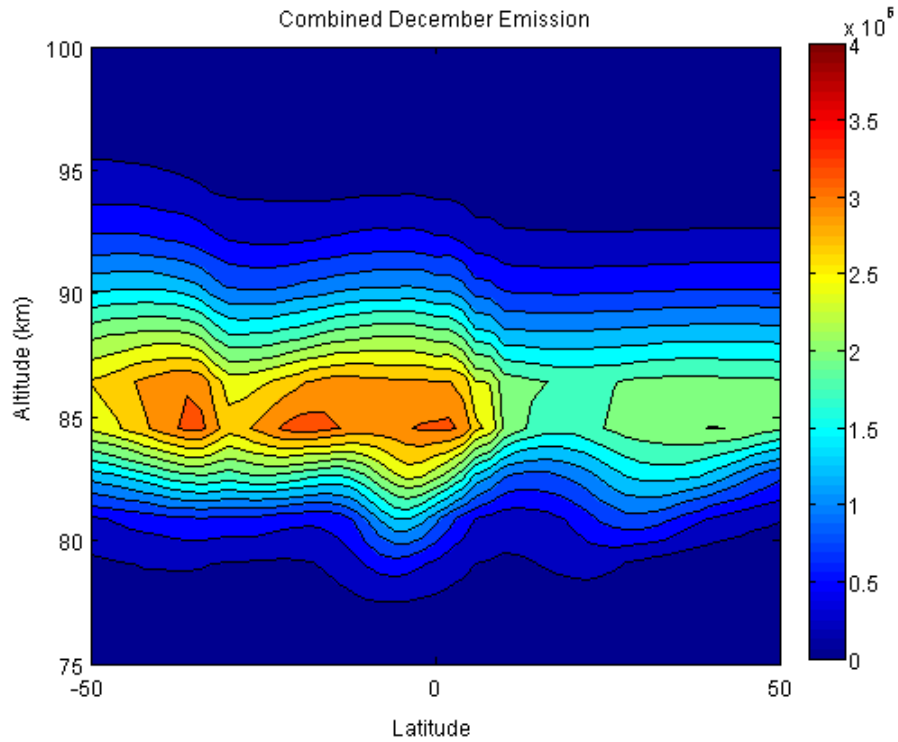
Figure 5.33: CMAT2 altitude-latitude distribution of the combined $\text{OH}^*(5-3)$ and $\text{OH}^*(4-2)$ nightglow emission rate in $\text{cm}^{-3}\,\text{s}^{-1}$ at $00\,\text{hrs}$ local time for December 21st, 2008.
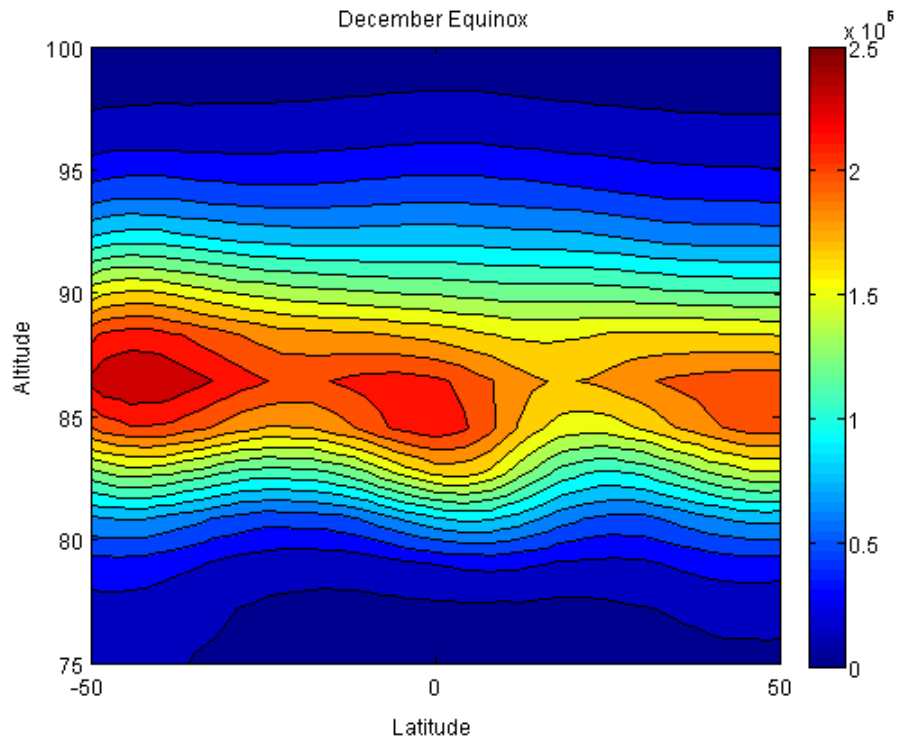
Figure 5.34: SABER altitude-latitude distribution of the combined $\text{OH}^*(5-3)$ and $\text{OH}^*(4-2)$ nightglow emission rate in $\text{cm}^{-3}\,\text{s}^{-1}$ at $00\,\text{hrs}$ local time for December 21st, 2008 recorded by SABER.

Figure 5.33 shows the combined modelled emissions for the $OH^*(5-3)$ and $OH^*(4-2)$ bands during the December solstice of 2008 while **Figure 5.34** shows the observed emissions for the same period. Once again it can be seen that CMAT2 successfully models the general features of the emission although the strength of the emission is still approximately 1.5 times higher than the observed emission at most latitudes. This factor decreases in the Northern hemisphere.

Both CMAT2 and SABER reveal a number of peaks in the emissions at the equator and at approximately $\pm 40°$ latitude. In both cases the strongest peak is located at $40°$ S although the equatorial peak in the CMAT2 emissions is only marginally less than the northern peak. In both cases the southern peak is the weakest. Looking at the latitudinal variation in the emissions CMAT2 shows an overall larger variation with latitude which is also less smooth than that demonstrated in the observed emissions. As with the analysis of the upper vibrational levels it appears that during solstice, CMAT2 predicts an increased level of OH^* production at the equator which prevents the smooth variation in the emission profile with latitude shown in the SABER measurements.

A clear altitudinal variation in the emission can be seen with emissions in the Northern hemisphere showing a peak at approximately 87 km in both profiles. The altitudinal gradient predicted by CMAT2 is steeper than the observed gradient. In the modelled emissions the Southern hemispheric peak is located at approximately 85 km while the observed emission profile shows a peak at 86 km. As with the previous analysis this variation in peak altitudes can be directly related to the mesospheric circulation previously described in **Chapter 1**.

5.5 Summary of Study 2 (5.3) and Study 3 (5.4)

In **Sections 5.3** and **5.4** the results of the CMAT2 model for 4 OH^* emission bands have been compared to observations made by the SABER instrument. In general it has been seen that CMAT2 successfully models a number of the primary features observed in these emissions including the location of the emission peaks throughout the year, as well as the altitudinal and latitudinal variations in the emissions with respect to time of year.

While these comparisons may appear repetitive, especially considering the similarity of features within each of the observed bands described, it is important to include all of these data to fully emphasise the model's capabilities. By analysing multiple OH* levels it is possible to test the model's capability to predict the general features of the emissions as well as the magnitude of the emissions from different vibrational levels. This ensures that the model does not become unstable predicting the lower vibrational levels.

In total, CMAT2 models 37 separate emission bands from the different vibrational states of OH*, the majority of which do not have dedicated observational channels today. No stringent test of these additional emission bands has been conducted as of yet although it is reasonably certain that the same characteristics and general features follow through for all emission bands.

It has been seen that in all cases the CMAT2 model predicts higher levels of emissions than those observed by the SABER instrument. This can be attributed to a known feature of the CMAT2 model which is currently under investigation (Dobbin, 2008). It is expected that once this issue is resolved, much better agreement will be obtained between model predictions and measurements. Once this has been completed it may be instructive to incorporate additional sources of OH* production. This is discussed in greater detail in **Chapter 6**. However, to do so at the present time, when the concentrations of the different vibrational levels are already in excess of the observed quantities would be difficult to justify.

Finally, this analysis has provided an important check of not only the CMAT2 models capability to predict emission strengths but also to accurately predict the mesospheric circulation within the atmosphere. From the predicted emission bands it can be seen that during solstice there is a clear difference in the altitudinal profiles of the mesopause which is in line with observations.

It is worth noting at this time that Smith *et al.* (2010) report atomic oxygen concentrations, retrieved from SABER data, which are typically a factor of between 2 and 5 times higher than the concentrations determined from other measurements (McDade *et al.,* 1985; Russell *et al.*, 2005; Mlynczak *et al.,* 2007) and used in empirical models. These night-time atomic oxygen concentrations have been derived from the

SABER observations of the $OH^*(9-8)$ and $OH^*(8-6)$ bands. While this result initially appears to support the atomic oxygen concentrations calculated by the CMAT2 model it is doubtful that this is the case. Verification of the SABER results is still required although at the time of writing there is no direct reason to suspect the instrument of being in error (Smith *et al.* 2010).

If these results can be verified from additional measurements, revealing O concentrations in better agreement with CMAT2 predictions, it is still unlikely that CMAT2 is calculating O concentrations correctly. This is because CMAT2 uses initial concentrations for O determined from the MSISE-90 empirical model. These concentrations are a factor of two lower than those predicted from the SABER measurements and it is unlikely that CMAT2 could recover such a large quantity of atomic oxygen especially over the course of the short-term model runs presented. Furthermore, if the concentrations of O derived from SABER measurements are assumed to be correct, it follows that the OH^* emissions calculated by CMAT2 should also be correct given that both the model and observations exhibit atomic oxygen concentrations that are a factor of two higher than expected. This would suggest that some other feature in the atmosphere calculated for by CMAT2 is augmenting the OH^* emissions by a factor of two. Inclusion of the reaction

$$O + O_3 \rightarrow O_2 + O_2$$

<div align="right">(R5.7)</div>

into the list of reactions required to maintain photochemical equilibrium within the mesopause, and which is incorporated into the CMAT2 model, could increase the concentrations of atomic oxygen within the region, although Smith *et al.* (2010) suggest that the increase would be no more than 40%. As will be detailed later, CMAT2 predicts mesopause temperatures that are approximately $10\,\mathrm{K}$ higher than SABER measurements which would counteract this effect. Clearly more study in this area is required.

Studies 1, 2 and 3 (**Sections 5.2**, **5.3**, and **5.4**) have tested the CMAT2 models capabilities to predict OH^* emissions both temporally (diurnal and seasonal variations) and spatially (altitudinal and latitudinal variations). As such only longitudinal variations remain to be discussed and are the subject of Study 4 (**Section 5.6**).

5.6 Study 4: Longitudinal Variations in OH^*

In the previous sections of this chapter variations in OH^* emissions with respect to altitude, latitude, local time and season have been investigated and in most cases it has been found that CMAT2 gives reasonable agreement with the observed features within the emissions. In this section the longitudinal variation in OH^* emissions will be investigated.

Baker *et al.* (2007) presents SABER observations of the longitudinal distribution in the $\text{OH}^*(5 - 3)$ and $\text{OH}^*(4 - 2)$ emissions during spring equinox conditions. These results have already been discussed in **Section 5.3** in relation to altitudinal and latitudinal variations.

Xu *et al.,* (2010) performed a more extensive analysis of the longitudinal variations in OH^* emissions using SABER data from 2002-2008. In this analysis, six 40-day intervals were chosen centred on days 15, 75, 135, 200, 260 and 320 of the year. Profiles within these data for which the local time was within 2 hours of midnight were used to construct images of the longitudinal variations in the $\text{OH}^*(9 - 7)$ and $\text{OH}^*(8 - 6)$ emissions between ± 53 ° latitude.

Figure 5.35 shows the results that correspond closest to equinox and solstice conditions from Xu *et al.* (2010). On the left are 'brightness maps' in which the OH^* emissions have been integrated from $75 - 100$ km between $\pm 53°$ latitude. On the right are individual profiles of the longitudinal variations in the emissions at latitudes $+20°, 0°,$ and $-20°$.
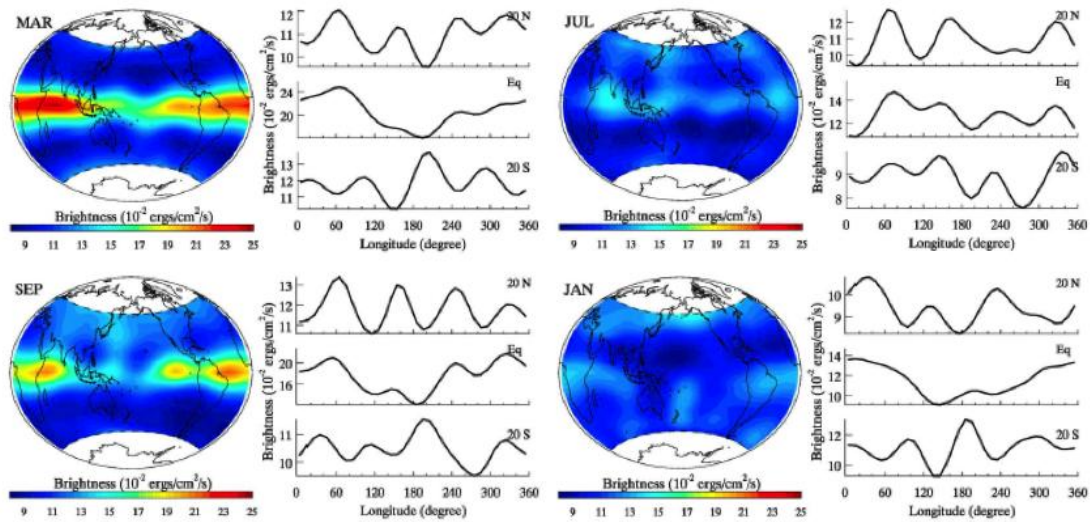
Figure 5.35: (left panels) Maps of 40 day average 2.0 μm OH*(9 − 7) and OH*(8 − 6) airglow brightness for 4 periods (March, July, September and January) averaged from 2002 to 2008; 53° N to 53° S. (right panels) The OH* airglow brightness at 20° N, 0°, and 20° S. (Note that the scales of the plots differ) (Xu *et al.*, 2010).

A number of features are evident within the data including a strong equatorial enhancement during equinox conditions also observed in **Figure 5.27**. The level of emissions during the March equinox is stronger than at any other time of year, including the September equinox. Airglow features during both solstices are significantly weaker than at equinox, especially over the equator, where the difference is up to a factor of two. These seasonal variations in the OH* can be attributed to seasonal changes in the diurnal tides which are known to have largest amplitudes during equinox (Marsh *et al.* 2006) and will be discussed in more detail in **Section 5.7**.

In the right panels of **Figure 5.35** are 3 individual longitudinal profiles for both equinox and solstice conditions which are used to identify waves features within the emissions. In the majority of these profiles a wavenumber 4 feature (4 complete periods over the full range of longitude) can be identified. The equatorial profiles also show a wavenumber 1 feature. This is most evident in the March equinox and December solstice profiles of **Figure 5.35** and in the mid- to high-latitude regions of **Figure 5.27**. **Figures 5.36** to **5.39** show individual longitudinal profiles for the combined OH*(9 − 7), OH*(8 − 6) emissions, produced by CMAT2, for equinox and solstice conditions of 2008. The three profiles in the right panels of each figure represent latitudes of +20°, 0°, and −20° and each emission profile has been integrated from 75 − 100 km in line with the profiles seen in **Figure 5.35**.
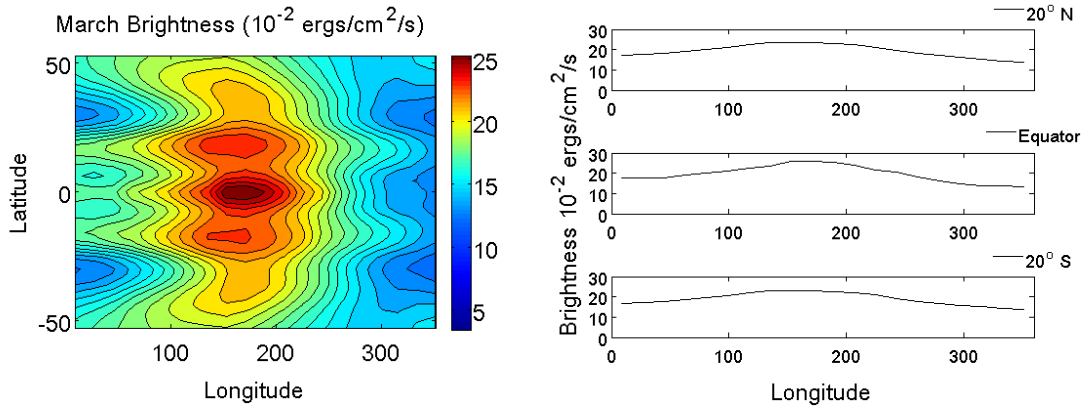
Figure 5.36: (left panel) CMAT2 longitudinal profile of OH$^*(9-7)$ and OH$^*(8-6)$ airglow brightness for March equinox 2008; 53° N to 53° S. (right panels) The OH* airglow brightness at 20° N, 0°, and 20° S.
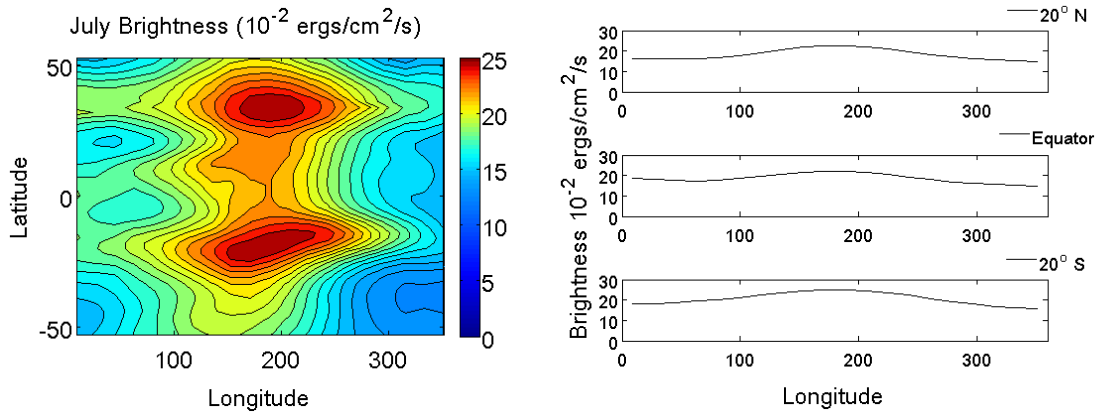
Figure 5.37: (left panel) CMAT2 longitudinal profile of OH$^*(9-7)$ and OH$^*(8-6)$ airglow brightness for June solstice 2008; 53° N to 53° S. (right panels) The OH* airglow brightness at 20° N, 0°, and 20° S.
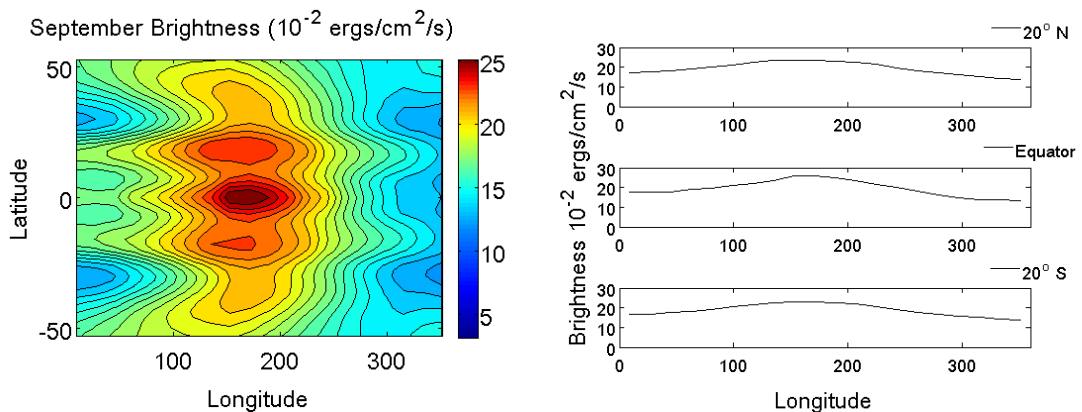
Figure 5.38: (left panel) CMAT2 longitudinal profile of OH$^*(9-7)$ and OH$^*(8-6)$ airglow brightness for September equinox 2008; 53° N to 53° S. (right panels) The OH* airglow brightness at 20° N, 0°, and 20° S.
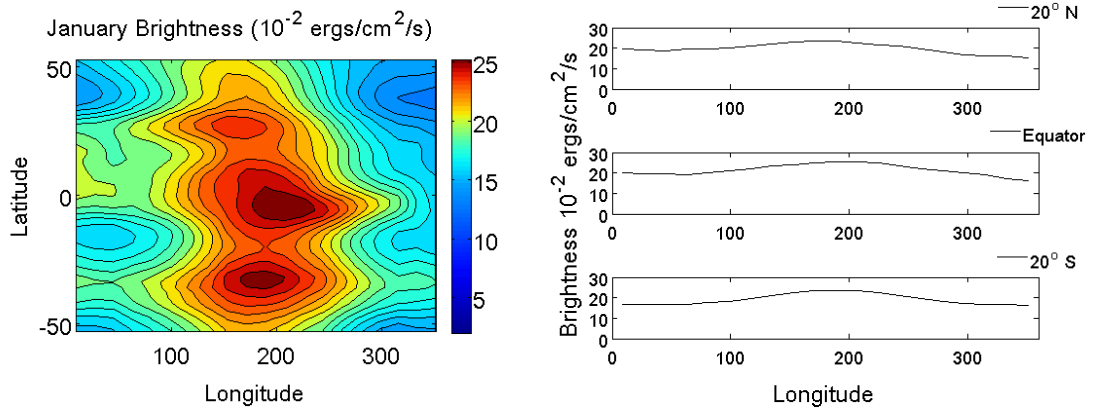
Figure 5.39: (left panel) CMAT2 longitudinal profile of OH$^*(9-7)$ and OH$^*(8-6)$ airglow brightness for December solstice 2008; 53° N to 53° S. (right panels) The OH* airglow brightness at 20° N, 0°, and 20° S.

It can be seen that while CMAT2 predicts average emission levels that are a factor of two higher than observations, as expected, it does not produce the same level of variability within the longitudinal profiles revealing only a stationary wave with wavenumber 1 at all times of the year. While this result is disappointing it is worth considering that a 'broadstrokes' comparison of the CMAT2 results with observations of the mid- to high-latitude regions presented in **Figure 5.27** both reveal this wavenumber 1 feature. This suggests that CMAT2 can replicate the basic features of the state of the atmosphere on a global scale but not the level of complexity and detail necessary for a comparison with the observations presented in Xu *et al.* (2010). This can be seen more clearly in **Figure 5.40** which shows the corresponding temperature variations with magnitudes of only a few Kelvin.

It is possible that the lack of variability within the CMAT2 model results is a consequence of an inadequate representation of the migrating and non-migrating tides within the model. Given that data used to construct **Figure 5.40** are 40 day average profiles surrounding local midnight, for approximately equinox and solstice conditions, only minor variations in the migrating tides are expected in the individual longitudinal plots during equinox and solstice (right panels). The effect of the migrating tides on OH* emission can be determined from a comparison of the global plots (left panels) as the tides have a strong semi-annual variation with maxima at the equinoxes (Xu *et al.,* 2009).

However, variations in the OH* emissions resulting from the non-migrating tides should be evident in the individual longitudinal plots (right panels). This is clear from the results displayed in **Figure 5.35** where Xu *et al*. (2010) identify the non-migrating diurnal (D0), westward wavenumber 2 (DW2) and eastward wavenumber 3 (DE3) tides in the individual longitudinal plots.

Since CMAT2 does not include a troposphere, in order to simulate tidal effects in the atmosphere, tidal forcing at the lower boundary is taken from the GSWM model (Hagan *et al.,* 1999). More details on modelling tides are presented in Hagan *et al.,* (1995). However, Marsh *et al.* (2006) and Roble and Shepherd (1997) report that the diurnal amplitude should be doubled in order to give better model data agreement within the mesosphere. Within the CMAT2 model this scaling factor has not been incorporated. Therefore, it is suspected that CMAT2 underestimates the effects of tides within the mesosphere and as such the dynamics of the mesosphere may require further investigation and refinement.

The lack of variability within the CMAT2 profiles may also be attributed, at least in part, to the size of the CMAT2 model grid. As described in **Chapter 2**, the CMAT2 standard model grid has 2° latitudinal, 18° longitudinal, and 1/3 scale height (~ 2 km) resolution. Thus the model has 91 latitudinal grid points, 63 altitudinal points, but only 20 longitudinal grid points. This makes the model less than ideal for detailed studies of longitudinal variations.

Furthermore, it should be remembered that CMAT2 is not typically designed for such an analysis. CMAT2 is designed to predict global distributions of atmospheric constituents at a particular time of day in Universal Time (UT). At any model time t the 20 longitudinal grid points therefore correspond to 20 different local times. In the above analysis it was required that all longitudes retain the same local time (local midnight). This is a trivial task when looking at observational data, as these data can be binned according to local time. However, this is difficult to produce from CMAT2 results. Retaining a specific local time can only be accomplished within CMAT2 by extracting discrete profiles for each longitudinal point over 24 model time steps. At each step a progression in longitude is matched by a regression in universal time in order to retain a local time that is within 24 minutes of local midnight.

Figure 5.40 from Xu *et al.* (2010) shows temperature distributions at 87 km which correspond to the data presented in **Figure 5.35**. Wave features with wavenumbers 4 and 1, are evident in the individual longitudinal profiles. **Figures 5.41** to **5.44** show the corresponding temperature profiles produced by CMAT2.
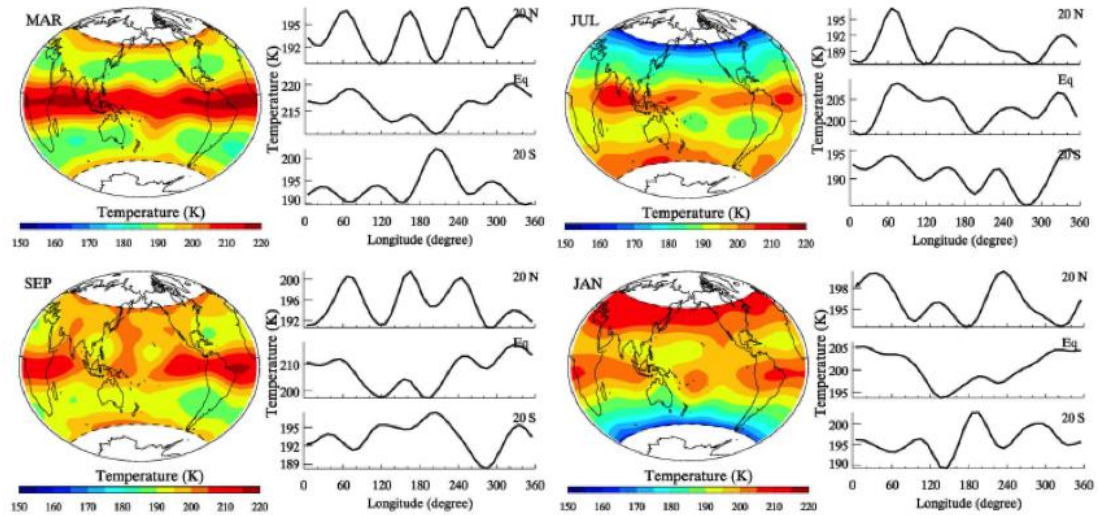
Figure 5.40: (left panels) Maps of 40 day average temperatures for 4 periods averaged from 2002 to 2008; 53° N to 53° S. (right panels) The temperatures at 20° N, 0°, and 20° S. (Note that the scales of the plots differ) (Xu *et al.,* 2010).
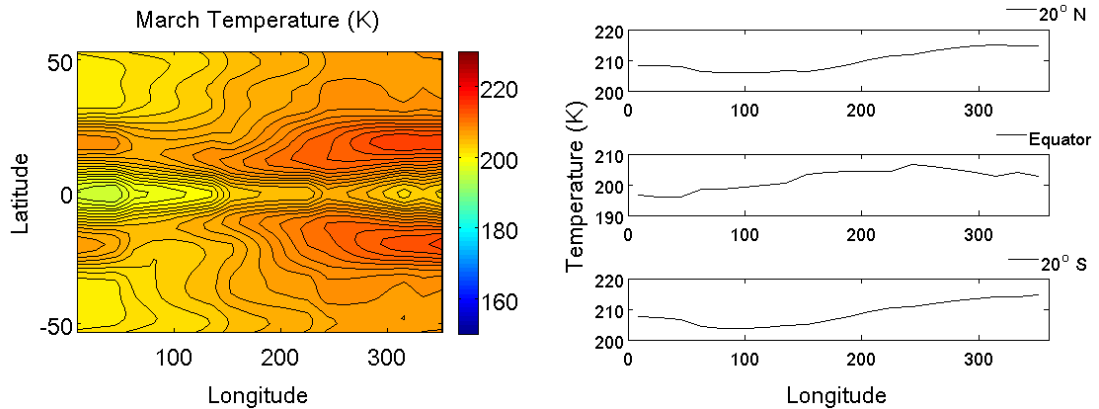
Figure 5.41: (left panel) CMAT2 longitudinal profile of temperatures for March equinox 2008; 53° N to 53° S. (right panels) The temperatures at 20° N, 0°, and 20° S.
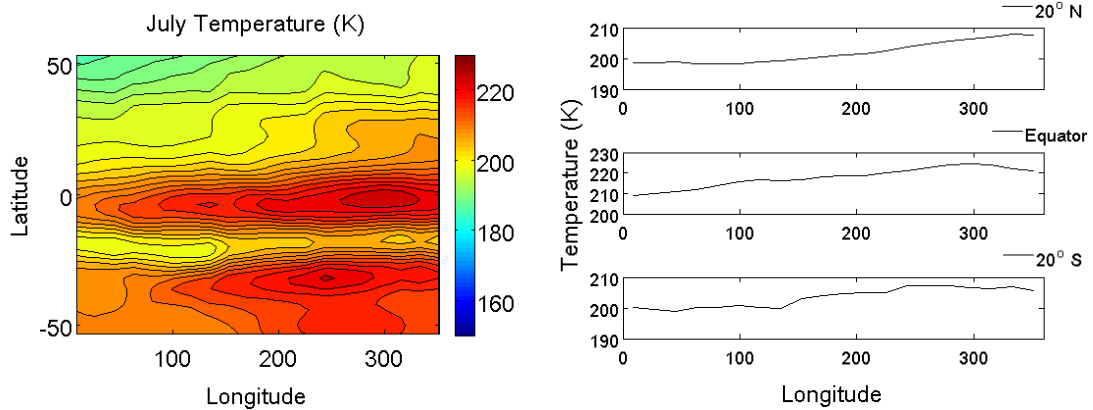
Figure 5.42: (left panel) CMAT2 longitudinal profile of temperatures for June solstice 2008; 53° N to 53° S. (right panels) The temperatures at 20° N, 0°, and 20° S.
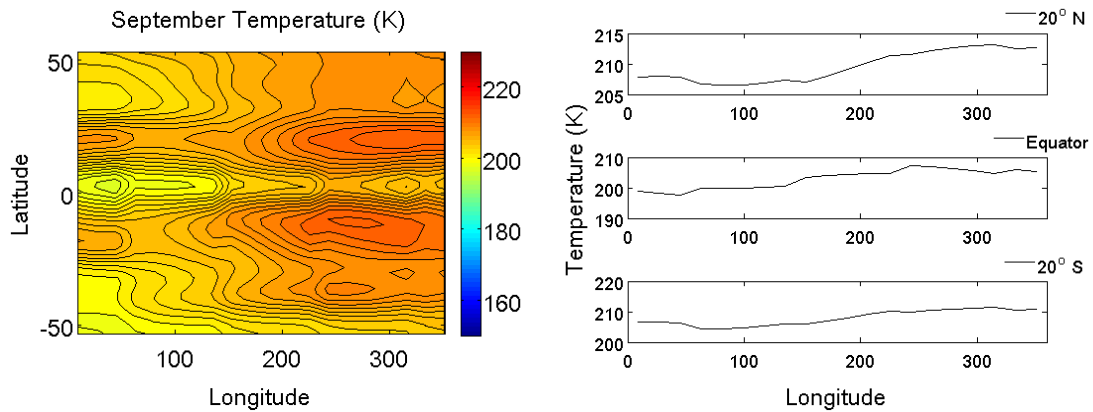
Figure 5.43: (left panel) CMAT2 longitudinal profile of temperatures for September equinox 2008; 53° N to 53° S. (right panels) The temperatures at 20° N, 0°, and 20° S.
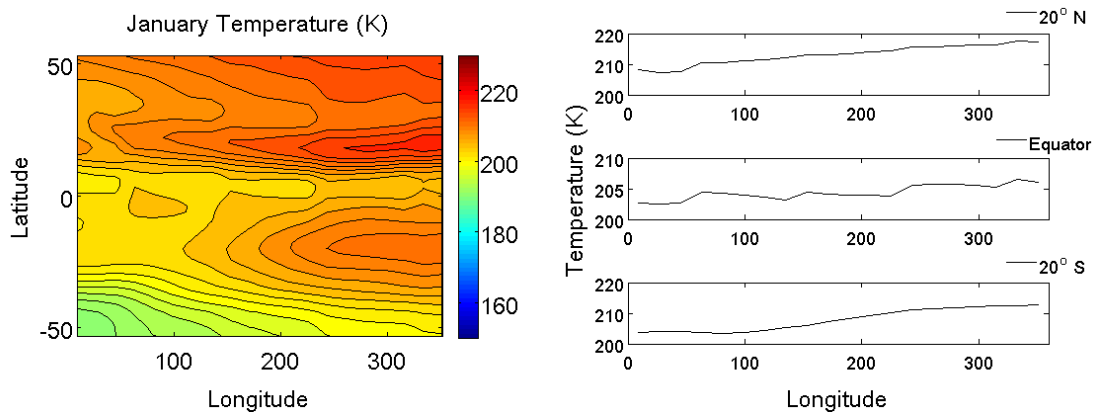
Figure 5.44: (left panel) CMAT2 longitudinal profile of temperatures for December solstice 2008; 53° N to 53° S. (right panels) The temperatures at 20° N, 0°, and 20° S.

It is clear that the CMAT2 model does not predict the same level of variation in the temperature profiles revealed in the SABER data. Examination of **Figure 5.40** shows that SABER observes variations in temperature of up to 10 K within 20°s longitude.

260

CMAT2 does not predict temperature variations greater than 3 K in the same interval. Therefore, in its current iteration CMAT2 cannot produce the same wave-like features in the temperature profiles observed in SABER data. The same is true for the volume emission rates profiles of OH^* which are temperature dependent.

As with the OH^* emission rate profiles, it may be possible that the lack of variation in CMAT2 temperatures is a result of inaccurate representations of the tidal features within the model for the reasons detailed previously. This further suggests that the CMAT2 model's mesospheric dynamical routines require further investigation and refinement.

Once again, a 'broadstrokes' comparison of the SABER and CMAT2 temperature profiles does reveal some similar features. During equinox in both sets of data, temperatures are highest surrounding the equator while at solstice additional peaks in temperatures are observed in the winter hemispheres. This feature is expected in the mesopause region and supports the suggestion that the general features within the atmosphere can be predicted well by CMAT2.

CMAT2 does offer alternative grid sizes which can be applied to model runs which may improve model data agreement slightly. However, since any increase in longitudinal resolution would have to be accompanied by a decrease in either latitudinal or altitudinal resolution alternative grids have not, at the time of writing, been applied to the model runs.

Given the relative success of the model thus far, it is reasonable to investigate variations in the emissions as a result of altered atmospheric parameters on a global scale. With this in mind, the following sections of this chapter will look at the effects of tides on the level of OH^* emissions within the atmosphere.

5.7   Study 5: The effect of tides on the combined diurnal emission from the $OH^*(9-7)$ and $OH^*(8-6)$ transitions

In this section the effect of the migrating tides on the local time variability of the OH^* emissions is examined. In order to accomplish this, the results from two model simulations will be presented. The first simulation represents a standard run in which all tidal features are present and operational. The second simulation is one in which

both the diurnal and semi-diurnal tides have been eliminated from the model run. This was accomplished by zonally averaging the solar and chemical heating rates at all points within the model grid and subsequently turning off all tidal forcing routines at the lower boundary. This method of eliminating tides has previously been described in Marsh *et al.* (2006). As CMAT2 is suspected to underestimate tidal features in the mesopause atmospheric temperatures are also zonally averaged to eliminate temperature dependence of reaction rates making the CMAT2 results more comparable with other models. The model results presented are for the equator and for 58° S and were chosen for comparison with the ROSE chemical model described in Rose and Brasseur (1989), Marsh *et al.* (2001) and Marsh *et al.* (2003).

Figure 5.45 shows the local time variability of the combined $OH^*(9-7)$ and $OH^*(8-6)$ volume emission rate as simulated by the CMAT2 model at altitudes of $84\,\mathrm{km}$, $88\,\mathrm{km}$ and $102\,\mathrm{km}$ over the equator on the 22nd of April 2002. The solid line represents the standard model run, including tidal features, while the dashed line shows the results of the second simulation in which all tidal features have been removed. The modelled temperatures at these altitudes are also displayed as are the modelled atomic oxygen mixing ratios.
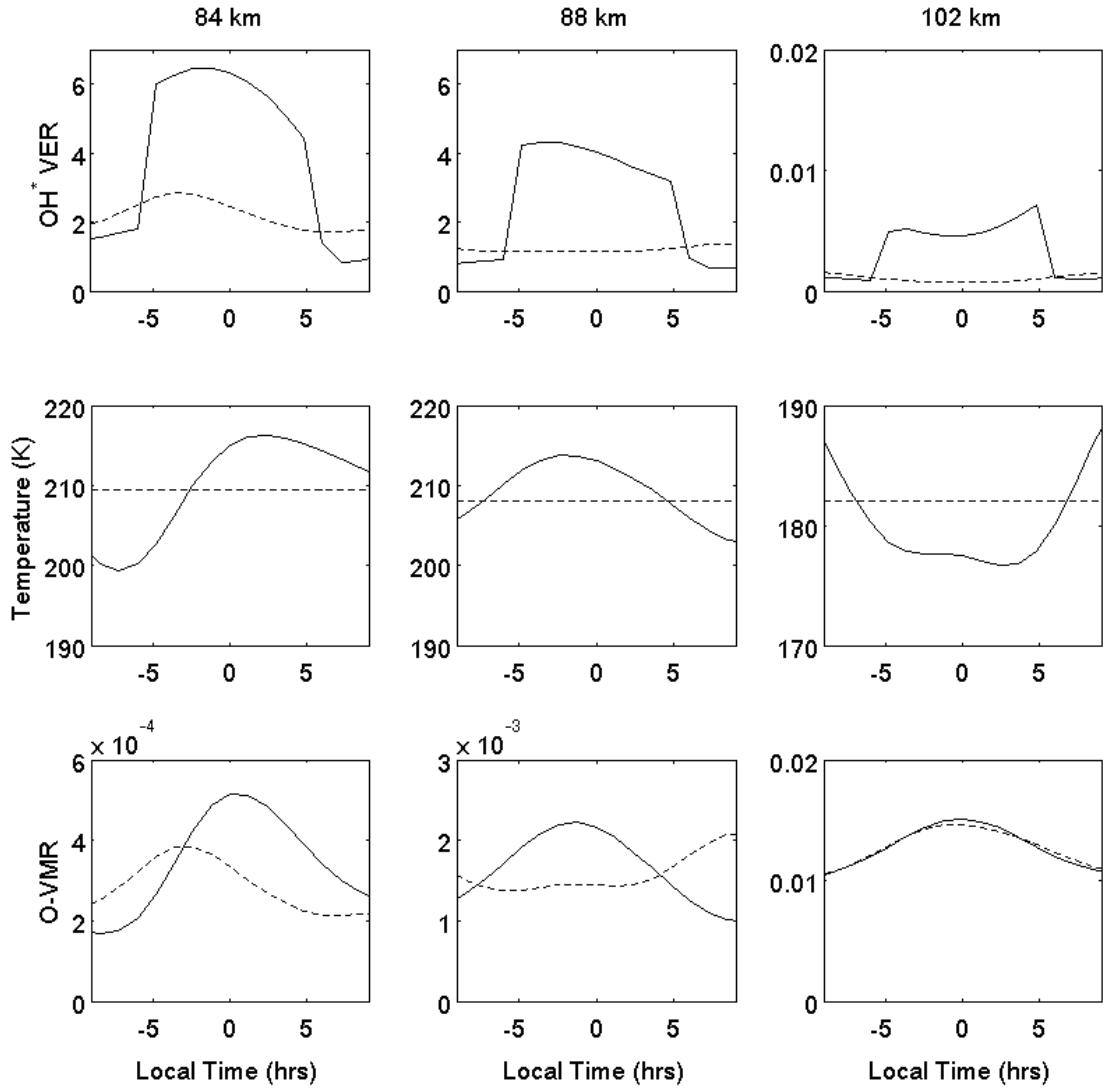
Figure 5.45: Simulated nocturnal variation in equatorial OH$^*(9-7)$ and OH$^*(8-6)$ emission in 1×10^{-7}ergs/cm^3/s at altitudes of $84, 88$ and 102 km on 22nd April 2002. Solid line is for standard simulation while dashed line is for simulation without diurnal or semidiurnal tides. Simultaneous temperature (middle) and atomic oxygen volume mixing ratio (bottom) variations are also shown.

These simulations show that the diurnal and semidiurnal tide affects the emission substantially. At 84 km, the elimination of tides from the model run can be seen to reduce the emissions by a factor of 3 during the night while at 88 km this increases to almost a factor of 4. At 102 km, CMAT2 predicts that the emission rate is already extremely low; however, the elimination of tides from the model can still be seen to reduce the level of emissions even further, again by a factor of 4.

At both 84 and 88 km the OH* emission rate follows both the trend in temperature and in the atomic oxygen mixing ratio as expected. Looking at column one of **Figure 5.45**

it can be seen that in the standard model run the peak in temperature corresponds to the peak in atomic oxygen mixing ratio and that the level of OH* emissions is also quite high. In the second model run, in which tides have been eliminated, the temperature profile flattens as does the atomic oxygen mixing ratio although not to the same extent. The OH* emission rate closely follows the O mixing ratio and both exhibit peaks at approximately 4 hrs before local midnight. A similar trend can be seen in column two of **Figure 5.45** at 88 km although at altitudes above this, at 102 km, this relationship does not hold and the O mixing ratio no longer follows the temperature variation.

The reduced emission rates predicted by the CMAT2 model in the second, 'no tides', simulation can be explained using the mechanism described by Marsh *et al.* (2006). After sunset, due to the absence of incoming solar radiation, atomic oxygen is no longer produced via photolysis reactions and its concentration starts to decrease as it is consumed primarily via chemical reactions with molecular oxygen, ozone and, both vibrationally excited and ground state hydroxyl. The lifetime of atomic oxygen can be therefore expressed simply as

$$\tau_O = (k_{O+O_2+M}[O_2][M] + k_{O+O_3}[O_3][M] + k_{O+OH}[OH])$$

(5.1)

where τ_O is the lifetime of atomic oxygen, k represents a reaction rate while $[O_2]$, $[O_3]$, $[M]$ and $[OH]$ represent the concentrations of molecular oxygen, ozone, the atmospheric density and both ground and vibrationally excited hydroxyl respectively. When calculated, τ_O is found to be 6 hours at 84 km, 1 day at 88 km and 2 months at 102 km (Marsh *et al.,* 2006). Without advection or diffusion, the level of atomic oxygen is therefore expected to decrease over the course of the night at these altitudes. At lower altitudes where the densities of the reactants are higher the consumption of atomic oxygen proceeds faster. Given that the level of OH* emissions is proportional to the amount of atomic oxygen, a decrease in the emission rates of OH* is therefore to be expected in the 'no tides' model run.

However, consideration of the above is not enough to explain the substantial increase in the levels of emissions at the equator in the standard run when compared to the 'no tides' run. Marsh *et al.* (2006) suggests that the differences in the level of emissions in OH* can further be attributed to increasing atomic oxygen concentrations within the

region despite the absence of a photochemical source and suggest that a dynamical source of O is involved. A downward wind could result in the increased temperatures observed in the standard runs surrounding local midnight through adiabatic heating. This would also lead to increased concentrations of atomic oxygen, since its mixing ratio increases with altitude, and explain the increased OH^* emissions at 84 km and 88 km. At 102 km where the temperatures of the standard run are lower than the 'no tide' run an alternative explanation is required.

Writing the production of OH^* at this altitude as

$$P = k_{O+O_2+M}[O][O_2][M]$$

$$(5.2)$$

where the symbols have their usual meanings Marsh *et al.* (2006) show that with the reaction rate k_{O+O_2+M}, which is given by $6.0 \times 10^{-34} \left(\frac{300}{T}\right)^{2.4}$, a drop in temperature of 20 K increases the reaction rate by ~29%. Also, assuming a constant pressure at 102 km a decrease in temperature of 20 K would increase the relative densities of the chemical species involved in OH^* production and as such increase production of OH^* by up to ~37% (Marsh *et al.*, 2006). Therefore, at all altitudes tidal features tend to increase the level of OH^* although via different mechanisms.

Figure 5.46 shows the local time variability of the same emission as simulated by the ROSE chemical model and published in Marsh *et al.* (2006). The standard line represents the standard model run, the dashed line represents a run in which tidal features have been eliminated while square boxes represent SABER measurements. The dotted line represents the expected change in OH^* due solely to losses in atomic oxygen.
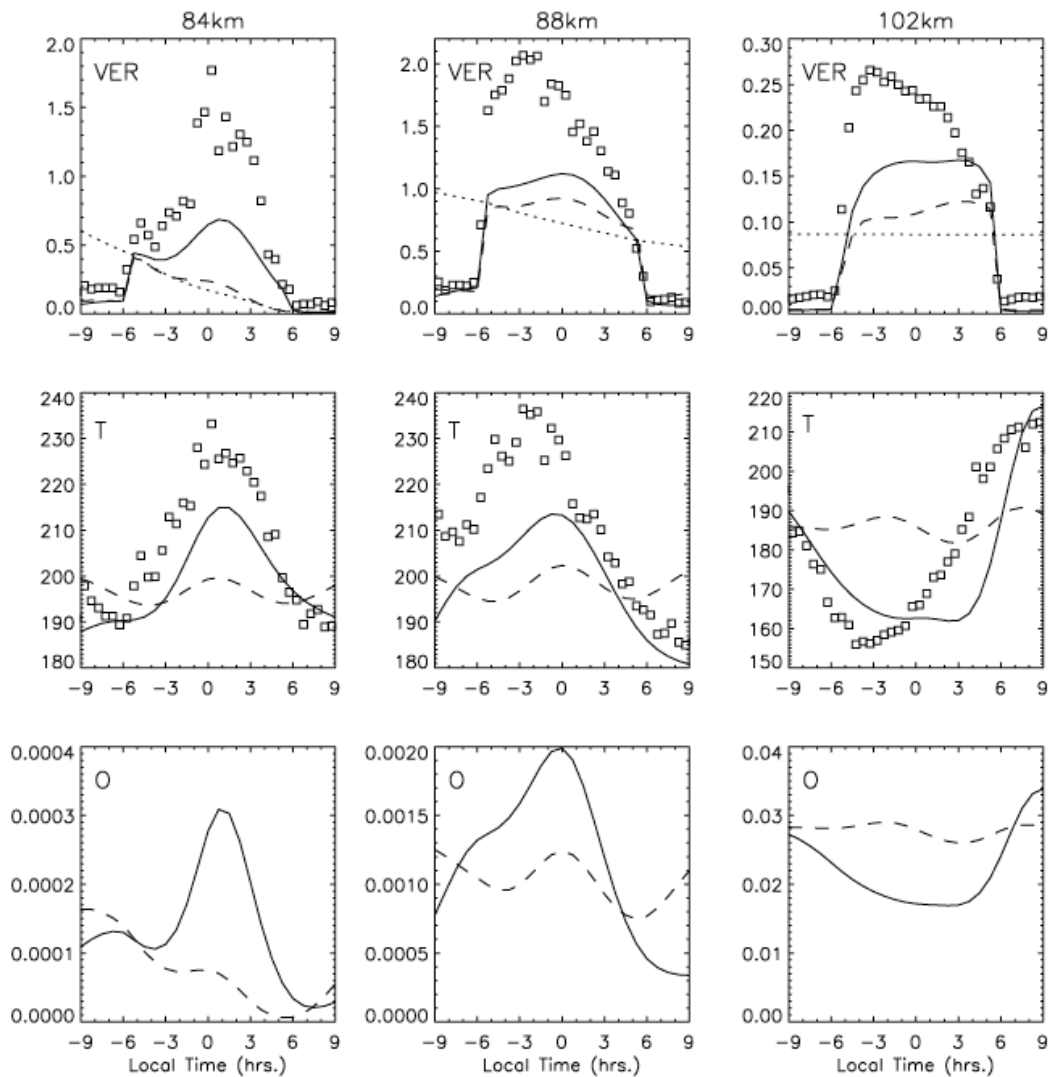
Figure 5.46: Simulated nocturnal variation in equatorial $OH^*(9-7)$ and $OH^*(8-6)$ emission in $1 \times 10^{-7} ergs/cm^3/s$ at altitudes of $84, 88$ and 102 km. Solid line is for standard simulation while dashed line is for simulation without diurnal or semidiurnal tides. Dotted line represents expected drop in night-time emissions due only to chemical loss of atomic oxygen. Simultaneous temperature (middle) and atomic oxygen volume mixing ratio (bottom) variations are also shown. SABER observations are shown for comparison (squares) Marsh *et al.* (2006).

Comparing **Figures 5.45** and **5.46** it can be seen that at all altitudes there are a number of differences between the CMAT2 model results, ROSE model results and SABER measured profiles although the general trends displayed in each are quite similar.

Firstly, in the standard run, at altitudes of 84 km and 88 km the CMAT2 model overestimates the OH^* emission rates by at least a factor of two, as has been established in the previous sections of this chapter. In **Figure 5.46** the standard run of the ROSE

model tends to underestimate the number of emissions at these same altitudes by approximately the same factor when compared to the SABER measurements. At 102 km the CMAT2 model predicts only negligible emissions from OH^* while both the ROSE Model and SABER measurements show small, but not insignificant emission rates.

The temperature and atomic oxygen mixing ratio profiles produced by both models can help explain these differences. While both the CMAT2 and ROSE models accurately reproduce the general trend in temperature, they both underestimate the magnitude of the temperature variations at all altitudes. Temperature variations of approximately 20 K are typically produced by both models while SABER measurements show temperature variations of up to 50 K. It has already been shown how temperature variations affect OH^* emissions levels. In the 'no tides' run the CMAT2 model predicts temperatures that are approximately 10 K higher than the ROSE model contributing to the increased levels of emissions.

Of greater significance is the variation in the atomic oxygen mixing ratios predicted by both models. It can be seen that at both 84 km and 88 km that the general trend in the atomic oxygen mixing ratio profiles are quite similar; however, the magnitude of the variation is somewhat larger in the results of the ROSE model.

The O mixing ratio profiles at 84 km produced by both models reveal that the CMAT2 model predicts a mixing ratio that is approximately a factor of two larger than that predicted by the ROSE model throughout the course of the night. This is a significant variation in the mixing ratio and certainly contributes to the substantially higher OH^* emission rate profile generated by CMAT2 model. At 88 km the O mixing ratios produced by both models are in better agreement although CMAT2 still predicts a slightly higher mixing ratio. At 102 km the trend is now reversed and CMAT2 predicts an atomic oxygen mixing ratio that is a factor of two less than that predicted by the ROSE model. This result explains why the CMAT2 model predicts only negligible levels of OH^* emissions above 100 km while the ROSE model produces small but not insignificant levels of emissions. Clearly the ROSE model predicts a much steeper gradient in the atomic oxygen mixing ratio profiles than CMAT2.

Notwithstanding the differences in the model results presented above it is worth noting that at 88 km, where the atomic oxygen mixing ratios predicted by both models are in close agreement, both the CMAT2 model and the ROSE model predict almost identical levels of OH^* emissions in their 'no tide' model runs. This is a significant result and suggests that differences in the results of both models can be attributed primarily to differences in the dynamical routines utilised by the models rather than any missing photochemistry.

In the above analysis only the emission profiles over the equator have been considered. Therefore, the analysis is repeated and results from the mid-latitude regions where tidal effects are at a minimum are presented.

Figure 5.47 shows the local time variability of the combined $OH^*(9-7)$ and $OH^*(8-6)$ volume emission rate as simulated by the CMAT2 model at altitudes of 84 km, 88 km and 102 km at 58° S on the 22nd of April 2002. The full line represents the standard model run, including tidal features, while the dotted line shows the results of a second simulation in which all tidal features have been eliminated. The modelled temperatures at these altitudes are also displayed as are the modelled atomic oxygen mixing ratios.
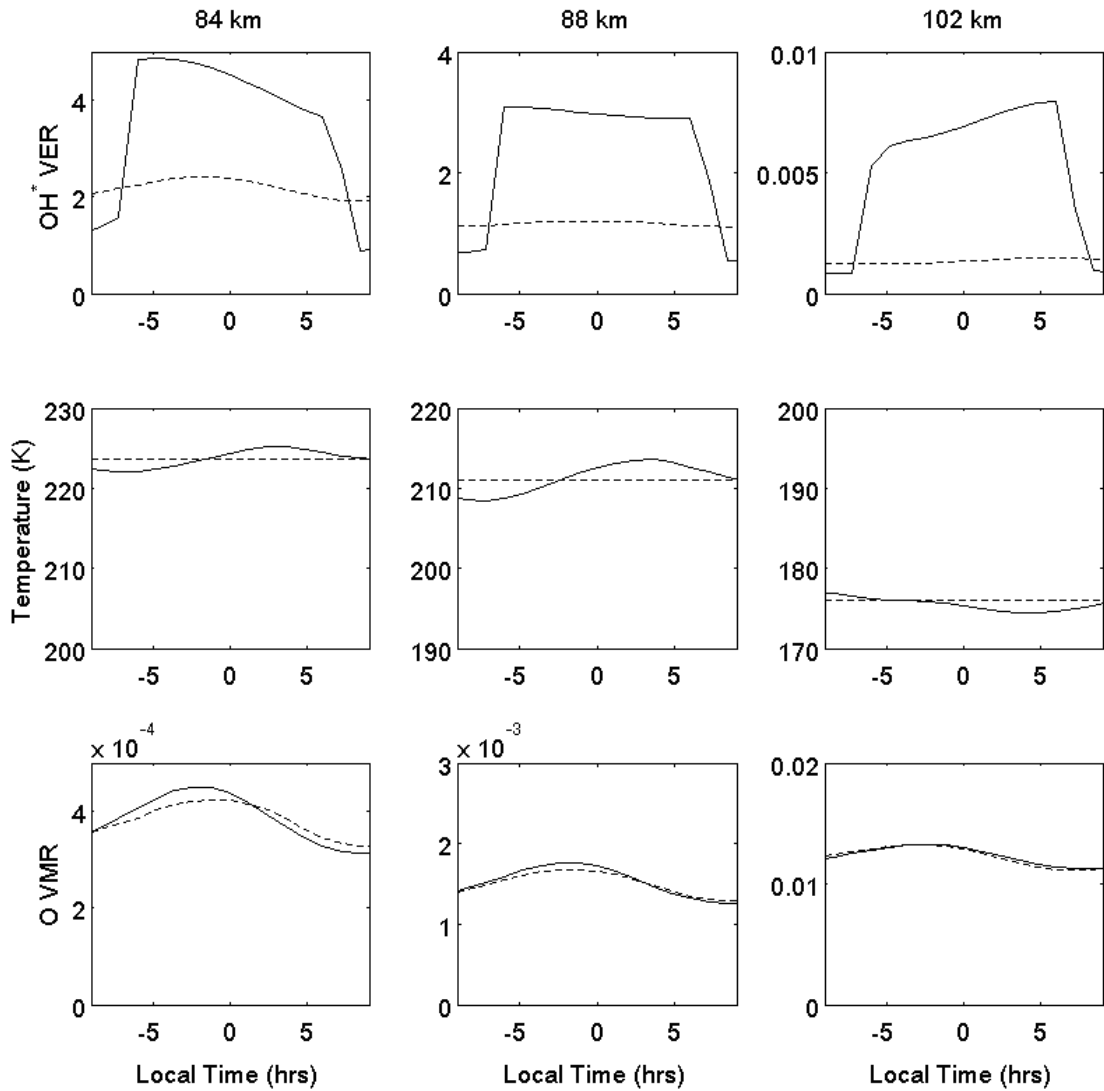
Figure 5.47: Simulated nocturnal variation in 58°S $OH^*(9-7)$ and $OH^*(8-6)$ emission in 1×10^{-7} ergs/cm^3/s at altitudes of 84, 88 and 102 km on 22nd April 2002. Solid line is for standard simulation while dashed line is for simulation without diurnal or semidiurnal tides. Simultaneous temperature (middle) and atomic oxygen volume mixing ratio (bottom) variations are also shown.

Once again these simulations show that the diurnal and semidiurnal tide affects the emission. At 84 km the elimination of tides from the model run can be seen to reduce the emissions by a factor of 2 during the night, while at 88 km this increases to almost a factor of 3. At 102 km CMAT2 predicts that the emission rate is already extremely low and the elimination of tides from the model reduces the level of emissions even further, by up to a factor of 4.

The level of variability in the OH* emission shown in **Figure 5.47** is unexpected considering the relatively minor variations in both temperature and atomic oxygen

volume mixing ratio (vmr). At both 84 and 88 km the OH^* emission rate follows the trend in the atomic oxygen mixing ratio, as is to be expected, although the variation in the atomic oxygen mixing ratio is not very large. Looking at column one of **Figure 5.47**, the standard model run shows an increase in atomic oxygen mixing ratio with local time up to approximately two hours before local midnight corresponding to an increase in the level of OH^* emissions. However, the magnitude of the increase in the O vmr cannot explain the increase in the level of OH^* emissions. The tidal routine within CMAT2 therefore augments the level of emissions via a different mechanism. This mechanism has yet to be determined.

In the second model run, in which tides have been eliminated, neither the temperature profiles nor the atomic oxygen mixing ratios vary significantly due to the fact that tidal amplitudes are low at these latitudes (Marsh *et al.,* 2006). This represents an ideal location to test the validity of model chemical scheme as tidal features should have little impact. **Figure 5.48** shows the local time variability of the same emission as simulated by the ROSE chemical model and published in Marsh *et al.* (2006). The solid line represents the standard model run, the dashed line represents a run in which tidal features have been eliminated while square boxed represent SABER measurements. The dotted line represents the expected change in OH^* due solely to losses in atomic oxygen.
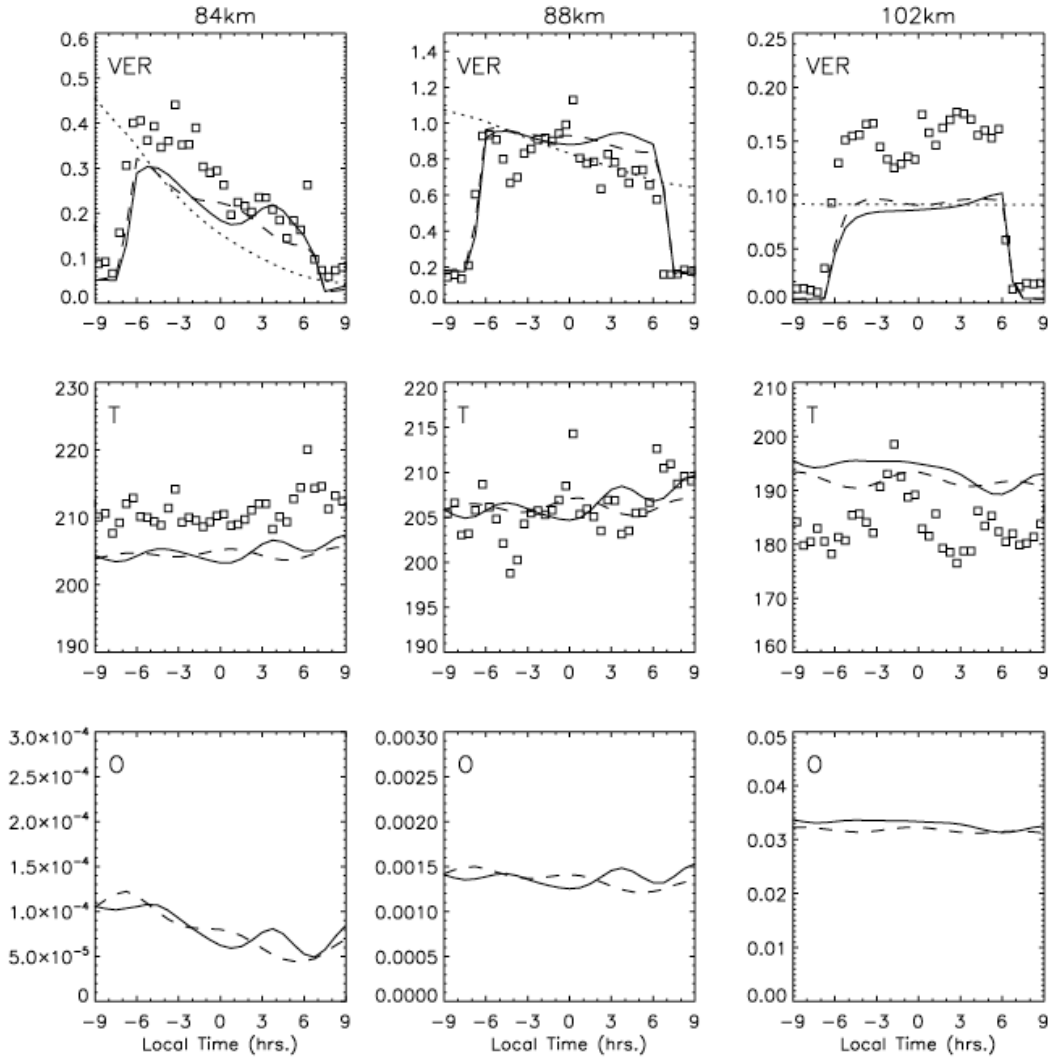
Figure 5.48: Simulated nocturnal variation in 58°S OH*(9 − 7) and OH*(8 − 6) emission in 1×10^{-7} ergs/cm³/s at altitudes of 84, 88 and 102 km. Solid line is for standard simulation while dashed line is for simulation without diurnal or semidiurnal tides. Dotted line represents expected drop in night-time emissions due only to chemical loss of atomic oxygen. Simultaneous temperature (middle) and atomic oxygen volume mixing ratio (bottom) variations are also shown. SABER observations are shown for comparison (squares) (Marsh *et al.*, 2006).

An initial comparison of **Figures 5.47** and **5.48** shows that in the standard model run, and at this latitude, the ROSE model performs better at predicting OH* emissions than the CMAT2 model. Yet the ROSE model still tends to underpredict the level of emissions by a small amount. CMAT2 successfully predicts the trend in OH* emissions although not the magnitude of the emission.

At 84 km, CMAT2 predicts emissions that are approximately a factor of 10 higher than those predicted by the ROSE model and recorded in SABER measurements. This is one of the most substantial differences in emission magnitudes observed to have being produced within the CMAT2 model results. This variation can be attributed to substantial differences in the atomic oxygen concentrations at this latitude. In **Figures 5.47** and **5.48** it can be seen that CMAT2 predicts an atomic oxygen volume mixing ratio that is up to 8 times higher than that predicted by the ROSE model at this particular latitude. While this appears excessive it should be remembered that Smith *et al.* (2010) report diurnal variations in atomic oxygen concentrations that vary by up to a factor of 10 . When this is combined with the fact that the CMAT2 modelled temperatures are predicted to be 20 K higher than ROSE model predictions and 10 K higher than SABER measurements these factors combine to substantially increase the level of OH* emissions at this altitude.

As in the previous case, at mid-latitudes, the reverse is true at 102 km where the CMAT2 model predicts an atomic oxygen volume mixing ratio that is a factor of two lower than that predicted by the ROSE model. The substantially lower O mixing ratio at these higher altitudes significantly reduces the level of OH* emissions predicted by CMAT2.

The best comparison exists at 88 km where both the temperature profile and atomic oxygen mixing ratio profile predicted by both models are in close agreement. While the standard model run performed by CMAT2 still produces emissions that are more than a factor of two higher than those predicted by the ROSE model and SABER measurements, the 'no tide' model run produces emissions that are in very good agreement with those predicted by the ROSE model and recorded by the SABER instrument. Therefore, it must be assumed that the tidal routine alters the level of OH* emission via another mechanism.

5.8   Summary of Study 5 (Section 5.7)

In **Section 5.7** the diurnal variability of the OH* airlgow emissions was analysed and the results of the CMAT2 model were compared to the results of both the ROSE chemical model and SABER observations. Based on the results of previous studies conducted in this chapter it was expected that at all times the CMAT2 model would over-predict the

level of emissions by at least a factor of two which can be attributed to excessive (by a factor of two) concentrations of atomic oxygen within the CMAT2 model results (Dobbin, 2008).

The results of **Section 5.7** have shown that accurate representation of the atomic oxygen concentrations and the resulting variations in the production rate of ozone in the atmosphere is of primary concern when modelling OH* emissions. The results of both CMAT2 and ROSE show that the level of emissions from OH* follows the trend in the atomic oxygen concentrations at mesopause altitudes. Variations in the level of emissions from OH* predicted by both models can be traced back primarily to variations in the atomic oxygen concentrations. These variations in O result from vertical transport and it has been shown that when tides are eliminated from the model runs and when the atomic oxygen mixing ratios, and temperatures, utilised by both models are in close agreement, both models predict similar levels of emissions from OH* which are also in line with SABER observations. This is most evident in columns two of **Figures 5.45** to **5.48** corresponding to altitudes of 88 km.

Looking at altitudes other than 88 km it can be seen that similar variations in the atomic oxygen mixing ratio profiles produced by both models show similar variations in the OH* emission profiles. This is most evident in columns one of **Figures 5.47** and **5.48** where at local midnight CMAT2 predicts an atomic oxygen mixing ratio that is a factor of 8 higher, and temperatures approximately 20 K higher, than those predicted by the ROSE model. In this extreme case CMAT2 predicts OH* emissions that are a factor of 10 higher than those predicted by the ROSE model and observed in SABER measurements. Since the root cause of this discrepancy is mostly likely attributable to atomic oxygen, it can be assumed that the chemistry of the model is correct and that with altered atomic oxygen concentrations the CMAT2 model can produce accurate results.

At 102 km the same trend can be observed. When the atomic oxygen volume mixing ratio predicted by CMAT2 is lower than that predicted by the ROSE model there is a substantial decrease in the level of emission from OH*. At these higher altitudes the temperature and densities of O, O_2 and M become more important for the production of OH* and subsequent emissions.

Finally in **Section 5.7** the effects of tidal routines on the levels of OH^* emissions were investigated. It was shown that tides increase the level of emissions at all altitudes although through different mechanisms. Within the mesopause, vertical transport of atomic oxygen from the upper atmosphere increases the level of emissions substantially through increased concentrations of atomic oxygen. Within the lower thermosphere tidally induced adiabatic cooling triggers increases in the reaction rates of the reactions involved in OH^* production as well as increased densities of the other reactants. At the equator these tidal effects have a significant impact on the level of emissions throughout the course of the night. At the mid-latitudes, the tidal routines in CMAT2 alter the level of emission via an additional mechanism that has yet to be determined. Neither varying temperatures or atomic oxygen concentrations can produce the observed increase in the level of emissions. This suggests that the further investigations of the CMAT2 dynamical routine within the mesosphere are required and additional refinement of the code is necessary.

5.9   Chapter 5 Summary

In this chapter the M1-D model was incorporated into the CMAT2 GCM. Initial testing of the new code involved a comparison of the CMAT2 model results with the model results of Ward (1999). It was found that CMAT2 could accurately reproduce many features of the Ward model which have been shown to be in good agreement with observations from the WINDII instrument. The diurnal variation of the emission was also investigated and it was found that this variation has a strong latitudinal dependence.

CMAT2 results were subsequently compared to direct measurements of the OH^* emission rates recorded by the SABER instrument. This represents a very stringent test of the model's capabilities since the SABER instrument can successfully measure even minute changes in atmospheric features as shown in Xu *et al.* (2010). In general CMAT2 performs well at predicting the morphology of the emission rates. The closest agreement is at equinox when the atmosphere is in its most stable period, while the greatest disagreement is at solstice. Some features predicted by SABER in the mid- to high-latitudes are not predicted by CMAT2 but this can, at least in part, be attributed to the sampling period required to produce 24 hrs local time coverage from SABER data. Comparison of these results with Baker *et al,* (2007) further suggest that additional

peaks at higher latitudes may be the result of a wavenumber 1 feature of the atmospheric tides.

CMAT2 is shown to consistently over-predict the level of emissions from OH^{*} typically by approximately a factor of two. This is attributed to a known feature of CMAT2 which over-predicts concentrations of O by approximately the same factor and is currently under investigation (Dobbin, 2008). Based on the results of this chapter this discrepancy is not thought to originate from the model photochemistry as possible additional sources of O would be counteracted by additional sinks. The CMAT2 tidal routines, resulting in transport of atmospheric constituents within the mesopause, are the main suspect as the source of the problem.

Studies of the longitudinal variation in OH^{*} at a fixed local time reveal that CMAT2 does not accurately represent variations in the emission which result from the non-migrating tides as shown in Xu *et al.* (2010). A wavenumber 1 feature is evident in the emissions although other wave features are not. This can be attributed to a number of factors including a possible inaccurate representation of the tidal features within the model. CMAT2 was also not designed for such a study and the methodology used in this comparison may also impact the results. As the data points are obtained from a full 24 hr model day, the level of uncertainty in the modelled emissions increases at each data point. Furthermore, a linear relationship between data points is assumed which eliminates features with a horizontal extent of less than 5000 km.

Investigations of the tidal features in the CMAT2 model suggest that tides are underrepresented. Tidal features were eliminated completely from the CMAT2 model using an approach similar to that described in Marsh *et al.* (2006) and the results were compared to SABER measurements and results from the ROSE chemical model. It was found that tides significantly modulate the emissions primarily through changes in the atomic oxygen concentrations at all latitudes but in particular at the equator. At mid- to high-latitudes where the magnitude of the diurnal tides are low, there was still modulation of the emissions which cannot be attributed to either concentrations of atomic oxygen or variations in temperature. Therefore, further investigations of middle atmospheric dynamics are required and CMAT2 code refinements may be necessary.

Chapter 6

Discussion and Conclusions

6.1   Introduction

This thesis has focused on the development of an atmospheric model which is capable of simulating the behaviour of the OH^* airglow emissions within the mesopause layer of the atmosphere. In **Chapter 1** the general features and background theory of the atmosphere were presented together with a detailed description of the mesopause layer. This was followed by a brief introduction to the different types of atmospheric models and the fundamental equations which they attempt to solve.

Chapter 2 described one particular atmospheric model, the CMAT2 GCM, in detail. This description followed a similar outline to that provided in Kalnay (2003) in which atmospheric modelling is described based on its fundamental assumptions, governing equations, numerical methods, grid resolution, and initial and boundary conditions. The model parameters were also discussed followed by the chemical, radiative and dynamical routines incorporated into the model.

Chapter 3 focused on the hydroxyl radical. Vibrationally excited hydroxyl was distinguished from ground state hydroxyl. The molecular energetics and selection rules were described in detail. An overview of the features observed in the OH^* emissions which this thesis attempts to model was also presented.

Chapter 4 describes the development of a 1-D model of OH^*, the M1-D model. The results of this model were compared to other previously developed models, such as that of Makhlouf *et al.* (1995) and von Savigny *et al.* (2012b). Further comparisons were made to SCIAMACHY measurements of the OH^* concentrations presented in von Savigny *et al.* (2012b) and SABER measurements presented in Xu *et al.* (2012). The model sensitivity to atomic oxygen and ozone concentrations was also investigated.

In **Chapter 5** the M1-D model, described in **Chapter 4**, was incorporated into the CMAT2 GCM. The CMAT2 model results in relation to OH^* concentrations, airglow emissions and volume emission rates in the mesopause were then presented. These results were obtained from a number of CMAT2 model runs at different times of year and under different atmospheric conditions. The results were compared to the best available observational data collected by the SABER instrument onboard NASA's TIMED satellite and to recent predictions of the ROSE 3-D chemical model presented in Marsh *et al.* (2006).

In this chapter a brief review of the work completed as part of this thesis will be presented. This will be followed by a discussion of the results obtained and conclusions reached. Based on these conclusions suggestions for future work will be made which may yield further improvements in relation to the CMAT2 model stability and performance as well as possible future studies which are now possible.

6.2 Review of Work Completed

The M1-D and CMAT2 models have been used to make predictions of both the spatial and temporal variability in the OH^* emissions within the atmosphere. The effect of the diurnal and semidiurnal migrating tides on the level of emissions has also been investigated. The results presented in **Chapter 4** and **Chapter 5** show that the M1-D model and CMAT2 model are able to simulate much of the morphology of the OH^* emissions within the mesopause region of the atmosphere although the magnitude of the emissions in the CMAT2 model are typically higher by a factor of 1.5 to 2.0.

6.2.1 The M1-D Model of OH^*

In **Chapter 4** the development of the M1-D photochemical model of OH^* was described. This model was designed to calculate concentrations of the first nine vibrational levels of OH^* in the mesosphere and considers chemical reactions, collisional deactivation via single and multi-quantum transitions and quenching, as well as airglow emissions.

Initial testing of this 1-D model involved a comparison of the modelled results with the results from other previously developed OH^* models such as the model of Makhlouf *et al.* (1995). Differences between the modelled results were examined and the model

sensitivity to concentrations of atomic oxygen, and ozone were thoroughly investigated. These investigations showed that the model was highly sensitive to variations in both the concentrations of atomic oxygen and ozone. The investigation also showed that utilising similar initial conditions the M1-D model produced similar results to the model of Makhlouf *et al.* (1995) without the inclusion of the controversial perhydroxyl reaction, given by

$$HO_2 + O \rightarrow OH^*(v \leq 6) + O_2$$
(R6.1)
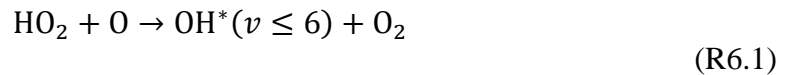
contributing to the overall concentrations of $OH^*(v \leq 6)$.

The M1-D model sensitivity to other factors, such as published branching ratios (Klenerman and Smith, 1987; Steinfeld *et al.*, 1987; Ohoyama *et al.,* 1985) for the reaction of hydrogen and ozone producing OH^*

$$H + O_3 \rightarrow OH^*(v = 6 - 9) + O_2$$
(R6.2)
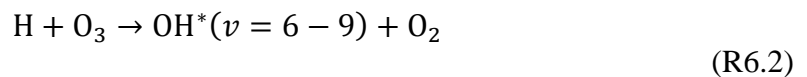
and Einstein *A* coefficients of (Mies, 1974; Turnbull and Lowe, 1988; Nelson *et al.,* 1990) governing the number of emissions were also investigated. These studies revealed only marginal differences in the predicted concentrations and subsequent emissions of OH^* and are therefore not included in this thesis. The frequently used branching ratios of Klenerman and Smith (1987), and the most recent Einstein *A* coefficients of Nelson *et al.* (1990) as well as the O_2 and N_2 collisional deactivation rates of Alder-Golden (1997) are therefore utilised in this model.

A comparison of the M1-D model results was made with SCIAMACHY data and the model of von Savigny presented in von Savigny *et al.* (2012b). It was found that the M1-D model results compared well with both data and model predictions showing a similar distribution of 4 km in the emission peak heights between $OH^*(v = 9)$ and $OH^*(v = 1)$. Elimination of quenching by atomic oxygen in the M1-D model and the von Savigny model showed a similar response, reducing the distribution in the emission peak heights to 2 and 1 km respectively, showing that O quenching must be considered in any model of OH^*. However, the M1-D model further showed a drop in the average emission peak height of the emissions from 86 to 83 km. This variation in the average peak height of the emissions cannot be predicted by the model of von Savigny.

Variations in atomic oxygen concentrations were also investigated and it was found that while the von Savigny model predicted a broadening in the altitudinal distribution of the emission layers with increasing O concentrations, the M1-D model predicted the opposite, as well as a drop in the emission peak heights of the OH^* emission layers. This difference in the model predictions was attributed to the changing altitudes of the emission peak heights predicted by the M1-D model. Increasing concentrations of atomic oxygen significantly increases OH^* production at the lower boundary of the emission layers where the concentration of N_2 and O_2 is still high. However, above 85 km increased atomic oxygen concentrations have the opposite effect, significantly reducing the amount of OH^* emissions through quenching (Smith *et al.*, 2010). The broadening of the emission layer predicted by von Savigny *et al.* (2012b) may therefore be the result of an effort by the model to reflect increased concentrations of OH^* at lower altitudes while maintaining a Gaussian profile with an average peak altitude at 87 km.

A further comparison of the M1-D model results was made with SABER observational data published in Xu *et al.* (2012). These results were compared to observational data at three separate latitudes (the equator and $\pm 40°$), during March equinox and June solstice conditions for the year 2003. Two separate vibrational levels $OH^*(v=8)$ and $OH^*(v=4)$ were chosen for the comparison and in all cases it was shown that the M1-D model could accurately predict the concentrations of both high and low vibrational level states of the OH^* species at the different latitudes given the appropriate initial conditions. However, it was also shown that the M1-D model typically predicted emission layer altitudes approximately $2-3$ km lower than observed by the SABER instrument.

6.2.2 The 3-D Model of OH^* (CMAT2)

In **Chapter 5** the M1-D model, described in **Chapter 4**, was incorporated into the CMAT2 GCM. A number of CMAT2 model runs were performed in order to test the models capability to simulate the spatial variability in the OH^* emission layer with respect to altitude, latitude and local time. Diurnal and seasonal variations in the emissions were also investigated. At each stage the CMAT2 model results were compared to either the predictions of other well established models, or the best available

observational data collected by the SABER instrument onboard NASA's TIMED satellite.

6.2.2.1   Study 1: Diurnal Variations

In the first study conducted, the CMAT2 model was used to make predictions of the diurnal variation in the $OH^*(9-8)$ emission under March equinox conditions. It was found that over the equator there was a sharp increase in the level of OH^* emissions almost immediately after sunset. The emission rate subsequently dropped steadily over the course of the night as atomic oxygen is consumed via the reaction

$$O + O_2 + M \rightarrow O_3 + M$$

$$(R6.3)$$

which is shortly followed by the reaction

$$H + O_3 \rightarrow OH^*(v = 6 - 9) + O_2.$$

$$(R6.2)$$
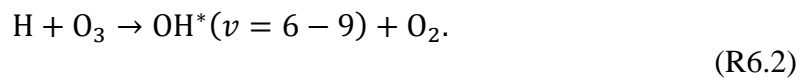
At sunrise there was a sharp drop in the number of OH^* emissions as photolysis of ozone, resulting from incoming solar radiation, takes precedence over the production of OH^*. This general feature in OH^* emissions is well established in the literature to date.

The latitudinal distribution of OH^* was subsequently examined in conjunction with the diurnal variability and it was found that at higher latitudes the OH^* emission layer exhibited different features. At higher latitudes there was a sharp rise in the level of emissions after sunset; however, a peak in the emission was not reached until approximately midnight after which there was a gradual decline in the emission rate until sunset, when the emission rate dropped significantly.

These model results were compared to the model predictions of Ward (1999) for the same time of year and under similar conditions. It was found that the CMAT2 model results compared quite well with the Ward model results which has been shown to be in agreement with the observational data from the WINDII instrument (Ward *et al.*, 1996).

6.2.2.2   Study 2 and Study 3: Seasonal Variations

In a second study, the CMAT2 model was used to predict the number of emissions from the $OH^*(9-7)$ and $OH^*(8-6)$ bands at both equinox and solstice conditions. The results of the model runs were then compared to observational data from the SABER instrument on board NASA's TIMED satellite. SABER data represents the best available data on the OH^* emissions to date and therefore this comparison represents a stringent test of the CMAT2 model's capabilities.

For the comparison, CMAT2 calculated the concentration of both $OH^*(v=9)$ and $OH^*(v=8)$ and the subsequent emissions from both vibrational levels. The individual emission rates were combined for comparison with the SABER data. It was found that the CMAT2 model typically overpredicts the level of emissions from OH^* by approximately a factor of two at all times of the year. This can be attributed to a known feature of the CMAT2 model where atomic oxygen concentrations calculated are a factor of two higher than those predicted by the majority of models and observations e.g. Russell *et al.* (2005). Additional possible sources for the discrepancy were considered, such as incorrect photochemistry, but were ruled out because the error in OH^* was found to follow the error in O concentrations.

Results from Smith *et al.* (2010) showing SABER observations in which derived O concentrations are a factor of two higher than expected were also considered. Since this thesis employs only short-term model runs (~ 5 days) and CMAT2 utilises MSISE-90 O concentrations as part of the initial conditions it is unlikely that CMAT2 could recover such quantities of O over such a short time. It is therefore suspected that even if further measurements of O reveal increased concentrations, validating the results of Smith *et al.* (2010), this will not explain satisfactorily the high CMAT2 O concentrations. Attempts to resolve this issue are ongoing and it should be noted that the CMAT2 model minor chemistry is not suspected as the underlying cause (Dobbin, 2008).

Taking this feature in OH^* into account, it was found that during both equinox and solstice, CMAT2 can predict the general features of the altitudinal and latitudinal distribution in OH^* emissions although the magnitude of the emissions calculated vary.

This study was subsequently repeated for the lower vibrational level emissions $OH^*(5-3)$ and $OH^*(4-2)$ (Study 3), and a similar response was observed.

6.2.2.3   Study 4: Longitudinal Variations

The previous studies of OH^* emissions conducted as part of this thesis typically mapped the diurnal and seasonal variations in the emissions with respect to altitude and latitude. Longitudinal variations in the emissions remained to be investigated. In the fourth study performed the longitudinal variations in OH^* emissions were analysed at times surrounding local midnight.

It was found that the CMAT2 model does not perform well when depicting longitudinal variations in OH^* emissions. These variations in the OH^* emissions exhibit significant wavelike features produced by variations in the non-migrating tides (England *et al.,* 2009; Xu *et al.,* 2010). Stationary (D0), westward wavenumber 2 (DW2) and eastward wavenumber 3 (DE3) are all observable in SABER observations. CMAT2 produces only a stationary (D0) variation. In its current incarnation, CMAT2 utilises the GSWM model to simulate tidal features and it has been found that the amplitudes of GSWM are typically too small to accurately reproduce tidal effects in the atmosphere. For this reason the amplitude of the diurnal tide is typically doubled in order to give better agreement within the mesosphere as detailed in Marsh *et al.* (2006). At this time this has not been implemented into the CMAT2 model. Implementation of this scaling factor may yield improved results.

6.2.2.4   Study 5: Tidal Effects

In the final study conducted for this thesis the effects of the migrating diurnal and semidiurnal tides on the level of OH^* emissions were examined. This was accomplished by comparing the results from two CMAT2 model runs. In the first run tides were included while in the second run tides were eliminated in a manner similar to that described in Marsh *et al.* (2006). The comparison was performed at the equator and at 58° S.

At the equator it was found that the migrating diurnal tide significantly modulates the level of OH^* emissions, primarily through variations in atomic oxygen. Elimination of tides at the equator substantially lowers the amount of atomic oxygen available for

production of O_3 and hence OH^* at 84 km and 88 km. Therefore, the emission rate drops as OH^* is produced at a slower rate.

At higher altitudes (102 km) the atomic oxygen mixing ratio is unaffected by the tides. Yet temperatures are higher and the emissions are reduced at this altitude in the "no tide" scenario. Given that the reaction rate constant associated with the production of ozone is given by

$$6.0 \times 10^{-34} \left(\frac{300}{T}\right)^{2.4},$$

(6.1)

it can be seen that an increase in temperature will decrease the rate of O_3 and thereby OH^* production. Furthermore, assuming a constant pressure surface, an increase in temperature will result in a decreased total number density. This can significantly affect the rate of OH^* production since the number densities of O, O_2 and M will all decrease. Similar results were observed in Marsh *et al.* (2006).

At the higher latitudes (58° S) the "no tide" run showed that the level of emissions dropped at all altitudes. Elimination of the diurnal tide has no significant effect on either the temperature or atomic oxygen mixing ratio. This is expected considering the tidal theory presented in **Chapter 1** which shows that the diurnal tide cannot propagate beyond approximately $\pm 30°$ latitude. The cause of the drop in the level of emissions has yet to be determined.

The model results presented in this section were compared to similar results from the ROSE chemical model. While the magnitude of the results varied significantly it was clear that the general features produced were quite similar. Discrepancies between the model results can be attributed largely to different atomic oxygen volume mixing ratios calculated by both models. It is doubtful that the discrepancies could be produced by an alternative mechanism considering the almost identical scaling factor exhibited in both O concentration and the levels of OH^* emissions.

In general it was found that the CMAT2 model overpredicts the level of OH^* measured by SABER while the ROSE model underpredicts the emissions, in particular at the equator. Of note is that at 88 km, where the atomic oxygen mixing ratios calculated by both models are quite similar, both models produce similar levels of emissions in their

"no tide" model runs. This suggests that the chemistry of both models is quite similar and accurate although the tidal routines utilised differ. It is suspected that the CMAT2 dynamical routines within the mesopause require further investigation and possible refinements.

6.3 Model Limitations

As with all computational models the CMAT2 model has a number of limitations. These make it suitable for certain types of atmospheric studies and unsuitable for others. In order to categorise the advantages and disadvantages of CMAT2, certain model characteristics, in respect of OH^* emissions, will be compared to the WACCM and HAMMONIA GCM's in their current forms.

6.3.1 Long and Short Term Studies

For the majority of this thesis it will have been noticed that the focus has been on spatial and diurnal variations of the OH^* emissions. This is due to the fact that the CMAT2 model cannot, at the current time, maintain numerical stability for more than five consecutive days when using a 'day stepping' mode. This is most likely attributable to activation of the chemical heating routine within the model which still requires further verification. This makes the CMAT2 model severely limited for detailed studies of long term variations in atmospheric features.

Such studies would require model runs for each consecutive day in turn before any variations could be analysed. The results from each modelled day run would be required as the initial conditions for the subsequent day increasing the likelihood of numerical instabilities. The alternative, of starting the model at spinup stage on each day before performing the model run would reduce the change of numerical instabilities being produced. This would mean that the results from each model day run would have no bearing on the behaviour of the atmosphere on the next day and therefore is hard to justify. This method would be unrealistic while also prohibitively time consuming.

The current version of the WACCM model is known to maintain numerical stability for much longer periods of time and therefore would be more applicable for long term studies of atmospheric variability. However, as the WACCM model only stores global results at daily increments of $00:00$ UTC it is severely limited in its scope for short-

term, diurnal variations as shown in Kowalewski *et al.* (2014). Diurnal variations must be inferred from the longitudinal variations with local solar time. Given that there exists significant longitudinal variations in OH^* emissions detailed previously (Xu *et al.,* 2010) this comparison cannot be taken too far. The CMAT2 model stores global data at hourly intervals. Therefore, it is much more suitable for short-term studies of diurnal variations in OH^* emissions as presented in this thesis.

The CMAT2 results presented in this thesis are self-consistent 'instantaneous' values that have been produced using the model's 'perpetual' mode. The SABER data used for comparison are combined profiles that have been observed over the course of sixty days. SABER requires a total of 60 days in order to observe a full 24 hours local time coverage. The plots produced are assumed to be representative of the atmospheric conditions at the centre of the range. Therefore, SABER measurements exhibit features which are representative of a time period of approximately two months rather than instantaneous values. Bearing this in mind, comparisons between the modelled and observed results should not be taken too far because some random variations between the modelled and observed features result from this variation in time coverage. However, as it is currently outside the scope of available technology to acquire global coverage of instantaneous atmospheric conditions this comparison represents the best available option.

6.3.2   Model Resolution

The basic grid of the CMAT2 model has $2° \times 18°$ horizontal resolution with respect to latitude and longitude. WACCM supports $1.9° \times 2.5°$ and $4° \times 5°$ horizontal resolution as standard (Garcia *et al.,* 2007) while HAMMONIA uses a spectral model grid with triangular truncation T31 which corresponds to approximately $3.75°$ resolution (Schmidt *et al.,* 2006).

It can be seen that CMAT2 has approximately the same scope for latitudinal studies as WACCM while a slightly better latitudinal resolution than HAMMONIA. Given that the majority of studies to date have focused on latitudinal and altitudinal variations in OH^* emissions CMAT2 represents a prime candidate for latitudinal studies.

At a longitude resolution of 18°, the CMAT2 model is clearly less suitable for detailed studies of longitudinal variations in OH*. Short scale longitudinal variations and temporal variations with periods less than 1 hr are not represented as the grid points are separated by approximately 2000 km and 1 hr 12 mins local time. Features with periods above this horizontal and temporal resolution are, at best, only poorly represented when compared with WACCM and HAMMONIA.

Furthermore, longitudinal variations at a particular local time are also quite difficult to investigate. In order to study pure longitudinal variations across the globe, which are independent of local time variations, 20 individual profiles representative of a particular longitude at a particular local time must be selected from a 24 hr model run before being combined. The resulting plots then assume a linear relationship between atmospheric constituents separated by approximately 2000 km completely ignoring small scale variations within the atmosphere. These features would be represented better by both WACCM and HAMMONIA.

However, the longitudinal resolution of CMAT2 (18°), while appearing coarse when compared to both WACCM (5°) and HAMMONIA (3.75°), also has its advantages. The calculation of OH* photochemistry requires significant computational resources increasing both model run time and required storage capacity. Choosing a model with decreased resolution in one axis therefore significantly reduces the amount of calculations required in model runs as well as model run times and the storage required. In its current form WACCM only stores global model predictions at $00\!:\!00$ UTC. This completely eliminates its capacity to predict diurnal variations in OH* emissions which are not influenced by longitudinal variations. The coarse CMAT2 longitudinal resolution thereby actually increases the model's capacity to look at diurnal variations at a temporal resolution of 1 hr. This represents an advantage of CMAT2 over both WACCM and HAMMONIA.

The horizontal resolution of CMAT2 is 1/3 scale height which in the mesopause corresponds to approximately 2 km. At mesopause altitudes the WACCM model has vertical resolution of 3.5 km (Garcia *et al.,* 2007) while HAMMONIA has a variable resolution of $2-3$ km depending on temperature (Schmidt *et al.,* 2006). As mentioned previously altitudinal variations are among the most studied features of the OH* emissions and are also included in this thesis. Therefore, despite poor longitudinal

resolution, it is the opinion of the author that, CMAT2 provided the best options for global studies of OH^*.

6.4 Future Work and Further Studies

Like all computational models there are number of areas within CMAT2 that require further work. However, this is not to make light of the current model code or its capabilities. As detailed above, the CMAT2 model has its limitations, and as such is better suited to certain subject areas than others. The developments described in this thesis have extended the scope of the model and some topics which were previously inaccessible are now available to be explored. Given the current scope of the model, there exist a number of possible studies that could be performed. Some possible future work and potential further studies are outlined below.

6.4.1 Atomic Oxygen

The most pertinent and immediate concern in the current version of the CMAT2 model is the persistent problem with atomic oxygen. CMAT2 typically predicts atomic oxygen concentrations that are a factor of two higher than those predicted by the previous generations of UCL models (Dobbin, 2008), MSISE-90 and other empirical databases (Picone *et al.,* 2002), and observational studies (Offermann and Dresher, 1973). Smith *et al.* (2010) offers observational evidence that the concentration of O may actually be a factor of $2 - 5$ times greater than currently employed in these models although further verification of this result is required. Even if this result is verified it is still doubtful that a link between CMAT2 results and SABER observations could be ascertained as CMAT2 utilises initial profiles for O which have been obtained from the MSISE-90 database and it is doubtful that CMAT2 could recover such a large quantity of O is such short model runs.

It would also be difficult to corroborate the results of this thesis with the atomic oxygen concentrations derived from SABER. Since the high night-time O concentrations are derived from OH^* emissions it would be expected that the high concentrations of O predicted by CMAT2 would therefore produce accurate determinations of OH^* emissions. Since this is not the case, further investigations are required on this topic.

The discrepancy in the atomic oxygen concentrations was first recorded in 2008 by Alison Dobbin, who subsequently performed an investigation of the CMAT2 code aimed at finding the root cause of the discrepancy. However, due to time constraints and the limited resources available to conduct the investigation the cause of this issue has not been found to date. A detailed internal report into this issue was compiled which suggests that the issue may be related to the dynamical routines within the model. A detailed study of the effectiveness of the GSWM tides within the model, and a doubling of the tidal amplitudes in line with Marsh *et al.* (2006), may provide a starting point from which further investigations into the atomic oxygen discrepancy can proceed.

6.4.2 Ozone

Within the current version of the CMAT2 model ozone profiles used as part of the initial conditions are generated from UGAMP climatologies. In recent years the GOMOS instrument on the ESA's ENVISAT (Ratier *et al.,* 1999) as well as the SABER instrument have collected large amounts of data in relation to ozone concentrations within the atmosphere. Given these readily available sources of data an updated ozone climatology could be incorporated into the model to reflect more current values of ozone within the atmosphere. Given the close relationship between atomic oxygen and ozone, this may also assist in solving the atomic oxygen problem described previously. Furthermore, as shown in **Chapter 4**, adopting SABER retrieved ozone profiles significantly improved the agreement between the M1-D model and observational results. It can therefore be assumed that an updated ozone climatology may also improve CMAT2 model results, in particular in relation to OH^* concentrations and emissions.

6.4.3 Additional Photochemistry

For this thesis the hydrogen-ozone reaction

$$H + O_3 \rightarrow OH^*(v = 6 - 9) + O_2$$

(R6.2)
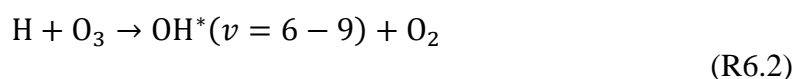
has been considered to be the only chemical reaction involved in the production of OH^*. This assumption is based on the most recent literature available (Xu *et al.,* 2012)

suggesting that **Reaction R6.2** is the only chemical source. However, arguments can still be made for the inclusion of the perhydroxyl reaction given by

$$HO_2 + O \rightarrow OH^*(v \leq 6) + O_2$$

(R6.1)
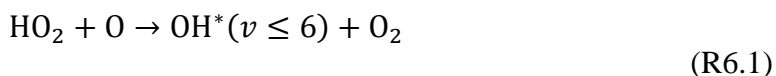
as a contributing source of OH^* production and emissions. Modification of the CMAT2 model code to include this reaction as a chemical source of OH^*, rather than ground state OH, may therefore affect the model results. Given that the current version of the CMAT2 model code typically overpredicts the concentrations and emissions from OH^*, it is hard to justify the inclusion of this additional chemical production without solving the atomic oxygen discrepancy first.

6.4.4 Mesospheric Heating

The focus of this thesis has been on incorporating a model of OH^* which can accurately simulate the temporal and spatial behaviour of these additional chemical species and their airglow emissions. The chemistry of the mesopause, reflecting concentrations and emission rates, has therefore been the primary concern.

As detailed in **Chapter 3**, **Reaction R6.2** also contributes significantly to the chemical heating within the mesopause. The CMAT2 code developed as part of this thesis calculates concentrations and emissions from OH^* species which are stored and output as model results. The concentrations of the chemical species involved are fed back into the model for the next time step iteration but the energetic feedback is not. The energetic feedback is still governed by the heating efficiency of Mlynczak and Solomon (1993). A study of the chemical heating in the middle atmosphere is therefore now accessible. Modification of the model code to eliminate the heating efficiency and allow for direct calculation of the chemical heating resulting from **Reaction R6.2** in the mesopause is possible with the incorporated photochemistry.

This energetic feedback was not incorporated into the CMAT2 code as part of this thesis as until recently there was an issue within the CMAT2 chemical heating routine which made it unstable. This issue is now thought to have been resolved as part of the work conducted for this thesis and a possible fix of the problem has been incorporated into the model code (Harris, private communication). However, further verification and

testing of the chemical heating routine is required before further amendments in this area should commence.

6.4.5 Spatial and Temporal Variations in Alternative OH^* Emission Bands

The results presented in this thesis have focussed on only 5 emission bands from OH^*, namely the $OH^*(9-8), (9-7), (8-6), (5-3)$ and $(4-2)$ bands. Yet the new CMAT2 model code incorporated as part of this thesis calculates a total of 37 emissions bands from OH^*. A comparison of the model results with ground and satellite based observations of these additional emission bands could be worthwhile.

The most obvious choice for continued study in this area would be to compare CMAT2 model results with observational data from the SCIAMACHY instrument on board the ESA's ENVISAT. SCIAMACHY observes emissions from the $OH^*(3-1), (6-2)$ and $(8-3)$ bands and have been used recently to derive the altitudinal distribution of the OH^* emission layers as discussed in **Chapter 4** and in von Savigny *et al.* (2012b). Emissions from the $OH^*(8-3)$ have also been studied extensively using ground based observations. A further study on comparisons of ground and satellite based observations with modelled data predicted by CMAT2 could be instructive.

6.4.6 OH Ground State Followup

In **Chapter 3** a distinction was made between OH in the ground state and OH^* in a vibrationally excited state. During the initial stages of this PhD a version of CMAT2 was adopted in which OH was not activated as a chemical species in the model. The minor chemistry involving OH was also inactive and no initial conditions for the species were available.

Therefore, work commenced on the establishment of an OH climatology based on observational data obtained from the Microwave Limb Sounder (MLS) instrument on board NASA's AURA satellite. Data from MLS for the year 2008 were binned with respect to latitude, longitude, altitude and local time and mapped onto a grid with the same resolution as the CMAT2 model grid. This data was read into the CMAT2 model and provided the initial conditions for the OH species. The associated chemistry was

activated and model output was produced which reflected observational data. Some of initial results from this work showing the global distribution of ground state OH for the year 2008 are presented in **Figure 3.3** of **Chapter 3**.

During a research visit to UCL it was found that CMAT2 had recently been updated to version 3.0. This update contained a number of model upgrades including a basic parameterisation for OH climatologies. Given that version 3.0 reflected a more up to date version of the CMAT2 code the upgraded code was adopted for the remainder of this thesis. The OH climatology was put aside in favour of the parameterisation.

As part of a future study it may be advantageous to continue development of this work. While parameterisations are very useful and effective tools in atmospheric models they are typically used to represent features within the atmosphere that are too small to be represented accurately on large model grids, or when there is insufficient understanding of processes involved in atmospheric phenomena. They are typically not used to provide initial conditions for atmospheric constituents where their accuracy may vary substantially with location and time. With such a wealth of data available on OH concentrations, which has already been validated by Pickett *et al.* (2008), replacing the parameterized OH climatology with actual OH measurements would represent a logical advance in CMAT2 code and could lead to a better representation of OH concentrations within the model.

References

A

Abreu, V.J., and Yee, J.H., Diurnal and seasonal variation of the night time OH (8-3) emission at low latitudes, *J. Geophys. Res.,* **94**, A9, 11949-11957, 1989.

Adler-Golden, S., Kinetic parameters for OH nightglow modelling consistent with recent laboratory measurements, *J. Geophys. Res.,* **109**, A9, 19969-19976, 1997.

Alexander, M.J., and Dunkerton, T.J., A spectral parameterization of mean-flow forcing due to breaking gravity waves, *J. Atmos Sci.,* **56**, 4167-4182, 1999.

Allen, M., Lunine, J.I., and Lang, Y.L., The vertical distribution of ozone in the mesosphere and lower thermosphere, *J. Geophys. Res.,* **89**, 4841-4872, 1984.

Andrews, D., A Stratospheric transport system, *Physics World,* **4**, 11, 41-46, 1991.

Andrews, D.A., *An Introduction to Atmospheric Physics*, 229 pp., Cambridge University Press, 2000.

B

Baker, D. J. and Romick, G. J.: The Rayleigh: interpretation of the unit in terms of column emission rate or apparent radiance expressed in SI units, *Appl. Optics*, **15**, 1966–1968, 1976.

Baker, D.J., and Stair, A.T., Rocket Measurements of the Altitude Distributions of the Hydroxyl Airglow*, *Physica Scripta,* **37**, 611-622, 1988.

Baker, D.J., Thurgood, B.K., Harrison W.K., Mlynczak, M.G., and Russell, J.M., Equatorial enhancement of the nighttime OH mesospheric infrared airglow, *Physica Scripta*, **75**, 615-619, 2007.

Banks, P.M., and Kockarts, G., *Aeronomy*. Part A, Academic Press, San Diego, California, 1973.

Bartels, J., The standardized Index Ks and the planetary index K_p, *IATME Bull.,* **126**, 97, IUGG Publ. Office, Paris, 1932.

Bates, D.R., and Nicolet, M., The photochemistry of atmospheric water vapour, *J. Geophys. Res.,* **55**, 301, 1950.

Bates, D.R., The temperature of the upper atmosphere, *Proc. Phys. Soc.,* London, **64B**, 805, 1951.

Battaner, E., Fernandez, M., and Quintana, J.M., The effect of quenching by atomic oxygen upon the diurnal variations of OH emission. Proc. 5th European Meeting of Upper Atmospheric Studies by Optical methods, Granada, 1977.

Battaner, E., and Lopez-Moreno, J.J., Time and altitude variations of vibrationally excited states of atmospheric hydroxyl, *Planet. Space Sci.,* **27**, 1421-1428, 1979.

Beig, G., Keckhut, P., Lowe, R.P., Roble, R.G., Mlynczak, M.G., Scheer, J., Fomichev, V.I., Offermann, D., French, W.J.R., Shepherd, M.G., Semenov, A.I., Remsberg, E.E., She, C.Y., Lubken, F.J., Bremer, J., Clemesha, B.R., Stegman, J., Sigernes, F., and Fadnavis, S., Review of mesospheric temperature trends, *Rev. Geophys.,* **41**, 4, 2003.

Berdyugina, S.V., and Solanki, S.K., The molecular Zeeman effect and diagnostics of solar and stellar magnetic fields, *Astronomy and Astrophysics*, **385**, 701-715, 2002.

Bertaux, J.L., Hauchecorne, A., Dalaudier, F., Cot, C., Kyrola, E., Fussen D., Tamminen, J., Leppelmeier, G.W., Sofieva, V., Hassinen, S., Fanton d'Andon, O., Barrot, G., Mangin, A., Theodore, B., Guirlet, M., Korablev, O., Snoeij, P., Koopmann, R., and Fraisse, R., First results on GOMOS/ENVISAT, *Adv. Space Res.,* **33**, 1029-1035, 2004.

Bjerknes, V., Das Problem der Wettervorhersage, betrachtet vom Standpunkte der Mechanik und der Physik, *Meteorologische Zeitschrift,* Wien, **21**, 1-7, 1904.

Boeker, E., and van Grondelle, R., *Environmental Phys.,* Wiley and Sons, Chichester, England, 1995.

Brasseur, G., and Solomon, S., *Aeronomy of the middle atmosphere*, 2nd Edition, D. Reidel Publishing Co., Dordrecht, Holland, 1986.

Brasseur, G., The response of the middle atmosphere to long-term and short-term solar variability: A two dimensional model, *J. Geophys. Res.,* **98**, D12, 22079-23090, 1993.

Brasseur, G., Hitchman, M.H., Walters, S., Dymek, M., Falise, E., and Pirre, M., An interactive chemical dynamical radiative two-dimensional model of the middle atmosphere, *J. Geophys. Res.,* **95**, D5, 5639-5655, 1990.

Breig, E.L., Secondary production processes for the hydroxyl atmospheric airglow, *Planet. Space. Sci.,* **18**, 1271, 1970.

Brode, W.R., *Chemical Spectroscopy*, 2nd Edition, Wiley, New York, 1958.

Burrage, M.D., Hagan, M.E., Skinner, W.R., Wu, D.L., and Hay, P.B., Long-term variability in the solar diurnal tide observed by HRDI and simulated by the GSWM, *Geophys, Res. Lett.,* **22**, 2641-2644, 1995.

C

Chang, R., *Basic Principles of Spectroscopy,* 2nd Edition, McGraw-Hill, New York, 1971.

Chapman, S. and Cowling, T.G., *The mathematical theory of non-uniform gases*, Cambridge University Press, New York and London, 1952.

Chapman, S. and Lindzen, R.S., *Atmospheric tides*, D. Reidel Publishing Co*.,* Dordrecht, 1970.

Charney, J.G. and Drazin, P.G., Propogation of planetary-scale disturbances from the lower into the upper atmosphere, *J. Geophys. Res.,* **66**, 83-109, 1961.

Charney, J.G., Fjörtoft, R., and von Neumann, J., Numerical Integration of the Braotropic Vorticity Equation, *Svenska Geofysiska Föreningen,* **2**, 4, 237-254, 1950.

Cherepanov, V.N., Electric dipole moment function of the OH molecule, *Russian Physics Journal*, **46**, 7, 2003.

Clancy, R.T., Sandor, B.J., Garcia-Munoz, A., Lefevre, F., Smith, M.D., Wolff, M.J., Montmessin, F., Murchie, S.L., and Nair, H., First detection of Mars atmospheric hydroxyl: CRISM Near-IR measurement versus LMD GCM simulation of OH Meinel band emission in the Mars polar winter atmosphere, *Icarus*, **226**, 227-281, 2013.

Codrescu, M.V., Fuller-Rowell, T.J., Roble, R.G., and Evans, D.S., Medium energy particle precipitation influences on the mesosphere and lower thermosphere, *J. Geophys. Res.,* **102**, A9, 19987-19997, 1997.

Colgrove, F.D., Johnson, F.S., and Hanson, W.B., Atmospheric composition in the lower thermosphere, *J. Geophys. Res.,* **84**, 811-822, 1966.

Conway, R.R., Summers, M.E., and Stevens. M.H., Satellite observations of upper stratospheric and mesospheric OH: The HO_x Dilemma, *Geophys, Res. Lett.,* **27**, 17, 2613-2616, 2000.

D

Dalgarno, A., and Smith, F.J., The thermal conductivity and viscosity of atomic oxygen, *Planet. Space, Sci.,* **9**, 1-2, 1962.

DeMore, W.B., Sander, S.P., Howards, C.J., Ravishankara, A.R., Golden, D.M., Kolb, C.E., Hampson, R.F., Kurylo, M.J., and Molina, M.J., Chemical kinetics and photochemical data for use in stratospheric modelling. Evaluation 12, *NASA Jet Propulsion Laboratory,* JPL Publication, **97**, 4, 1997.

Dickinson, R.E., Ridley, E.C., and Roble, R.G., A three-dimensional general circulation model of the thermosphere, *J. Geophys. Res.,* **86**, 1499-1512, 1981.

Dobbin, A.L., *Modelling studies of possible coupling mechanisms between the upper and middle atmosphere*, PhD. Thesis, University of London*,* 2005.

Dobbin, A.L., CMAT2: Model Developments, Capabilities and Limitations, *Internal UCL Report*, private communication, 2008.

E

England, S.L., Dobbin, A.L, Harris, M.J., Arnold, N.F., and Aylward, A.D., A study into the effects of gravity wave activity on the diurnal tide and airglow emissions in the equatorial mesosphere and lower thermosphere using the Coupled Middle Atmosphere and Thermosphere (CMAT) general circulation model, *J. Atmos. Sol. Terr. Phys.,* **68**, 293-308, 2006.

England, S.L., Zhang, X., Immel, T.J., Forbes, J.M., and DeMajistre R., The effect of non-migrating tides on the morphology of the equatorial ionospheric anomaly: seasonal variability, *Earth Planets Space.,* **61**, 493-503, 2009.

Englert, C.R., Stevens, M.H., Siskind, D.E., Harlander, J.M, Roesler, F.L., Pickett, H.M., von Savigny, C., and Kochenash, A.J., First results from the Spatial Heterodyne Imager for Mesospheric Radicals (SHIMMER): Diurnal variation of mesospheric hydroxyl, *Geophys. Res. Lett.,* **35**, L19813, 2008.

F

Fernando, R.P., and Smith, I.W.M., Vibrational relation of NO by atomic oxygen, *Chem. Phys. Lett.,* **66**, 218-222, 1979.

Fomichev, V.L., and Schved, G.M, Parameterization of the radiative flux divergence in the 9.6 micro-meter O_3 band, *J. Atm. Terr. Phys.,* **47**, 11, 1037-1049, 1985.

Fomichev, V.L., Blanchet, J.P., and Turner, D.S., Matrix parameterization of the 15 μm band cooling in the middle and upper atmosphere for variable CO_2 concentration, *J. Geophys. Res.,* **103**, D10, 11505-11528, 1998.

Foster, J.C., Holt, J.M., Musgrove, R.G., and Evans, D.S., Ionospheric convection associated with discrete levels of particle precipitation, *Geophys, Res. Lett.,* **13**, 656, 1986.

Fritts, D.C., and Alexander, M.J., Gravity wave dynamics and effects in the middle atmosphere, *Rev. Geophys.,* **41**, 1, 1003, doi:10.1029/2001RG000106, 2003.

Fritts, D.C., and Isler, J.R., Mean motion and tidal and two-day structure and variability in the mesosphere and lower thermosphere over Hawaii, *J. Atmos. Sci.,* **51**, 2145-2164, 1994.

Fuller, E.N., and Schettler, P.D., Giddings, J.C., *Industrial and engineering chemistry,* **58**, 19, 1966.

Fuller-Rowell, T.J., and Rees, D., A three-dimensional time-dependant global model of the thermosphere, *J. Atmos. Sci.,* **37**, 2545-2567, 1980.

Fuller-Rowell, T.J., *A three dimensional time dependant global circulation model of the thermosphere*, PhD Thesis, University of London, 1981.

Fuller-Rowell, T.J., and Rees, D., Derivation of a conservation equation for mean molecular eight for a two-constituent gas within a three-dimensional time-dependant model of the thermosphere, *Planet. Space Sci.* **31**, 1209, 1983.

Fuller-Rowell, T.J., A two dimensional, high-resolution, nested-grid model of the thermosphere: 1 Neutral response to an electric field "Spike", *J. Geophys. Res.,* **89**, A5, 2971-2990, 1984.

Fuller-Rowell, T.J., and Evans, D.S., Height-integrated Pedersen and Hall conductivity patterns inferred from the TIROS-NOAA satellite data, *J. Geophys. Res.,* **92**, 7606, 1987.

Fuller-Rowell, T.J., Modelling the solar cycle change in nitric oxide in the thermosphere and upper mesosphere, *J. Geophys. Res.,* **98**, 1571-1580, 1993.

Fuller-Rowell, T.J., Rees, D., Quegan, S., Moffett, R.J., Codrescu, M.V., and Millward, G.H., A coupled thermosphere ionosphere model (CTIM), Solar terrestrial energy program (STEP), Handbook of Ionospheric Models, edited by R.W. Schunk, 1996.

G

Gao, H., Xu, J.Y., Chen, G.M., Yuan W., and Beletsky, A.B., Global distributions of OH and O_2 (1.27 μm) nightglow emissions observed by TIMED satellite, *Science China Technological Sciences,* **54**, 2, 447 − 456, 2011.

Garcia, R.R., and Solomon, S., A numerical model of the zonally averaged dynamical and chemical structure of the middle atmosphere, *J. Geophys. Res.,* **88**, C2, 1379-1400, 1983.

Garcia, R.R., Marsh, D.R., Kinnison, D.E., Boville, B.A., and Sassi, F., Simulation of secular trends in the middle atmosphere, 1950-2003, *J. Geophys. Res.,* **112**, D09301, 2007.

Garvin, D., Chemically induced vibrational excitation: A study of hydroxyl radicals formed in the $H + O_3$ atomic flame, *J. Am. Chem. Soc.*, **81**, 13, 1959.

Garvin, D., Broida, H.P., and Kostkowski, H.J., Chemically induced vibrational excitation: Hydroxyl radical emission in the 1-3 Micron Region Produced by the $H + O_3$ Atomic Flame, *J. Chem. Phys.,* **64**, 2518-2527, 1960.

Giraud, A., and Petit, M., *Ionospheric Techniques and Phenomena,* 1st Edition, D. Reidel Publishing Company, Dordrecht, Holland, 1978.

Goldman, A., Schoenfeld, W.G., Goorvitch, D., Chackerian, C., Dothe, H., Melen, F., Abrams, M.C., and Selby, J.E., Updated line parameters for the OH $X^2 II − X^2 II$ (v'', v') transitions, *J. Quant. Spectrosc. Radiat. Transfer,* **59**, 3-5, 453-469, 1998.

Grygalashvyly, M., Sonnemann, G.R., Lübken, F.J., Hartogh, P., and Berger, U., Hydroxyl layer: Mean state and trends at mid-latitudes, *J. Geophys. Res. Atmos.,* **119**, 12391-12419, doi:10.1002/2014JD022094, 2014.

H

Hagan, M.E., Forbes, J.M., and Vial, F., On modelling migrating solar tides, *Geophys, Res. Lett.,* **22**, 893-896, 1995.

Hagan, M.E., Burrage, M.D., Forbes, J.M., Hackney, J., Randel, W.J., and Zhang, X., GSWM-98: Results for migrating solar tides, *J. Geophys. Res.,* **104**, 6813-6827, 1999.

Hargreaves, J,K., *The upper atmosphere and solar-terrestrial relations: An introduction to the aerospace environment*, Van Nostrand Reinhold Publishing, New York, 1979.

Harris, M.J., *A new coupled middle atmosphere and thermosphere circulation model: Studies of dynamic, energetic and photochemical coupling in the middle and upper atmosphere*, PhD Thesis. University of London, 2001.

Harris, M.J., Arnold, N.F., and Aylward, A.D., A study into the effect of the diurnal tide on the structure of the background mesosphere and thermosphere using the new coupled middle atmosphere and thermosphere (CMAT) general circulation model, *Ann. Geophys.,* **20**, 225-235, 2002.

Hedin, A.E., Extension of the MSIS thermosphere model into the middle and lower atmosphere, *J. Geophys. Res.,* **96**, A2, 1159-1172, 1991.

Herzberg, G., *Molecular Spectra and Molecular Structure*: *Vol 1 – Spectra of Diatomic Molecules*, 2nd edition, Robert E. Kreiger Publishing Company, 1989.

Herzberg, G., The atmospheres of the planets, *J. R. Astron. Soc. Can.,* **45**, 100, 1951.

Hickey, M.P., and Walterscheid, R.L., Wave-modified mean exothermic heating in the mesopause region, *Geophys, Res. Lett.,* **21**, 22, 2413-2416, 1994.

Hill, E., and Van Vleck, J.H., On the quantum mechanics of the rotational distortion of multiplets in molecular spectra, *Phys. Rev.,* **32**, 250, 1928.

Hines, C.O., Internal gravity waves at ionospheric heights, *Can. J. Phys.,* **38**, 1441-1481, 1960.

Hinteregger, H.E., The extreme ultraviolet solar spectrum and its variation during a solar cycle, *Ann. Geophys.,* **26**, 547, 1970.

Holton, J.R., The dynamic meteorology of the stratosphere and mesosphere, Meteor. Monog. **15**, 37, *Amer. Met. Soc.,* MA, 1975.

Houghton, J.T., The stratosphere and mesosphere, *Q. J. R. Meteorol. Soc.*, **104**, 1-29, 1978.

I

Iribane, J.V., and Cho, H.R., *Atmospheric Physics,* D. Reidel Publishing Company, Dordrecht, Holland, 1980.

J

Jacchia, L.G., and Kopal, Z., Atmospheric oscillations and the temperature of the upper atmosphere, *J. Meteorol., 9*, 13-23, 1951.

Jacobson, M.Z., *Fundamentals of Atmospheric Modelling*, 2nd Edition, Cambridge University Press, 2005.

Johnston, J.E., and Broadfoot, A.L., Midlatitude observations of the night airglow: Implications to quenching near the mesopause, *J. Geophys. Res., 98*, A12, 21593-21603, 1993.

K

Kalnay, E., *Atmospheric Modelling, Data Assimilation and Predictability*, Cambridge University Press, 2003.

Kaufmann, M., Lehmann, C., Hoffmann, L., Funke, B., Lopez-Puertas, M., vonSavigny, C., and Riese, M., Chemical heating rates derived from SCIAMACHY vibrationally excited OH limb emission spectra, *Adv. Space Res., 41*, 1914-1920, 2007.

Keating, G.M., Chiou, L.S., and Hsu, N.C., Improved Ozone Reference Models for the COSPAR International Reference Atmosphere, *Adv. Space Res., 18*, 9/10, 11-58, 1996.

King, W.T., and Crawford, B., The integrated intensity of the nitric oxide fundamental band, *J. Quant. Spectrosc. Radiat. Transfer, 12*, 443-447, 1972.

Klenerman, D., and Smith, I.W.M., Infrared chemiluminescence studies using a SISAM spectrometer. Reactions producing vibrationally excited OH, *J. Chem. Soc. Faraday. Trans. 2*, 83, 229-241, 1987.

Kockarts, G., Nitric oxide cooling in the terrestrial thermosphere, *Geophys, Res. Lett., 7*, 2, 137-140, 1980.

Kovacs, I., *Rotational structure in the spectra of diatomic molecules*, American Elsevier Publishing Company, New York, 1960.

Kowalewski, S., von Savigny, C., Palm, M., McDade, I.C., and Notholt, J., On the impact of the temporal variability of the collisional quenching process on the mesospheric OH emission layer: a study based on SD-WACCM4 and SABER, *Atmos. Chem. Phys., 14*, 10193-10210, 2014.

Krassovsky, V.I., and Lukashenia, V.T., On the question of identifications of the night sky spectrum in the neighbourhood of 10,000 $\mathring{A}$, *Dokl. Akad. Nauk SSSR., 80*, 735, 1951.

Krassovsky, V.I., Shefov, N.N., and Yarin, V.I., On the OH airglow, *J. Atm.. Terr. Phys., 21*, 46, 1961.

Krassovsky, V.I., Sherov, N.N., and Yarin, V.I., Atlas of the airglow spectrum 3000-12400 $\mathring{A}$, *Planet. Space Sci.,* **9**, 883-915, 1962.

L

Langhoff, S.R., Werner, H.J., and Rosmus, P., Theoretical transition probabilities for the OH Meinel system, *J. Mol. Spect.,* **118**, 507-529, 1986.

Langhoff S.R., Bauschlicher, C.W., and Tayler, P.R., Theoretical study of the dipole moment function of $OH(X^2II)$, *J. Chem. Phys.*, **86**, 6992, 1987.

Langhoff S.R., Bauschlicher, C.W., and Tayler, P.R., Theoretical study of the dipole moment function of $OH(X^2II)$, *J. Chem. Phys.*, **91**, 5953, 1989.

Langel, R.A., International geomagnetic reference field, 1991 revision, *EOS Trans.,* AGU, **73**, 182, 1992.

Le Texier, H., Solomon, S., and Garcia, R.R., Seasonal variability of the OH Meinel Bands, *Planet. Space Sci.,* **35**, 8, 977-989, 1987.

Le Texier, H., Solomon, S., Thomas, R.J., and Garcia, R.R., OH* (7-5) Meinel band dayglow and nightglow measured by the SME limb scanning near-infrared spectrometer: comparison of the observed seasonal variability with two-dimensional model simulations, *Ann. Geophys.,* **7**, 365-374, 1989.

Levin, E., Partridge, H., and Stallcop, J.R., Collision integrals and high temperature transport properties for N-N, O-O, and N-O, *J Thermophys. Heat Trans.,* **4**, 469-477, 1990.

Li, S., Matthews, J., and Sinha, A., Atmospheric hydroxyl radical production from electronically excited NO_2 and H_2O, *Science*, **319***, 5870, 1657-1660, 2008.

Lindzen, R.A., Thermally driven diurnal tide in the atmosphere, *Q. J. R. Meteorol. Soc.,* **93**, 18-42, 1967.

Lindzen, R.A., Turbulence and stress due to gravity wave and tidal breakdown, *J. Geophys. Res.,* **86**, C10, 9707-9714, 1981.

Liu, H., and Hagan, M.E., Local heating/cooling of the mesosphere due to gravity wave and tidal coupling, *Geophys, Res. Lett.,* **25**, 15, 2941-2944, 1998.

Liu, H., Hagan, M.E., and Roble, R.G., Local mean state changes due to gravity wave breaking modulated by the diurnal tide, *J. Geophys. Res.,* **105**, D10, 12381-12396, 2000.

Liu, H., and Shepherd, G.G., An empirical model for the altitude of the OH nightglow emission, *Geophys, Res. Lett.,* **33**, L09805, 2006.

Lopez-Gonzalez, M.J., Rodriguez, E.R., Wiens, H., Shepherd, G.C., Sargoytchev, S., Brown, S., Shepherd, M.G., Aushev, V.M., Lopez-Moreno, J.J., Rodrigo, R., and Cho,

Y.M., Seasonal variations of O_2 atmospheric and $OH(6-2)$ airglow and temperature at mid-latitudes from SATI observations, *Ann. Geophys,* **22**, 819-828, 2004.

Lopez-Moreno, J.J., Rodrigo, R., Moreno, F., Lopez-Puertas, M., and Molina, A., Rocket measurements of O_2 infrared atmospheric system in the nightglow, *Planet. Space Sci.,* **36**, 5, 459-467, 1988.

M

Mahan, B.H., *College Chemistry*, Addison-Wesley Publishing Company, 1966.

Makhlouf, U.B., Picard, R.H., and Winick, J.R., Photochemical-dynamical modelling of the measured response of airglow to gravity waves, *J. Geophys. Res.,* **100**, D6, 11289-11311, 1995.

Marsh, D., Smith, A., Brasseur, G., Kaufmann, M., and Grossman, K., The existence of a tertiary ozone maximum in the high-latitude middle atmosphere, *Geophys, Res. Lett.,* **28**, 24, 4531-4534, 2001.

Marsh, D., Smith, A., and Noble, E., Mesospheric ozone response to changes in water vapour, *J. Geophys. Res.,* **108**, D3, 4109-4114, 2003.

Marsh, D. R., A. K. Smith, M. G. Mlynczak, and J. M. Russell III, SABER observations of the OH Meinel airglow variability near the mesopause, *J. Geophys. Res.*, **111**, A10S05, doi:10.1029/2005JA011451, 2006.

Martyn, D.F., and Pulley, O.O., The temperatures and constituents of the upper atmosphere, *Proc. Roy. Soc.,* **A154**, 455-486, 1936.

Matsuno, T., A quasi one-dimensional model of the middle atmosphere circulation interacting with internal gravity waves, *J. Meteor. Soc. Japan,* **60**, 215-226, 1982.

McDade, I.C., Llewellyn, E.J., and Harris, F.R., Atomic oxygen concentrations in the lower auroral thermosphere, *Adv. Space Res.,* **5**, 229-232, 1985.

McDade, I.C., and Llewellyn, E.J., Kinetic parameters related to sources and sinks of vibrationally excited OH in the nightglow, *J. Geophys. Res.,* **92**, A7, 7643-7650, 1987a.

McDade, I.C., Llewwllym E.J., Murtagh, D.P., and Greer, R.G.H., ETON 5: Simultaneous rocket measurements of the OH Meinel $\Delta v = 2$ sequence and (8,3) band emission profiles in the nightglow, *Planet. Space Sci.,* **35**, 9, 1137-1147, 1987b.

McDade, I.C., The altitude dependence of the $OH(X^2II)$ vibrational distribution in the nightglow: some model expectations, *Planet. Space Sci.,* **39**, 1049-1057, 1991.

Medvedev, A.S., and Klassen, G.P., Vertical evolution of gravity wave spectra and the parameterization of associated wave drag, *J. Geophys. Res.,* **100**, 25841-25853, 1995.

Medvedev, A.S., Klassen, G.P., and Bolville, B.A., The parameterization of gravity wave drag based on the nonlinear diffusion of wave spectra. In: Hamilton, K (Ed.)

Gravity Wave Processes: Their parameterizations in global climate models, Springer, Berlin, 309-525, 1997.

Medvedev, A.S., and Klassen, G.P., Parameterization of gravity wave momentum deposition based on non linear wave interactions: basic formulation and sensitivity tests, *J. Atmos. Sol. Terr. Phys.,* **62**, 1015-1033, 2000.

Medvedev, A.S., and Klassen, G.P., Thermal effects of saturating gravity waves in the atmosphere, *J. Geophys. Res.,* **108**, D2, 4040, 2003.

Meinel, A.B., OH emission bands in the spectrum of the night sky, *Astrophys. J.,* **111**, 555, 1950.

Melo, S.M.L, Lowe. R.P., and Russell, J.P., Double-peaked hydroxyl airglow profiles observed from WINDII/UARS, *J. Geophys. Res.,* **105**, D10, 12397-12403, 2000.

Melo, S.M.L., McDade, I.C., and Takahashi, H., Atomic oxygen density profiles from ground based nightglow measurements at 23°S, *J. Geophys. Res.,* **106**, D14, 15377-15384, 2001.

Meriwether, J.W., and Gerrard, A.J., Mesosphere Inversion Layers and Stratosphere Temperature Enhancements, *Rev. Geophys.,* **42**, RG3003, 2004.

Meyer, W., PN_-CI and CEPA studies of electron correlation effects. II. Potential curves and dipole moment functions of the OH radical, *Theor. Chim. Acta,* **35**, 277, 1974.

Meyer, C., Gravity wave interactions with the diurnal propagating tide, *J. Geophys. Res.,* **104**, D4, 4223-4239, 1999a.

Meyer, C., Gravity wave interactions with mesospheric planetary waves: A mechanism for penetration into the thermosphere-ionosphere system, *J. Geophys. Res.,* **104**, 28181-28196, 1999b.

Mies, F.H., Calculated vibrational transition probabilities of OH(X^2II), *J. Mol. Spectros.,* **53**, 150-188, 1974.

Millward, G., Moffett, R.J., Quegan, S., and Fuller-Rowell, T.J., A coupled thermosphere-ionosphere-plasmasphere model (CTIP), *Solar Terrestrial Energy Program (STEP) Handbook,* editor R.W. Schunk, 1996.

Mlynczak, M.G., and Solomon, S., Middle atmosphere heating by exothermic chemical reactions involving odd hydrogen species, *Geophys, Res. Lett.,* **18**, 37-40, 1991a.

Mlynczak, M.G., and Solomon, S., Reply, *Geophys, Res. Lett.,* **18**, 1793-1794, 1991b.

Mlynczak, M.G., and Solomon, S., A detailed evaluation of the heating efficiency in the middle atmosphere, *J. Geophys. Res.,* **98**, D6, 10517-10541, 1993.

Mlynczak, M.G., Zhou, D.K., and Adler-Golden, S., Kinetic and spectroscopic requirements for the inference of chemical heating rates and atomic hydrogen densities from OH Meinel band measurements, *Geophys, Res. Lett.,* **25**, 5, 647-650, 1998.

Mlynczak, M.G., Martin-Torres, F.J., Crowley, G., Kratz, D.P., Funke, B., Gang Lu, Lopez-Puertas, M., Russell, J.M., Kozyra, J., Mertens, C., Sharma, R., Gordley, L., Picard, R., Winick, J., and Paxton, L., Energy transport in the thermosphere during the solar storms of April 2002, *J. Geophys. Res.,* **110**, A12S25, 2005.

Mlynczak, M.G., Marshall, B.T., Martin-Torres, F.J., Russell III, J.M., Thompson, R.E., Remsberg, E.E., and Gordley, L.L., Sounding of the atmosphere using broadband emission radiometry observations of daytimes mesospheric $O_2(^1\Delta)$ 1.27 μm emission and derivations of ozone, atomic oxygen, and solar and chemical energy deposition rates, *J. Geophys. Res.,* **112**, D15306, 2007.

Müller-Wodarg, I., *Modelling perturbations propagating through the mesopause into the Earth's upper atmosphere*, PhD. Thesis, University of London, 1997.

Müller-Wodarg, I., Aylward, A.D., and Fuller-Rowell, T.J., Tidal oscillations in the thermosphere: a theoretical investigation of their sources, *J. Atm. Sol. Terr. Phys.,* **63**, 899-914, 2001.

Mulligan, F.J., Horgan, D.F., Galligan, J.G., and Griffin, E.M., Mesopause temperatures and integrated band brightnesses calculated from airglow OH emissions recorded at Maynooth (53.2°N, 6.4°W) during 1993, *J. Atm. Terr. Phys.,,* 57, **13**, 1623-1637, 1995.

Murgatroyd, R.J., and Singleton, F., Possible meridional circulation in the stratosphere and mesosphere, *Q. J. Met. Soc.,* **87**, 125, 1961.

Murphy, R.E., Infrared emission of OH in the fundamental and first overtone bands, *J. Chem. Phys.,* **54**, 4852, 1971.

N

NASA, Studying Earth's Environment From Space, 2008 Available at: http://www.ccpo.odu.edu/SEES/index.html, [Accessed 2008].

Nelson, D.D., Schiffman, A., Nesbitt, D.J., Orlando, J.J., and Burkholder, J.B., $H + O_3$ Fourier transform infrared emission and laser absorption studies of $OH(X^2II)$ radical: An experimental dipole moment function and state-to-state Einstein A coefficients, *J. Chem. Phys.,* **93**, 10, 1990.

Nicolet, M., Ozone and Hydrogen reactions, *Ann. Geophys.,* **26**, 531, 1970.

NOAA, Ocean Service Education, 2008, Available at http://oceanservice.noaa.gov/education/kits/currents/media/coriolis_effect.gif, [Accessed 2010].

O

Offermann, D., and Dresher, A., Atomic oxygen densities in the lower thermosphere as derived from *in situ* 5577-A night airglow and mass spectrometer measurements, *J. Geophys. Res.,* **78**(28), 6690-6700, 1973.

Ohoyama, H., Kasai, T., Yoshimura, Y., Kimura, H., and Kuwata, K., Initial distribution of vibration of the OH radicals in the $H + O_3 \rightarrow OH(X^2 II) + O_2$ reaction, *Chem. Phys. Lett.,* **118**, 236-266, 1985.

Ojeda, M.G., El ozono estratosferico, *Tethys*, **3**, 47-58, 2006.

Oshio, M., Madea, R., and Sakagami, H., Height distribution of local photoionization efficiency, *J. Radio. Res. Lab. Japan.,* **13**, 245-577, 1966.

P

Parish, H.F., *Modelling the response of the thermosphere to lower atmosphere tides*, PhD. Thesis, University of London, 1989.

Pekeris, C.L., Atmospheric oscillations, *Proc. Roy. Soc.,* **A158**, 650-691, 1937.

Petitdidier M., and Teitelbaum, H., Lower thermosphere emissions and tides, *Planet. Space Sci.*, **25**, 711 1977.

Piccioni, G., First detection of hydroxyl in the atmosphere of Venus, *Astron. Astrophys.,* **483**, L29-L33, 2008.

Pickett, H.M, Drouin, B.J., Canty, T., Salawitch, R.J., Fuller, R.A., Perun, V.S., Livesey, N.J., Waters, J.W., Stachnik, R.A., Sander, S.P., Traub W.A., Jucks, K.W., and Minschwaner, K., Validation of Aura microwave limb sounder OH and HO_2 measurements, *J. Geophys. Res.,,* **113**, D16S30, 2008.

Pickett, H.M., Read, W.G., Lee, K.K., and Yung, Y.L., Observation of night OH in the mesosphere, *Geophys, Res. Lett.,* **33**, L19808, 2006.

Picone, J.M., Hedin, A.E., Drob, D.P., and Aikin, A.C., NRLMSISE-00 empirical model of the atmosphere: Statistical comparisons and scientific issues, *J. Geophys. Res.,* **107**, A12, 1468, 2002.

Plane, J., The Mesosphere and Thermosphere, *NCAS Atmospheric Measurement Summer School,* Powerpoint presentation, (2009) Available at : https://www.google.ie/url?sa=t&rct=j&q=&esrc=s&source=web&cd=1&ved=0CCIQFj AA&url=https%3A%2F%2Fwww.ncas.ac.uk%2Findex.php%2Fen%2Fdocuments%2F doc_download%2F751-arran13-mesosphere-thermosphere&ei=iOSJVJayDITR7QbsmIDwDQ&usg=AFQjCNHu_1WGozW5LkHv q6dN_1wnS0vPmA&sig2=zyIw4SoT9QM4mNIXKc_2zQ&bvm=bv.81456516,d.ZGU [Accessed: 2012].

Q

Quegan, S., Bailey, G.J., Moffett, R.J., Heelis, R.A., Fuller-Rowell, T.J., Rees, D., and Spiro, A.W., A theoretical study of the distribution of ionization in the high-latitude ionosphere and the plasmasphere: First results of the mid-latitude trough and the light ion trough, *J. Atm. Terr. Phys.,* **44**, 619, 1982.

R

Ratier, G., Levrini, G., Popescu, A., Paulsen, T., Readings, C., and Langen, J., GOMOS: Envisat's contribution to measuring long-term trends in ozone and other trace gases, *European Space Agency Bulletin,* **97**, 1999.

Rees, M.H., *Physics and chemistry of the upper atmosphere*, Cambridge atmospheric and space science series, Cambridge University Press, 1989.

Remedios, J., *et al.*, The UARS reference atmosphere project, 1998 Available at: *http://hyperion.gsfc.nasa.gov/Analysis/UARS/urap/contacts_information.html,* [Accessed: 1998].

Richardson, L.R., *Weather Prediction by Numerical Process*, Cambridge University Press, 1922.

Rishbeth, H., and Garriott, O.K., *Introduction to ionospheric physics*, Academic Press, New York and London, 1969.

Rishbeth, H., Thermospheric winds and the F-region: A review, *J. Atm. Terr. Phys.,* **34**, 1-37, 1972.

Roach, F.G., and Gordon, J.L., *The Light of the Night Sky*, D. Reidel Publishing Co., Dordrecht, Holland, 1973.

Roble, R.G., Ridley, E.C., and Dickinson, R.E., On the global mean structure of the thermosphere, *J. Geophys. Res.,,* 92, A8, 8745-8758, 1987.

Roble, R.G., and Ridley, E.C., A thermosphere-ionosphere-mesosphere-electrodynamics general circulation model (TIME-GCM): Equinox solar cycle minimum simulations (30-500 km), *Geophys, Res. Lett.,* **21**, 6, 417-420, 1994.

Roble, R.G., Energetics of the mesosphere and thermosphere, *Upper mesosphere and lower thermosphere: A review of experiment and theory,* geophysical monograph, **87**, AGU, 1995.

Roble, R.G., and Shepherd, G.G., An analysis of wind imaging interferometer observations of O(1S) equatorial emission rates using the thermosphere-ionosphere-mesosphere-electrodynamics general circulation model, *J. Geophys. Res.,* **102** (A2), 2467-2474 1997.

Rose, K., and Brasseur, G., A three-dimensional model of chemically active trace species in the middle atmosphere during disturbed winter conditions, *J. Geophys. Res.,* **94**, 16397-16403, 1989.

Russell, J., and Lowe, R.P., Atomic oxygen profiles (80-94 km) derived from Wind Imaging Interferometer/Upper Atmospheric Research Satellite measurements of

hydroxyl airglow: Validation of technique, *J. Geophys. Res.,* **108**, D21, 4662-4669, 2003.

Russell, J.P., Ward, W.E., Lowe, R.P., Roble, R.G., Shepherd, G.G., and Solheim, B., Atomic oxygen profiles (80 to 115 km) derived from Wind Imaging Interferometer/Upper Atmospheric Research Satellite measurements of the hydroxyl and greenline airglow: Local time-latitude dependence, *J. Geophys. Res.,* **110**, D15305, 2005.

S

Salah, J.E., Interim standard for the ion-neutral atomic oxygen collision frequency, *Geophys, Res. Lett.,* **20**, 1543-1546, 1993.

Samson, J.A.R., and Pareek, P.N., Absolute photoionization cross sections of atomic oxygen, *Phys. Rev. A – General Physics,* 3rd series, **31**, 1470-1476, 1985.

Schmidt, H., Brasseur, G.P., Charron, M., Manzini, E., Giorgetta, M.A., and Diehl, T., The HAMMONIA Chemistry Climate Model: Sensitivity of the Mesopause Region to the 11- Year Solar Cycle and CO_2 Doubling, *American Meteorological Society Journal of Climate – Special Edition*, pp 3903, 2006.

Schunk R.W., and Walker, J.C.G., Theoretical ion densities in the lower ionosphere, *Planet. Space. Sci.,* **21**, 1875-1896, 1973.

Seinfeld, J.H., and Pandis, S.N., *Atmospheric Chemistry and Physics: From Air Pollution to Climate Change,* 2nd Edition, John Wiley and Sons, 2006.

Sheen, Y.K., and Byun, Y.I., The night sky spectrum of Mount Bohyun, *J. Kor. Astron. Soc.*, **37**, 87-90, 2004.

Shepherd, G.G., The middle atmosphere, *J. Atmos. Sol. Terr. Phys.,* **62**, 1587-1601, 2000.

Shepherd, M.G., Evans, W.F.J., Hernandez, G., Offermann , D., and Takahashi, H., Global variability of mesospheric temperature: Mean temperature field, *J. Geophys. Res.,* **109**, 2004.

Shved, G.M., Kutepov, A.A., and Ogibalov, V.B., Non-local thermodynamic equilibrium in CO_2 in the middle atmosphere, I Input data and populations of the v_3 mode manifold states, *J. Atmos. Sol. Terr. Phys.,* **60**, 289-314, 1998.

Sivjee, G.G., Airglow Hydroxyl Emissions, *Planet. Space Sci.,* **40**, 2/3, 235-242, 1992.

Sivjee, G.G., and Hamwey, R.H., Temperature and chemistry of the polar mesopause OH, *J. Geophys. Res.,* **92**, A5, 4663-4672, 1987.

Smith, A., Physics and chemistry of the mesopause region, *J. Atmos. Sol. Terr. Phys.,* **66**, 839-857, 2004.

Smith, A.K., Marsh, D.R., Mlynczak, M.G., and Mast, J.C., Temporal variations of atomic oxygen in the upper mesosphere from SABER, *J. Geophys. Res.,* **115**, D18309, 2010.

Solomon, S., Garcia, G.G., Olivero, J.J., Bevilacqua, R.M., Schartz. P.R., Clancy, R.T., and Muhleman, D.O., Photochemistry and transport of carbon monoxide in the middle atmosphere, *J. Atmos. Sci.,* **42**, 1072-1083, 1985.

Spencer, J. E., and G. P. Glass, Some reactions of OH($v = 1$), *Int. J. Chem. Kinet.*, **9**, 111-122, 1977.

States, R.J., and Gardner, C.S., Thermal structure of the mesopause region (80-105 km) at 40°N latitude. Part 1: Seasonal Variations, *J. Atmos. Sci.,* **57**, 66-77, 1999.

Stevens, W.J., Das, G., Wahl, A.C., Krauss, M., and Neumann, D., Study of the ground state potential curve and dipole moment of OH by the method of optimized valence configurations, *J. Chem. Phys.,* **61**, 9, 3686-3699, 1974.

Steinfeld, J.I., Adler-Golden, S.M., and Gallagher, J.W., Critical survey of data on the spectroscopy and kinetics of zone in the mesosphere and thermosphere, *J. Phys. Chem. Ref. Data.,* **16**, 911, 41, 1987.

Strobel, D.F., Parameterisations of the atmospheric heating rate from 15 to 120 km due to O_2 and O_3 absorption of solar radiation, *J. Geophys. Res.,* **83**, 6225, 1978.

Summers, M.E., Zonally averaged trace constituent climatology, *Tech. Pub. NRL/MR/7641-93-7416, Nav. Res. Lab.,* Washington, D.C., 1993.

Summers, M.E., Conway, R.R., Siskind, D.E., Stevens, M.H., Offermann, D., Riese, M., Preusse, P., Strobel, D.F., and Rusell III, J.M., Implications of satellite OH observations for middle atmosphere H_2O and ozone, *Science,* **277**, 1967-1970, 1997.

Swider, Jr., W., and Gardner, M.E., On the accuracy of certain approximations for the Chapman function, *Appl. Opt.,* **8**(3), 725, http://dx.doi.org/10.1364/AO.8.000725, 1969.

T

Takahashi, H., Sahai, Y., Clemesha, B.R., Batista, P.P., and Teixeira, N.R., Diurnal and seasonal variations of the OH(8,3) airglow band and its correlation with OI5577A, *Planet. Space Sci.,* **25**, 541-547, 1977.

Takahashi, H., and Batista, P.P., Simultaneous measurements of OH (9,4), (8,3), (7,2), (6,2) and (5,1) bands in the airglow, *J. Geophys. Res.,,* **86**, 5632, 1981.

Taylor, G.I., The oscillations of the atmosphere, *Proc. Roy. Soc.,* **156**, 318-326, (1936).

Thorne, A.P., *Spectrophysics,* 2nd Edition, Chapman and Hall, London, 1988.

Torr, M.R., Torr, D.G., Ong, R.A., and Hinteregger, H.E., Ionization frequency − I. Ionization frequencies for major thermospheric constituents as a function of solar cycle 21, *Geophys, Res. Lett.,* **6**, 771, 1979.

Torr, M.P., Richards, P.G., and Torr, D.G., A new determination of ultraviolet heating efficiency in the thermosphere, *J. Geophys. Res.,,* **85**, 6819, 1980a.

Torr, M.R., Torr, D.G., and Hinteregger, H.E., Solar flux variability in the Schumann-Runge continuum as a function of solar cycle 21, *J. Geophys. Res.,,* **85**, 6063, 1980b.

Turnbull, D.N., and Lowe, R.P., Vibrational population distribution in the hydroxyl night airglow, *Can. J. Phys.,* **61**, 244, 1983.

Turnbull, D.N., *An empirical determination of the electric dipole moment function and transition probabilities of* OH^2II, PhD Thesis, The University of Western Ontario, 1987.

Turnbull, D.N., and Lowe, R.P., An empirical determination of the dipole moment function of $OH(X^2II)$, *J. Chem. Phys.,* **89**, 5, 1988.

Turnbull, D.N., and Lowe, R.P., New hydroxyl transition probabilities and their importance in airglow studies, *Planet. Space. Sci.,* **36**, 6, 723-738, 1989.

V

Volland, H., *Atmospheric tidal and planetary waves*, Kluwer Academic Publishers, Dordrecht, Holland, 1988.

von Savigny, C., Eichmann, K.U., Robert, C.E., Burrows, J.P., and Weber, M., Sensitivity of tropical mesopause temperatures to the 27-day solar cycle, *Geophys, Res. Lett.,* **39**, L21804, 2012a.

von Savigny, C., McDade, I.C., Eichmann, K.U., and Burrows, J.P., On the dependence of the OH* Meinel emission altitude on vibrational level: SCIAMACHY observations and model simulations, *Atm. Chem. Phys. Discussions*, **12**, 5817-5849, 2012b.

W

Ward, W.E., Wang, D.Y., Solheim, B.H., and Shepherd, G.C., Observations of the two-day wave in WINDII data during January 1993, *Geophys, Res. Lett.,* **23**, 2923-2926, 1996.

Ward, W.E., A Simple Model of Diurnal Variations in the Mesospheric Oxygen Nightglow, *Geophys, Res. Lett.,* **26**, 3565-3568, 1999.

Wayne, R.P., *Chemistry of Atmospheres: An introduction to the chemistry of the atmospheres of Earth, the planets and their satellites,* 1st Edition, Clarendon Press, 1985.

Weinstock, J., Nonlinear theory of gravity waves: momentum deposition, generalized Rayleigh friction, and diffusion, *J. Atmos. Sci.,* **35**, 1022, 1982.

Werner, H.J., Rosmus, P., and Reinsch, E.A., Molecular properties from MCSCF-SCEP wave functions. I. Accurate dipole moment functions of OH, OH^- and OH^+, *J. Chem. Phys.,* **79**, 905, 1983.

Wiens, R. H., and Weill, G., Diurnal, annual and solar cycle variations of hydroxyl and sodium nightglow intensities in the Europe-Africa sector, *Planet. Space Science*, **21**, 1011–1027, 1973.

Wilke, C.R., Diffusional Properties of Multicomponent Gases, *Chem. Eng. Prog.,* **46**, 95-104, 1950.

Winick, J.R, Carovillano, R.L., and Forbes. J.M., Photochemical processes in the mesosphere and lower thermosphere, in *Carovillano*, R.L. and *J. M. Forbes* (eds.). *Solar- Terrestrial Physics*. Reidel, Dordrecht, Boston and Lancaster, (1983). 677-732, 1983.

Winick., J.R., Picard, R.H., Sharma, R.D., and Nadile, R.M., Oxygen singlet delta 1.58 micrometer (0-1) limb radiance in the upper stratosphere and lower mesosphere, *J. Geophys. Res.,* **90**, 9804-9814, 1985.

Woodgate, G.K., *Elementary Atomic Structure*, Oxford University Press, Oxford, 1980.

X

Xu, J.Y., Simulation of response of sodium layer to the propagation of gravity wave, *Sci. China Ser E-Tech Sci.,* **47**, 335-342, 2004.

Xu, J.Y., Smith, A.K., Yuan, W., Liu, H.L., Qian Wu, and Mlynczak, M.G., Global structure and long-term variations of zonal mean temperature observed by TIMED/SABER, *J. Geophys. Res.,* **112**, D24106, 2007.

Xu, J.Y., Smith A.K., Liu, H.L., Yuan, W., Qian, Wu., Guoying, Jiang., Mlynczak, M.G., Russell, J.M., and Franke, S.J., Seasonal and QBO variations in the migrating diurnal tide observed by TIMED, *J. Geophys. Res.,* **114**, D13107, 2009.

Xu, J., Smith, A.K., Jiang, G, Gao, H., Wei, Y., Mlynczak, M.G., and Russell, J.M., Strong longitudinal variations in the OH nightglow, *Geophys, Res. Lett.,* **37**, L21809, 2010.

Xu, J., Gao, H., Smith, A.K., and Zhu, Y., Using TIMED/SABER nightglow observations to investigate hydroxyl emission mechanisms in the mesopause region, *J. Geophys. Res.,* **117**, D02301, 2012.

Y

Yiğit, E., Aylward, A.D., and Medvedev, A.S., Parameterization of the effects of vertically propagating waves for thermosphere general circulation models: Sensitivity study, *J. Geophys. Res.,D: Atmospheres,* **113**, 13, D19106, 2008.

Yiğit, E., and Medvedev, A.S., Heating and cooling of the thermosphere by internal gravity waves, *Geophys, Res. Lett.,* **36**, L14807, 2009.

Z

Zhang, S.P., and Shepherd, G.G., The influence of the diurnal tide on the O(1S) and OH emission rates observed by WINDII on UARS. *Geophys. Res. Lett.* **26**, 529-532, 1999.

Zhu, X., Yee, J.H., Lloyd, S.A., and Strobel, D.F., Numerical modelling of chemical-dynamical coupling in the upper stratosphere and mesosphere, *J. Geophys. Res.,* **102**, D11, 23,995-24,012, 1999.